Monolithic integrated reflective transceiver in indium phosphide

Monolithic Integrated Reflective Transceiver in Indium Phosphide

Cover illustration by Marcel Lenoire

Monolithic Integrated Reflective Transceiver in Indium Phosphide

PROEFSCHRIFT

ter verkrijging van de graad van doctor
aan de Technische Universiteit Eindhoven,
op gezag van de rector magnificus, prof.dr.ir. C.J. van Duijn,
voor een commissie aangewezen door het College voor Promoties
in het openbaar te verdedigen op
donderdag 18 juni 2009 om 16.00 uur

door

Ling Xu

geboren te Anhui, China

Dit proefschrift is goedgekeurd door de promotor:

prof.dr.ir. M.K. Smit

Copromotor:
dr. X.J.M. Leijtens

This work was supported by the Dutch Ministry of Economic Affairs through the Freeband Project Broadband Photonics Access, the Smartmix project Memphis and the NRC photonics grant.

Typeset using LyX, printed in The Netherlands.
Cover illustration by Marcel Lenoire

A catalogue record is available from the Eindhoven University of Technology Library

Xu, Ling

Monolithic Integrated Reflective Transceiver in Indium Phosphide
Proefschrift. – ISBN: 978-90-386-1891-3
NUR959
Trefw.: opto-elektronica / geïntegreerde optica / modulatoren / optische telecommunicatie .
Subject headings: optoelectronic devices / integrated optoelectronics / electro-optical modulation / optical fiber communication.

to my baba, mama and Brian

Contents

Chapter 1

Introduction

This chapter briefly describes the reason of deploying a fiber-to-the-home (FTTH) network, the evolution of the user access network, and the architecture of an optical access network. A dynamically reconfigurable time and wavelength division passive optical network (TDM-WDM-PON) developed in the Broadband Photonics Project (BBP) is introduced, and the motivation for developing a monolithic integrated reflective transceiver is explained and the goal of the research is given. Next, the development history of the bi-directional transceiver is reviewed. The main components in the integrated bi-directional transceiver are discussed, and considerations on the choices made for each component in the transceivers in this thesis are given. Finally, the outline of the thesis is presented.

1.1 Introduction

Bandwidth demand from the user has driven the explosion of the communication traffic volume [1]. The statistics show that the monthly internet traffic has reached more than 20 Gbytes per capita in some regions at the year-end of 2008, such as Hongkong and South Korea. The average annual internet traffic in the backbone network is doubling every two years [2, 3].

With users' increasing demand for always-on fast internet communication, video-based multimedia, fast peer-to-peer file transfer, high definition TV, on-line gaming, remote medical care and remote working besides conventional services, such as voice telephone, TV, and radio, the last mile continues to be a major bottleneck in the internet [4]. Its low bandwidth and low flexibility prevent the deployment of new services and the development of new applications [5].

Since the beginning of 1990s, the technology used for the user access network has experienced a number of generations from the analog telephone line, integrated services digital network (ISDN), digital subscriber line (Asymmetric DSL (ADSL) and Very-high-bitrate DSL (VDSL)), cable TV (CaTV) to fiber-to-the-home (FTTH). The bandwidth has been upgraded from several Kbit/s over the telephone line to Gbit/s over passive optical networks

	Bandwidth[1]	access medium	distance limited[2]	bandwidth limited	DVD movie [3] download time
FTTH	1.25 Gbit/s	fiber	No	No	30.4 s
FTTH	622 Mbit/s	fiber	No	No	1 min
FTTH	155 Mbit/s	fiber	No	No	4.04 min
VDSL	50 Mbit/s	twisted pair	500 m	Yes	12.53 min
CaTV	40 Mbit/s	coax	1000 m	yes	15.67 min
ADSL	10 Mbit/s	twisted pair	2500 m	Yes	1.04 hour
ISDN	128 Kbit/s	twisted pair	7 km	Yes	3.4 days
Modem	56 Kbit/s	twisted pair	>7 km	Yes	7.8 days

[1] Currently, the maximum available bandwidth per user within the limited distance if applicable.
[2] The distance between the headend station to the user home.
[3] Based on 4.7 Gbytes

Table 1.1: Current maximum available bandwidth per user at user access network for different access line technologies.

(PON) in some regions. The features of the popular existing access lines are compared in table 1.1 in terms of the maximum available bandwidth per user, the distance limitation and the bandwidth scalability. Although VDSL and CaTV have evolved into a higher speed, they have reached their limit and are available only within a shorter reach due to radio frequency (RF) attenuation over the twisted pair/coax [4]. It is generally agreed that FTTH will be the ultimate solution to the demands on the bandwidth in the access network due to its tremendous bandwidth as compared to the coax and the copper twisted pair [4–8].

Currently, the most widely available bitrate of FTTH has reached 100 Mbps per subscriber in Asia, Europe and North America. In Japan, the DSL subscriber growth rate began to fall in 2004 while the number of FTTH subscribers keeps steadily growing, Fig. 1.1. The reason was that the price of FTTH was adjusted and started to be comparable to that of DSL and others. A lot of subscribers started to shift from DSL to FTTH for the larger bandwidth and the number of subscribers for FTTH has surpassed DSL in Japan at the end of 2008. Outside Japan, the number of subscribers for FTTH keeps increasing as well.

Besides the high bandwidth-price ratio, a study commissioned by the FTTH Council Europe has suggested that fiber to the home is a green technology considering the environmental costs associated with the use of non-renewable energy and emissions of greenhouse gases [9].

However, the bandwidth demand at the user access network will keep increasing, and it has been estimated that the required bandwidth will surpass 1 Gbit/s per home in the future 10 years at the user access network [10]. Economical upgradability and scalability of an access network have to be taken into account. To meet the challenges in the bandwidth, economical scalability and cost-effectiveness, a dynamic reconfigurable network architecture has been proposed and studied in the Broadband Photonics project (BBP), within which the research presented in this thesis has been carried out to develop a cost-effective

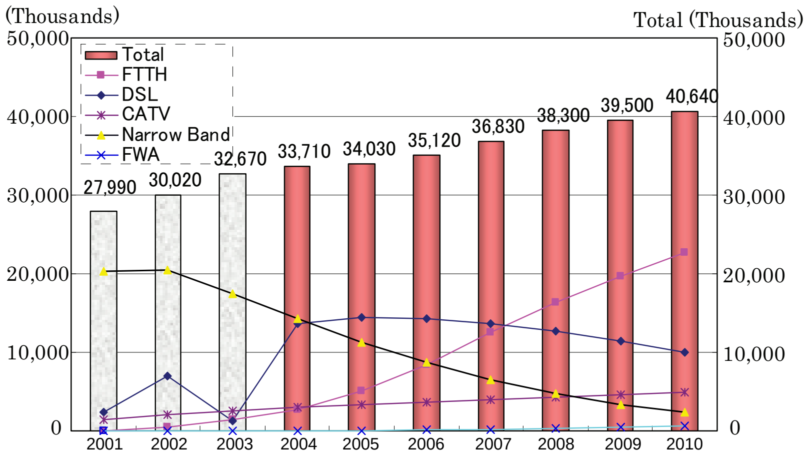

Figure 1.1: Current and predicted internet penetration (number of subscriptions) by types of access line (estimated by Yano Research Institute Ltd.: As of March 15, 2005) (source: Yano Research, Japan)

transceiver, the optical circuit of the optical network unit (ONU) which is a module installed at each user's home to process the downstream and the upstream data.

One of the main cost drivers in the user network is the cost of the equipment inside the network, especially the ONU, since it has a direct impact on the cost per customer. In a multi-wavelength network, one way to reduce the cost of the user access network is to use a colorless transceiver, instead of a wavelength specific one. In this way the transceivers at each home can be identical, suitable for mass production, therefore the cost can be reduced.

The work presented in this thesis focuses on developing a colorless transceiver for the proposed dynamically reconfigurable access network in the BBP project. The goals of the research on the transceiver are to:

- develop the concept of a high bandwidth and cost effective transceiver. The target bandwidth is first at 1 Gbit/s, and then upgrade to 10 Gbit/s;

- optimize the performance of the components of the transceiver to meet the specifications for the network operation;

- investigate the possibility to realize a cost effective monolithically integrated transceiver based on currently available material and technology in the COBRA research institute.

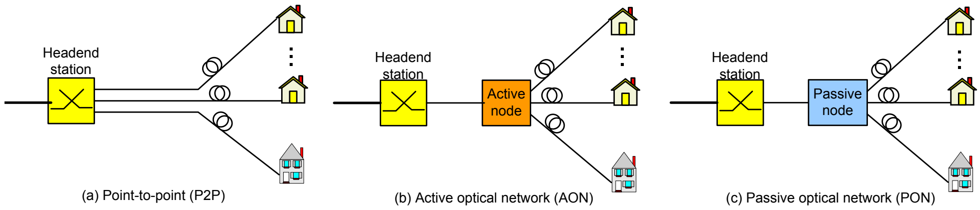

Figure 1.2: Three different fiber access network architectures: (a) Point-to-point (P2P), (b) active optical network (AON), (c) passive optical network (PON).

1.2 Outline of this chapter

In section 1.3, a short introduction on the optical access network architectures will be given. The advantages and disadvantages of each scheme will be briefly discussed.

In section 1.4, the agile TDM-WDM-PON proposed in the Broadband Photonics Project is presented. Some features between the agile TDM-WDM-PON in the BBP project and the other popular PONs are compared. The wavelength allocation scheme in the BBP project is presented, and the target specifications of the first colorless transceiver are specified.

In section 1.5, several operation methods to realize a colorless transceiver are described. The operation methods of the reflective transceiver in this thesis are specified and the reasons are addressed.

In section 1.6, previous works on the transceivers are reviewed. The comparison between different transceivers is presented.

In section 1.7, the components of the transceiver are discussed, and the reasons for the choices for each component are given.

In section 1.8, the outline of the thesis is given.

1.3 Optical access network

Different fiber access network architectures can be deployed in a FTTH network, such as point-to-point (P2P), active optical network (AON), and PON [4], as shown in Fig. 1.2. In the P2P architecture, each home is connected with the local exchange with its own optical fiber, which requires high costs in the installed fiber plant and in the line terminating equipment. In an AON, one single fiber carries all traffic to an active node which is connected with several end users through branching fibers. Comparing with the P2P architecture, there are much fewer optic fibers installed at the local exchange, and the wavelength resources in the headend station can be shared by all the end users connected with the active node. Consequently, it is more cost-effective than P2P. However, the active node needs constant powering and maintenance. PON has the same architecture as the AON, except that the active node is replaced by a passive node, such as a power splitter/combiner or a wavelength demultiplexer. The detailed comparison between AON and PON can be referred to [11, 12].

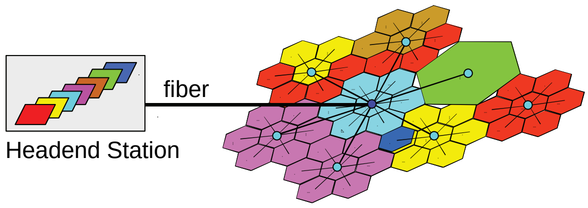

Figure 1.3: Dynamically routing wavelengths to access network cells for flexible service provisioning.

Basically, PON is a better choice for network operators who would like to supply a very large number of users with a modest cost in the network technology, while AON is beneficial for high profit end customer segments, such as business customers, universities, local authorities, since in these cases flexibility, quality and security are demanded [12].

1.4 A dynamic reconfigurable user access network

Taking the future network scalability into account, a dynamic reconfigurable PON for the user access has been proposed by combining the advantages of both wavelength division multiplexing (WDM) technique and time division multiplexing (TDM) technique, and this proposed architecture is referred to as agile TDM-WDM-PON. In the next sections, firstly we explain the concept of the agile TDM-WDM-PON, and then compare the difference between the agile TDM-WDM-PON, WDM-PON and TDM-PON. In section 1.4.4, the wavelength allocation schemes in the agile TDM-WDM-PON are introduced and discussed. The target specifications of the transceiver in the agile TDM-WDM-PON is presented in section 1.4.5.

1.4.1 Introduction of agile TDM-WDM-PON

By assigning the wavelengths dynamically to the ONUs through wavelength routing, the access network capabilities can be significantly enhanced [4, 13]. The idea of the dynamic routing can be understood from Fig. 1.3 [4]. In the headend station, multiple wavelength channels (shown in different colors) are fed to the access network through the optical fiber. By wavelength-selective routing which is controlled by the operator, each wavelength channel can be assigned to one or more regional cells. Within the regional cell, each wavelength channel can be either allocated for only one user or shared among several users through a TDM access strategy by giving each user a time slot in this wavelength channel [4]. Thus a very flexible TDM-WDM PON is obtained. In this way, the aggregate capacity available from the headend station can be shared or partitioned flexibly among network areas in order to meet the dynamic traffic demands at the user site.

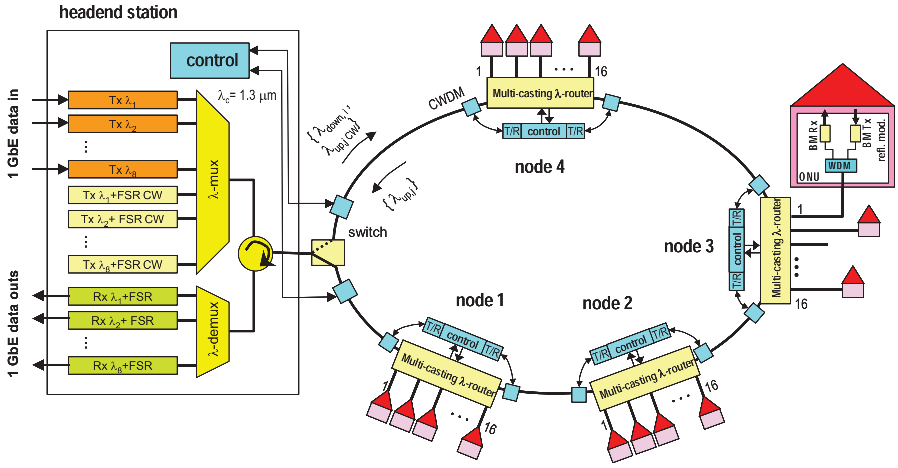

Figure 1.4: Target access network architecture proposed in BBP: a reconfigurable TDM-WDM-PON.

1.4.2 Target reconfigurable access network and its key components

The proposed architecture of the reconfigurable network in the BBP project is shown in Fig. 1.4. It is forseen first to deliver 1 GbE (so 1.25 Gbit/s) capacity per wavelength channel to 64 homes in total connected with 4 different passive nodes. The headend station delivers two wavelength channels per home, one for the downstream and the other one for the upstream. In total, eight pairs of wavelength channels are deployed in the headend station, and a wavelength multiplexer is used to combine the downstream and continuous wave (CW) source for the upstream channel.

The control unit in the headend station communicates with the λ-routing nodes and with the optical protection switch. The network operator thus can control the capacity allocation among the homes, and can protect the network against a single fiber break. This control channel is preferably implemented out-of band with respect to the data signal channels, in order not to interfere with or depend on these. The control channel may be realized on a common wavelength channel in the 1.3 μm band, which is shared and easily accessible by each node deploying low-cost low bit rate electro-optical transceivers operating with an Ethernet protocol. The 1.3 μm control channel is separated from the data channels by a coarse WDM (de-)multiplexer (CWDM) at each side of a node. At the headend station, the control channel can be injected in both counter propagating ways, depending on failure conditions in the ring. For example, when there is no failure, the control channel may be injected only clockwise. When there is a fiber break between node 2 and 3, it may be injected both clockwise and counterclockwise, in order to reach every node.

In the wavelength routing node, as shown in Fig. 1.5, only the wavelengths which meet the resonance condition of the ring are added or dropped. Therefore, one wavelength can

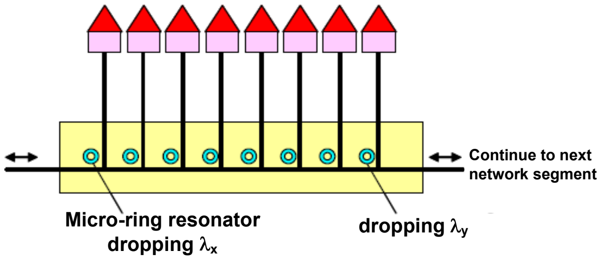

Figure 1.5: Schematic view of a wavelength router composed of micro-ring resonators.

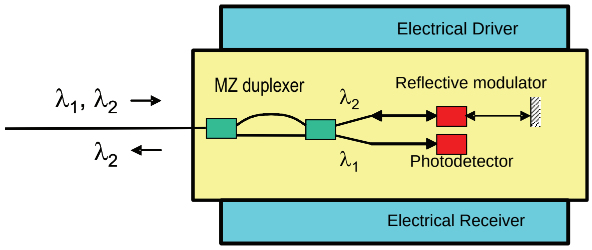

Figure 1.6: The schematic view of an integrated ONU, which is composed of a transceiver, an electrical driver, and an electrical receiver.

be dropped for one home or all homes by tuning the resonance conditions of the rings. The micro-ring resonators in the BBP project are designed with a free spectral range (FSR) corresponding to the channel spacing between the upstream and the downstream channel, thus both the upstream and the downstream channel from the headend station are dropped at the same micro-ring resonator, and the returned modulated upstream channel is added. The wavelength router is controlled by the headend station to allocate capacity according to actual demand. For detailed information about the design and the realization of the wavelength ring router we refer to [14].

At each home, a reflective ONU is deployed to handle both the upstream and the downstream data, as shown in Fig. 1.6. It consists of three parts: an optical transceiver, an electrical driver and an electrical receiver. The two incoming wavelengths from the headend station are separated by a wavelength duplexer (WD), and then guided to a reflective modulator and a photodetector respectively. The downstream data is detected by the photodetector and amplified by the receiver of the ONU, and the CW light is modulated by the upstream data through the driver, reflected back through the router and received by the burst mode (BM) receiver (Rx) at the headend station.

As introduced in section 1.4.1, the wavelength channel allocated to a cell is not fixed, therefore the ONU installed at user's home needs to be non-wavelength specific. The colorless reflective transceiver is the subject of this thesis, and it will be investigated based on InP monolithic integration technology.

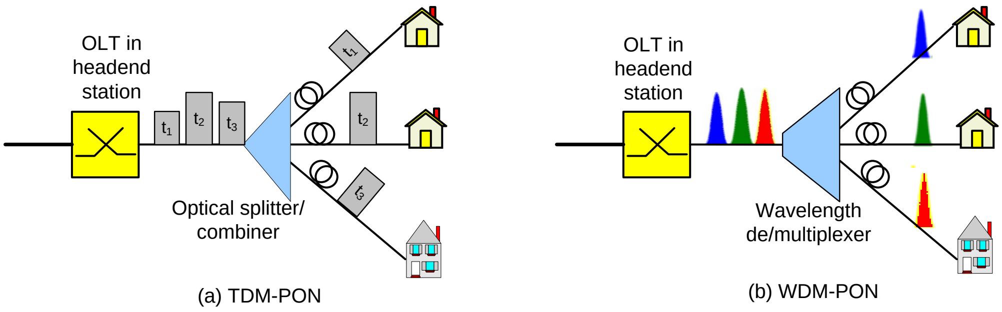

Figure 1.7: Time division multiplexing PON (TDM-PON) and wavelength division multiplexing PON (WDM-PON).

1.4.3 Comparison with TDM-PON and WDM-PON

Besides the proposed agile TDM-WDM-PON, other well known PON solutions are TDM-PON and WDM-PON, as shown in Fig. 1.7. The following comparison between those solutions is based on the assumption that the bandwidth per wavelength channel is 1.25 Gbit/s, and the number of the users is 64 after the passive node in the TDM-PON and the WDM-PON.

TDM-PON has received attention for its high-speed data rate at relatively low operating cost and moderate complexity. It has been successfully deployed in Japan and in the USA for broad bandwidth. In the TDM-PON (Fig. 1.7(a)), several users share the same wavelength(s) by dividing the signal into different time slots. This method requires careful synchronization of the packet transmission at the OLT and the ONUs, therefore the cost of the terminal equipment is high. The disadvantage of this system is that the total bandwidth available per user is limited by the total number of the users. The average data rate per home therefore is 1.25 Gbit/s/64 = 19.5 Mbit/s. The maximum number of users is limited by the power splitting ratio of the optical splitter. Since each home receives only a fraction of the transmitted power after the optical power splitter, the link power budget available is limited.

In the WDM-PON (Fig. 1.7(b)), each home gets a dedicated wavelength channel which is determined by the wavelength de/multiplexer, therefore each user gets full bandwidth, and the data communication between the OLT and the ONU can happen at any time, and there is no interaction or coupling between the subscribers on a WDM-PON. It is easy to upgrade the system capacity by changing the transceiver in the headend station and the ONU at user's home. Since there is no power splitting, when the insertion loss of wavelength de/multiplexers is low, the link power budget is high, hence allows a long fiber feeder link. However, since each user always gets full bandwidth, the efficiency of the capacity allocation is low. The cost of WDM-PON is high since each user requires a dedicated source. For 64 users, 64 transceivers are needed in the headend station. Accommodating more homes in the network requires adding more transceivers at OLT and users' home and replacing the wavelength de/multiplexers at the passive node.

	agile TDM-WDM-PON	TDM-PON	Static WDM-PON
Average data rate per home (Gbit/s)	0.155	0.0195	1.25
Peak data rate per home (Gbit/s)	1.25	1.25	1.25
Number of homes	64	64	64
Statistical multiplexing	yes	yes	no
Maximum length of the subscriber access line	(moderately) long	short	long
Cost of the network technology	(moderately) high	low	high
Efficiency of the capacity allocation	high	(moderately) high	low
Cost in scaling to more homes	low	low	high

Table 1.2: Comparison of some PON solutions based on a bandwidth of 1.25 Gbit/s per wavelength channel and 64 users in the TDM-PON and the WDM-PON.

The agile TDM-WDM-PON, as shown in Fig. 1.4, combines the advantages of both the TDM-PON and the WDM-PON. A wavelength channel can be fully devoted to a single user or can be distributed to several users. When a user requires the full capacity, it can be achieved by allocating a wavelength pair only for this user. The agile TDM-WDM-PON can bring all eight wavelength pairs (Fig. 1.4) in the headend station into a common resource pool, then the available bandwidth of the agile TDM-WDM-PON is 8×1.25 Gbit/s, i.e. a 10 Gbit/s. The average available capacity per home is 10 Gbit/s/64 = 155 Mbit/s. By the wavelength routing in the nodes, the signal power is efficiently distributed, which favors a high link power budget. Upgrading of the network to higher capacity is relatively easy by just adding a transceiver with a new wavelength pair in the headend station (provided that the added pair is within the tuning range of the wavelength router). Adding a new group of homes requires adding a new wavelength router. However, the maximum number of the users per wavelength router is limited by the power tap ratio of the wavelength router when the system is operating in the broadcasting mode.

Table 1.2 summarizes the main characteristics of the three PON alternatives. It highlights the strengths of the reconfigurable agile TDM-WDM-PON.

1.4.4 Wavelength allocation schemes in agile TDM-WDM-PON

Two different wavelength allocation schemes have been considered in the reconfigurable access network. The first scheme uses 8 pairs of interspersed upstream and downstream wavelengths with a 200 GHz channel spacing (interspersed duplexer), and the wavelength ranges from 1530 nm to 1560 nm, as shown in Fig. 1.8. Another wavelength allocation scheme, Fig. 1.9, divides the whole wavelength band into one guard band (150 GHz) and two subbands. The guard band is located between two subbands which consist of the 8 down-

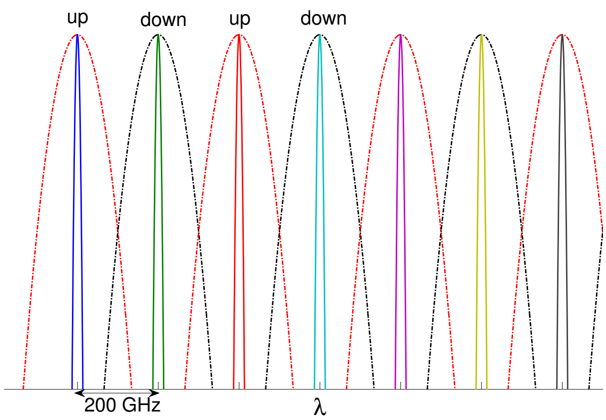

Figure 1.8: Incoming wavelengths (narrow bands) from the local exchange with the passbands of the wavelength duplexer whose channel spacing between upstream and downstream is 200 GHz.

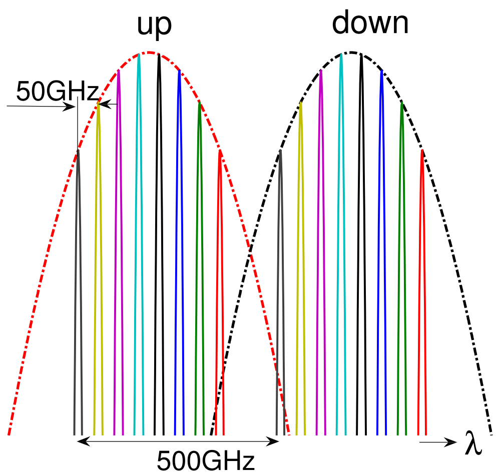

Figure 1.9: Incoming wavelengths (narrow bands) from the local exchange with the passbands of the wavelength duplexer whose channel spacing between the upstream and the downstream is 500 GHz. Within each downstream or upstream passband there are eight wavelengths spaced 50 GHz.

Parameters	value	unit
Return loss	>45	dB
wavelength range	1540~1550 1530~1560	nm
Polarization dependent loss	0.5	dB
Tuning delay	<40	ms
RSOA		
Fiber-fiber gain of the RSOA	0	dB
Bandwidth of the upstream	1.0	Gbit/s
Photoreceiver		
Sensitivity of the photoreceiver	−25	dBm
Bandwidth of the downstream	1	GHz
Tunable wavelength duplexer		
Fiber-chip coupling loss	<4	dB
Insertion loss of the wavelength duplexer	<3	dB
Isolation level of the wavelength duplexer	>15	dB
Tuning range of the wavelength duplexer	2π	rad

Table 1.3: Target specifications on the transceiver in the agile TDM-WDM-PON.

stream channels and 8 upstream channels respectively. Within the subband, the channels are spaced by 50 GHz, and the space between the upstream wavelength and downstream wavelength is 500 GHz. The whole operation wavelength range is from 1540 nm to 1550 nm.

The reason for selecting the second wavelength allocation scheme (500 GHz channel spacing) is to ease the requirements on the thermally tunable ring wavelength router. The first scheme puts stricter requirements on the design of the ring wavelength router, it has to be able to be tuned up to 30 nm from 1530 nm to 1560 nm to cover all the wavelength pairs in the local exchange, which would cause a higher electrical power dissipation. In the second allocation scheme it only needs to be tuned within a 10 nm range from 1540 nm to 1550 nm.

Another difference between these two schemes is the tuning of the duplexer. In principle, once the interspersed duplexer is tuned to maximize the transmission of a pair of wavelengths, it should be kept there for the other wavelength pairs, while the grouped duplexer needs fine-tuning whenever the network is reconfigured. In Chapter 2, the wavelength duplexers will be discussed in detail.

1.4.5 Target specifications of the transceiver

At the start of the BBP project, we have set target specifications for the integrated transceiver and they are listed in table 1.3.

- Return loss: every component in the network introduces reflections. If the reflection is too high, interference between the transmitted and reflected data degrades the signal quality. Combining the anti-reflection (AR) coating and angled facet, a facet reflectivity as low as 10^{-5} can be achieved [15]. Besides, low on-chip reflection is also important to lower the crosstalk between the reflected upstream data and the downstream data inside the transceiver.

- Wavelength range: this depends on the wavelength allocation scheme, see section 1.4.4.
- Polarization dependent loss: In an installed network, there is no control over the polarization state of the incoming light. Therefore, all components have to be polarization independent. The polarization dependent loss has to be below 0.5 dB. Polarization independence is very hard to realize, especially for the SOA. In this work to prove the concept, the polarization dependence of the SOA was not considered.
- Tuning delay: the tuning time should stay below 40 ms which is the network reconfiguration time.
- Fiber-fiber gain of the RSOA: the RSOA can lase due to the residual reflections when integrated with other components, therefore the gain of the RSOA is limited. The target fiber-fiber gain is 0 dB, which compensates for the fiber-chip coupling loss and the insertion loss of the wavelength duplexer.
- Bandwidth of the upstream: the first target upstream bandwidth is 1.0 Gbit/s by directly modulating the RSOA.
- Sensitivity of the photodetector: the requirement on the photodetector sensitivity is −25 dBm at 1.0 Gbit/s.
- Bandwidth of the downstream: 1 Gbit/s downstream data is delivered from the headend station, and the photodetector can easily achieve this bandwidth. The photodetector which had been developed within the COBRA research institute reached more than 30 GHz [16]. The main target for the photodetector development will be investigating the bandwidth limit when the photodetector is in an SOA layer stack.
- Fiber-chip coupling loss: fiber-chip coupling loss is due to the mode mismatch between the waveguide mode and a tapered, lensed fiber, about 4 dB.
- Insertion loss of the wavelength duplexer: the insertion loss specified here is an on-chip loss, <3 dB.
- Isolation level of the wavelength duplexer: the isolation level is the power difference between the upstream and downstream channel at one of the output ports of the duplexer. The target isolation level is higher than 15 dB within the wavelength range to reduce the optical crosstalk between the upstream and the downstream data.
- Tuning range of the wavelength duplexer: the required phase change in tuning should be 2π to sufficiently cover all the wavelength pairs in the headend station.

1.5 Operation methods to realize a colorless transceiver

Several schemes have been proposed to build a colorless transceiver at the user site, such as spectrum-slicing [17, 18], injection-locking of the laser [19–21], laser light injected in a reflective semiconductor optical amplifier (RSOA) [22] and RSOA re-modulation [23]. Spectrum slicing involves a broadband optical source with a narrow band periodic optical slicing filter in the optical network splitting point. The filter separates the broadband spectrum into several unique wavelengths for WDM channels. Since only a narrow part of spectrum of the original source is used, the power of the filtered channel is low. In [17], a spectral slicing WDM-PON using a wavelength-seeded RSOA has achieved 1.25 Gbit/s upstream operation over 25 km. However, this method also has a limitation on the modulation speed because of several sources of noise such as intensity noise and optical beat noise and chromatic dispersion which are inherent properties of multimode or broadband sources [24]. This operation scheme is not suitable for the agile TDM-WDM-PON proposed in the BBP project because the agile TDM-WDM-PON routes any wavelength pair in the headend station to the transceiver, while the sliced wavelength in this operation scheme is fixed by the narrow band optical filter.

The injection-locking method uses a multimode slave laser, such as a Fabry-Perot laser (FP), which excites only one mode when a well-adjusted external optical signal is coming in. The injected light can be from a filtered broadband source [19–21] or a coherent laser [25]. In [19, 20], a low cost WDM-PON based on amplified spontaneous emission (ASE) injected in a Fabry-Perot laser diode was demonstrated with 155 Mbit/s for both downstream and upstream. This scheme has been commercialized in South Korea since 2005. The data rate is limited by the high intensity noise due to the broadband source. In comparison, the CW laser injection locking reduced the intensity noise and reached higher bit rates up to 10 Gbit/s [25] in the lab. However, this method generally requires careful control of the modulation index, the laser bias current and the injection power and the frequency of the external optical signal [26]. It is difficult to realize an injection locking transceiver in an integrated circuit since it needs two on-chip reflectors to form the Fabry-Perot cavity.

In the remodulation WDM-PON scheme proposed in [23, 27], the downstream optical signal is remodulated by the RSOA for upstream transmission. In this scheme, the transmission performance of the upstream signal is degraded due to the remodulation of the modulated downstream signal [22].

Different from the laser injection locking scheme in which the slave laser is pumped above the threshold current, the laser light injected RSOA scheme employs a RSOA which is pumped below the threshold current. A continuous wave (CW) laser light from a single mode laser diode is injected into the RSOA and directly modulated with the upstream data through the injection current which changes the gain of the RSOA, thus the amplitude of the light. Since the injected light is single mode, the spontaneous-spontaneous beating noise and chromatic dispersion can be avoided. Another advantage of this method is the large operation optical bandwidth of the RSOA which can be easily maintained and all the wavelengths in the local exchange can be shared by the RSOAs at the end users. In [22], it has demonstrated that a WDM-PON can operate at 1.25 Gbit/s with a low optical injection power below −27 dBm. However, the performance of this scheme is influenced by the feedback of the optical signals into the RSOA and by the Rayleigh backscattering. Furthermore, the spurious optical reflections in the fiber network caused by bad splices or connectors need to be avoided.

Based on the network architecture (Fig. 1.4) and the feasibility of monolithic integration with a photodetector and a wavelength duplexer, we will investigate two operation schemes to achieve colorless ONU: laser injected RSOA modulator and employing a reflective Michelson phase modulator.

1.6 Previous works on the transceivers

A variety of optical transceivers for broadband optical access networks have been reported, based on micro-optic integration, hybrid integration of laser and detector chips on a Planar-Lightwave-Circuit (PLC) [28–30] or on a single Photonic Integrated Circuit (PIC) [31–40], shown in Table 1.4.

Based on the micro-optic integration approach, the light which comes from the network or the laser diode propagates in the free space inside the transceiver, and two wavelengths for upstream and downstream data are separated by a thin film filter. A schematic view of this type of transceiver is shown in Fig. 1.10(a). The downstream data (λ_1) is reflected by the thin film filter while the upstream data generated by the laser at λ_2 passes through the filter to the network. This approach involves prepackaging of the discrete components, such as the laser diode and the photodetector, and later assembling them together with lenses and a thin film filter (TFF) in a common housing. This type of bi-directional transceiver has been commercialized and demonstrated in [20] with 155 Mbit/s colorless operation for both the downstream and the upstream data by slicing the spectrum of the superluminescent diodes. However, this type of transceiver does not meet the specification issued in the reconfigurable access network because a packaged laser is included.

Compared with the micro-optic approach, hybrid integration based on the PLC technology reduces the cost in the packaging because it doesn't package each active component separately. PLC technology offers an optical bench, on which optical parts such as the laser diode, the photodetector and an optical fiber can be mounted by passive alignment technology. This passive alignment technology enables to apply an automated assembling machine, thus enabling cost reduction and mass production [45]. Besides the cost reduction in the packaging, PLC technology can provide some or all passive optical functions as well, such as waveguiding [29], duplexing/triplexing [43], and they can be optimized individually for low optical transmission loss and low coupling loss with the optical fiber. In [30], a PLC-module containing an integrated Spot-Size converter to lower the fiber-chip coupling loss has been reported. However, in both the micro-optic approach and the PLC technology, some components of the transceiver, such as the laser, the photodetector and the TFF (if needed), still need to be fabricated and mounted separately, which later need to be aligned and assembled with the passive components, such as lenses or a duplexer/triplexer. This added complexity restricts the cost and volume scalability factors in the transceiver man-

Integration	WD	Tx	upstream data rate	downstream data rate	year	comm. [1]
Micro-optic	TFF	FP	155 Mbit/s	155 Mbit/s	2006 [20]	yes
PLC	TFF	DFB	– [2]	–	1996 [28,41]	yes
PLC	TFF	DFB	1.25Gbit/s	1.25 Gbit/s	2002 [30]	yes
PLC	TFF	DFB	1.25 Gbit/s	1.25 Gbit/s	2003 [29,42]	yes
PLC	DC [3]	FP	1.25 Gbit/s	1.25 Gbit/s	2006 [43]	no
PIC	in-line	DBR	200 Mbit/s	155 Mbit/s	1990 [32]	no
PIC	in-line	DFB	54 Mbit/s	155 Mbit/s	1998 [36]	no
PIC	in-line	DFB	155 Mbit/s	155 Mbit/s	2002 [40]	no
PIC	DC	DFB	2 GHz	500 MHz	1994 [33]	no
PIC	MZI [4]	DFB	622 Mbit/s	1.8 Gbit/s	1994/1995 [34,44]	no
PIC	DC	DFB	–	230 MHz	1996 [35]	no
PIC	Y-junction	DFB	500 Mbit/s	7 GHz	1996 [31]	no
PIC	Y-junction	DFB	–	–	1999 [39]	no
PIC	MZI	SOA	1 Gbit/s	14 GHz	this thesis	no
PIC	MZI	PHM	10 Gbit/s	35 GHz	this thesis	no

[1] Commercialized
[2] – means the data was not mentioned in the article.
[3] Directional coupler
[4] Mach-Zehnder Interferometer

Table 1.4: Overview of the bi-directional transceivers developed for the user access network. WD in the second column is a wavelength de/multiplexer which separates two wavelengths allocated for the upstream and the downstream respectively. The explanations for the items in the second column can be referred to Section 1.7.1. Tx in the third column is the transmitter modulated with the upstream data.

ufacturing. The bidirectional transceivers in both the micro-optic approach and PLC technology are commercially available.

A further cost reduction can be achieved by integrating all optical functions into a single Photonic Integrated Circuit (PIC), since the effort for module aligning, mounting and housing is strongly reduced as compared to hybrid integration [31, 34, 37, 46]. Several transceiver PICs in InP have been published based on different architectures and components [31, 34, 37, 39, 44, 46], as shown in Fig. 1.10. They have demonstrated the feasibility of compact size and good performance. However, up to now, there is no PIC transceiver commercialized due to some inherent technological challenges such as the suppression of the electrical and optical crosstalk, and the difficulties to lower the development and fabrication costs [37].

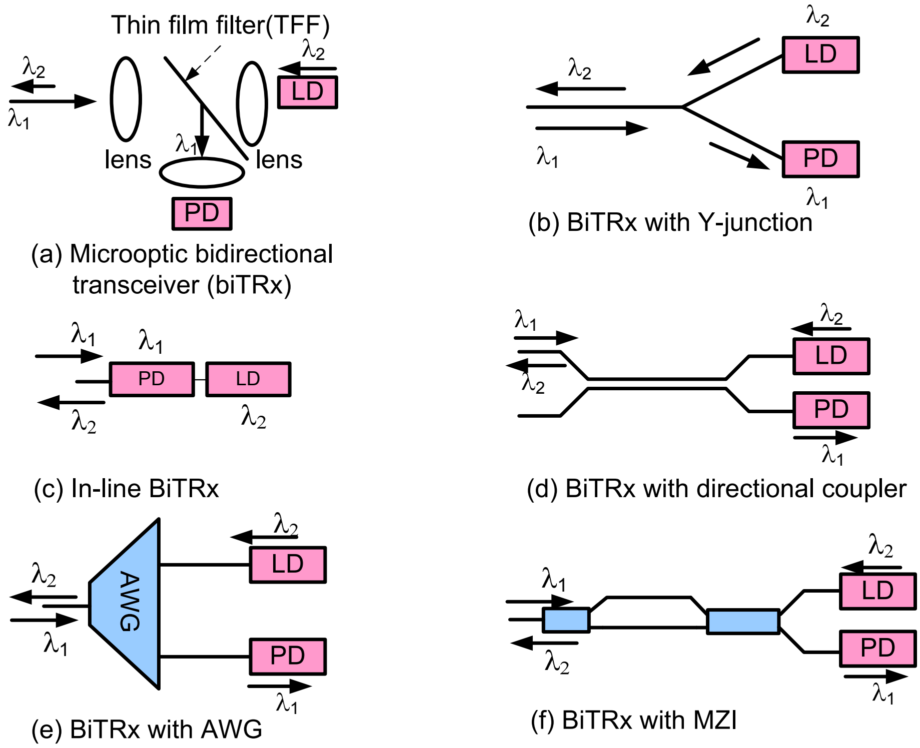

Figure 1.10: The schematic view of different types of developed bi-directional transceivers on Micro-optic approach (a), hybrid PLC technology (b,d,e,f) and PIC (b−f).

Besides the differences in the components and the performance, the previous transceivers are bi-directional, while the transceivers in this thesis are reflective. In bi-directional transceivers, a laser is adopted as the upstream transmitter, while in the reflective transceiver the upstream transmitter is a reflective colorless modulator, such as a reflective SOA or a reflective phase modulator.

In this thesis, the reflective transceivers will be investigated based on InP monolithic integration technology to lower the cost. The schematic views of the designed reflective transceivers in this thesis are shown in Fig. 1.11. In the first scheme, a RSOA functions as a modulator to transmit the upstream data, while in the other schemes a Michelson phase modulator is employed to be driven by the upstream data, which can achieve a higher modulation rate and better extinction ratio. The detailed design and measurement results are described in Chapter 7. The electrical and optical crosstalk level of the realized devices will be analyzed in Chapter 7 as well, and the fabrication technology which is used to fabricate the devices in Fig. 1.11 is described in Chapter 6.

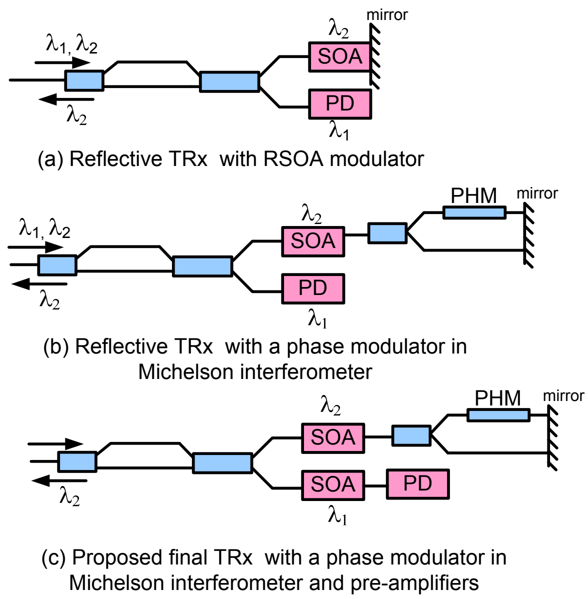

Figure 1.11: The schematic views of the colorless reflective transceivers based on InP technology described in this thesis. The un-named boxes are 1×2 and 2×2 3-dB coupler.

1.7 Components in the transceiver

As shown in Fig. 1.10, 1.11 and table 1.4, the transceiver consists of three basic components: a wavelength de/multiplexer that separates/routes the upstream and the downstream data; a receiver that detects the downstream data; and a modulator that carries the upstream data to the network.

For monolithic integration with the active components, the material system of the reflective transceiver is based on InP/InGaAsP which is available in the COBRA research institute. In the following part, we will give a short overview of the performance of different types of components and we will give our considerations for the final choice of the components to be integrated into our reflective transceivers.

1.7.1 Wavelength de/multiplexer

In table 1.4, all transceivers, except for the transceiver developed in this thesis, are developed for the wavelength pair with large spacing, for example 1310 nm/1490 nm (1550 nm).

The thin film filter (TFF) in table 1.4 is a polyimide or dielectric based multilayer filter which reflects one wavelength while transmitting the other wavelength [47]. This device is not suitable for monolithic integration with active components.

A Y-junction duplexer, as shown in Fig. 1.10(b), is based on the propagation constant difference between the fundamental mode and the first order mode. This type of wavelength de/multiplexer suffers from instabilities due to the large taper width which can support higher order modes that degrade the wavelength selectivity. Moreover, it is difficult to fabricate due to the stringent requirements on the lithographic resolution necessary to obtain a sharp intersection angle. Additionally, this device is relatively long, up to centimeters, due to the small effective index difference between the fundamental mode and the first order mode. It becomes especially long when the channel spacing between two wavelengths is small, which is the case in the Broadband Photonics project.

A directional coupler duplexer is based on power transfer from one waveguide to the other waveguide at a certain coupling length. It has similar problems in coupling control as the Y-junction filter. It has particular requirements on the fabrication and control of the gap between two waveguides.

Another layout is an in-line transceiver. It takes advantage of a material which is transparent for one wavelength while absorbing the other wavelength. This is not suitable for our application which has a channel spacing of 1.6 nm (200 GHz channel spacing) and 4 nm (500 GHz channel spacing) between the upstream and the downstream signals.

The array waveguide grating (AWG) is an attractive and common wavelength demultiplexer which is commercially used in the WDM telecom network, and integrated into a PIC for multi-functionality [16, 48–51]. Based on InP technology, AWGs have been realized with compact dimensions [52], and polarization insensitive operation [53, 54].

A Mach-Zehnder interferometer (MZI) wavelength duplexer consists of two 3 dB couplers connected by waveguides with unequal lengths corresponding to the channel spacing. Comparing with a Y-junction and a directional coupler, it doesn't have critical sharp intersections, thus it is easier to fabricate. For separating only two channels, an MZI has smaller dimension than an AWG, especially when the wavelength demultiplexer should have a tuning option. Furthermore, the MZI wavelength duplexer is more tolerant to the lithography during fabrication.

In this thesis, AWG and MZI duplexers will be investigated and compared. The focus will be on realizing a tunable wavelength duplexer which is polarization insensitive in transmission. Its polarization insensitive tuning is achieved based on both electro-optical (EO) and thermal effects, see Chapter 2.

1.7.2 Modulator

Several ways can be employed to modulate the light with the upstream data in the transceiver, such as direct modulation of a laser [31, 34, 37, 46], direct modulation of an SOA [18, 23, 55, 56], electro-absorption (EA) modulator [57–62], or a phase modulator (PHM) [63–66].

Direct modulation of the laser can reach a high bandwidth up to 20~30 GHz [67, 68], which is much higher than what is needed in the access network now. Besides, the laser can be monolithically integrated with other active and passive components. However, it is challenging to produce a wavelength tunable laser at low cost.

An SOA can be modulated by changing the injection current, which changes the gain of the SOA. The advantage of directly modulating the SOA is that the SOA has a large operational wavelength range and compensates for the transmission loss and the fiber-chip coupling losses. It has been investigated in different operation schemes mentioned in section 1.5. However, the modulation bandwidth of the SOA is limited to a few GHz due to the carrier lifetime. The record for the small signal bandwidth is 3 GHz, by working in a highly saturated region [69].

The advantages of EA modulators are their low modulation voltage, high switching speed, small size and the possibility to integrate them with other devices like passive waveguide devices, lasers, amplifiers and detectors. However, EA modulators make use of the bandgap shift of the material (usually quantum well material) under a reverse bias voltage, thus they add an extra transmission loss, typically around 8~10 dB [70, 71]. Furthermore, it has a smaller operational wavelength range than an SOA. The SOA-EA combination has been demonstrated in a PON to carry the upstream data with 5 Gbit/s over 80 km long reach in [72].

The phase modulator (PHM) is based on the phase change which changes the power at the output port due to interference. The size of a Michelson PHM in InP is half length of the MZI modulator. It can be monolithically integrated with other components. In [73], a 40 Gbit/s InP-based MZI phase modulator has been reported.

With respect to monolithic integration, bandwidth requirement and colorless operation in the access network, two types of modulator, a directly modulated RSOA and a reflective Michelson modulator, will be investigated in this thesis in Chapter 4 and Chapter 7, respectively.

1.7.3 Photodetector

High efficiency, broad bandwidth and low polarization dependent loss (PDL) are the key requirements for the photodetector. The bandwidth of the photodetector is limited by the carrier transit time and the RC time constant, and the efficiency is determined by the interaction length between the light and the absorption layer. In order to improve the sensitivity of the integrated photodetector, a spot size converter [74] can be integrated to reduce the fiber-chip coupling loss, or a SOA is integrated to amplify the incoming light before the photodetector to improve the responsivity and the sensitivity [49,75,76]. In terms of monolithic integration, a high performance waveguide photodetector (WGPD) based SOA layer stack will be analyzed in detail in Chapter 5, and later integrated into the transceivers described in Chapter 7.

1.8 Thesis outline

The thesis can be separated into three parts: the first part (Chapter 2–Chapter 5) focuses on the performance of each component in the transceiver; the second part (Chapter 6) describes the fabrication technology for realizing the components and the monolithic integrated reflective transceiver; the third part (Chapter 7) concentrates on the design, realization characterization and analysis of the reflective transceiver with monolithic integration of all the individual components into one single chip.

The thesis is organized as follows:

- Chapter 2 gives a short overview of the theory of electro-optical effects in bulk InP/InGaAsP material. Based on this theory, simulations have been carried out to investigate the influence of the doping and thickness of each layer on the switching voltage and transmission loss for both TE and TM polarization. Experiments have been carried out for the waveguide phase shifters in two different layer stacks for high switching efficiency or for low transmission losses for both TE and TM polarization. Based on the measurement results, we designed and fabricated a polarization insensitive tunable wavelength duplexer using either electro-optical or thermal effects. Under reverse bias voltage using the electro-optical effects, this wavelength duplexer showed fast switching time of 0.14 ns (rise time) and 0.2 ns (fall time).

- Chapter 3 introduces two passive components, an MMI-loop mirror and an MMI-reflector which can be monolithically integrated into a PIC to realize on-chip reflection. The novel MMI-reflector combines small dimensions with good reflectivity. These two components greatly enhance the flexibility in the design of the photonic integrated circuit.

- Chapter 4 studies the theory of a reflective SOA based on rate equations. A series of simulations have been done to find the limiting factors for the modulation bandwidth. We also fabricated a novel reflective SOA integrated with an MMI-loop mirror based on a semi-insulating substrate, which can operate error free at 1.25 Gbit/s with −14 dBm input optical power.

- Chapter 5 presents a high performance waveguide photodetector based on a SOA layer stack. A photoreceiver which hybridly integrated a high bandwidth InP photodetector with an electrical amplifier circuit on SiGe has been used to test its operation in the BBP system.

- Chapter 6 discusses the fabrication technology which was developed for realizing the monolithic integrated circuits, and applied to fabricate all the devices described in this thesis.

- Chapter 7 presents the design and characterization results of the three generations of monolithically integrated colorless transceiver. The one which integrates a reflective phase modulator is promising for future 10 Gbit/s operation. The crosstalk between the SOA and the photodetector is analyzed.

The research presented in this thesis has been funded by the Dutch Ministry of Economic Affairs through the Freeband Project Broadband Photonics Access, the Smartmix project Memphis and the NRC photonics grant.

Chapter 2

Phase shifter and wavelength duplexer in InP

This chapter firstly reviews the electro-optic effects which can be applied for phase shifters and phase shifter based components. Based on the theory, a series of simulations have been carried out to see the influence of the thickness and the doping of the phase shifter layer stack on the switching efficiency. According to the simulation results, two material layer stacks are presented for a high switching efficiency-loss ratio. A wavelength duplexer was designed for polarization insensitive operation, and the measurement results show that it has not only polarization insensitive transmission, but also polarization insensitive tuning within a large wavelength range. It can operate with both electro-optical and thermal effect. The switching time of this wavelength duplexer in electro-optic operation is about 0.14 ns rise time and 0.2 ns fall time. In the last part of this chapter, we compare the performance of an AWG and an MZI-duplexer for our application.

2.1 Phase shifter

2.1.1 Introduction

The phase shifter (PHS) is one of the fundamental building blocks in photonic integrated circuits (PICs) [77]. In the reflective transceiver, the PHS is required firstly to tune the wavelength duplexer (Section 2.2) to match the incoming wavelength pairs, and later to realize a phase modulator to carry the upstream data (Chapter 7). Among the different material systems for the phase shifter, InP-InGaAsP material has been chosen in this thesis because of its potential for monolithic integration with the SOA/laser and photodetector which are needed in the reflective transceiver. Phase shifters in InP have been successfully applied in different devices in the COBRA research institute, such as a phase modulator [78], an optical space switch [79–81], a tunable add-drop de/multiplexers [82] and an electro-optical tunable laser [83].

The main requirements for the phase shifter are a high switching efficiency, fast switching, polarization independence and low optical transmission loss [84]. A PHS in InP can work with thermal effect [85], forward carrier injection and reverse bias voltage. A PHS based on thermal effect can be compact, low loss and polarization insensitive, however its switching speed is very low, in the millisecond range due to slow heat transfer. Another disadvantage of thermal tuning is that the generated heat influences the performance of the other components in a PIC if these components are located very closely.

The PHS based on forward carrier injection has been demonstrated with small dimension [86], low loss, and polarization insensitivity [87, 88]. However, it has a similar problem in heat dissipation and switching speed which are limited by the carrier recombination time to the nanosecond range.

The phase shifter under reverse bias voltage doesn't generate heat during operation, and has a very low current flow through the device, thus low power consumption. It can have a fast switching time, from a tenth of a nanosecond [78] to picoseconds [89]. These properties are important in our application to combine low power consumption, fast tuning and high modulation speed.

In the next sections, we will first review the electro-optic effects in bulk InP/InGaAsP material when applying a reverse bias voltage (Section 2.1.2). Based on an initial layer structure of the phase shifter given in (Section 2.1.3), we model the influence of the thickness and the doping level of each layer on the switching efficiency and loss for both TE and TM polarization. In Section 2.1.4, two different layer stacks are proposed, in which the waveguide phase shifters were fabricated and characterized to check the optical transmission loss, the switching efficiency and the polarization dependence in switching voltage (PDV).

2.1.2 Theory of the electro-optical phase shifter

An example of a p-i-n junction is shown in Fig. 2.1. It consists of an intrinsic waveguide layer of InGaAsP(Q1.25) between two InP layers with p and n-type doping, respectively. When increasing the reverse bias voltage, both the width of the depletion region and the electric fields at the depletion region increase. $E0_{max}$ and $E1_{max}$ are the maximum electric field at the interfaces. Due to the electric field and the variation in the free carrier concentration, the refractive index of the material changes. An overview of the related electro-optical (EO) effects in the bulk InP material will be given in the following sections, and detailed explanations can be found in [81, 90–95].

Field-induced effects

The Pockels effect occurs due to the deformation of the index ellipsoid caused by the electric field. It exists only in non-centrosymmetric materials, and InP/InGaAsP is one of the materials which have a Pockels effect. The Pockels effect is linearly proportional to the electric field, and dependent on the orientation of the waveguide with respect to the crystal direction. It is polarization dependent. It doesn't affect TM polarized light while giving TE

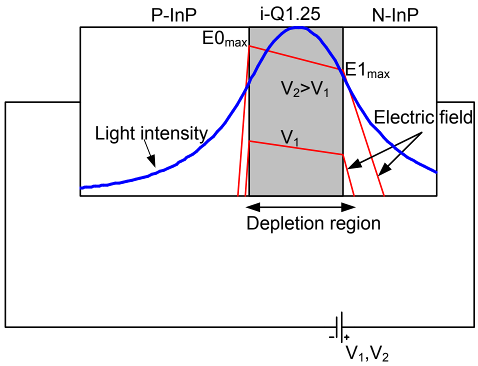

Figure 2.1: A schematic view of a p-i-n junction under reverse bias voltage with depletion region and electric field.

polarized light a positive refractive index change (Δn) for the light propagating along the $[1\bar{1}0]$ direction and a negative Δn for light propagating along the [110] direction. The induced change in index is given by [90]:

$$\Delta n_{\text{pockels}} = \pm\frac{1}{2} n_0^3 r_{41} |E| \tag{2.1}$$

where n_0 is the refractive index, r_{41} is the linear electro-optic coefficient that is dependent on the material, and E is the applied electric field due to the reverse bias voltage. The Pockels coefficients r_{41} of InP and Q1.25 have been measured to be about 1.4×10^{-12} m/V, and 1.6×10^{-12} m/V respectively. [93, 96].

The Kerr effect occurs together with the Pockels effect, but has quadratic relation in response to an electric field [90], and can be written as:

$$\Delta n_{\text{kerr}} = \frac{1}{2} n_0^3 s_{12,11} E^2 \tag{2.2}$$

where s_{12} and s_{11} are the quadratic coefficients for TE and TM polarization respectively. They are primarily determined by the Franz-Keldysh effect which changes the bandgap shape, and thus the optical absorption induced by an electric field [97, 98]. Here we use the experimentally fitted model and data given in [81] for Q1.25, $s_{12} = 11.9\times10^{-20}\text{m}^2/\text{V}^2$ for TE polarization and $s_{11} = 21.5\times10^{-20}\text{m}^2/\text{V}^2$ for TM polarization at a wavelength of 1.55 μm. The Kerr effect is weak in InP, about one order smaller than in Q1.25.

Carrier induced effects

The Plasma effect is related to intra-band transitions during which some carriers transit to a higher energy level in the same band. The carrier density change due to such an intra-band transition causes a refractive index change. The dependence of Δn_{plasma} on the doping level N_{d} is linear [91, 92, 94]:

$$\Delta n_{\text{plasma}} = A(E)N_{\text{d}} = \frac{N_{\text{d}}\lambda^2 e^2}{8\pi^2\epsilon_0 c^2 n \cdot m} \tag{2.3}$$

$$\text{InP}: \quad A(E) = 3.65 \times 10^{-27}\,\text{m}^3 \tag{2.4}$$

$$\text{Q1.25}: \quad A(E) = 5.7 \times 10^{-27}\,\text{m}^3 \tag{2.5}$$

where e is the electron charge, ϵ_0 is the vacuum permittivity, c is the light speed in vacuum, n is the refractive index, and m is the effective mass for electrons or holes. The plasma effect is isotropic, but wavelength dependent.

The Band-filling effect is related to free carriers filling the empty states in the bands which causes a decrease in the absorption coefficient. When applying a reverse bias voltage, the free carrier concentration changes in the depletion region. As a consequence, the refractive index changes. Since it is a result of free carriers, doping the structure has the equivalent effect as forward injection, provided that the carriers are free. The Band-filling effect is isotropic and it is much stronger in InGaAsP than in InP and proportional to the carrier concentration. We use the proportionality constant for InP and InGaAsP from [91]:

$$\Delta n_{\text{BF}} = A_{\text{BF}} \cdot N_{\text{d}} \tag{2.6}$$

$$\text{InP}: \quad \Delta n_{\text{BF}} = 5 \cdot 10^{-21} N_{\text{d}} \tag{2.7}$$

$$\text{Q1.25}: \quad \Delta n_{\text{BF}} = 14 \cdot 10^{-21} N_{\text{d}} \tag{2.8}$$

where N_{d} is the carrier concentration in the material.

Thus the total refractive index change Δn can be written as:

$$\Delta n = \Delta n_{\text{pockels}} + \Delta n_{\text{kerr}} + \Delta n_{\text{plasma}} + \Delta n_{\text{BF}} \tag{2.9}$$

in which $\Delta n_{\text{pockels}} = 0$ for TM polarization.

In a p-i-n junction structure shown in Fig. 2.1, however, not the whole optical flux $I(x)$ will see the refractive index change, but only the refractive index change in the depletion region which overlaps with the mode will contribute to the phase change. We take this into account by defining an effective refractive index change ΔN_{eff}, resulting from averaging the total refractive index change Δn over the depletion region change produced by the applied voltage V:

$$\Delta N_{\text{eff}} = \frac{\int_{-\infty}^{+\infty} \Delta n \cdot I(x)dx}{\int_{-\infty}^{+\infty} I(x)dx} \tag{2.10}$$

$$E_{\max}(V) = \sqrt{\frac{qN_{\text{d}}2(\phi_{\text{i}} - V)}{\varepsilon_s}} \tag{2.11}$$

$$d_{\mathrm{dep}}(V) = \sqrt{\frac{2\varepsilon_s(\phi_i - V)}{qN_{\mathrm{d}}}} \tag{2.12}$$

$$\Delta\phi(V) = \left(\frac{2\pi}{\lambda}\right) \cdot \Delta N_{\mathrm{eff}} L \tag{2.13}$$

in which ε_{s} is the permittivity of the material, ϕ_{i} is the built-in potential, d_{dep} is the width of the depletion region at a voltage V, $\Delta\phi$ is the phase shift, λ is the wavelength and L is the length of the phase shifter.

From the field and carrier induced effects, the carrier induced effects are more efficient as follows from equations (2.1),(2.2),(2.3),(2.6) and (2.11).

2.1.3 Modeling of the phase shifter

In the p-i-n junction shown in Fig. 2.1, the p-InP cladding is close to the film, and it overlaps with a large portion of the light. Due to the high absorption coefficient of the p-dopant, this type of p-i-n layer stack prevents the realization of a device with low optical loss. In order to obtain a low loss phase shifter, a buffer cladding layer is inserted to isolate the waveguide layer from the p-InP top cladding layer. Furthermore, in order to increase the switching efficiency, the waveguide layer should be doped at a certain level to take advantage of the carrier effects (band-filling and plasma) without sacrificing the low loss [91]. In the following part, we will go through the influence of the thickness and the doping level of each layer on the switching voltage and loss for both polarizations. We start with a layer stack which is used in COBRA with the initial values for the thickness and doping level in Fig. 2.2, in which n.i.d. means non-intentionally doped, typically measured around $N_{\mathrm{d}} = 1 \sim 5 \times 10^{15}/\mathrm{cm}^3$ with n-type dopant. The simulation has been carried out for a 2 mm long phase shifter. While investigating the influence of one parameter, the other parameters are kept constant.

Waveguide layer

In order to understand the influence of d_{film}, the width of the depletion region d_{dep} and the distribution of the electrical field E were calculated for two different thicknesses, 500 nm and 600 nm under the same reverse bias voltage, as shown in Fig. 2.3. From the figures, we can see that more light is confined in the film and less in the pn-junction and other layers when the thickness of the waveguide layer increases. d_{dep} and E are identical under the same reverse bias voltage, which means the total Δn are the same for both thicknesses. However, there is a smaller fraction of the light in the depletion region when the waveguide layer is thicker, therefore $\int_{-\infty}^{+\infty} \Delta n \cdot I(x)dx$ (numerator in equation (2.10)) is smaller. Therefore, the switching voltage increases when the thickness of the waveguide layer increases, shown in Fig. 2.4 (left). However, the optical transmission loss decreases with increasing waveguide layer thickness.

If the n-doping level of the waveguide layer is very high, only the buffer cladding layer is depleted and little depletion occurs in the waveguide layer, Fig. 2.5(a), thus only a small

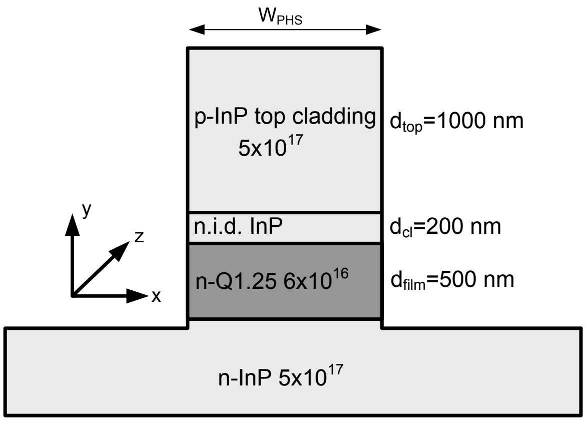

Figure 2.2: A waveguide phase shifter structure with the initial doping level and layer thickness as used in the COBRA research institute for simulation. The waveguide layer composition is Q1.25. d_{top} is the thickness of the top cladding layer, d_{cl} is the thickness of the buffer cladding layer and d_{film} is the thickness of the waveguide layer.

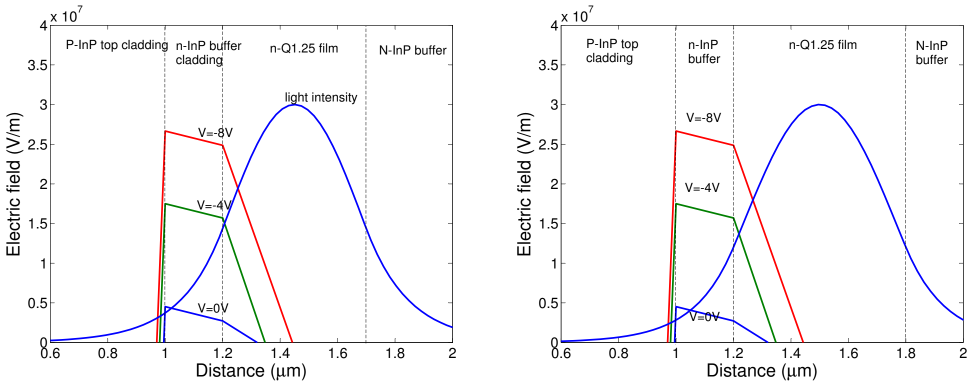

Figure 2.3: Calculated light intensity distribution, electric field and the width of the depletion region under the same reverse bias voltage for 500 nm (*left*) and 600 nm (*right*) thick film while the other parameters are kept constant.

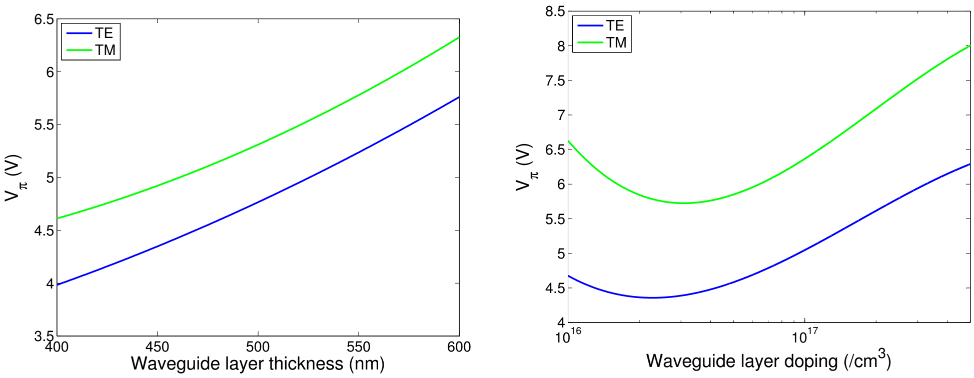

Figure 2.4: Simulated switching voltage (V_π) as a function of the waveguide layer thickness (*left*) and the doping level in the waveguide layer (*right*) while the other parameters are kept constant.

fraction of the light sees Δn in the depletion region, which results in a poor phase shifting efficiency.

When the waveguide layer is doped at a low level, it is completely depleted even at a low reverse bias voltage, see Fig. 2.5(b). Due to the low carrier concentration in the waveguide layer, both the field and the carrier induced effects are low, thus small Δn in the depletion region. After the film layer is depleted, the refractive index change in the waveguide layer results mostly from the field induced effects which are not efficient. Although most of the light sees the refractive index change, it still needs a high reverse bias voltage to reach π phase shift. The simulated switching voltage as a function of the doping level in the waveguide layer is given in Fig. 2.4 (right). An optimum value for $\geq \pi$ phase shift is obtained for $3 \times 10^{16}/\mathrm{cm}^3 - 5 \times 10^{16}/\mathrm{cm}^3$ doping level where the carrier induced refractive index change is high and most of the light sees the refractive index change, Fig. 2.5(c) and (d).

From Fig. 2.4(right), we can see that the PDV is bigger (~2 V, instead of ~0.7 V at optimum doping level) when the doping level of the waveguide layer is very low ($< 3 \times 10^{16}/\mathrm{cm}^3$). It is because the effective index change results mostly from the electric field induced effects, which is polarization dependent, after the waveguide layer is completely depleted. When the waveguide layer is very highly doped ($> 3 \times 10^{17}/\mathrm{cm}^3$), PDV increases as well. The reason is that the depletion occurs mostly in the buffer cladding layer (Fig. 2.5(a)), and the field induced effective index change in the depleted buffer cladding layer has a larger contribution factor to the total effective index change when compared to the waveguide layer with an optimum doping level. The field induced effective index change in the depleted InP buffer cladding layer is polarization dependent.

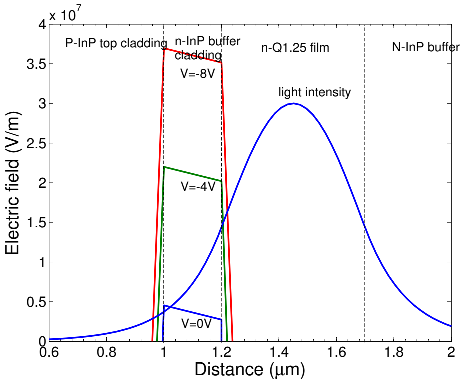

(a) $N_\mathrm{d} = 5 \times 10^{17}/\mathrm{cm}^3$

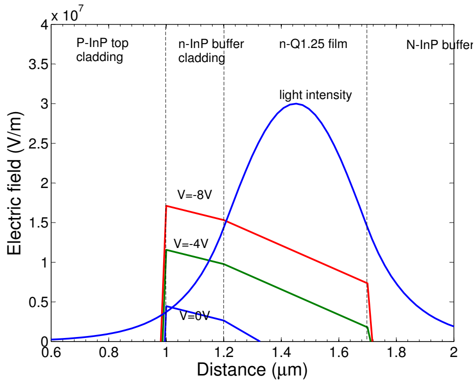

(b) $N_\mathrm{d} = 1 \times 10^{16}/\mathrm{cm}^3$

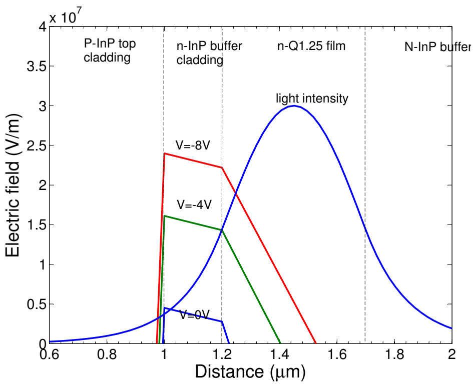

(c) $N_\mathrm{d} = 4 \times 10^{16}/\mathrm{cm}^3$

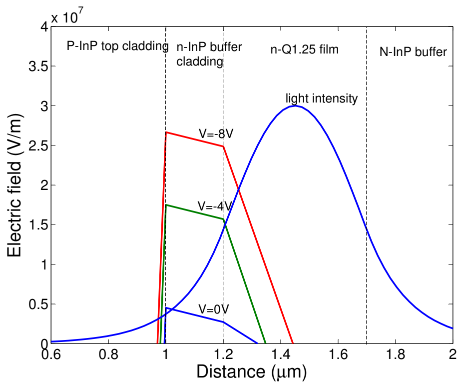

(d) $N_\mathrm{d} = 6 \times 10^{16}/\mathrm{cm}^3$

Figure 2.5: Calculated electric field and the width of the depletion region under the same reverse bias voltage for the doping level of (a) $N_\mathrm{d} = 5 \times 10^{17}/\mathrm{cm}^3$, (b) $1 \times 10^{16}/\mathrm{cm}^3$ (c) $4 \times 10^{16}/\mathrm{cm}^3$ and (d) $N_\mathrm{d} = 6 \times 10^{16}/\mathrm{cm}^3$ in the waveguide layer while the other parameters are kept constant.

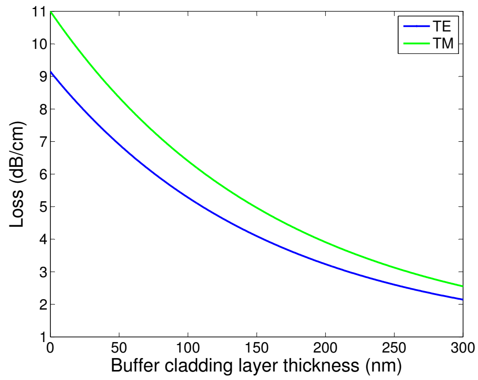

Figure 2.6: Simulated transmission loss due to free carrier absorption as a function of the thickness of the buffer cladding layer by means of waveguide scattering matrix formalism (WASMF) [99]. The waveguide layer stack is shown in Fig. 2.2 with the given doping level and the thickness for the other layers.

Buffer cladding layer

Now, we simulate the influence of the thickness and the doping level of the buffer cladding layer on the loss, switching voltage and PDV. The buffer cladding layer isolates the p-dopant with high absorption coefficient from the waveguide layer, and it is normally non-intentionally doped or n-doped. The optical transmission loss caused by the free carrier absorption decreases dramatically from 9 dB/cm (11 dB/cm) to 2.1 dB/cm (2.5 dB/cm) for TE (TM) polarization when d_{cl} increases from 0 nm to 300 nm, Fig. 2.6.

The width of the depletion region and the distribution of E are calculated for two different thickness, 200 nm and 100 nm, see Fig. 2.7. When d_{cl} is small, the p-n junction will be located closer to the waveguide layer which results in a wider depletion region in the waveguide layer and a higher electric field at the same reverse bias voltage, and therefore a higher Δn. Furthermore, due to larger depletion region in the film, $\int_{-\infty}^{+\infty} \Delta n \cdot I(x) dx$ is high, which means better switching efficiency. The simulated switching voltage as a function of d_{cl} is shown in Fig. 2.8 (left) which describes a clear trend in the relation between the switching voltage and the thickness of the buffer cladding.

The PDV reduces when d_{cl} decreases, as shown in Fig. 2.8(left). The reason is that Δn mainly comes from the depletion of the carriers in the film, and the carrier induced effects are polarization independent.

The doping level in the buffer cladding layer is important because it determines the strength of the electric field, the width of the depletion region and the location of the depletion region (p-side or n-side). If the doping level of the buffer cladding layer is low, the depletion occurs at the n-side, the buffer cladding layer will be completely depleted and the waveguide layer starts to be depleted even at a small V_{bias}. Due to the carrier depletion in the film where the light is mostly confined, $\int_{-\infty}^{+\infty} \Delta n \cdot I(x) dx$ is high, thus the switching

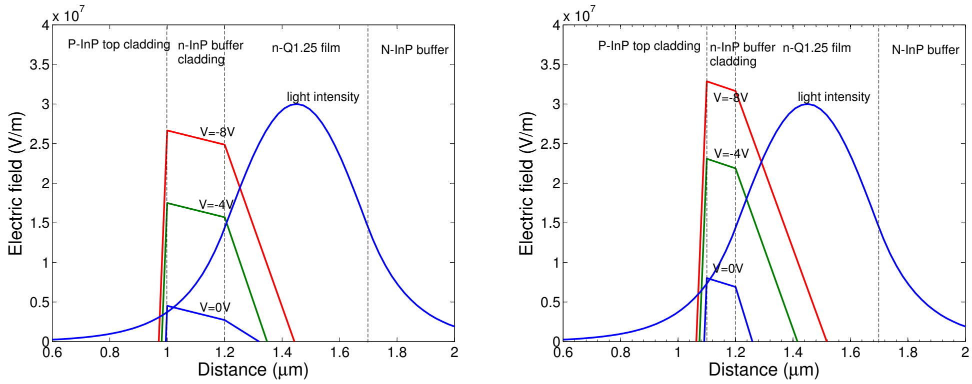

Figure 2.7: Calculated electric field and the width of the depletion region under the same reverse bias voltage for a buffer cladding layer thickness of 200 nm(*left*) and 100 nm (*right*) while the other parameters are kept constant.

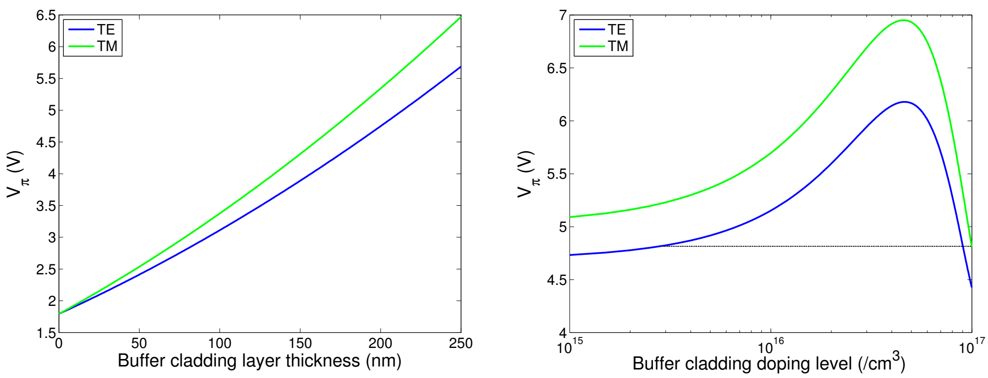

Figure 2.8: Simulated switching voltage (V_π) as a function of the thickness (*left*) and the doping level (*right*) of the buffer cladding layer while the other parameters are kept constant.

voltage is small.

When the doping level of the buffer-cladding layer increases, d_{dep} becomes smaller in the waveguide layer under the same V_{bias} although Δn in the buffer cladding layer increases due to a higher electrical field and a higher change in the carrier concentration level. The increase of N_{eff} in the buffer cladding layer can't compensate for the loss of N_{eff} in the waveguide layer because the light is mostly confined in the waveguide layer. Therefore the total phase shifting efficiency becomes lower when the doping level of the buffer cladding layer increases.

However, when the doping level exceeds a certain level ($5 \times 10^{16}/\text{cm}^3$in this case), the electric field is so strong under the same V_{bias} that the waveguide layer is depleted strongly once the buffer cladding layer is completely depleted, see Fig. 2.9(c). The strong electric field and the larger depletion cause a large change in the refractive index, especially in the waveguide layer. Thus the switching voltage decreases again. This result applies only when the buffer cladding layer can be depleted at relatively low voltage. If the doping level is too high, the depletion occurs at the p-InP side and only part of the buffer cladding layer depletes, far from the waveguide layer, thus $\int_{-\infty}^{+\infty} \Delta n \cdot I(x)dx$ is very low. The electric field and the depletion region have been calculated for a doping level of $3 \times 10^{17}/\text{cm}^3$, as shown in Fig. 2.9(d). The buffer cladding layer is not completely depleted even under $V_{\text{bias}} = -12\,\text{V}$.

The simulated switching voltage as a function of the doping level up to $1 \times 10^{17}/\text{cm}^3$ is shown in Fig. 2.8 (right). From the figure, we can see that the switching voltages are the same for TE and TM polarizations for two certain doping levels, but the contributions from the different EO effects are different. To illustrate this, we calculate the phase shift from each effect for doping levels of $9.3 \times 10^{16}/\text{cm}^3$ (left) and $3 \times 10^{15}/\text{cm}^3$ (right) shown in Fig. 2.10. In the left figure, we can see that the field induced EO effect contributes more to the phase change than in the right figure due to the strong electric field caused by the high doping level.

Top cladding layer

The doping level of the p-type top cladding layer is important to determine the location of the depletion region. If the doping level of the p-type top cladding layer is lower than the n-doping level of the adjacent layer, the depletion will occur mainly at the p-side, where the light intensity is low, consequently the switching voltage is high. If the doping level of the p-type top cladding layer is much higher than the doping level of the n-type buffer cladding and the waveguide layer, the depletion under reverse bias occurs mainly in the n-type region, and the overlap between the optical field and the refractive index change is high, thus the switching voltage decreases, Fig. 2.11.

When the doping level of p-type top cladding layer is high, the depletion under reverse bias occurs mainly in the n-type doped region, consequently, the thickness of the top cladding layer which is normally much thicker than the depletion region in p-InP will not influence the switching voltage. On the other hand, high p-doped top cladding layer will cause higher optical transmission loss.

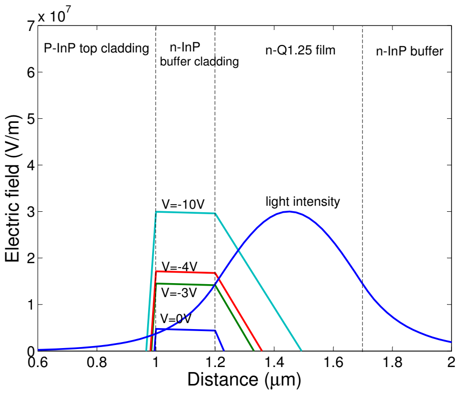

(a) $N_\mathrm{d} = 1 \times 10^{15}/\mathrm{cm}^3$

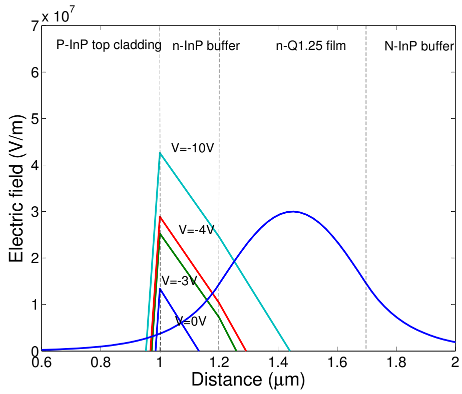

(b) $N_\mathrm{d} = 5 \times 10^{16}/\mathrm{cm}^3$

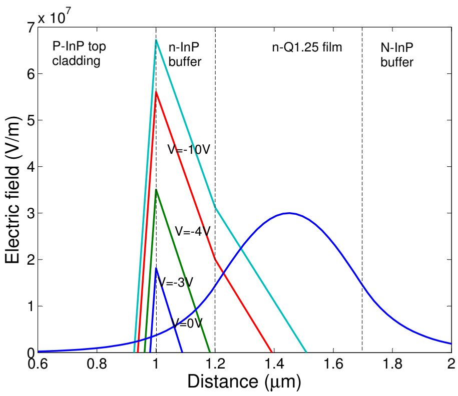

(c) $N_\mathrm{d} = 1 \times 10^{17}/\mathrm{cm}^3$

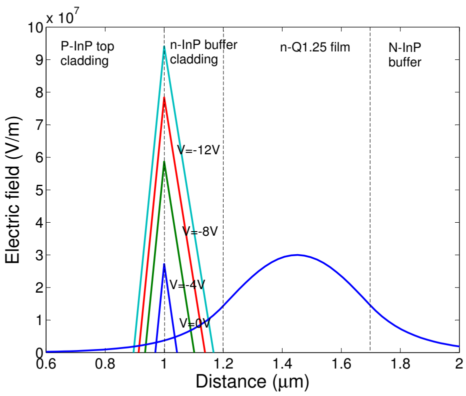

(d) $N_\mathrm{d} = 3 \times 10^{17}/\mathrm{cm}^3$

Figure 2.9: Calculated electric field and the width of the depletion region under the same reverse bias voltages for doping levels of (a) $1 \times 10^{15}/\mathrm{cm}^3$, (b) $5 \times 10^{16}/\mathrm{cm}^3$, (c) $1 \times 10^{17}/\mathrm{cm}^3$ and (d) $3 \times 10^{17}/\mathrm{cm}^3$ in the buffer cladding layer while the other parameters are kept constant..

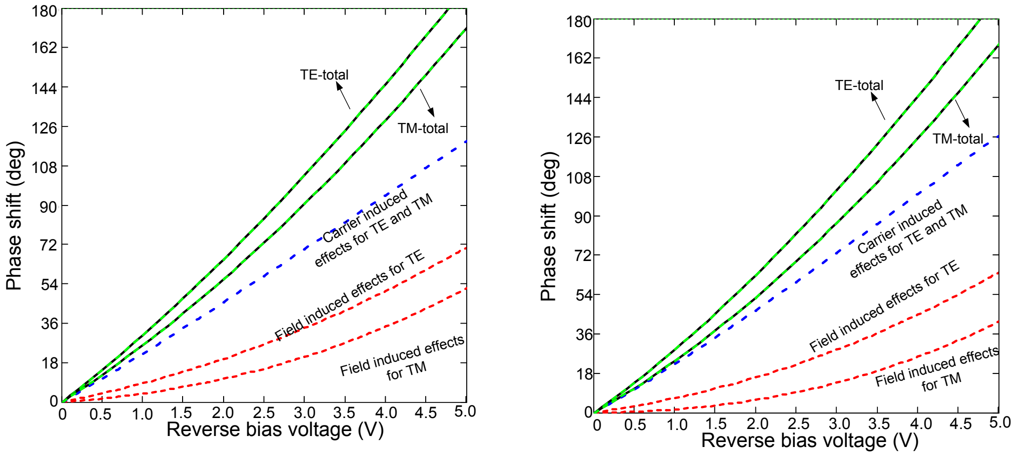

Figure 2.10: Simulated phase shift for TE and TM polarization for the buffer cladding layer with doping levels of $9.3 \times 10^{16}/\mathrm{cm}^3$ (*left*) and $3 \times 10^{15}/\mathrm{cm}^3$ (*right*).

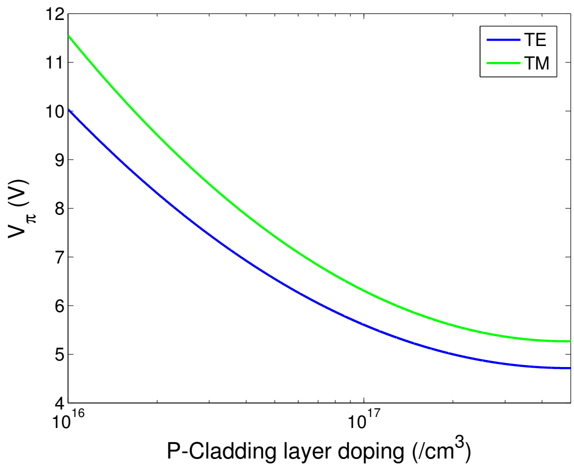

Figure 2.11: Simulated switching voltage (V_π) as a function of the doping level in the top cladding layer while the other parameters are kept constant.

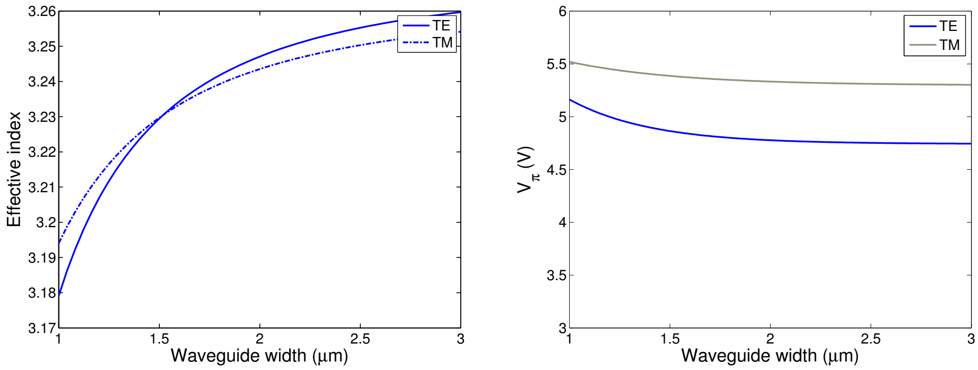

Figure 2.12: The calculated effective index for different waveguide widths (*left*) and the corresponding switching voltage for different widths (*right*).

Waveguide width

The effective index of a waveguide phase shifter changes with the width W_{PHS}, thus the optical mode confinement in the transverse (y) direction changes as well. The calculated effective index for deeply etched waveguides from 1 μm to 3 μm is given in Fig. 2.12(left), and the corresponding simulated switching voltage is shown in Fig. 2.12(right). The switching voltage is almost not influenced by W_{PHS} when $W_{\mathrm{PHS}} \geq 1.8\,\mu$m. When W_{PHS} is below 1.5 μm, the switching voltage increases, which happens more obviously for TE polarization than for TM polarization because the effective index of TE polarization (N_{effTE}) changes more than N_{effTM} in the same range from 1μm to 3 μm. In addition, PDV decreases when $W_{\mathrm{PHS}} < 1.5\,\mu$m where N_{effTM} begins to be bigger than N_{effTE}.

2.1.4 Waveguide phase shifter

First test for waveguide phase shifter (WGPHS)

Based on the above simulation results for the loss and the switching voltage, a wafer (number MO516) with the following layer stack specification of Fig. 2.13 was grown, . The highly doped p-InGaAs top layer serves as a contact layer, and the top cladding layer is gradually doped from $1 \times 10^{18}/\mathrm{cm}^3$ to $5 \times 10^{17}/\mathrm{cm}^3$. The top cladding layer is 1.3 μm thick in total so that the optical field is sufficiently far from the highly p-doped InGaAs contact layer and metal pads to prevent excessive loss. The buffer cladding layer is 200 nm thick, non-intentionally doped based on the consideration on the loss and switching efficiency (see Fig. 2.8). The waveguide layer is 500 nm thick to ensure single mode behavior in the transverse direction, doped with $6 \times 10^{16}/\mathrm{cm}^3$ (see Fig. 2.4). The simulated switching voltages are $V_\pi = 4.75$ V for TE polarization and $V_\pi = 5.25$ V for TM polarization.

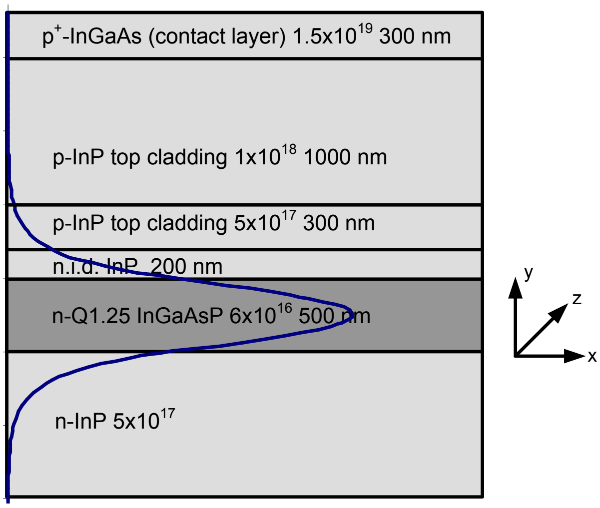

Figure 2.13: Layer stack of the waveguide phase shifter and the distribution of the mode intensity in the transverse direction (y-direction). The unit of the doping level is $/\mathrm{cm}^3$.

Measurement results on WGPHS

A group of 3 μm wide straight shallowly etched (100 nm etched into the waveguide layer) waveguide phase shifters were fabricated in this wafer, and cleaved with a length of 2 mm. The measured propagation losses of a 3 μm wide shallowly etched waveguide are 4 dB/cm and 5 dB/cm for TE and TM polarization respectively. To measure the switching voltage, an erbium doped fiber amplifier (EDFA) was used as a broadband light source. The light was coupled into the waveguide via a microscope objective, and due to reflectivities at the two cleaved facets, Fabry-Perot fringes will be observed in the transmission spectrum. When a reverse bias voltage was applied over the electrode on the waveguides, due to the phase change the transmission spectrum shifts. The switching voltage (V_π) was measured to be 2.6 V for TE and 3.2 V for TM, which are much lower than the simulated values given above. The corresponding switching efficiencies are 34.6°/(V·mm) and 28°/(V·mm) for TE and TM polarization respectively.

Such a high efficiency results from two aspects which were not taken into account in the former simulations. First, the actual waveguide layer thickness of this wafer was 460 nm measured by selective wet chemical etching, 40 nm thinner than the specification. According to Fig. 2.4(left), the switching voltage decreases. Secondly, zinc (Zn), which is used as the p-dopant, diffuses into the buffer cladding layer during growth and relocates the pn junction down toward the waveguide layer [100–102]. The pn junction is made visible with a secondary electron image (SEI), Fig. 2.14 (right), about 100 nm above the film. According to Fig. 2.8(left), the switching voltage decreases when the thickness of the buffer cladding layer is reduced.

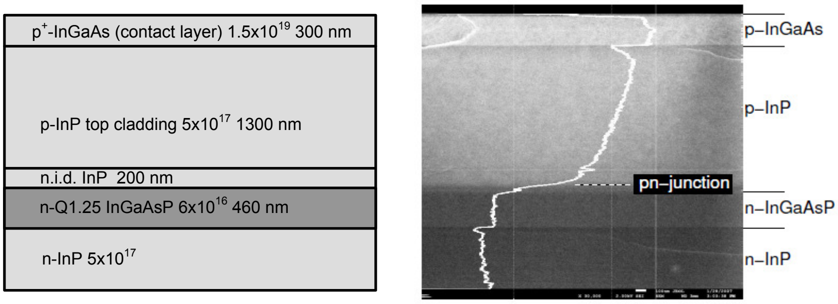

Figure 2.14: Actual layer stack thickness of MO516 for the phase shifters(*left*) and secondary electron imaging (SEI) at low voltage (*right*). The bright-dark transition indicates the pn-junction.

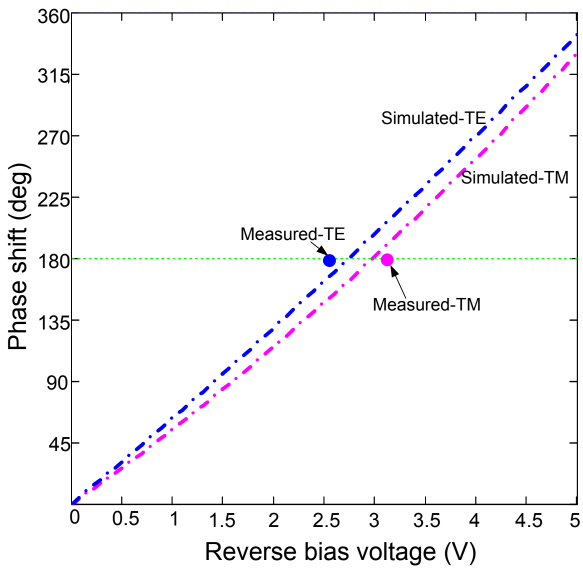

Figure 2.15: Measured switching voltage (big dots) and simulated phase-voltage relationship for both TE and TM polarization (dashed lines) for the first layer stack.

Based on the actual waveguide layer thickness (460 nm) and the actual location of the pn-junction (100 nm), we carried out the simulation again, and the simulated total phase shift as a function of the voltage is given in Fig. 2.15. The simulated V_π is about 2.5 V for TE and 2.9 V for TM which is quite closed to the measured value.

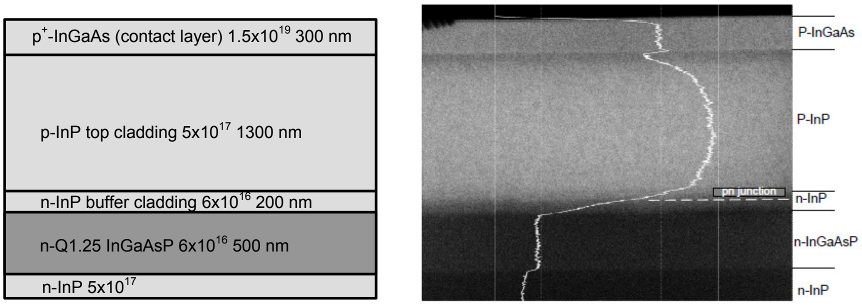

Figure 2.16: (*Left*) The measured layer thickness for the second grown wafer (MO758) and (*right*) the Zn diffusion profiles determined by secondary electron imaging (SEI) at low voltage.

Second test for WG PHS

In the first test results, the waveguide loss is about 4~5 dB/cm, which was partly caused by the Zn-diffusion into the buffer cladding layer. In order to further reduce the transmission loss while keeping the switching efficiency high, the second layer stack (MO758) was grown with the measured layer thickness shown in Fig. 2.16(left).

The difference between the two different layer stacks exists in the InP buffer cladding layer above the film, which is now n-doped with $6 \times 10^{16}/\mathrm{cm}^3$, instead of n.i.d in the first layer stack. The reason for this change is that the diffusion depth of p-dopant (Zn) is dependent on the n-doping level of the buffer cladding layer [103–105]. By increasing the doping level of the n-InP buffer cladding, the Zn diffuses less deep, and the pn-junction will be located further from the waveguide layer. Consequently, the free carrier absorption loss will be reduced. However, this will increase the switching voltage (V_π) because the depletion occurs less in the waveguide layer, and the refractive index change overlaps with small fraction of the light in the buffer cladding layer, see Fig. 2.9. Comparing the SEI images in Fig. 2.14 and Fig. 2.16, we can see that the pn-junction in Fig. 2.16 is further from the film layer (about 155 nm) than that in Fig. 2.14 (about 100 nm), which corresponds to 1 dB lower loss due to the free-carrier absorption (see Fig. 2.6).

In order to compare the loss and the switching efficiency with the first layer stack, a group of waveguide phase shifters have been designed, ranging in width from 1 μm to 3.2 μm. Five identical waveguide phase shifters for each width have been placed next to each other. The measured transmission loss of a 3 μm wide shallowly etched phase shifter is below 3 dB/cm for TE polarization, and 4 dB/cm for TM polarization, 1 dB lower than the loss based on the first layer stack, which matches the simulation results in Fig. 2.6.

The recorded phase change for a 2 mm long, 2 μm wide deeply etched (etched through the film layer) phase shifter as a function of the switching voltage (V_π) is shown in Fig. 2.17, which shows that the switching efficiency is about $21°/(\mathrm{V}\cdot\mathrm{mm})$ for TE and $17°/(\mathrm{V}\cdot\mathrm{mm})$ for TM, slightly lower than the efficiency of the first layer stack. The measured switching

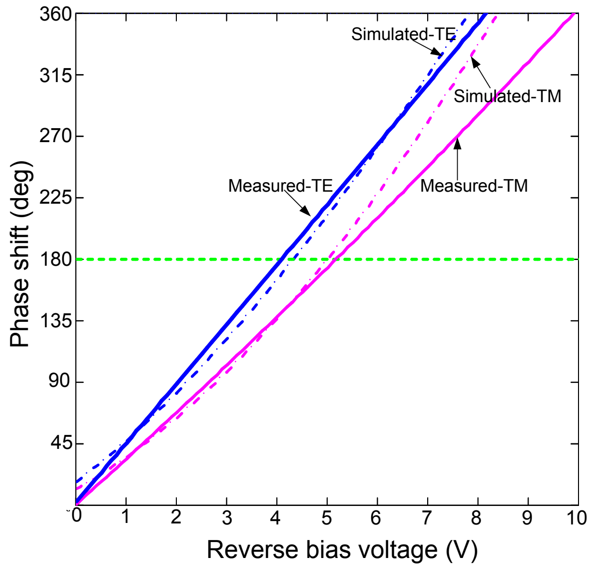

Figure 2.17: Measured (solid lines) and simulated (dash lines) phase shift as a function of the reverse bias voltage for a 2 μm wide, 2 mm long deeply etched waveguide phase shifter. The simulation shown is based on a layer stack with a 155 nm thick buffer cladding layer.

voltages (V_π) for the waveguides with different widths are given in Fig. 2.18, and the measurement has been done for all five waveguide phase shifters for each width. The switching voltage will slightly increase for both TE and TM polarization when the waveguide width decreases below 2 μm width, due to the reducing overlap of the optical field and the refractive index change. The PDV becomes smaller when the waveguide width is below 1.6 μm which matches with the simulation results shown in Fig. 2.12.

2.1.5 Conclusion

We have simulated the influence of the thickness and the doping level of each layer on the switching efficiency and the transmission loss for both TE and TM polarizations. Based on the simulation and measurement results, an overview on the performance is given in table. 2.1 which takes the integration with an SOA and a photodetector (PD) into consideration. Changing the doping level and changing the thickness of the passive components do not really influence the performance of the SOA/PD, since the waveguide layer and the buffer cladding layer of the passive devices are grown in different steps from the active components (see Chapter 6). From the table we can see that there exists a trade-off between the switching efficiency and the transmission loss. To achieve low loss operation, for example, we can increase the thickness of both the waveguide layer and the buffer cladding layer, but

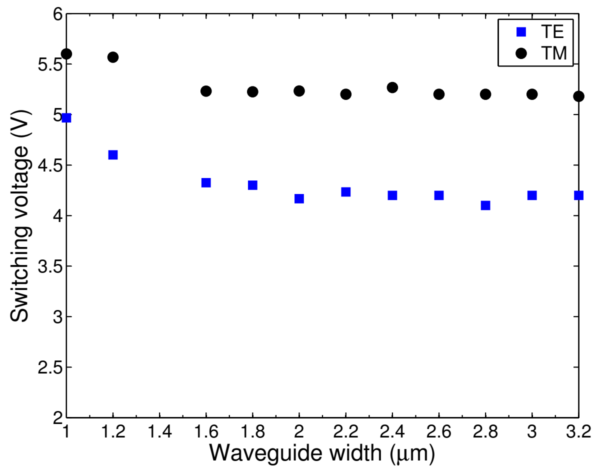

Figure 2.18: Average switching voltage of five identical 2 mm long deeply etched phase shifters at different widths.

design parameter	PHS			SOA/PD	
	V_π	loss	PDV	R_s	$f_{3\mathrm{dB}}$
film layer thickness ↑	↑ −	↓ +	○	○	○
film layer doping ↑	↓↑	↑ −	↓↑	○	○
buffer cladding thickness ↑	↑ −	$\underline{\downarrow}$+	↑	○	○
buffer cladding doping ↑	↑↓	↑ −	○	○	○
top cladding thickness ↑	○	$\underline{\downarrow}$+	○	↑ −	↓ −
top cladding doping ↑	$\underline{\downarrow}$+	↑ −	○	↓ +	↑ +
waveguide width ↑	$\overline{\uparrow}$−	$\underline{\downarrow}$+	$\overline{\uparrow}$	↓ +	↓ −

○ almost no influence
↓↑ there exists an optimum value between
↑↓ there exists a worst value between
$\underline{\downarrow}$ decreases to certain value
$\overline{\uparrow}$ increases to certain value
+ better performance
− worse performance
Note: When one of the design parameters changes, the other parameters are kept constant.

Table 2.1: Summary of the trade-offs in the phase shifter (PHS), SOAs and photodetector.

the switching efficiency will be reduced. In order to achieve high efficiency, the most efficient ways are to reduce the thickness of the buffer cladding layer and dope the waveguide layer with optimum carrier concentration level, but the loss will increase. The PDV can be reduced with thinner buffer cladding layer and waveguide width.

Comparing the two layer stacks tested, the first layer stack has a higher efficiency up to $34.6°/(\mathrm{V}\cdot\mathrm{mm})$ and less PDV, 0.6 V for a 3 μm wide shallowly etched waveguide phase shifter, but higher waveguide transmission loss. The second layer stack has slightly lower efficiency up to $21°/(\mathrm{V}\cdot\mathrm{mm})$ for TE and $17°/(\mathrm{V}\cdot\mathrm{mm})$ for TM polarization, lower transmission loss, but larger PDV, ~1 V for a 3 μm wide deeply etched WG PHS.

In the next section, we will investigate the performance of a tunable wavelength duplexer based on the phase shifter analyzed in this section.

2.2 Tunable wavelength duplexer

2.2.1 Introduction

In Chapter 1, we have described the building components of the reflective transceiver, a wavelength duplexer, a reflective modulator and a photodetector. In this section, we will present the design and characterization results of the tunable wavelength duplexer.

The wavelength duplexer separates two wavelengths carrying the downstream and the upstream data and guides them to the photodetector and the reflective modulator respectively. It should have low insertion loss and good isolation level, and the target loss and isolation level given in table 1.3 are below 3 dB and better than 15 dB respectively within the operation wavelength range, given in Chapter 1. Since the polarization state of the optical signal in the optical fiber which accesses the reflective transceiver is not stable, the wavelength duplexer has to be polarization insensitive (below 0.5 dB polarization dependent loss). Furthermore, the transceiver has to function at all wavelength pairs in the headend station (Fig. 1.4), therefore the wavelength duplexer has to be tunable (at least 2π) to match the incoming wavelength pair to maximize the transmission. In this section, we will concentrate mostly on the tuning based on the electro-optic effects analyzed in the former sections.

Placing the phase shifter at a special orientation with respect to $[1\bar{1}0]$ direction will yield polarization independent operation under a reverse bias voltage [106–108]. However, this method involves sacrificing the Pockels effect for TE polarization which is dependent on the crystal orientation (Section 2.1.2), hence lowering the switching efficiency to about $9°/\mathrm{V}\cdot\mathrm{mm}$.

Besides the bulk InP material we used and discussed in the first part, InP-InGaAsP quantum well material has also been widely used to achieve polarization insensitive operation [109, 110]. The first polarization independent electro-optic switch based on strained quantum wells is presented in [109] with a switching efficiency up to $60°/\mathrm{V}\cdot\mathrm{mm}$. However, the measurement results showed that the switching voltage was dependent on the wavelength, and optical transmission loss is up to 38 dB/cm. In [110], the waveguide transmission loss was reduced to about 7 dB/cm, but the switching voltage-length product increased up to 8.6°/V·mm. Compared to the polarization insensitive phase shifters based on quantum well material, the phase shifters in our layer stack show better switching efficiency-loss ratio.

Based on the measurement results given in Section 2.1.4, the layer stack which gives high efficiency and less polarization dependence in switching voltage will be employed to realize a fast tunable wavelength duplexer under reverse bias voltage.

As we introduced in Chapter 1, two different wavelength allocation schemes have been considered in the Broadband Photonics project. In this section, both the interspersed wavelength duplexer (200 GHz channel spacing) and grouped duplexer (500 GHz channel spacing) were designed, fabricated and characterized. Two effects will be applied to tune the WD, electro-optical effects and thermal effects, and they will be introduced in detail in the next sections.

This part is arranged as follows: Section 2.2.2 will present the simulation and design of the tunable wavelength duplexer. Section 2.2.3 gives the measurement results on the polarization dependence, the switching efficiency, and the switching time of the tunable wavelength duplexer based on both electro-optical and thermal effects.

2.2.2 Design and modeling of the wavelength duplexer

The wavelength duplexer has to be designed with the right channel spacing, free of polarization dependence, with a good isolation level between the upstream and the downstream data, and a low loss. In this section, we will present the modeling results of the wavelength duplexer on the channel spacing and polarization dependence by means of circuit simulation software [111].

Length difference versus channel spacing

The Mach-Zehnder Interferometric (MZI) wavelength duplexer consists of two 3 dB MMI couplers connected by two waveguides (MZI-arms) with unequal length. When light with two different wavelengths enters the first 3 dB MMI, it is split into the two MZI-arms with equal power, and the two unequal MZI-arms introduce a phase difference. In order to spatially separate these two wavelengths in different output ports, the length difference ΔL should meet the following requirement:

$$\left(\frac{2\pi N_{\mathrm{g}1}}{\lambda_1} - \frac{2\pi N_{\mathrm{g}2}}{\lambda_2}\right) \times \Delta L = \pi \tag{2.14}$$

$$N_{\mathrm{g}i}(\lambda) = N_{\mathrm{eff}i}(\lambda) + \lambda \frac{\mathrm{d}N_{\mathrm{eff}i}(\lambda)}{\mathrm{d}\lambda}, \quad i = 1, 2 \tag{2.15}$$

in which $N_{\mathrm{g}1}$ is the group index at λ_1, $N_{\mathrm{g}2}$ is the group index at λ_2 and ΔL is the MZI-arm length difference in the waveguides between two MMIs. If the wavelength difference $\Delta\lambda = \lambda_2 - \lambda_1 \ll \lambda_i$ and $N_{g1} \approx N_{g2}$, the above equation can be simplified as : $\Delta L \approx \frac{\lambda_1}{2N_{g1}\Delta\lambda}$. In our case, after substituting the central wavelength $\lambda = 1.55\,\mu$m, $N_g \approx 3.67$, $\Delta\lambda = 4$ nm (1.6 nm), we obtained that ΔL is 81.3 μm (204.4 μm), for 500 GHz (200 GHz) channel spacing.

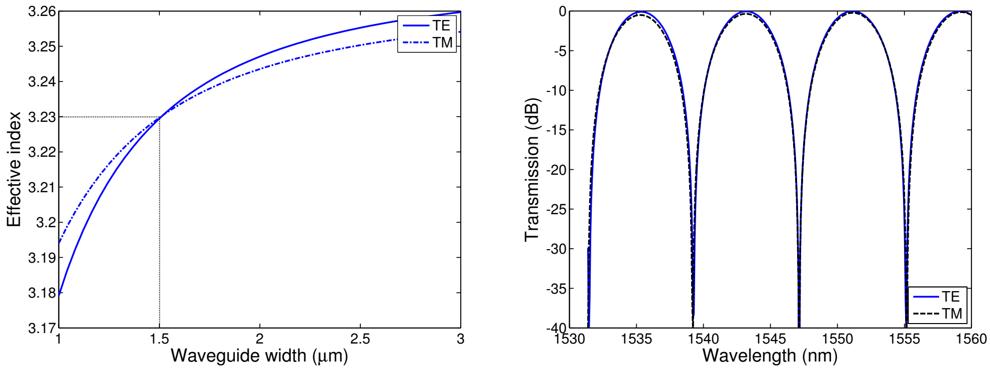

Figure 2.19: (*Left*) Effective index of TE and TM polarized light at $\lambda = 1550$ nm as a function of the width of a deeply etched waveguide width. (*Right*) Simulated transmission spectrum of the wavelength duplexer when the MZI-arms are 1.5 μm wide and deeply etched, and the length difference is 81.3 μm.

Polarization independence

The effective indices of the TE and TM modes are a function of the waveguide width. Based on the layer stack shown in Fig. 2.13, we calculated the effective index of deeply etched waveguides with different widths for both TE and TM polarization, Fig.2.19 (left). We can see that the effective indices of TE- and TM polarization are equal ($n_{\text{effTE}} = n_{\text{effTM}} = 3.23$) for a 1.5 μm wide deeply etch waveguide. The simulated transmission spectrum of the duplexer based on 1.5 μm wide MZI-arms is shown in Fig. 2.19 (right). It is polarization independent and has 500 GHz channel spacing.

Tolerance analysis for the polarization independence

During the fabrication, the waveguide width deviates from the designed value. The width of the MZI-arm is especially critical because it determines the polarization dispersion (wavelength difference between TE and TM at peak or bottom transmission), which is a function of the phase difference between TE and TM polarization, and written as

$$\Delta\lambda_{\text{TE}-\text{TM}} = \frac{\Delta\phi_{\text{TE}-\text{TM}}}{\pi} \cdot \Delta\lambda \tag{2.16}$$

$$\Delta\phi_{\text{TE}-\text{TM}} = \frac{2\pi}{\lambda} \cdot (N_{\text{effTE}} - N_{\text{effTM}}) \cdot \Delta L \tag{2.17}$$

in which $\Delta\lambda_{\text{TE}-\text{TM}}$ is the polarization dispersion, $\Delta\phi_{\text{TE}-\text{TM}}$ is the phase difference between TE and TM due to birefringence, $\Delta\lambda$ is the channel spacing and ΔL is the length difference between two MZI-arms.

The simulated phase difference between TE and TM polarization for a deeply etched waveguide is shown in Fig. 2.20. The 15% of the channel spacing ($\Delta\lambda$) is indicated for about

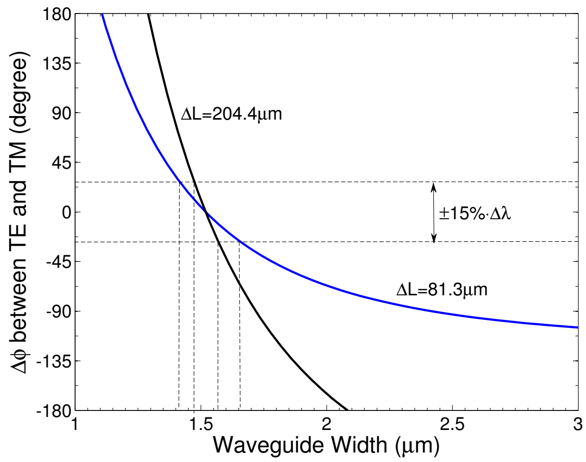

Figure 2.20: The phase difference between TE and TM polarization as a function of the width of a deeply etched waveguide.

0.5 dB polarization independent loss. Two curves are corresponding to two wavelength allocation schemes, $\Delta L = 204.4\,\mu$m (200 GHz) and $\Delta L = 81.3\,\mu$m (500 GHz). From the figure, we can see that when the width of the 200 GHz duplexer decreases to 1.3 μm, the phase difference between TE and TM is π, which means that TE and TM polarization exit at different output ports. Therefore, it is more critical to control the width of the MZI-arms for a duplexer with longer arm length difference (smaller channel spacing).

Designed MZI-tunable wavelength duplexer

Based on the simulation results, the wavelength duplexers for both types of wavelength allocation schemes were designed. Some MZI-duplexers are designed to be tunable with metal electrodes for both electro-optical and thermal tuning. The total mask layout of the designed MZI-tunable wavelength duplexer is shown in Fig. 2.21. The access waveguides of the device were designed 3 μm wide and shallowly etched (100 nm into the film) to minimize the insertion loss. All MMIs were deeply etched through the waveguide layer to be more tolerant to etch-depth variations during the fabrication. The MZI-arms were deeply etched, 1.5 μm wide. The bending radius for the deeply and shallowly etched waveguides are 350 μm and 500 μm respectively. For the tunable wavelength duplexer, each arm was provided with two metal pads to apply the reverse bias voltage or the electrical current. Only one of the two arms will be used at a time for characterization. In order to prevent electrical connection between the two MZI-arms while we apply the reverse bias voltage, two 150 μm long isolation sections were inserted after the first 1×2 3-dB MMI and before the second 2×2 3-dB MMI. The isolation was achieved by etching the material until the p-n junction. The metal electrodes were 4 μm wide and 300 nm thick. MZI-duplexers were designed with

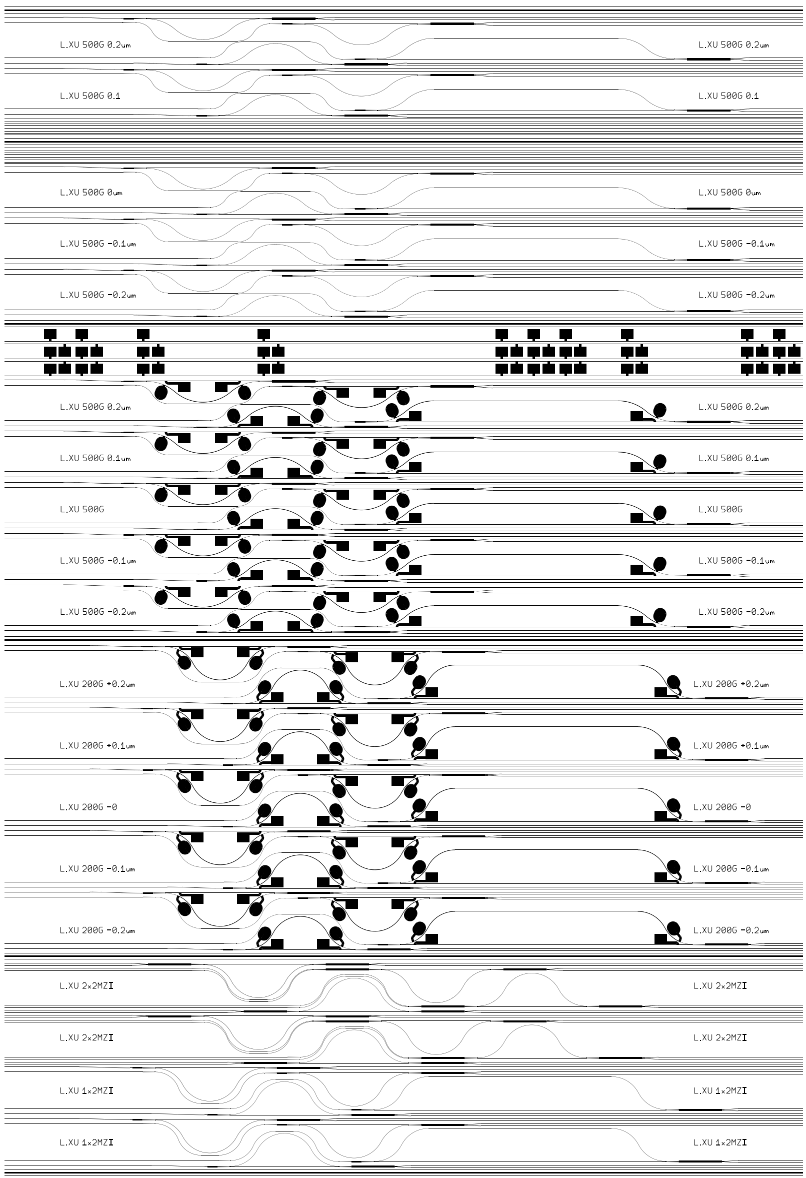

Figure 2.21: Mask layout of the tunable duplexers with 500 GHz (above) and 200 GHz (below) channel spacing.

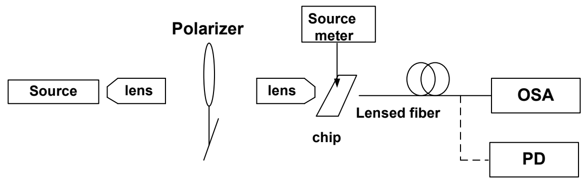

Figure 2.22: Measurement setup used for the characterization of the wavelength duplexer.

different widths with a step of 100 nm to investigate the influence of the width deviation on the polarization dependence, crosstalk and excess loss. The upper part without metal pads has the identical layout as the tunable wavelength duplexers below to test the influence of the metal on the excess loss and crosstalk.

2.2.3 Characterization of the wavelength duplexer

The fabrication process of this chip is described in Chapter 6. The characterization started with loss measurements on the straight waveguides without InGaAs contact layer and metal contact. The measured waveguide transmission losses for a 3 μm wide shallowly etched waveguide and a 1.5 μm wide deeply etched waveguide was 8 dB/cm and 12 dB/cm respectively. The high loss, especially for the shallowly etched waveguides, was induced by the sidewall roughness which was caused by the polymer deposition during reactive ion etching (RIE). This polymer accumulated more when Titanium (Ti) was used as a hard mask to protect the shallowly etched region because Ti was difficult to be removed completely, and the residuals caused extra roughness.

The measurement setup used for all the characterization in this chapter is shown in Fig. 2.22, in which the source can be a broadband light source or a tunable laser, and the source meter (current source or voltage source) was used only when characterizing the tunable wavelength duplexer.

When we measure the transmission spectrum, an Erbium Doped Fiber Amplifier (EDFA) is employed as a broadband light source. The laser source was used to measure the switching curves. The polarizer selects only one polarization, TE or TM, to be coupled in the chip through a microscope objective. At the output side, a lensed fiber is used to collect the light, and guide it to an optical spectrum analyzer (OSA) to record the spectrum, or a power meter (PD) to record the optical power.

Non-tunable MZI-wavelength duplexer

First we measured the non-tunable MZI-wavelength duplexers which have no InGaAs contact layer and tuning electrodes.

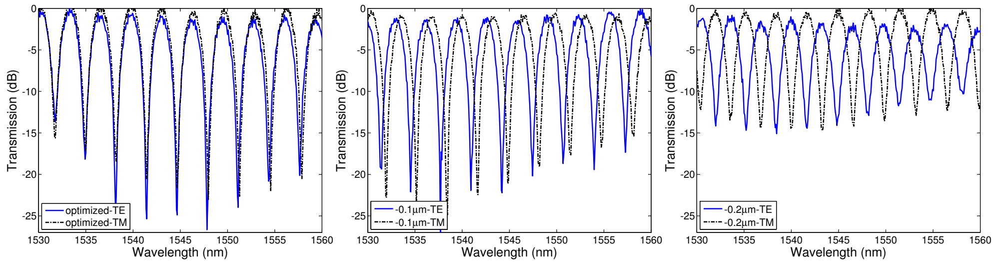

Figure 2.23: Transmission spectrum for both TE and TM polarizations for the 1×2 MZI-wavelength duplexer with different waveguide widths: design width +0 μm (*left*), -0.1 μm (*middle*) and -0.2 μm(*right*)

Width deviation

The transmission spectrum for the wavelength duplexers with different waveguide widths are shown in Fig. 2.23. The transmission spectrum of the optimized wavelength duplexer gives more than 25 dB isolation level between two different ports at the designed wavelength (1550 nm), and it is polarization insensitive. When the width of all the waveguides decrease 100 nm or 200 nm, the isolation level decreases, and it is not polarization insensitive any more.

The isolation level is mainly dependent on the quality of the MMIs. When the MMI width deviates from the optimum value, both the power split ratio and the phase difference between two output ports deviated, and thus the isolation level of the wavelength duplexer was reduced.

The polarization dependence depends on the width of the MZI-arms. When the width of the MZI-arms changes, the effective indices of TE and TM polarization are different, thus the wavelength duplexer becomes polarization dependent. Fig. 2.23(left) shows a good polarization insensitive duplexer, while the middle and the left figure show a polarization dispersion of 0.84 nm and 1.6 nm respectively, corresponding to 94° and 180° phase difference between TE and TM polarization, which are in agreement with the simulation values shown in Fig. 2.20. When the waveguide width decreases 200 nm, TE polarization exits from the opposite port as TM polarization, as indicated in Fig. 2.23(left).

Polarization insensitivity

We measured two wavelength duplexers with the same waveguide width optimized for polarization independent operation. The location in the wafer and the channel spacing are different, 200 GHz and 500 GHz respectively. The recorded spectra for both TE and TM polarizations are shown in Fig. 2.24. From the figures, we can see that the measured channel spacing between up and downstream data is 202 GHz and 496 GHz, about ±1% deviating from the specification; the excess loss is less than 2 dB for both polarizations; the isolation level is about 25 dB near the designed wavelength in the left figure, and 15 dB in the right

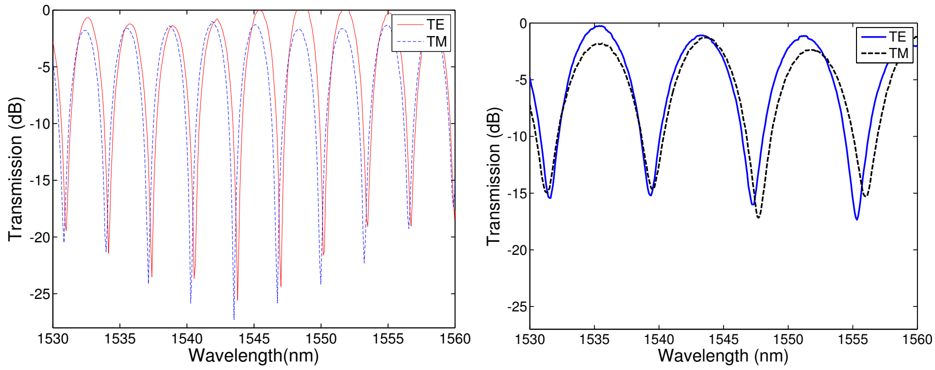

Figure 2.24: Measured transmission spectrum for both TE and TM polarization for 200 GHz interspersed (*left*) and 500 GHz grouped wavelength duplexer (*right*).

Figure 2.25: Photograph of a tunable wavelength duplexer which was measured with both electro-optical and thermal effects

figure. Both the isolation level and the excess loss have met the target specifications given in table 1.3. It is difficult to judge the polarization dependent loss (PDL) of the duplexer because the measurement setup was not optimized for this PDL characterization.

Besides the polarization dependent loss, polarization dispersion is used as well in the literature [53, 112] to evaluate the polarization dependence of the duplexer. In Fig. 2.24, the polarization dispersion is about 15% of the channel spacing, which is sufficient in our application.

In Fig. 2.24, these two wavelength duplexers (200 GHz and 500 GHz) show different isolation level, which may result from the non-uniform exposure during the waveguide lithography and non-uniformity of the material, such as the thickness of the waveguide layer and the doping level.

Tunable wavelength duplexer

In this section, the characterization results of the tunable wavelength duplexer will be presented. Photo of a fabricated tunable duplexer with metal electrodes on the MZI-arms is shown in Fig. 2.25. It has a 2.1 mm long straight phase shifter, and a 2.13 mm long phase shifter at another arm with 400 μm long curved waveguides.

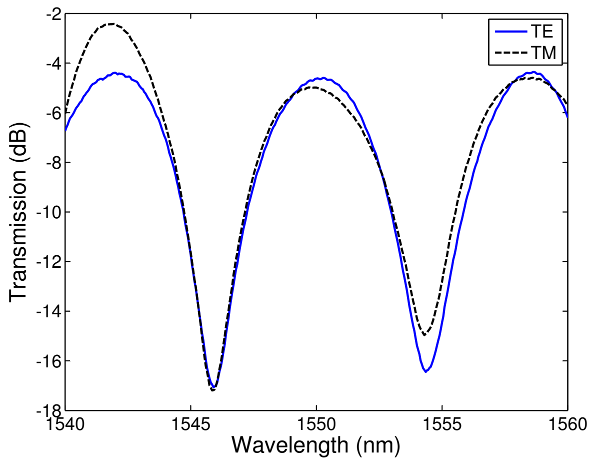

Figure 2.26: The measured transmission spectrum of the tunable wavelength duplexer at 0 V for both TE and TM polarization.

Transmission spectrum of the tunable wavelength duplexer

The recorded transmission spectrum of this device at 0 V reverse bias voltage is given in Fig. 2.26, which shows polarization independence at a wavelength range from 1540 nm to 1560 nm. The isolation level is better than 10 dB within the same wavelength range, which is worse than the non-tunable duplexer possibly due to non-uniform exposure during lithography and the loss imbalance between two tunable MZI-arms. The excess loss is about 5 dB for both TE and TM polarization, 3 dB more than the non-tunable duplexer due to the overlap between the tail of the optical field and the contact layer. A uniform surface of the wafer and uniform photoresist can minimize the possibility of non-uniform exposure during lithography.

Phase voltage relation

To measure the switching voltage of the wavelength duplexer, a tunable laser was used as a light source. TE or TM polarized light was selected respectively with the polarizer. If one of the MZI-arms is reversely biased, the phase of the light changes, thus the output power fluctuates with varying voltage. By recording the power fluctuation, the relation between the phase and the voltage can be obtained. The measurement has been done both on the straight and the curved phase shifters. Fig. 2.27 shows that the switching voltage is independent of the biased arm. The extinction ratios for both TE and TM are better than 14 dB at 1546.45 nm.

In order to extract the phase-voltage relationship, the following equations were used to

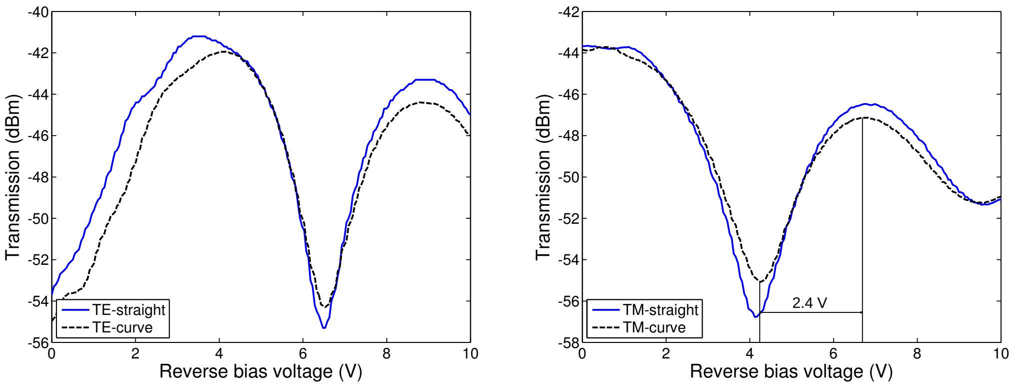

Figure 2.27: Switching curves for different wavelengths (left at $\lambda = 1546.45\,\text{nm}$, and right at $\lambda = 1550.35\,\text{nm}$) for both TE and TM polarization when the reverse bias voltage was applied on the straight phase shifter (straight) and the curved phase shifter (curve).

fit the measurement data for both TE and TM polarizations.

$$P = A + BV + Ce^{-DV}\cos(\phi) \tag{2.18}$$

$$\phi = aV^2 + bV + c \tag{2.19}$$

$$\phi(V = 0) = c \tag{2.20}$$

Where

A is the mean value of the output power.

B models the linear power fluctuation due to the applied voltage.

C is the modulation depth of the output power due to the varying phase shift in the biased MZI-arm.

D is the attenuation of the light amplitude caused by band edge shift in the biased MZI-arm.

ϕ is the output phase of the phase shifter.

a is the phase change due to quadratic effects, such as the Kerr and Franz-Keldysh effects.

b is the linear variation of the phase with the voltage applied due to Pockels and carrier induced effects.

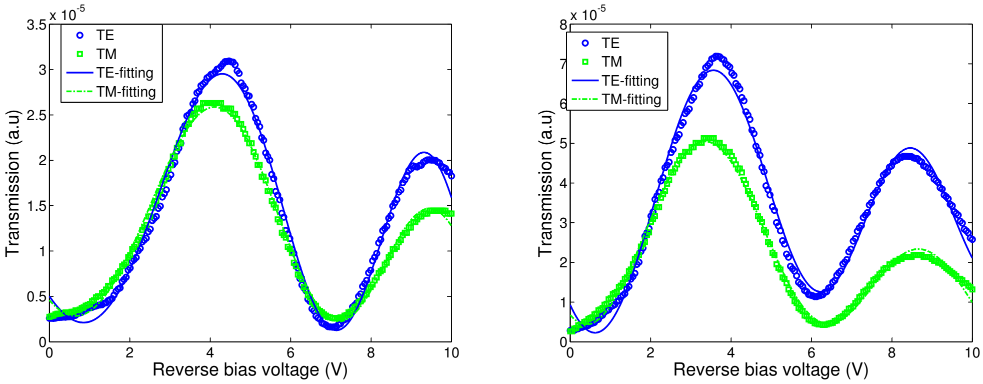

Figure 2.28: Switching curves for both TE and TM polarization at λ = 1562.3 nm (left) and λ = 1538.52 nm (right) based on electro-optical effects under reverse bias voltage. The dots and squares are the measured values, and the continuous curves are the fitting results according to equation 2.18.

λ	TE		TE		TM		TM	
(nm)	a	b	V_π	$V_{2\pi}$	a	b	V_π	$V_{2\pi}$
1538.52	0.030607	0.91698	3.11	5.75	0.021257	0.91682	3.19	6.00
1546.45	0.038796	0.77252	3.40	6.20	0.01505	0.99732	3.10	5.80
1554.45	0.03847	0.75158	3.53	6.25	0.023339	0.86831	3.34	6.20
1562.3	0.045173	0.6419	3.83	6.67	0.036643	0.68117	3.83	6.76
average	0.0383	0.7707	3.47	6.23	0.024072	0.8659	3.37	6.19

Table 2.2: The extracted a and b at different wavelengths for both TE and TM polarization according to the fitting results.

c is the initial phase, should be zero for the peak transmission wavelengths.

Two fitting results at different wavelengths are shown in Fig. 2.28, from which we can see the fitting curves match the measurement data well. The same measurement and fitting have been repeated for two other different wavelengths. From the fitting, the parameters in the equations at different wavelengths are extracted, in which a and b describe the relation between the phase and the bias voltage, given in table 2.2, and the corresponding V_π and $V_{2\pi}$ at different wavelengths are presented as well for both polarizations. The relation between V_π ($V_{2\pi}$) and the wavelength for both TE and TM polarization is shown in Fig. 2.29. From the table, we can see that the difference in V_π and $V_{2\pi}$ between TE and TM polarization is less than 0.2 V (PDV) for most fitting results. If we translate this PDV into the wavelength mismatch $\Delta\lambda_{\text{mis}}$ between the incoming light from the local exchange and the λ_{peak} of the duplexer passband, it is equal to about $\Delta\lambda_{\text{mis}} = 6\% \cdot \Delta\lambda$ in which $\Delta\lambda$ is the channel spacing between the downstream and the upstream data. The excess loss due to this mismatch is

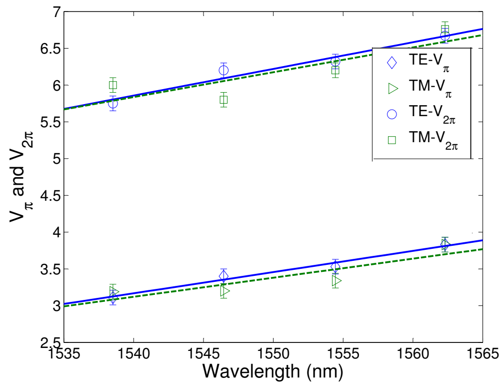

Figure 2.29: Tuning voltage for π and 2π phase shift as a function of the wavelength. The solid and dash lines are the linear fitting for both TE and TM polarizations.

negligible.

However, the maximum voltage difference is 0.8 V to obtain the same π and 2π phase shift from 1535 nm to 1565 nm, corresponding to $\Delta\lambda_{\text{mis}} = 25\% \cdot \Delta\lambda$ for both wavelength allocation schemes. It means that the wavelength duplexer has to be tuned after each network reconfiguration to optimize the transmission for both the interspersed wavelength duplexer and the grouped wavelength duplexer due to the wavelength dependent tuning.

We also compared the extracted averaged parameters a and b from the measurement with the simulation based on a 100 nm buffer cladding layer due to Zn diffusion, and the simulation results and the measurement are in good agreement, as shown in Fig. 2.30.

Based on the simulation results in section 2.15 and the measurement results on the arm independence, polarization independence and wavelength dependence, it is obvious that carrier induced effects are much stronger than the field induced effects because the carrier induced effects are polarization independent, but wavelength dependent, while the field induced effects are polarization dependent, see section 2.1.2.

Switching time under reverse bias voltage

The requirement on the tuning delay is below 40 ms which is the network reconfiguration time, and it can be easily obtained with an EO switch. The setup given in Fig. 2.31 has been used to quantify the switching time of the tunable wavelength duplexer. We drive this device with a pulse pattern generator (PPG) which has about 30 ps rise and fall time. The recorded output optical bit sequence at −5.2 V is shown in Fig. 2.32, from which the rise time (fall time) is estimated to be about 0.14 ns (0.2 ns). This value is far smaller than the required tuning delay, and it also indicates that this material is suitable for a fast optical switch and high speed modulator which will be introduced in Chapter 7.

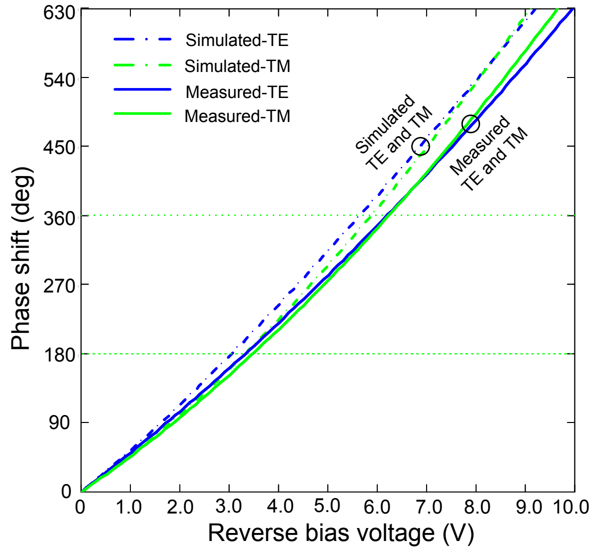

Figure 2.30: The simulated (dash) and extracted (solid) phase-voltage relation for the tunable wavelength duplexer. The darker line is for TE polarization, and the grey line is for TM polarization. The simulation is based on the layer stack given in Fig. 2.2 with a 100 nm thick buffer cladding layer.

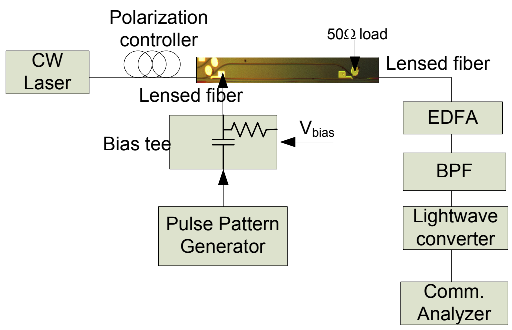

Figure 2.31: Setup for measuring the switching time of the tunable wavelength duplexer.

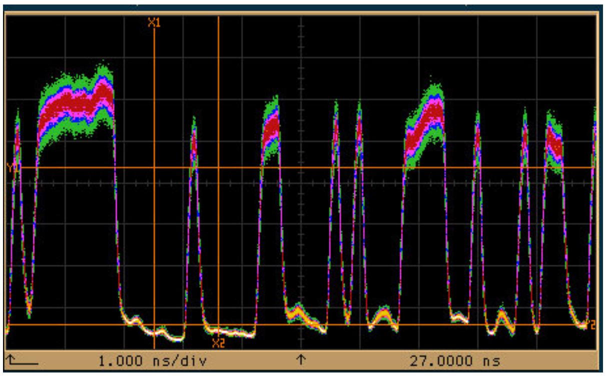

Figure 2.32: The output optical bit sequence at 5 Gbit/s when the tunable wavelength duplexer was biased at −5.2 V.

Thermal tuning

Thermal tuning is based on the changes in the refractive index due to the temperature variation, and it is polarization and wavelength insensitive [93]. The refractive index change of III-V material is proportional to the temperature change [93], and the temperature change has a linear relation with the injected electrical power. Thus we can write

$$\Delta n_{\mathrm{T}} = a_{\mathrm{T}} \cdot P \tag{2.21}$$

in which Δn_{T} is the refractive index change due to a temperature change, $a_{\mathrm{T}}$is the linear temperature coefficient, and P is the injected electrical power.

For the device shown in Fig. 2.26, instead of applying a reverse bias voltage, an electrical current I was injected through the electrode above the waveguides. Due to the electrical resistance of the metal electrode, heat will be generated which will change the refractive index of the material, and therefore the phase. Due to the phase change in one of the MZI-arms, the output optical power will fluctuate according to the injection current. The measured resistance of the 2.13 mm long electrode is about $R = 106\,\Omega$. The recorded switching curves for both TE and TM polarizations are shown in Fig. 2.33, and the extracted phase-injection power relation is found by fitting the equation

$$P = A + B \cdot I + Ce^{-D \cdot I} \cos(a \cdot I^2 + c) \tag{2.22}$$

Where

A is the mean value of the output power.

B models the linear power fluctuation due to the injection current.

C is the modulation depth of the output power due to the varying phase shift in the biased MZI-arm.

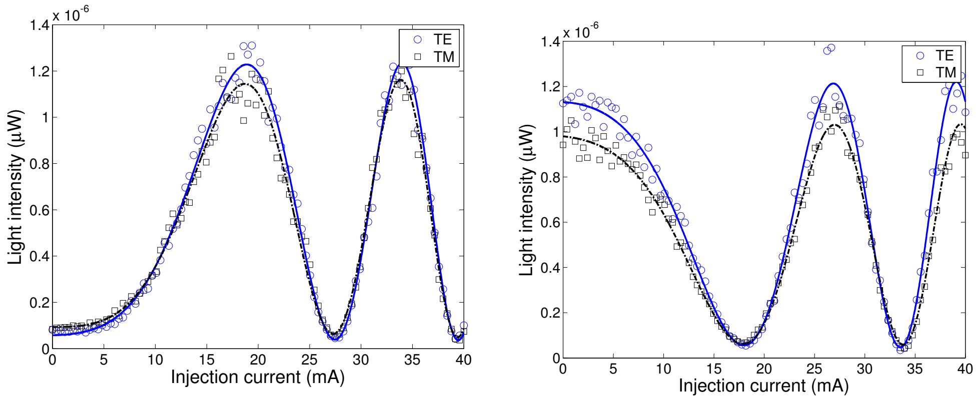

Figure 2.33: Transmission power as a function of the injected current over the electrode for both TE and TM polarization when $\lambda = 1554.4$ nm (left) and 1558.1 nm (right).

D is the attenuation of the light amplitude in the biased MZI-arm.

ϕ is the output phase of the phase shifter.

a is the temperature coefficient for the injected electrical power.

c is the initial phase, should be zero for the peak transmission wavelengths.

The fitting results for the phase and the electrical current are given in Fig. 2.33. The extracted temperature coefficient a_T in equation (2.21) is about 0.0089/W, and the extracted relation between the phase change and the injection electrical power is given in Fig. 2.34. The result shows that the thermal tuning is polarization insensitive, and the tuning power for obtaining π phase shift, P_π, is about 40 mW. The measurement results show that the phase change is linear with the injected electric power (i.e. quadratic with the injected current).

Thermo-optic tuning is dependent on the electrical power, which is a function of the electrical current and resistance, instead of being dependent on the length of the phase shifter. Thus, the phase shifter can be made compact. However, the switching time of such a device is in the millisecond range.

2.2.4 Polarization insensitive AWG

The arrayed waveguide grating (AWG) is a well known wavelength demultiplexing device [113], and it can also be used in our project as an alternative for the MZI duplexer to separate λ_1 and λ_2 to the modulator and the detector. To compare the performance in terms of insertion loss, crosstalk, and polarization dependence between the AWG and the MZ duplexer, an AWG was designed and fabricated, shown in Fig. 2.35, based on the same material

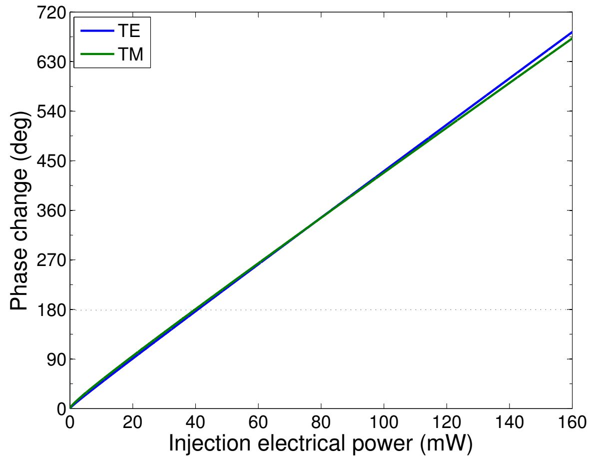

Figure 2.34: The extracted relation between the phase change and the injected electrical power for a 2.1 mm long phase shifter with electrode resistance $R = 106\,\Omega$.

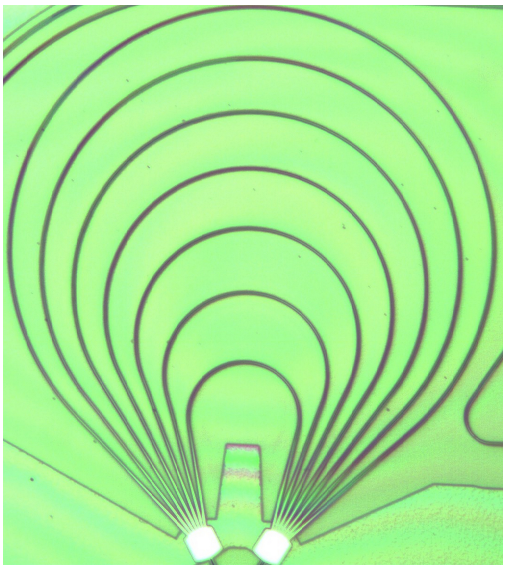

Figure 2.35: Photo of the fabricated and measured AWG with 200 GHz channel spacing.

Parameter	Value
center wavelength λ_c	1550 nm
number of channels	2
channel spacing $\Delta\lambda_{ch}$	1.6 nm (200 GHz)
free spectral range $\Delta\lambda_{FSR}$	3.2 nm
arm length difference	202.9 μm
AWG arm width	1.5 μm

Table 2.3: Common parameters for the AWG and the MZI-wavelength duplexer with 200 GHz channel spacing shown in Fig. 2.21.

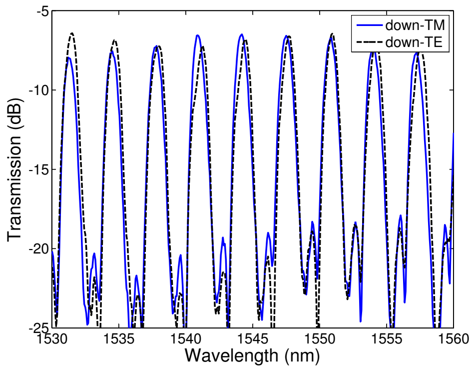

Figure 2.36: Transmission spectrum of a polarization insensitive AWG.

layer stack as the MZI-wavelength duplexer discussed above. The common design parameters for both the AWG and the MZI-wavelength duplexer are given in Table. 2.3.

To compare the performance of the AWG and the MZI-wavelength duplexer for our application, we also measured the transmission spectrum of the AWG, Fig. 2.36. The results showed that the isolation level of the AWG is about 15 dB, mainly due to non-perfect waveguide lithography. The excess loss of the device is about 6.5 dB, which is higher than MZI-duplexer ($\lesssim$ 2 dB) because the AWG-arms were deeply etched, and the peak wavelength deviation between TE and TM polarization is comparable to that of the MZI-duplexer ($\simeq$ 0.23 nm). Furthermore, if the AWG has to be tunable, the size will be much bigger than the tunable MZI duplexer, and the fabrication of the tunable AWG is also more challenging. The passband of the MZI-wavelength duplexer is broader than that of an AWG, which is favored in our application. Thus, we can draw the conclusion that MZI-duplexer has more advantages when it has to be tunable, and the number of channels is only two.

2.2.5 Conclusion and discussion

The non-tunable duplexer achieved polarization insensitive transmission, 25 dB isolation level at the designed wavelength, and lower than 2 dB excess loss. The polarization independent operation was achieved with a proper waveguide layer stack, and proper width (1.5 μm wide) of the deeply etched MZI-arms.

The tunable duplexer is polarization insensitive and efficient, when the tuning employs either electro-optical or thermal effects. In order to cover the whole wavelength operation range (2π phase shift), it needs about 6.2 V (2.1 mm long phase shifter) under EO effects, and 80 mW electrical power when employing thermal effect to tune the wavelength duplexer. The achieved isolation level is about 10 dB, possibly due to non-uniform lithography and the power imbalance between two MZI-arms covered by the metal. The measured excess loss is about 5 dB, 3 dB more than the non-tunable duplexer most likely due to the overlap between the optical field and InGaAs contact layer and the metal contact layer. The switching time of the duplexer under EO effects is 0.14 ns (rise time) and 0.2 ns (fall time).

Comparing with the target specifications on the tunable wavelength duplexer, the insertion loss and the isolation level need to be further improved. A uniform surface of the wafer and uniformly spun photoresist can minimize the possibility of non-uniform exposure during lithography which causes waveguide width deviation. The thickness of the layer stack should be well controlled during the growth to minimize the overlap between the optical field and the contact layer.

Polarization independent operation depends on the proper waveguide geometry, thus it is very critical to control the waveguide width during the mask fabrication, optical lithography, and waveguide etching, especially for a duplexer with smaller channel spacing. For a duplexer with 500 GHz channel spacing (200 GHz channel spacing), the width of the MZI-arm should be controlled within a deviation of ±150 nm (±60 nm) to obtain a polarization dispersion of less than 15% of channel spacing.

Chapter 3

MMI loop mirror and MMI reflector

In this chapter, we present two reflective components, an MMI-loop mirror and an MMI reflector, which can be used to achieve on-chip reflection of the light in the photonic integrated circuit. They not only offer good reflectivity, but also require no additional fabrication steps and can greatly enhance the flexibility in the design of the photonic integrated circuit. Besides the concept and design of these two components, two methods are introduced and applied to calibrate the reflectivity. Based on the fabricated MMI-loop mirror and MMI reflector, the maximum achieved reflectivity is about 65%±10% for the MMI-loop mirror and more than 78%±10% for the MMI-reflector.

3.1 Introduction

As we introduced in Chapter 1, the CW light which comes from the local exchange travels back to the network after modulation with the upstream data. Therefore, a component or a mirror which has a high reflectivity and a large optical bandwidth is needed in the reflective transceiver. The commonly used methods to achieve a high reflectivity with a large optical bandwidth in a PIC are integration of a deeply etched DBR grating [114, 115] and applying a high-reflection (HR) coating at the output facet of the chip. In theory, both solutions can provide close to 100% reflectivity [116, 117], and the reflectivity can be chosen flexibly, by applying a proper coating to the facet, or by choosing the number of grating periods. The disadvantage of using the cleaved facet is that the location of the mirror cannot be freely chosen, but is determined by the circuit and sample geometry. Components in the PIC needing the reflector have to be extended to the facet, which limits the design flexibility. For the sub-micrometer DBR gratings, the fabrication is challenging, and when integrating the gratings with other photonic components, they add additional complexity to the fabrication procedures [115].

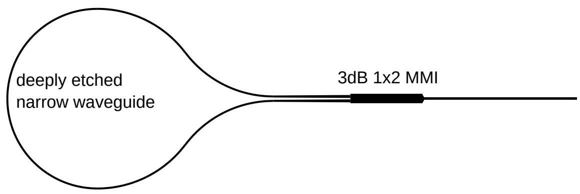

Figure 3.1: Layout of a MMI-loop mirror.

In this chapter, we will introduce two reflective components, an MMI-loop mirror and an MMI reflector, as an alternative to the HR coating and DBR mirror to achieve high reflectivity and more flexibility in the PIC. The advantages of these two components are that they don't require additional fabrication steps, and can be integrated on-chip flexibly in any direction and at any place. In section 3.2, we shortly discuss the concepts and the designs of these two components. In section 3.3, we present two reflectivity calibration methods and the corresponding characterized reflectivities of the components based on these two methods.

3.2 Concept and design

3.2.1 MMI loop mirror

The MMI loop mirror is composed of a 3 dB 1×2 MMI splitter/combiner and curved waveguides, Fig. 3.1. When the light enters the MMI, it will be split in two parts with equal power and equal phase, and then be guided back by the curved waveguides and recombine at the MMI. In principle, it can reach hundred percent reflectivity. In practice, its reflectivity is limited by the propagation loss in the curved waveguide and by the insertion loss of the MMI. In addition, the MMI splitter/combiner has a weak wavelength dependence.

The 1×2 3-dB MMI is designed 8 μm wide and 67 μm long, deeply etched with 2.5 μm wide access waveguides. It is optimized for TE polarization. In the curves we apply 1.5 μm wide deeply etched narrow curved waveguides which are connected to the access waveguides of the MMI through adiabatic linear tapers. The tapers connect a 2.5 μm wide deeply etched waveguide with a 1.5 μm wide deeply etched waveguide, and they are 70 μm long, simulated with a two dimensional BPM software from Phoenix. The experimentally measured excess loss of a single adiabatic linear taper is less than 0.1 dB. The radius of the curved waveguides is 80 μm. The reflectivity of the loop mirror was simulated by means of a circuit simulation software [111], and the results are shown in Fig. 3.2 for both TE and TM polarization. In the simulation, the waveguide transmission loss due to side wall roughness, scattering and free carrier absorption is not taken into account. The simulation result shows that the reflectivity can be more than 90% for a wavelength range of 1530 nm to 1560 nm for both TE and TM polarization.

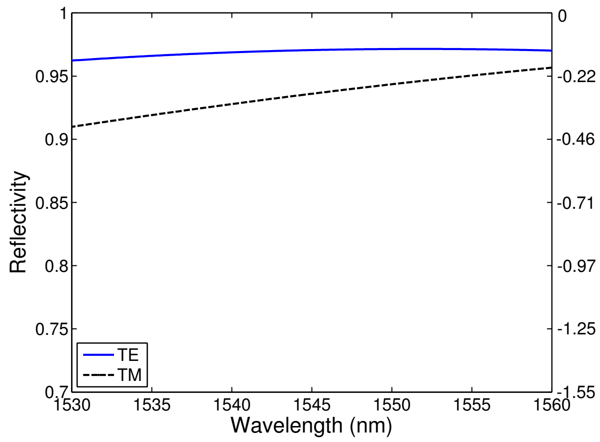

Figure 3.2: The simulated reflectivity of the MMI-loop mirror as a function of the wavelength for both TE and TM polarization. The left axis is the reflectivity, and the corresponding reflectivity in dB is shown at right axis. The simulated results do not include the loss of the curved waveguides.

3.2.2 MMI reflector

An MMI reflector is illustrated in Fig. 3.3. It works as follows: (a) The light enters a 1×2 3dB MMI, and at a certain length (L_{MMI}) it will be imaged into two light spots [118]. (b) When two 45° (which is larger than the critical angle of 17.3°) mirrors are placed at the position of the images as indicated in Fig. 3.3, the mirrored image will focus at the axis of the MMI. The beams continue propagating and are reflected back by the mirrors to the input port. (c) Due to the penetration of the light into the medium behind the mirror, the actual position of the mirror has to be shifted slightly forward. The effective penetration depth can be calculated according to [119]

$$d_{\mathrm{p}} = \frac{1}{\sqrt{\beta^2 - n^2 k_0^2}} \tag{3.1}$$

in which β is the propagation constant in the waveguide layer, and n is the refractive index of the medium behind the mirror, k_0 is the wave vector. It is important to notice that no light is focused at the corners of the reflecting facets, that will typically show some rounding due to the limited fabrication resolution. For additional tolerance, we avoid rounding of the mirror facets close to the outer corners by extending them as shown in the right side of Fig. 3.3. In addition, possible unwanted reflections from the input facet of the MMI are reduced by using angled corners, see the left side of the Fig. 3.3 [120].

The 1×2 3dB MMI of the MMI-reflector is designed to be 6 μm (W_{MMI}) wide and 37.86 μm (L_{MMI}) long, and it has a 2 μm wide access waveguide. The whole component is deeply etched. The mask layout of this MMI reflector is shown in Fig. 3.4, in which the facet means the 45° etched mirror, and L-reflector is the total length of the MMI-reflector,

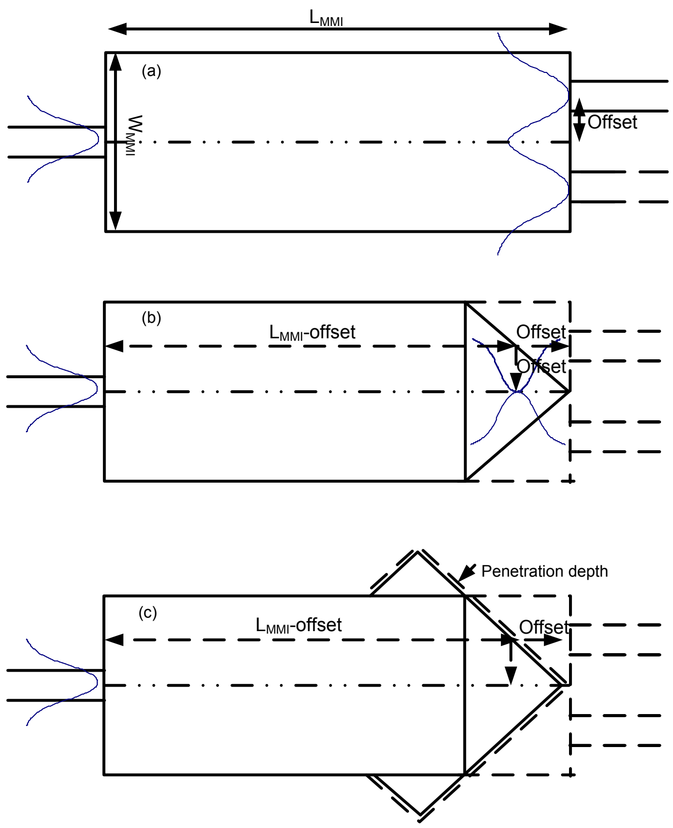

Figure 3.3: Diagram of the principle of the MMI-reflector.

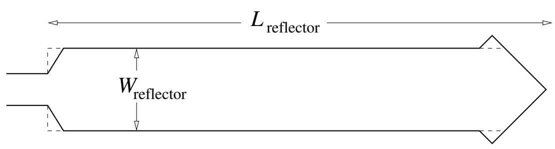

Figure 3.4: Mask layout of the MMI reflector. L-reflector is equal to $L_{\mathrm{MMI}} - \sqrt{2}d_{\mathrm{p}}$.

equal to $L_{\mathrm{MMI}} - \sqrt{2}d_{\mathrm{p}}$.

The reflectivity of the MMI reflector depends on the the etched waveguide sidewall angle. A typical SEM photo of a waveguide deeply etched by reactive ion etching (RIE) is shown in Fig. 3.5(top), from which we can see that the waveguide side wall is not straight, but has a certain angle, marked with two white lines. The angle of the sidewall is caused by the edge erosion of the mask material (SiNx in our case) which was taken advantage of to efficiently

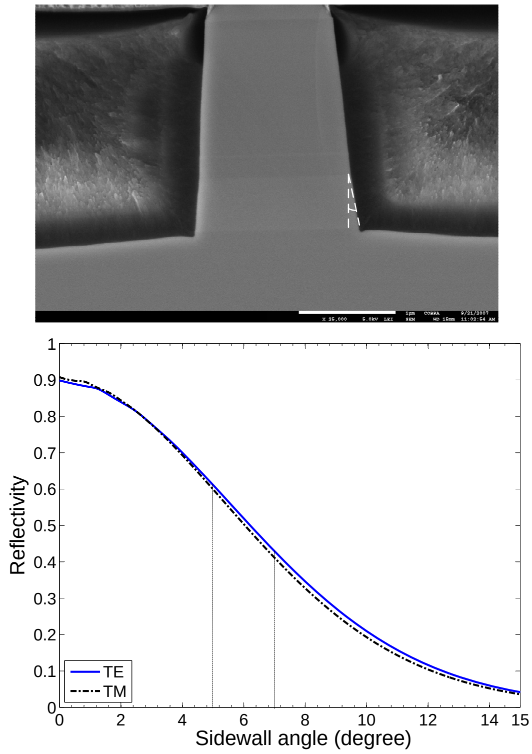

Figure 3.5: (*Top*) A SEM photo of a deeply etched waveguide by RIE with a non-zero (~5°) sidewall angle. (*bottom*) The simulated influence of the sidewall angle on the reflectivity of the MMI reflector. The sidewall roughness is not taken into account.

remove the polymer deposited on the sidewall during etching with a chemistry of $CH_4 : H_2$, since a small angle due to the mask erosion can expose more polymer on the sidewall to the ion bombardment. Typically, this sidewall angle of a deeply etched waveguide with RIE is between 5° to 7°. In order to see the influence of the sidewall angle, we used a software [121] which can calculate the reflectivity as a function of the horizontal and vertical angle of the mirror. It firstly decomposes the input field into a plane wave spectrum, then computes the reflection coefficient of the plane wave and reconstructs the spatial reflected field, and in the end calculates the overlap between the input field and the reflected field. Simulation results, in Fig. 3.5(bottom), show that the reflectivity drops from 90% to 45% when the angle increases from vertical (0°) to 7°. The MMI reflector has weak wavelength and polarization dependence. Simulation shows that the reflectivity variation within a 60nm range (1520 nm–1580 nm) can be as small as 0.07 dB (1.6% deviation). For the polarization dependence of the reflectivity we find 0.07 dB as well.

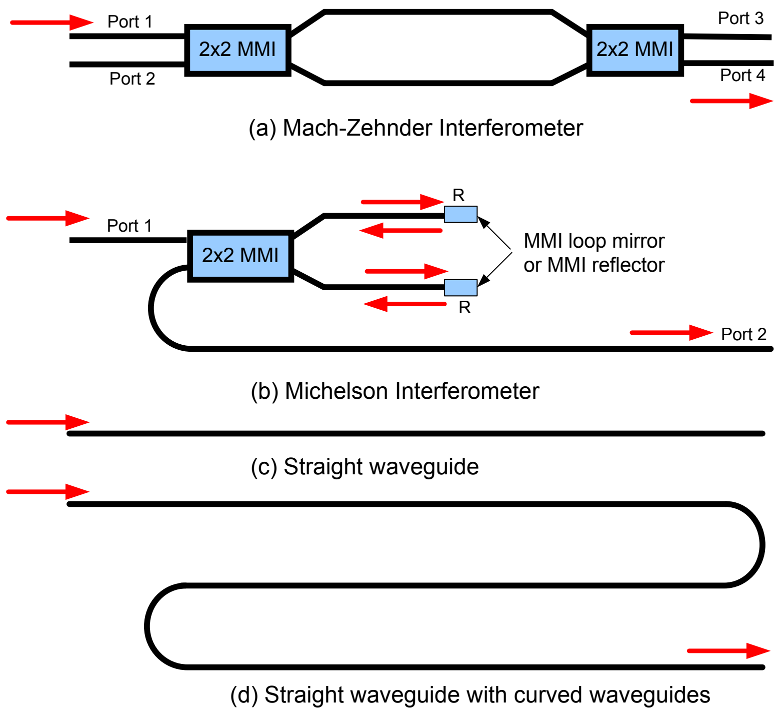

Figure 3.6: The principle of the passive method by using a Mach-Zehnder interferometer and a Michelson interferometer.

3.3 Reflectivity characterization

It is difficult to measure the reflectivity of the MMI loop mirror and the MMI reflector directly. Therefore, we have designed some circuits to facilitate the reflectivity calibration. In the following sections, we will describe the methods and the corresponding characterization results.

3.3.1 Passive method

Method description

The passive method is based on two interferometers, a Mach-Zehnder interferometer (MZI) and a Michelson interferometer (MI) which has half the length of the MZI and two reflectors (MMI loop mirrors or MMI reflectors) at the end of the two branches, as shown in Fig. 3.6 (a) and (b). Port 2 of the MI is led to the other side of the chip for the convenience of the characterization. The loss of the 180° curved waveguide is extracted by comparing the out-

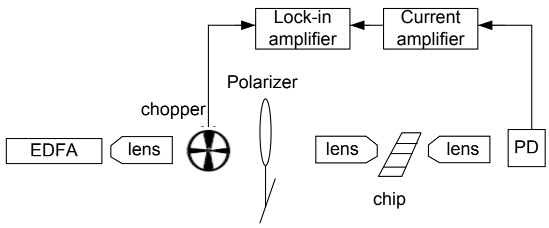

Figure 3.7: The measurement setup to characterize the reflectivity of the MMI-reflector.

put power of a straight waveguide and the power of a straight waveguide with two curved waveguides, as shown in Fig. 3.6(c) and (d). By comparing the power at port 2 of the MI ($P_{\text{port2-MI}}$) and the power at port 4 of the MZI ($P_{\text{port4-MZI}}$), the reflectivity of the reflector can be calibrated through equation

$$R_{\text{dB}} = -10\log\left(\frac{P_{\text{port4-MZI}}}{P_{\text{port2-MI}}}\right) + \alpha_{\text{curve}} \tag{3.2}$$

in which α_{curve} is the loss of the 180°bent waveguide.

Characterization results

The circuits for the reflectivity calibration are fabricated with RIE. In order to measure the output power, we used the measurement setup shown in Fig. 3.7. The light source is an EDFA, and the polarization is selected through a polarizer. The chopper modulates the light and sends the reference frequency to the lock-in amplifier. Two microscope objectives are used to couple the light in and out of the chip. The optical power is detected by a photodetector, the photocurrent is amplified by the current amplifier and transformed into a voltage which is read by the lock-in amplifier.

Based on this method, the measured reflectivity of the MMI-loop mirror is 60% ± 10% and 65% ± 10% for TE and TM polarization respectively. The error margin comes from the waveguide loss variation along this wafer.

The reflectivities of the MMI reflectors are measured to be 55% ± 20%. The large error margin results from three aspects: 1) the waveguide transmission loss varies along the wafer; 2) the power imbalance between two branches of a 2 × 2 3-dB MMI is about 1 dB for both polarizations, which introduces an uncertainty in the measurement results; 3) the reflectivity of the MMI reflector is sensitive to the sidewall angle etched by RIE, as shown in Fig. 3.5.

MMI-reflector etched by ICP technique

Different from RIE etching, inductively coupled plasma (ICP) etching uses a $Cl_2:Ar:H_2$ chemistry instead of $CH_4:H_2$ in RIE, and the polymer build-up is much lower in the ICP

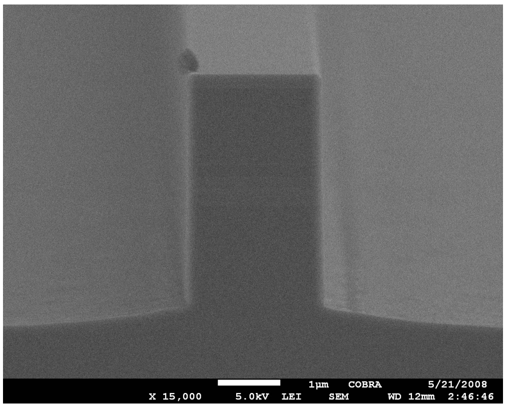

Figure 3.8: SEM picture of a deeply etched waveguide fabricated with ICP etching.

process because the process pressure is lower (10−18 mTorr in ICP versus 60 mTorr in the RIE). ICP can work at lower pressure during etching because of the higher plasma density. Therefore, ICP yields a more vertical sidewall, which is beneficial to fabricate a MMI reflector. An SEM picture of a deeply etched waveguide with ICP is shown in Fig. 3.8, which has a much straighter side wall than the waveguide shown in Fig. 3.5. The measured reflectivity of the MMI reflector is about 78%±10% (1.1 dB±0.5 dB), about 30% higher than the reflectivity obtained with the waveguide etched by RIE.

3.3.2 Active method

In this section, we will introduce the active method using different devices to calibrate the reflectivity of the MMI reflector.

Method description

The active method is based on the Fabry-Perot laser and the SOA structure, as shown in Fig. 3.9. A reference laser has two cleaved facets with known reflectivities, and the other laser has a cleaved facet at one side, and a MMI reflector at the other side.

The threshold gain of a Fabry-Perot (FP) laser depends on the total loss in the cavity, and the reflectivities at the facets. It can be written as

$$g_{\mathrm{th}} = \alpha + \frac{1}{2L} \ln\left(\frac{1}{R_1 \cdot R_2}\right) \tag{3.3}$$

in which g_{th} is the threshold mode gain, α is the total loss of the waveguide including the active and passive parts, L is the length of the laser, R_1 and R_2 are the reflectivities at the facets of the FP laser.

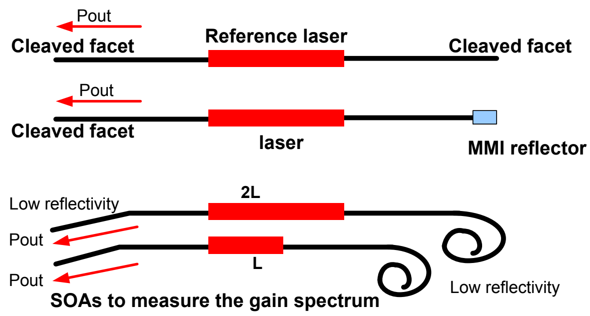

Figure 3.9: A schematic view of the devices needed in the active method to calibrate the reflectivity of the MMI reflector.

By comparing the difference in the threshold current and the output optical power of these two lasers, we can infer whether the reflectivity of the reflector is higher or lower than the reflectivity of the cleaved facet.

We quantify the reflectivity of the MMI reflector through equation

$$R_{\text{reflector}} = R_{\text{facet}} \cdot \exp\left[(g_{\text{th1}} - g_{\text{th2}}) \cdot 2L\right] \tag{3.4}$$

in which $R_{\text{reflector}}$ is the unknown reflectivity of the reflector, R_{facet} is the reflectivity of the cleaved facet, g_{th1} is the threshold gain of the reference laser, g_{th2} is the threshold gain of the laser with unknown reflectivity $R_{\text{reflector}}$.

In order to obtain the modal gain g, we measure the ASE spectrum of two SOAs with the same injection carrier densities, and calculate the modal gain g through equation

$$g = \frac{1}{L} \cdot \ln\left(\frac{P_{2\text{L}}}{P_{\text{L}}} - 1\right) \tag{3.5}$$

$$g = \Gamma \cdot g_{\text{m}} - \alpha \tag{3.6}$$

in which $P_{2\text{L}}$ is the output ASE power from the SOA with a length of $2L$, P_{L} is the output ASE power from the SOA with a length of L, Γ is the mode confinement factor and g_{m} is the material gain. For the detailed explanation on the measurement methods for the modal gain spectrum, we refer to [122]. To prevent the feedback, one side of the SOA is angled with 7° to reduce the facet reflectivity, and another side of the SOA is designed with the spiral curves to remove the reflection. The SOA generated ASE spectrum is recorded from the angled access waveguide, as shown in Fig. 3.9.

Characterization results

All the lasers and SOAs are fabricated with RIE etching, therefore the sidewall angle plays the same critical role in the reflectivity as the devices etched with RIE introduced in the former passive method.

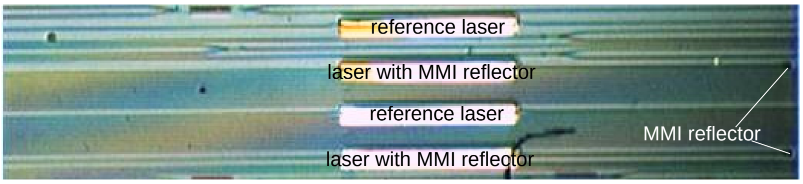

Figure 3.10: Photo of the fabricated lasers for calibrating the reflectivity of the MMI-reflector with the active method.

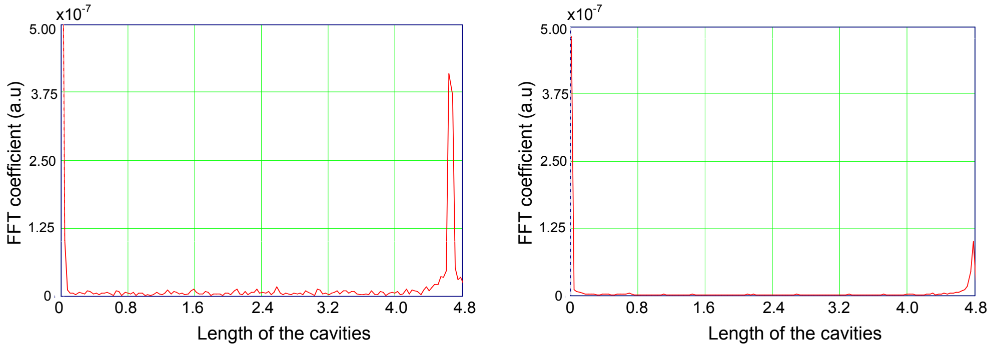

Figure 3.11: The reflection cavities in the FP-lasers with (*left*) and without (*right*) MMI-reflector.

The fabricated lasers and SOAs are based on quantum wells, and the lasers are 2 μm wide and 1000 μm long. The reflectivity of the cleaved facet is about 34.4%. The two SOAs which will be used to measure the gain spectrum are 2 μm wide, and 1 mm long and 500 μm long respectively. All lasers and SOAs are shallowly etched by reactive ion etching (RIE). The waveguide entering and exiting the active region is adiabatically angled with 12° to minimize the undesired reflectivity at the active-passive butt-joint. The total cavity length of the reference laser and the laser integrated with a MMI reflector is 4.77 mm and 4.63 mm respectively. The fabricated lasers are shown in Fig. 3.10.

The measured waveguide propagation losses of a 2 μm wide shallowly etched waveguide are about 4 dB/cm and 5 dB/cm for TE and TM polarization respectively. Therefore, the influence of the waveguide propagation loss due to the cavity length difference (140 μm) on the threshold current can be neglected.

In order to confirm that the measured reflection is coming from the MMI reflector rather than other residual reflections, we record the subthreshold ASE spectrum and analyze it using a Fourier transformation [123, 124]. The Fourier transformation shows peaks in the spectrum which can be related to the length of the cavities formed by the reflections in the circuit. The resolved reflection cavities are shown in Fig. 3.11. The cavity length given in Fig. 3.11 is a single trip length. The main reflection cavity is 4.63 mm long for a laser

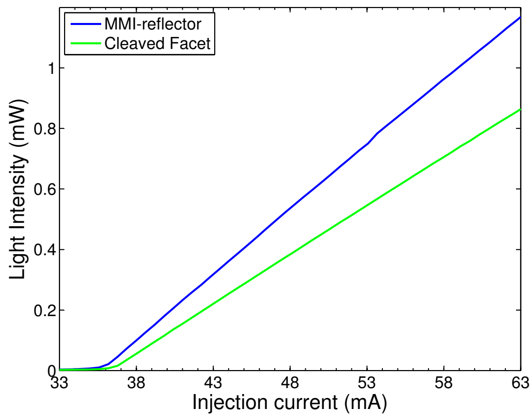

Figure 3.12: Light intensity as a function of the currents for both types of lasers at T = 20°C.

integrated with a MMI-reflector, and this length is corresponding to the distance from the cleaved facet to the MMI-reflector. Therefore, the light is reflected from the MMI-reflector. The main cavity length of the reference laser is 4.77 mm long corresponding to the distance from the cleaved facet to the cleaved facet.

When we increase the injection current, all lasers start lasing. The threshold current of the reference laser is 36.8 mA (corresponding to current density of 1.84 kA/cm^2), and the threshold current of the laser with a MMI-reflector is 35.6 mA (1.78 kA/cm^2). The measured light intensity as a function of the injection current is shown in Fig. 3.12. Besides a lower threshold current, the laser with a MMI-reflector also has a higher output optical power than the reference laser, which indicates that the reflectivity of the MMI-reflector is higher than the cleaved facet (0.344).

To quantify the reflectivity of the MMI-reflector, we measure the modal gain spectrum through two SOAs with different lengths, and the obtained spectrum is shown in Fig. 3.13. Assuming that the current injection efficiency is the same for these lasers, the threshold current densities of both types of lasers are within a range of 1.5 – 2 kA/cm^2 in Fig. 3.13, and the measured difference in the current densities between two types of lasers is 0.06 kA/cm^2. If we take the peak wavelength shift with the carrier density into account, the conservative estimation of the mode gain difference ($g_{th1} - g_{th2}$) is within 1.4 ± 0.4 /cm. Therefore, the reflectivity of this integrated MMI-reflector is 46% ± 4% according to equation (3.4), which is lower than the reflectivity obtained with ICP etching.

3.4 Conclusion and discussion

We have demonstrated two reflective components, the MMI loop mirror and the MMI reflector, which can be used as alternatives to a HR coating or a DBR grating in the photonic

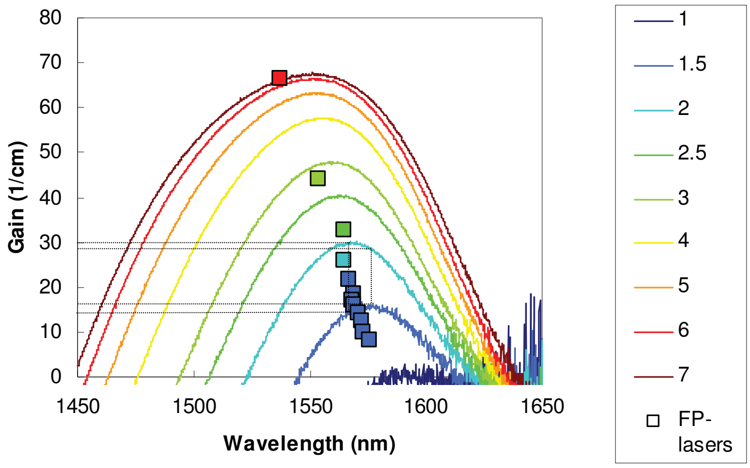

Figure 3.13: Mode gain spectra obtained from the test SOAs which are based on the same width, same material and same fabrication technology. The curves indicate the current densities (in kA/cm^2). The squares which indicate the threshold current density are obtained from the FP-lasers with two cleaved facets, assuming 3 dB/cm passive waveguide loss and 0.344 reflection at both facets.

integrated circuit. They offer a good reflectivity, and their fabrication procedures are compatible with the other passive and active components, which we have shown in the chips fabricated for the reflectivity calibration. Moreover, they can be put at any place and oriented in any direction, therefore they enhance the flexibility in the design of the photonic integrated circuit. A disadvantage of these two components is that they have only one access port and no through port which can be used to monitor the light.

Currently, the maximum achieved reflectivity is about 65%±10% from the MMI-loop mirror and more than 78% ± 10% from the MMI-reflector etched by ICP. The reflectivity of the MMI-loop mirror is sensitive to the waveguide transmission loss. Compared to the MMI reflector, the MMI loop mirror has larger dimension, but it doesn't have strict requirement on the sidewall angle, thus it is suitable for all the etching techniques. The MMI reflector is much smaller (6 μm×37.86 μm) and has been demonstrated with higher reflectivity using ICP etching.

For silica-based materials, the 45° is still slightly beyond the critical angle, hence the light will experience total internal reflection. This concept will be applicable for a large range of waveguiding materials.

Chapter 4

Reflective SOA modulator integrated with MMI loop mirror

A colorless reflective SOA which integrates a SOA and a MMI-loop mirror is analyzed in this chapter in terms of the modulation bandwidth and operation wavelength range. A series of simulations based on rate equations has been carried out to investigate the influence of the optical input power and the electrical current on the effective carrier life lifetime and the quality of the eye diagram. The measurement results have shown that this loop-RSOA can be operated error free (Q>6) in a large wavelength range from 1530 nm to 1560 nm with 1.25 Gbit/s data with $2^{23}-1$ *pseudorandom binary sequence while the injected optical power is* -14 *dBm before the chip.*

4.1 Introduction

As we introduced in Chapter 1, a reflective modulator which carries the upstream data is an important component in a monolithic integrated reflective transceiver. A semiconductor optical amplifier (SOA) is a promising candidate due to its small size, simple electrical pumping, broad spectral range and opportunities for integration and mass production. The small size and compatibility with semiconductor laser sources, detectors and other passive components offer the possibility of photonic integration, and the electrical injection offers the possibility of simple modulation [55]. The broad spectral range allows it to perform "colorless" operation in the user access network. In such applications, the choice of the wavelength is done in the local exchange, and identical subscriber transceivers can be installed for all subscribers without planning of the wavelength to be used for the specific users in advance.

In this chapter, we will investigate the modulation bandwidth and operational wavelength range of a reflective SOA based on an active-passive butt-joint layer stack grown in the COBRA research institute.

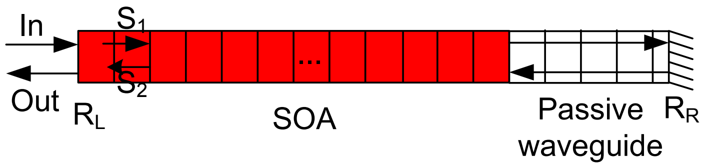

Figure 4.1: Schematic view of a RSOA segmented for modeling.

The following sections are organized as follows: Section 4.2 will describe the theory of the SOA based on rate equations. The effective carrier lifetime which determines the direct modulation bandwidth of a SOA is derived from these equations, and the simulation results follow in Section 4.3. Section 4.5 present the measurement results on the loop reflective SOA. Finally, we discuss the results.

4.2 Theoretical analysis

4.2.1 Rate equations

In this section, we will present a bi-directional time domain model based on rate equations including nonlinear gain coefficients for the reflective SOA. The SOA and the integrated waveguide is divided into identical segments (Fig. 4.1) in which injected carriers and photons are assumed to be uniformly distributed in the segments and the loss is independent of the location. Each section has its own input fields and output fields which serve as the input fields for the next section. The equations [125, 126] for the propagation of the photon density and the carrier density N within each segment are :

$$\frac{\partial N}{\partial t} = -(S_1+S_2)\cdot\frac{g_{\mathrm{m}}\cdot v_{\mathrm{g}}}{1+C_2\cdot(S_1+S_2)} - R(N) + \frac{I}{q\cdot A_{\mathrm{active}}L} \tag{4.1}$$

$$\frac{\partial S_1}{\partial t} = S_1\cdot\frac{g_{\mathrm{m}}\cdot v_{\mathrm{g}}}{1+C_2\cdot(S_1+S_2)} - S_1\cdot\alpha_{\mathrm{int}}\cdot v_g + C_3\cdot N^2 \tag{4.2}$$

$$\frac{\partial S_2}{\partial t} = S_2\cdot\frac{g_{\mathrm{m}}\cdot v_{\mathrm{g}}}{1+C_2\cdot(S_1+S_2)} - S_2\cdot\alpha_{\mathrm{int}}\cdot v_g + C_3\cdot N^2 \tag{4.3}$$

$$\frac{\partial \phi_1}{\partial z} = \frac{\frac{1}{2}\cdot\alpha_{\mathrm{T}}\cdot g_{\mathrm{m}}\cdot v_{\mathrm{g}}\cdot C_2\cdot(S_1+S_2)}{1+C_2\cdot(S_1+S_2)} - \frac{1}{2}\alpha_{\mathrm{N}}\cdot g_{\mathrm{m}}\cdot v_{\mathrm{g}} \tag{4.4}$$

$$\frac{\partial \phi_2}{\partial z} = \frac{\frac{1}{2}\cdot\alpha_{\mathrm{T}}\cdot g_{\mathrm{m}}\cdot v_{\mathrm{g}}\cdot C_2\cdot(S_1+S_2)}{1+C_2\cdot(S_1+S_2)} - \frac{1}{2}\alpha_{\mathrm{N}}\cdot g_{\mathrm{m}}\cdot v_{\mathrm{g}} \tag{4.5}$$

$$C_2 = \varepsilon_1\cdot\hbar\cdot\omega_0\cdot v_g\cdot\frac{A_{\mathrm{active}}}{\Gamma} \tag{4.6}$$

in which N is the carrier density, S_1 and S_2 are the forward and backward transmission photon densities within the cavity, ϕ_1 and ϕ_2 are the phases of the forward and backward signals, g_m is the modal gain, v_g is the group velocity along the cavity, C_2 is the nonlinear gain factor due to spectral hole burning and carrier heating; $R(N)$ is recombination rate, I is the injection current into the SOA, q is the electron charge, A_{active} is the cross section of the active region, L is the length of the SOA, Γ is the linear confinement factor (fraction of the photons that travel within the active region), α_{int} is the internal loss per unit length due to waveguide scattering and free-carrier absorption, and C_3 is the power spectral density of the optical ASE noise, α_T and α_N are the temperature and carrier density linewidth enhancement factor, ε_1 is the nonlinear gain compression factor related to the material, $\hbar$ is the Planck constant, and ω_0 is the nominal frequency of the light.

In the above equations, the modal gain g_m in the active region can be expressed as a logarithmic model which has been validated experimentally in [127]:

$$g_m = \Gamma \cdot a \cdot N_0 \cdot \ln\left(\frac{N}{N_0}\right) \tag{4.7}$$

$$G = \exp\left[(g_m - \alpha_{int}) \cdot L\right] \tag{4.8}$$

in which a is the linear material gain coefficient, N_0 is the transparency carrier density, and G is the signal gain.

The recombination rate $R(N)$ in equation 4.1 includes radiative and non-radiative carrier recombination processes [128, 129], and can be described as:

$$R(N) = A \cdot N + B \cdot N^2 + C \cdot N^3 \tag{4.9}$$

where A is the inverse of the carrier lifetime, B is the bimolecular radiative recombination coefficient and C is the Auger recombination coefficient.

The spectral density of the spontaneous emission added to the output of an amplifier is

$$C_3 = (G - 1) \cdot \hbar \cdot \omega \cdot n_{sp} \cdot g_m / (g_m - \alpha_{int}) \tag{4.10}$$

where n_{sp} is the inversion parameter of the spontaneous emission.

At steady state, a relation between the injected electrical current and the carrier density below the lasing threshold can be extracted from the simplified equation

$$A \cdot N + B \cdot N^2 + C \cdot N^3 = \frac{I}{q \cdot A_{active} \cdot L} \tag{4.11}$$

Based on the above equations, we have built a numerical model which records the carrier density, the power and the phase of the optical signal at each segment of the RSOA.

4.2.2 Modulation bandwidth

For a SOA directly modulated by the electrical current, the modulation amplitude of ΔN of the carrier density for a given variation of ΔI of the modulation current is given by [130]

$$\Delta N(f_{\mathrm{mod}}) = \frac{\Delta I(f_{\mathrm{mod}})}{q \cdot V} \cdot \frac{\tau_{\mathrm{eff}}}{\sqrt{1 + (\omega \cdot \tau_{\mathrm{eff}})^2}} \tag{4.12}$$

where ω is the modulation frequency, and τ_{eff} is the effective carrier lifetime which can be written as [131–134]

$$\tau_{\mathrm{eff}}^{-1} = \frac{\partial R(N)}{\partial N} + \frac{\partial}{\partial N}\left(\frac{g_{\mathrm{m}} \cdot v_{\mathrm{g}} \cdot S}{1 + C_2 \cdot S}\right) \tag{4.13}$$

Thus we can derive τ_{eff} from equation (4.1), equation (4.7) and equation (4.9) as

$$\tau_{\mathrm{eff}}^{-1} = (A + 2B \cdot N + 3C \cdot N^2) + (S_1 + S_2) \cdot \frac{a \cdot N_0 \cdot v_{\mathrm{g}}}{1 + C_2 \cdot (S_1 + S_2)} \cdot \frac{1}{N} \tag{4.14}$$

in which the first item inside the bracket ($(A + 2B \cdot N + 3C \cdot N^2)$) is the differential carrier lifetime τ_{d}, and the second item accounts for the speed-up associated with stimulated recombination. The effective carrier lifetime can be rewritten in terms of the instantaneous optical power P as

$$\tau_{\mathrm{eff}}^{-1} = (A + 2B \cdot N + 3C \cdot N^2) + \frac{P}{\hbar\omega_0 \cdot A_{\mathrm{active}}} \cdot \frac{\Gamma \cdot a \cdot N_0}{1 + \varepsilon_1 P} \cdot \frac{1}{N} \tag{4.15}$$

$$P = \hbar\omega_0 \cdot V_g \cdot \frac{A_{\mathrm{active}}}{\Gamma} \cdot S \tag{4.16}$$

The carrier modulation response exhibits the low-pass characteristic with an optical 3 dB bandwidth of

$$\Delta f_{\mathrm{3dB}} = \frac{1}{2\pi \cdot \tau_{\mathrm{eff}}} \tag{4.17}$$

In equation (4.15) there are three elements that determine the modulation bandwidth. The first is related to the material parameters such as A, B, C, a, and N_0 which are determined by the material. The second element is the carrier density, which can be changed by the injection current. The third is the photon density, which could be controlled by injecting external optical power.

The equations lead to simple guidelines for achieving high modulation bandwidth by realizing SOA with

- large confinement factor (Γ)
- high differential gain (a)
- short carrier lifetime (large A, B, C)

Table 4.1: Parameters used in the simulation for the RSOA.

Symbol	Description	Value
λ	nominal wavelength	1.55 μm
L	SOA length	1000 μm
W	active region width	1.8 μm
d	thickness of the active layer	120 nm
Γ	linear optical confinement factor	0.259 [127]
n_g	group effective index	3.7
R_L	left facet reflectivity	0.001
R_R	right facet reflectivity	0.9
N_0	transparency carrier density	$0.5 \cdot 10^{24}\,\mathrm{m}^{-3}$ (measured)
a	linear gain coefficient	$3.24 \cdot 10^{-20}\,\mathrm{m}^2$ [127]
A	one over the carrier lifetime	$1.67 \cdot 10^9\,\mathrm{s}^{-1}$ [127]
B	bimolecular recombination rate	$2.602 \cdot 10^{-16}\,\mathrm{m}^3/\mathrm{s}$ [127]
C	Auger recombination coefficient	$5.269 \cdot 10^{-41}\,\mathrm{m}^6/\mathrm{s}$ [127]
α_N	carrier density linewidth enhancement factor	4.0 [127]
ε_1	nonlinear gain coefficient	0.2/W [127]
C_2	nonlinear gain coefficient	$1.75 \cdot 10^{-24}\,\mathrm{m}^3$ [127]
α_{int}	scattering loss and free carrier loss in the cladding	2000 /m [127]
α_T	temperature linewidth enhancement factor	2 [127]
n_{sp}	spontaneous inversion	2 [127]
β	spontaneous emission coupling coefficient	10^{-5}
α_{int}	internal loss in the active region	2000 /m [127]

or operating the SOA at

- high injection current (I_{bias})
- high input optical power level (P_{in})

In the next sections, we will investigate the influence of the operation conditions, namely I_{bias} and P_{in}, on the modulation bandwidth for a device with fixed values of Γ, a and A, B, C.

4.3 Simulation of the reflective SOA

In this section, we will first use a numerical model to analyze the carrier density, optical power and effective carrier lifetime along the reflective SOA as a function of the injection current and input optical power. A commercial software tool VPI-Photonics is used to analyze the influence of the electrical current and the input optical power on the modulated optical bit sequence and eye diagrams. All the parameters used in the simulation are listed in table 4.1.

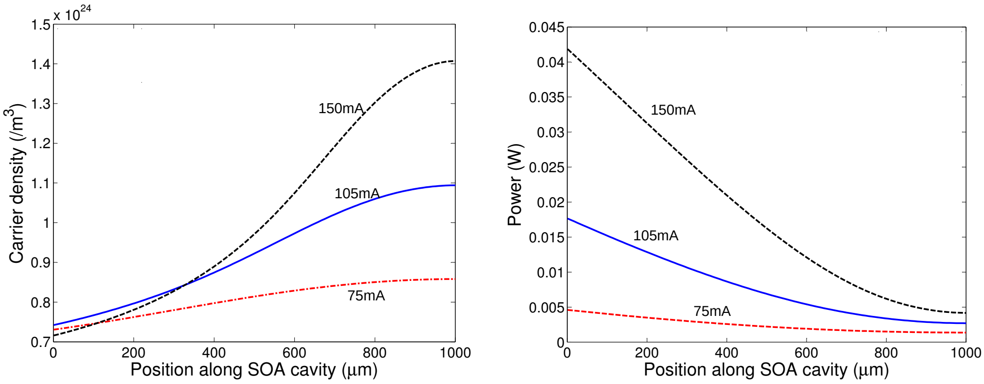

Figure 4.2: The calculated carrier density (*left*) and optical power (*right*) along the reflective SOA at different injection currents when $P_{\text{in}} = -10\,\text{dBm}$. The position of $0\,\mu$m at the x-axis means the fiber access side, and the position of $1000\,\mu$m is the facet with HR coating.

4.3.1 Effective carrier lifetime

We have built a numerical model based on rate equations. In this model the RSOA has $T = 1 - R_{\text{L}} = 100\%$ transmission at the access side, and $R_{\text{R}} = 100\%$ reflectivity at the other side for the simplicity . It is a bi-directional model, and the whole RSOA is segmented into 124 sections ($8\,\mu$m per section). The carrier density and the photon density over a wavelength are considered as uniformly distributed within $8\,\mu$m section. The standing wave pattern caused by the interference between forward and backward propagating light is not taken into account. The nonlinear gain coefficient is considered as the same for the forward and backward propagating light, which is a common approximation in the numerical models for the SOA, for example in [135]. When the input optical power is high, the gain saturation could be underestimated.

By means of this model, the evolution of the photon density and carrier density is calculated for all sections. Examples of carrier and power distribution along the SOA at different injection currents are shown in Fig. 4.2(left), from which we can see that the carrier density is lower at the access side of the SOA where the CW light enters and exits. The reason for this is that the total optical power is higher at the access side which saturates the device and consumes more carriers, Fig. 4.2(right). By substituting the carrier density and optical power into equation (4.15), the effective carrier lifetime versus the position at the SOA at different injection currents is calculated and shown in Fig. 4.3. The same calculation has been repeated for different input optical power as well. We observe that the effective carrier life time is shortened by increasing both the input optical power and the injection current which contributes to both items in equation (4.15). When $I_{\text{bias}} = 150\,\text{mA}$, the effective carrier lifetime becomes as low as 100 ps at the access side with $P_{\text{in}} = -10\,\text{dBm}$, corresponding to ~1.6 GHz bandwidth.

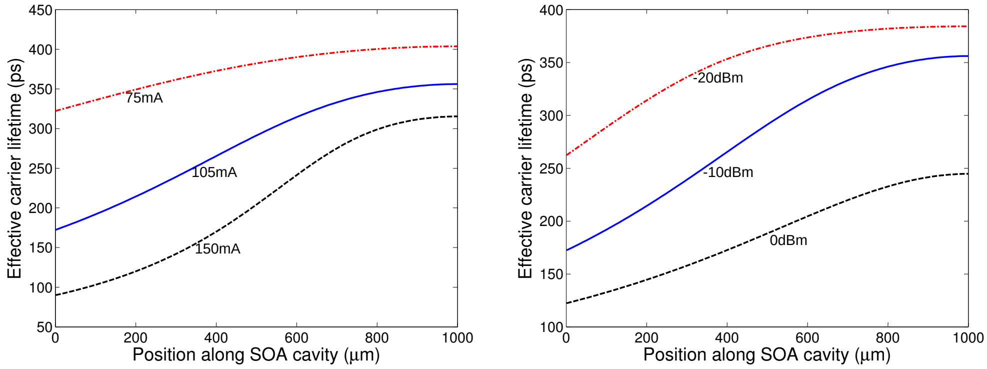

Figure 4.3: The calculated effective carrier lifetime along the SOA cavity as a function of the injected electrical current when $P_{\text{in}} = -10\,\text{dBm}$ (*left*) and the input optical power at $I_{\text{bias}} = 105\,\text{mA}$(*right*). The position of 0 μm at the x-axis means the fiber access side, and the position of 1000 μm is the facet with HR coating.

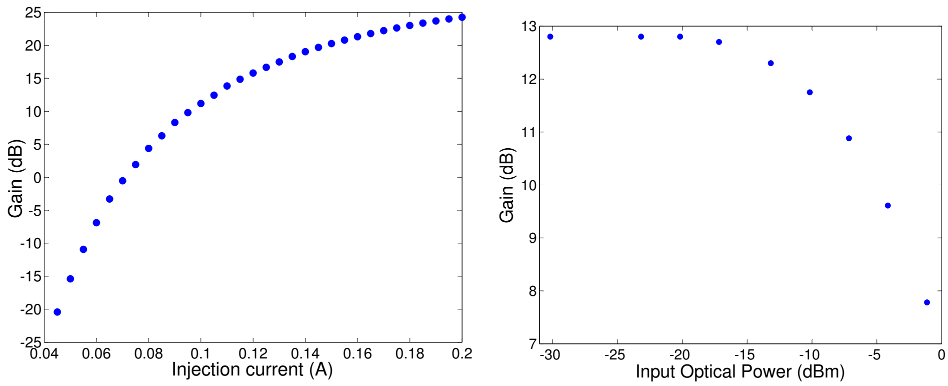

Figure 4.4: (*left*) Gain-current (G-I) curve of the RSOA for the parameters as listed in table 4.1 with $P_{\text{in}} = -17\,\text{dBm}$. (*right)* Simulated gain saturation as a function of the input optical power (G-P curve) for the RSOA when $I_{\text{bias}} = 105\,\text{mA}$.

4.3.2 Gain of the RSOA

In order to include the influence of the ASE noise due to the facet reflectivity in the simulation, we use a commercial software tool VPI-photonics to analyze the device performance in terms of gain and eye diagrams under different operation conditions.

Based on rate equations (4.1 to 4.3) and the modal gain in equation (4.7), the gain of the RSOA has been simulated as a function of both the electrical current and the input optical power, and the simulation results are shown in Fig. 4.4. To obtain the G-I curve, the input

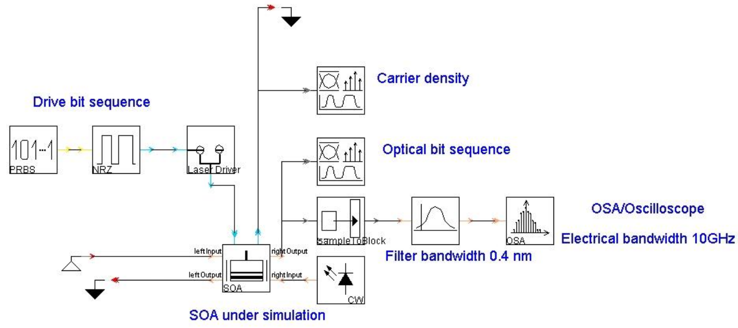

Figure 4.5: The schematic view for the dynamic simulation in VPI-Photonics.

optical power was set at $P_{\text{in}} = -17\,\text{dBm}$. From the G-I curve, we can see that there are two regions: in the first region, the gain of the SOA increases linearly with the electrical current below 100 mA, while for higher currents the gain increases slowly and finally clamps at the threshold gain. The first region is called the linear region while the other region is called the gain saturation region. According to the G-I curve, the modulation can have a higher extinction ratio at the linear region than at the saturation region with the same current modulation amplitude.

In the G-P curve, the gain starts to drop when the output optical power ($P_{\text{in}} + G$) exceeds a certain level. This can be explained by the relation between the population inversion created by the injection current and the carrier consumption due to amplification [136]. As we increase the input power, a point arrives where the rate of consumption is greater than the rate of pumping, such that the population inversion level can no longer be maintained at a constant value and starts to drop. Thus the gain of the system starts to drop. The output optical power at which the gain is compressed by 3 dB is known as the saturation output power P_{sat} determined by the material and waveguide geometry [136,137]. It is about 5 dBm here according to Fig. 4.4(right).

4.3.3 Dynamic simulation

The schematic layout of the simulation setup is shown in Fig. 4.5. The SOA is set with the parameters given in table 4.1. The CW light from the laser diode is injected in the right side of the SOA with 0.1% reflectivity and reflected back at the other side with 90% reflectivity. The pseudo-random binary sequence (PRBS) code is an ideal square bit sequence, and the visual analyzer records the carrier density and the output bit sequence as a function of time.

The optical band pass filter (BPF) has 0.4 nm bandwidth to filter away part of the ASE noise, and the electrical bandwidth of the oscilloscope is set to 10 GHz. The optical spectrum analyzer (OSA) records the output spectrum. The modulation amplitude is set at $I_{\text{p-p}}$ = 15 mA which is sufficient to analyze the influence of the parameters of the input optical power and the bias direct current (DC).

Injection current effect

The simulation has been carried out with fixed input optical power $P_{\text{in}} = -10\,\text{dBm}$ for different injection currents. The simulated output bit sequence and eye diagrams at different injection currents are shown in Fig. 4.6. According to Fig. 4.4(left), 75 mA is located in the linear region, 105 mA is at the transition point between the linear gain region and gain saturation region, and 150 mA is in the saturation region. From Fig. 4.6, we can see that the output optical power increases with the electrical current, and the extinction ratio ($ER = 10\log(P_1/P_0)$) decreases from 6.2 dB when $I_{\text{bias}} = 75\,\text{mA}$ to 1.3 dB when $I_{\text{bias}} = 150\,\text{mA}$.

The 10%−90% rise time τ_{rise} (fall time τ_{fall}) is 0.7 ns (1.1 ns) when $I_{\text{bias}} = 75\,\text{mA}$, and it is reduced to 0.19 ns for both rise and fall time when $I_{\text{bias}} = 150\,\text{mA}$. The larger difference between rise and fall time at low bias current is caused by the larger difference in carrier density and optical power between "0" and "1" level. The reduced rise and fall time at I_{bias}=150 mA can be explained by an increased number of carriers and photons inside the cavity which shorten the carrier lifetime according to equation (4.15) and Fig. 4.2. The relation between the effective carrier lifetime τ_{eff} and the 10% − 90% rise (fall) time is approximately $\tau_{\text{rise/fall}} = 2.2\tau_{\text{eff}}$, which matches well with the numerical simulation results given in Fig. 4.3(left).

From Fig. 4.6, we can see that the noise at both 1 and 0 levels increases with the injection current, especially at 0 level. The reason is that gain increases with the injection current, and thus ASE noise increases. The SOA biased at $I_{\text{bias}} = 105\,\text{mA}$ shows a better eye diagram in terms of the noise on the signal. The reason is that when the bias current is low, the amplification of the signal is small, thus more vulnerable to the ASE noise. On the other hand, when the bias current is too high, the ASE Fabry-Perot ripples caused by the facet reflectivities starts to interfere with the signal, which deteriorate the quality of the modulated eye. The simulated OSA spectra at 105 mA and 150 mA are shown in Fig. 4.7 , in which the ASE Fabry-Perot ripple is about 7 dB when $I_{\text{bias}} = 150\,\text{mA}$.

Therefore, an optimum bias current for the RSOA is a high current in the linear gain region (see G-I curve in Fig. 4.4(left)), which offers high signal gain and larger extinction ratio. The ASE ripple at this optimum current should be low.

Input optical power effect

The bias current was set at $I_{\text{bias}} = 105\,\text{mA}$ which generates 13 dB fiber-fiber gain at low input optical power, according to Fig. 4.4. Fig. 4.8 shows the output optical bit sequences and the eye diagrams at different input optical powers.

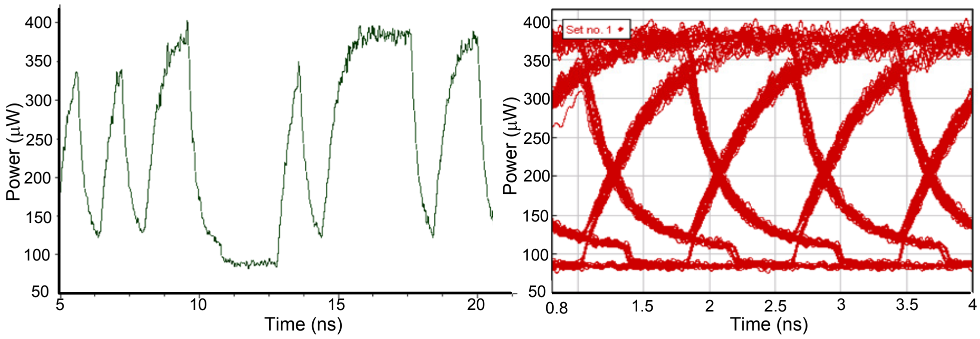

(a) $I_{\text{bias}} = 75\,\text{mA}$, $\tau_{\text{rise}} = 0.7\,\text{ns}$, $\tau_{\text{fall}} = 1.1\,\text{ns}$

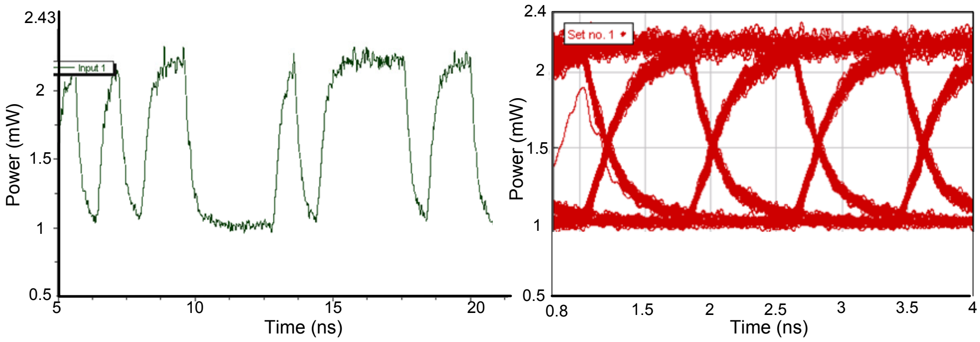

(b) $I_{\text{bias}} = 105\,\text{mA}$,$\tau_{\text{rise}} = 0.4\,\text{ns}$, $\tau_{\text{fall}} = 0.44\,\text{ns}$

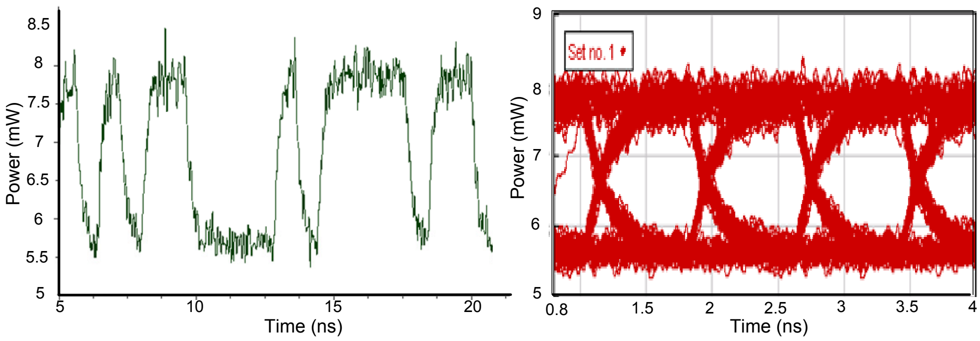

(c) $I_{\text{bias}} = 150\,\text{mA}$, $\tau_{\text{rise}} = 0.19\,\text{ns}$, $\tau_{\text{fall}} = 0.19\,\text{ns}$

Figure 4.6: Simulated output optical bit sequence (*left*) and eye diagrams (*right*) at 1.25 Gbit/s for RSOA when the I_{bias}=75mA, I_{bias}=105mA, I_{bias}=150mA.

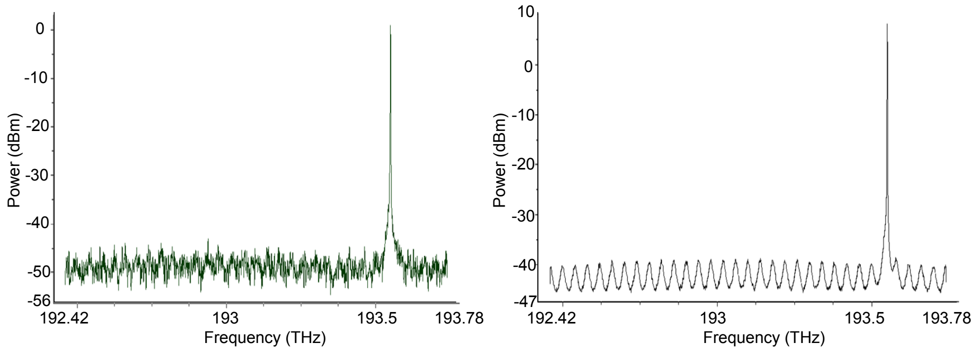

Figure 4.7: The simulated ASE spectra at 105 mA (*left*) and 150 mA (*right*) when $P_{\text{in}} = -10$ dBm.

According to Fig. 4.4(right), the RSOA operates in the linear region, nearly −3 dB saturation region and deep saturation region when the input optical power is corresponding to −20 dBm, −10 dBm, and 0 dBm respectively. The corresponding extinction ratios in Fig. 4.8 are about 4.2, 3.4 and 2.5 when $P_{\text{in}} = -20$ dBm, −10 dBm, and 0 dBm.

From the bit sequence, we can see that the rise (fall) time is about 0.58 ns (0.68 ns) when the input optical power is −20 dBm, and it has been shorten to 0.28 ns when $P_{\text{in}} = 0$ dBm, which matches well with the calculated τ_{eff} in numerical model shown in Fig. 4.3(right). Besides, the noise is highly suppressed when $P_{\text{in}} = 0$ dBm, and the reason is that the amplification of the ASE is reduced when the device is highly saturated. However, the extinction ratio (ER) is reduced when the device operates at the saturation region.

Therefore, there is a trade-off between the rise time, the noise suppression and the extinction ratio. When the input optical power is high, the rise time is shorter and the noise is suppressed, but the extinction ration decreases. The optimum operation region for the RSOA is in the nearly saturation region according to the eye quality shown in Fig. 4.8.

In the next section, we will experimentally investigate the influence of the injection current and the input optical power on the eye diagrams of a RSOA.

4.4 Design of a loop RSOA

The reflective SOA described here consists of a SOA and a MMI-loop mirror, as shown in Fig. 4.9. Once the CW light from the local exchange enters the device, the light will be amplified and modulated by the SOA and later reflected back by the loop mirror.

The reflective SOA is based on the layer stack shown in Fig. 4.10, in which Q1.55 is the active layer, 120 nm thick sandwiched between two 190 nm thick Q1.25 waveguide layers. The SOA is 2 μm wide and 1000 μm long, and the total optical path of the MMI-loop mirror is 600 μm long. The preparation of the butt-joint wafer and the fabrication processes of this

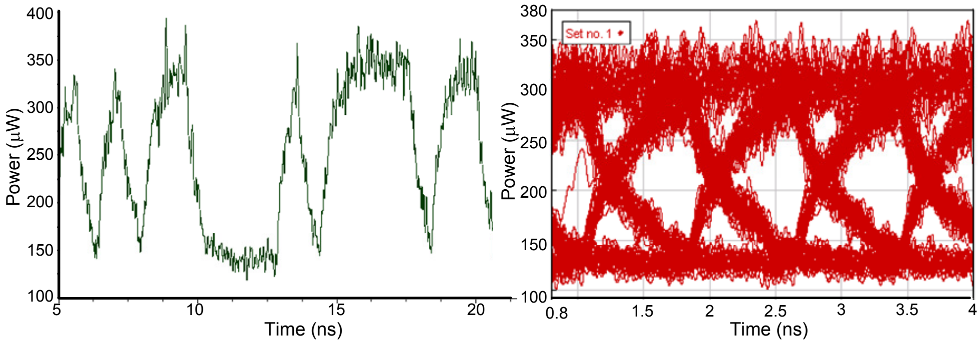

$P_{\text{in}} = -20\,\text{dBm}$ @ linear region $\tau_{\text{rise}} = 0.58\,\text{ns}$, $\tau_{\text{fall}} = 0.68\,\text{ns}$

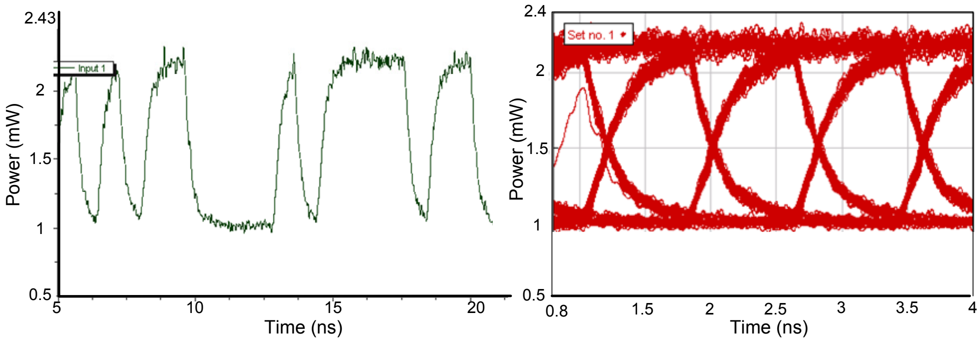

$P_{\text{in}} = -10\,\text{dBm}$ @ low saturation region $\tau_{\text{rise}} = 0.4\,\text{ns}$, $\tau_{\text{fall}} = 0.44\,\text{ns}$

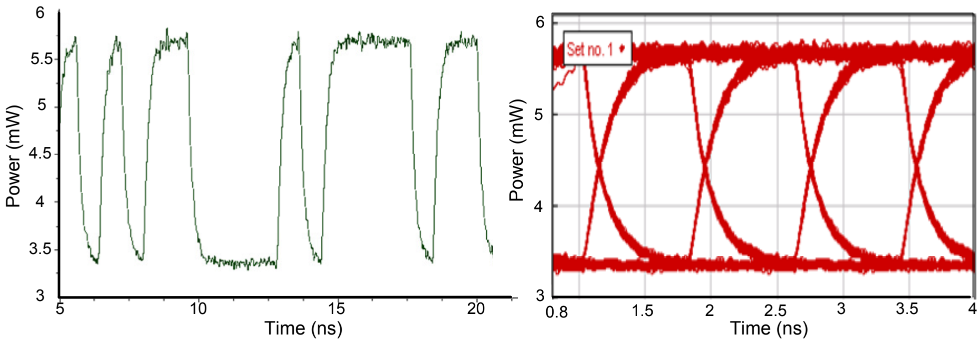

$P_{\text{in}} = 0\,\text{dBm}$ @ high saturation region $\tau_{\text{rise}} = 0.28\,\text{ns}$, $\tau_{\text{fall}} = 0.28\,\text{ns}$

Figure 4.8: Simulated output optical bit sequences (*left*) and eye diagrams (*right*) at 1.25 Gbit/s for a RSOA with the parameters listed in table 4.1 when the input optical power $P_{\text{in}} = -20\,\text{dBm}$, $P_{\text{in}} = -10\,\text{dBm}$ and $P_{\text{in}} = 0\,\text{dBm}$ at $\lambda = 1.55\,\mu\text{m}$.

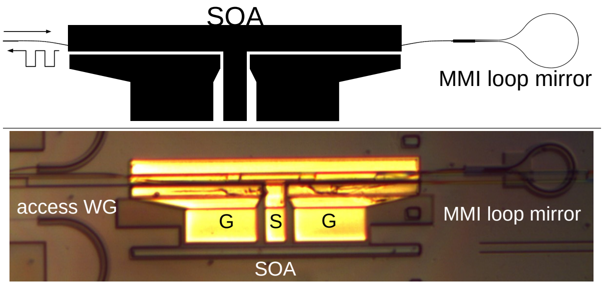

Figure 4.9: Mask layout and a photograph of a fabricated reflective SOA integrated with a MMI loop mirror.

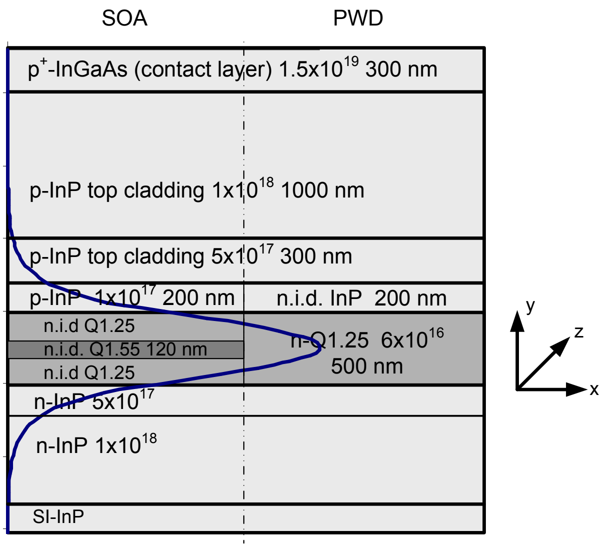

Figure 4.10: Active-passive butt-joint layer stack with specifications based on a semi-insulating substrate, and the transverse mode-profile is shown.

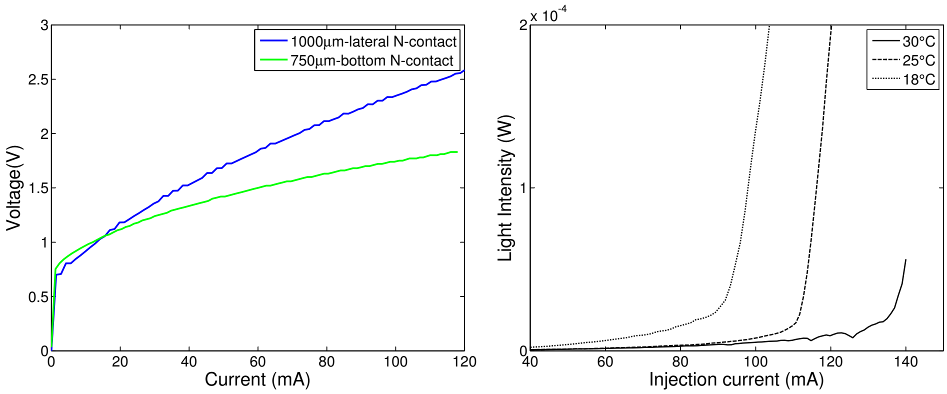

Figure 4.11: Current–voltage (I-V) curve (left) and the output light intensity of a 1000 μm long SOA integrated with a MMI-loop mirror with lateral ground contact as a function of the injection current, at temperatures of 30°C, 25°C and 18°C (right).

device will be described in Chapter 6.

One side of the device is a cleaved facet which has 33% reflectivity for TE polarization, and the reflectivity of the loop mirror is about 60%, as given in Chapter 3. During the measurement, the temperature was stabilized through a Peltier element.

4.5 Characterization of a loop-RSOA

4.5.1 Static measurement

In this part, we will first measure the series resistance of the SOA which has the lateral ground contacts as shown in Fig. 4.9, and then compare it with the device based on N-contact at the backside. The series resistance is important for later impedance matching during the dynamic measurements. To find the proper bias current for the RSOA, the lasing threshold current and the ASE spectrum will be measured. Furthermore, according to the simulations, the device operates better in the low saturation region, thus the saturation input optical power will be measured as well.

The series resistance of this 1000 μm long SOA is measured to be about 15 Ω, higher than the resistance measured for the bottom contacted SOA, as shown in Fig. 4.11. One of the reasons is the high lateral N-contact resistance [138], which accounts for about 3.5 Ω extra. The other extra resistance is caused by the residual photoresist or polyimide on the contact surface during the extra processing steps (see Chapter 6).

The measured light intensity-current (LI) curves for this device at different temperatures are shown in Fig. 4.11. From the LI-curve, we can see that the SOA starts to lase at about 90 mA, 110 mA and 140 mA at 18°C, 25°C and 30°C. The low threshold current limits the operational bias current range and the device gain. Fig. 4.12 shows the ASE spectra at

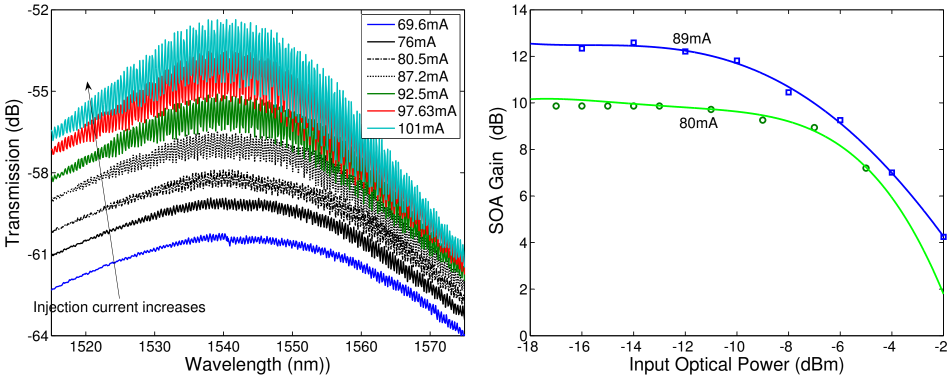

Figure 4.12: The output ASE spectrum measured with 0.05 nm resolution at different injection currents at room temperature 25°C(*left*). The measured chip gain as a function of the input optical power (before fiber-chip coupling) (*right*). The fiber chip coupling loss is regarded as 5 dB including the facet reflection loss.

different injection currents at 25°C. The gain peak shifts from 1545 nm to 1540 nm when the injection current is measured from 69 mA to 101 mA, and the ripple at the peak wavelength is less than 1 dB when the injection current is below 90 mA.

The 3 dB input saturation power, shown in Fig. 4.12(right), is −7 dBm (−9 dBm) at 80 mA (89 mA) injection current which is sufficient for our purpose to do the dynamic testing since the input optical power in the access network is generally below −10 dBm.

4.5.2 Dynamic measurement

The dynamic measurement has been carried out in the measurement setup shown in Fig. 4.13. We used a tunable laser as CW light source, and the polarization state is controlled by a polarization controller. The DC bias was kept at 81 mA where the chip gain is about 15 dB, and ASE ripple is low. The modulation amplitude was set at 250 mV in the pattern generator (PPG). A 35 Ω resistance is added between the bias tee and the PPG in order to reduce the RF reflection caused by the impedance mismatch between the SOA and the PPG.The light was directly modulated through the loop RSOA with a 1.25 Gbit/s NRZ format bit pattern. The pattern length is $2^{23}-1$ pseudo-random binary sequence (PRBS). After modulation and amplification, the light is transmitted back through the fiber circulator and amplified by the EDFA. The bandpass filter (BPF) has 2.5 nm bandwidth. The modulated light was firstly transformed into an electrical signal by the lightwave converter, and finally was fed to a digital communication analyzer. Back-to-back BER measurements have been carried out with a commercial receiver for different input optical power levels. The input optical power (P_{in}) in the following sections is the optical power measured before fiber-chip coupling, and the received optical power (P_{receive}) is the power received by the commercial

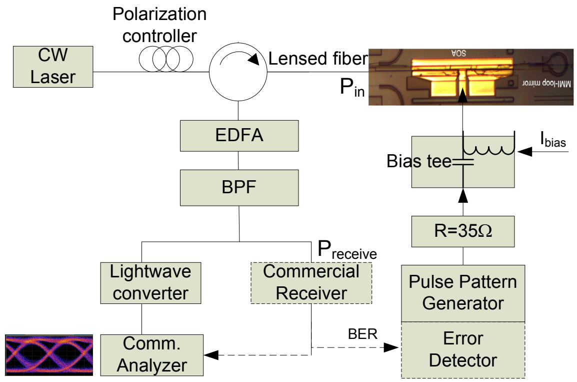

Figure 4.13: Eye diagram and BER measurement setup for the loop RSOA.

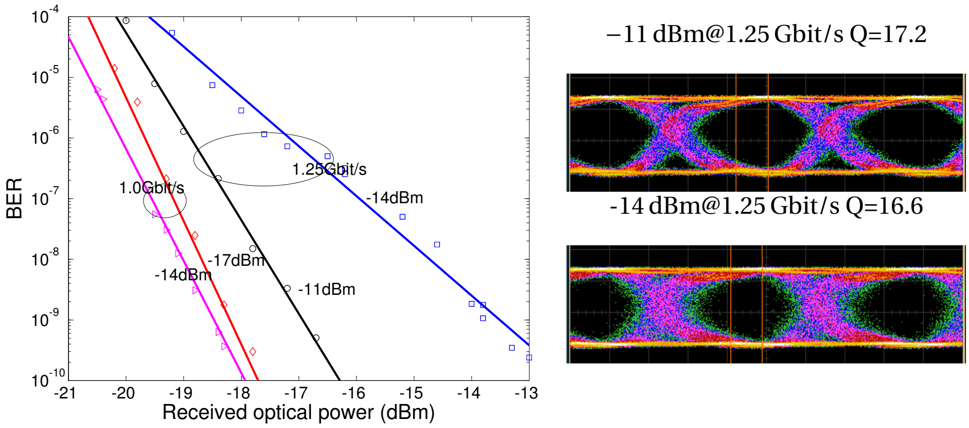

Figure 4.14: Measured BER performance at 1.25 Gbit/s and 1 Gbit/s for different injected optical power level (*left*) and two eye diagrams at 1.25 Gbit/s recorded after the commercial receiver with different input optical powers (*right*). The input wavelength is 1555 nm.

receiver, see Fig. 4.13.

Dependence on the input optical power

As we see from equation (4.15), a higher photon density shortens the effective carrier lifetime, and suppresses the noise [139]. We recorded the eye diagrams and back-to-back BER for 1.25 Gbit/s (1 Gbit/s) with different input optical power, and the results are shown in Fig. 4.14. The measured modulation extinction ratios are 5 dB (6 dB) for 1.25 Gbit/s (1 Gbit/s) at I_{bias} = 81 mA. From the eye diagrams, we can see that the eyes are clearer

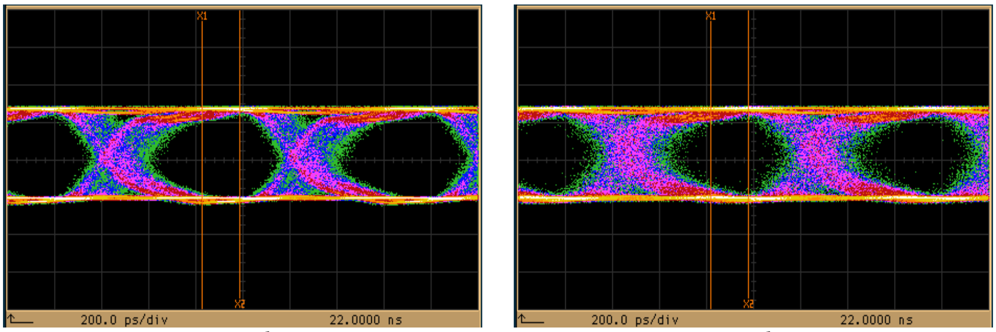

90 mA @1.25 Gbit/s Q=19 81 mA @1.25 Gbit/s Q=16.6

Figure 4.15: Eye diagram after the commercial receiver at λ =1555 nm and 1.25 Gbit/s bitrate for the injected optical power of −14 dBm when the bias current is 90 mA (*left*) and 81 mA (*right*) at T = 25°C. The modulation amplitude is kept at 250 mV for both measurements.

and the Q factor is higher when $P_{\text{in}} = -11$ dBm. The back-to-back bit error rate, in Fig. 4.14(left), shows that this RSOA modulator can operate error free (bit error rate below 10^{-9}) at 1.25 Gbit/s (1 Gbit/s) with $P_{\text{in}} = -14$ dBm (-17 dBm) when the received optical power (P_{receive}) at the commercial receiver is higher than -13 dBm (−18 dBm). In comparison with the laser injected QW RSOA reported in [22], our device needs 17 dB higher received power at the commercial receiver to achieve error free operation at 1.25 Gbit/s, mainly due to its low available gain.

Dependence on the injection current

In order to check the influence of the current, we fixed the input optical power P_{in} at −14 dBm, and changed the bias current. The measured eye diagrams after the commercial receiver at I_{bias}=90 mA and 81 mA at 1.25 Gbit/s data rate are shown in Fig. 4.15. At both currents, the device operates in the linear region according to Fig. 4.12. The figure with higher injection current shows less noise due to a larger amplification of the input signal which suppresses the ASE noise. The measured modulation extinction ratios are 7.3 dB and 5 dB respectively. The Q factors of the eye diagrams after the commercial receiver are 19, and 16.6 respectively, which is sufficient to achieve error free operation.

Wavelength dependence

One of the most important requirement for the RSOA modulator is the colorless operation, thus the measurement has been repeated at different wavelengths at 1 Gbit/s, and the recorded eye diagrams through a light wave converter are shown in Fig. 4.16. All the eyes are clear open with Q factor higher than 8 and extinction ratio more than 6.

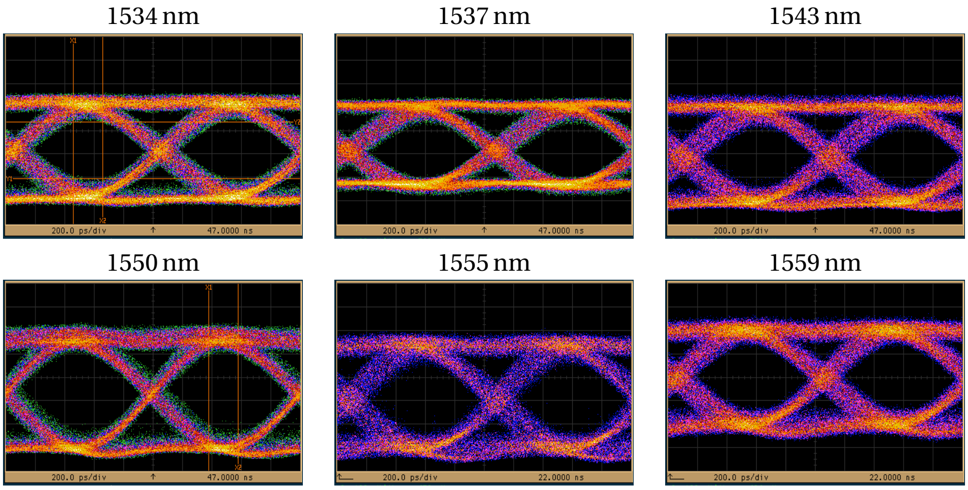

Figure 4.16: Eye diagrams at 1 Gbit/s for different wavelengths while the injection current is 81 mA, the modulation amplitude is 250 mV, and $P_{\text{in}} = -9$ dBm.

4.6 Discussion and conclusion

According to the effective carrier lifetime derived from rate equations, the modulation bandwidth of a SOA can be enhanced with a high injection current and a high optical input power. According to a numerical model the effective carrier lifetime can be shortened below 100 ps with a high injection current, corresponding to 1.6 GHz bandwidth. Simulation results achieved with commercial software (VPI-photonics) show that the bias current should be sufficiently high while not causing strong ASE ripples to achieve better performance. High optical input power suppresses the noise and enhances the bandwidth, but at the cost of the extinction ratio.

With a realized loop-RSOA we have demonstrated error free operation for 1.25 Gbit/s data with $2^{23}-1$ PRBS and −14 dBm optical input power before the chip. Increasing the optical input power further suppresses the noise and relaxes the requirements on the received power at the commercial receiver. By adjusting the input optical power and the injection current, the device can obtain a high Q factor and an extinction ratio up to 7.3 dB. This device has proved the possibility of colorless operation at 1 Gbit/s in the wavelength range from 1530 nm to 1560 nm. Its layer stack and the fabrication technology are compatible with the other components, such as the passive waveguide devices and the photodetector, and thus suitable for the monolithic integration. Comparing with the target specifications on the RSOA shown in table 1.3, the loop-RSOA has met the specifications.

This device is polarization dependent, and the eye quality is dependent on the adjustment of the polarization controller. One solution is integrating a polarization converter [140] between the SOA and the mirror, however it will increase the complexity during the fabrication, and the technology to integrate such a component needs to be investigated.

Due to the facet reflectivity, the measurements have been limited to low injection currents, thus low SOA gain. Applying an AR coating at the input facet can further improve the performance of this device.

Chapter 5

High performance InP based photodetector in an SOA layer stack

A waveguide photodetector based on semi-insulating indium phosphide (InP) was simulated, designed and fabricated. The layer stack for this photodetector was optimized for use as an optical amplifier or laser and it can be combined with the passive components. By using a semi-insulating substrate and deep etching of a photodetector with small area, an efficient and high-speed photodetector was made, which allows for easy integration of source, detector and passive optical components on a single chip. A 3 dB bandwidth of 40 GHz and 0.25 A/W external RF responsivity is measured at 1.55 μm wavelength for a 1.5 μm wide and 30 μm long waveguide photodetector at −4.7 V bias voltage. The polarization dependence in the responsivity is less than 0.27 dB. A photoreceiver for the user access network has been realized by combining the InP photodetector and a SiGe amplifier through wire bonding. The eyes are clear open up to 4 Gbit/s with a Q factor higher than 11. The bandwidth of the photoreceiver is limited by the transimpedance amplifier.

5.1 Introduction

Monolithic integration of different optical building blocks, such as passive waveguide devices (PWD), semiconductor optical amplifiers (SOA), photodetectors (PD) and modulators allows for flexible design of photonic integrated circuits. Previously, devices based on a combination of PWDs, absorbers and SOAs have been reported by COBRA research institute, such as multiwavelength ring lasers [141] and mode locked lasers [142]. In our application, the transceiver integrates an SOA and a photodetector into a single chip. Although the bandwidth requirement in the BBP project for the user access network is only up to 10 GHz, one of the research goals is to investigate the limit of the bandwidth of the photodetector which is in an SOA layer stack and operated by reversely biasing the pn-junction.

Others have presented the PD with increased sensitivity by monolithic integration of the waveguide PD and the SOA in a common layer stack [49,75,76]. In [49], the PD based on bulk material has achieved 20 GHz, and in [76] the PD was based on multi-quantum well and achieved 40 Gbit/s operation. However, the latter PD is highly polarization dependent [76].

Previous work in COBRA on a photodetector in a SOA layer stack has reached a bandwidth of 30 GHz [16]. Based on the former research results, a smaller area deeply etched photodetector has been realized in this work, which achieved 40 GHz bandwidth. Furthermore, an analysis on the series resistance has been carried out and the options to reduce the resistance are given. In addition, polarization dependence in the responsivity is characterized for the photodetectors with different lengths. In the last part of this chapter, a hybrid photoreceiver for the user access network and its performance are introduced.

5.2 Properties of the photodetector

5.2.1 Bandwidth

The bandwidth of the PD is determined by the photon-generated carrier drift time bandwidth (f_{tr}) and RC time bandwidth $f_{\mathrm{RC-3dB}}$, and the total bandwidth f_{total} can be written as [143]

$$\frac{1}{f_{\mathrm{total}}^2} = \frac{1}{f_{\mathrm{tr}}^2} + \frac{1}{f_{\mathrm{RC-3dB}}^2} \tag{5.1}$$

Transit time bandwidth

The transit time bandwidth depends on the thickness of the depletion region and the drift velocity of the carriers. In theory, the transit time bandwidth (f_{tr}) of a waveguide PD approximately is [144]

$$f_{\mathrm{tr}} \approx \frac{3.5 \cdot \bar{v}}{2\pi d_{\mathrm{dep}}} \tag{5.2}$$

$$d_{\mathrm{dep}} = \sqrt{\frac{2\varepsilon_s(\phi_{\mathrm{i}} - V)}{q \cdot N_{\mathrm{d}}}} \tag{5.3}$$

$$\frac{1}{\bar{v}^4} = \frac{1}{2}\left(\frac{1}{v_{\mathrm{e}}^4} + \frac{1}{v_{\mathrm{h}}^4}\right) \tag{5.4}$$

in which d_{dep} is the thickness of the depletion region, ε_{s} is the permittivity of the material, ϕ_{i} is the built-in potential in the pn-junction, V is the bias voltage, q is the electron charge, N_{d} is the doping level and v_{e} and v_{h} are the electron and hole drift velocity in the depletion region. v_{e} and v_{h} are dependent on the electric field (E), the saturation velocities of the

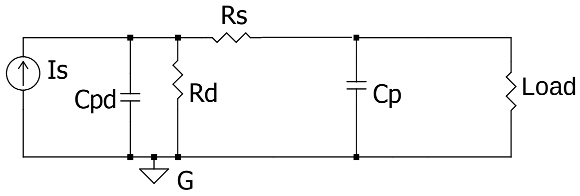

Figure 5.1: The equivalent electrical circuit of a PD for RC bandwidth. The load resistance (R_L) is 50 Ω.

electron ($v_{sat,e}$) and hole ($v_{sat,h}$) and the mobilities of the electron (μ_e) and hole (μ_h) in the intrinsic material, given by

$$v_e = \frac{\mu_e \cdot E + \beta \cdot v_{sat,e} E^{\gamma}}{1 + \beta E^{\gamma}} \tag{5.5}$$

$$v_h = v_{sat,h} \tanh\left(\frac{\mu_h E}{v_{sat,h}}\right) \tag{5.6}$$

in which β and γ are the coefficients. Since v_h is smaller than v_e, the transit time is mostly limited by v_h.

RC bandwidth

A PD can be modeled by an equivalent circuit [145] shown in Fig. 5.1. The current source I_s is the photon-generated current which is parallel with the photodiode junction capacitance C_{pd} and junction resistance R_d, and in series with device series Resistance R_s, plus the probe pad capacitance C_p in parallel with a 50 Ω load. The junction capacitance C_{pd} is determined by the depletion layer thickness d_{dep} and the area of the photoabsorption layer A:

$$C_{pd} = \frac{\varepsilon_s A}{d_{dep}} \tag{5.7}$$

Assuming that the dark current of a PD is very low ($\ll \mu$A), R_d becomes very large and its effect is negligible. The circuit transfer function can be calculated

$$\frac{I_s(\omega)}{I_s(0)} = \frac{1}{1 - \omega^2 C_{pd} C_p R_s R_L + j\omega(C_p R_L + C_{pd}(R_s + R_L))} \tag{5.8}$$

For a PD with small dimension and short impedance matched probe pads, C_{pd} and C_p are very small, around tens of femto-Farad (fF), and the second order item in the denominator can be ignored when $f_{RC} \ll 200\,$GHz. Thus the 3 dB RC bandwidth (f_{RC-3dB}) can be written as

$$f_{RC-3dB} = \frac{1}{2\pi((C_p R_L + C_{pd}(R_s + R_L))} \tag{5.9}$$

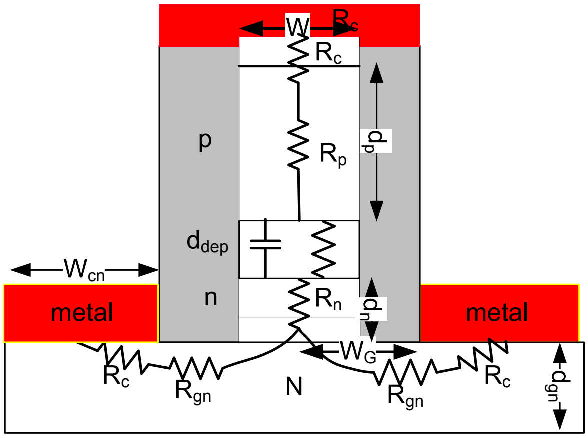

Figure 5.2: Cross-section of the PD and the corresponding resistance and capacitance in the PD.

For a PD structure with ground-signal-ground (GSG) design, shown in Fig. 5.2, the series resistance R_s consists of the following components:

$$R_{metal} = \frac{\rho_{metal} L_{metal}}{W_{metal} d_{metal}} \text{ metal resistance} \tag{5.10}$$

$$R_{cp} = \frac{\rho_{cp}}{L_{pd} \cdot W_{pd}} \text{ total p-contact resistance} \tag{5.11}$$

$$R_{cn} = \frac{\rho_{cn}}{L_{pd} \cdot W_{pd}} \text{ total n-contact resistance} \tag{5.12}$$

$$R_{vp} = \frac{\rho_{p-sheet} d_p}{L_{pd} \cdot W_{pd}} \text{ vertical p-layer sheet resistance} \tag{5.13}$$

$$R_{vn} = \frac{\rho_{n-sheet} d_n}{L_{pd} \cdot W_{pd}} \text{ vertical n-layer sheet resistance} \tag{5.14}$$

$$R_{ng} = \frac{\rho_{n-sheet} W_G}{L_{pd} \cdot d_{gn}} \text{ n-layer gap resistance} \tag{5.15}$$

where ρ_{metal} is the metal resistivity, W_{metal} is the width of the metal, d_{metal} is the thickness of the metal, ρ_p and $\rho_n$are p- and n-contact resistivity, $\rho_{p-sheet}$ and $\rho_{n-sheet}$ are the p- and n-sheet resistivity, L_{pd} and W_{pd} are the length and width of the PD, W_{cn} is the width of the n-contact area, d_p and d_n are the vertical travel distance of the electrons and the holes in p- and n-layer, d_{gn} is the thickness of the n-sheet in the gap region.

The resistivities of the p-layer ($\rho_{\text{p-sheet}}$) and n-layer ($\rho_{\text{n-sheet}}$) are inverse proportional to the mobility of the electrons (μ_n) and holes (μ_p) in the material, and the doping level of p- and n-layer [146].

$$\rho_{\text{p,n-sheet}} = \frac{1}{q \cdot N_{\text{p,n}} \cdot \mu_{\text{p,n}}} \tag{5.16}$$

Thus the total device series resistance R_s is

$$R_s = R_{\text{metal}} + R_{\text{cp}} + R_{\text{vp}} + R_{\text{vn}} + (R_{\text{ng}} + R_{\text{cn}})/2 \tag{5.17}$$

5.2.2 Quantum efficiency

The quantum efficiency of a PD is given by

$$\eta_{\text{in}} = 1 - \exp(\Gamma \cdot \alpha \cdot L) \tag{5.18}$$

$$\eta_{\text{ex}} = \eta_{\text{in}}(1 - R_{\text{facet}})\eta_c \tag{5.19}$$

where Γ is the confinement factor, α is the absorption coefficient of the material, L is the length of the PD, R_{facet} is the facet reflectivity of the PD, and η_c is the fiber-chip coupling efficiency. For a waveguide PD, L is equal to the length of the PD L_{pd}.

Responsivity R_{resp} is another parameter directly related to the quantum efficiency. It is the ratio of the photon-generated current (I_{ph}) to the input optical power (P_{in})

$$R_{\text{resp}} = \frac{I_{\text{ph}}}{P_{\text{in}}} = \eta_{\text{in,ex}} \frac{q \cdot \lambda}{h \cdot c} \tag{5.20}$$

5.3 Simulation and design

The simulation will be performed based on the layer structure shown in Fig. 5.3, which is the same as the layer stack for the reflective SOA in Chapter. 4, but operates under reverse bias voltage. The other parameters for calculating the bandwidths and the series resistance of the waveguide PD with different size are given in table 5.1. Since the film layer has a very low intentional doping level, it will be completely depleted even under a small reverse bias voltage. In order to reach the saturation velocity for both electrons and holes, the required electric field is about 70 kV/cm based on equation (5.5) and (5.6) [16,93,147], corresponding to about −4 V, and 550 nm d_{dep} for the layer stack shown in Fig. 5.3. The calculated f_{tr} is 46 GHz, which is independent of the dimension of the PD.

The simulated RC time bandwidth for different widths and lengths is shown in Fig. 5.4(left). The total bandwidth is primarily limited by the transit time for a 30 μm long, below 2 μm wide device. The RC bandwidth is the limiting factor for a device wider than 4 μm. The simulated total bandwidth based on the transit and RC time is shown in Fig. 5.4(right) for different widths and lengths.Based on these results, the width of the waveguide PD on this layer stack was designed 1.5 μm to achieve the best performance while normal optical lithography could still precisely define the waveguide. The calculated total

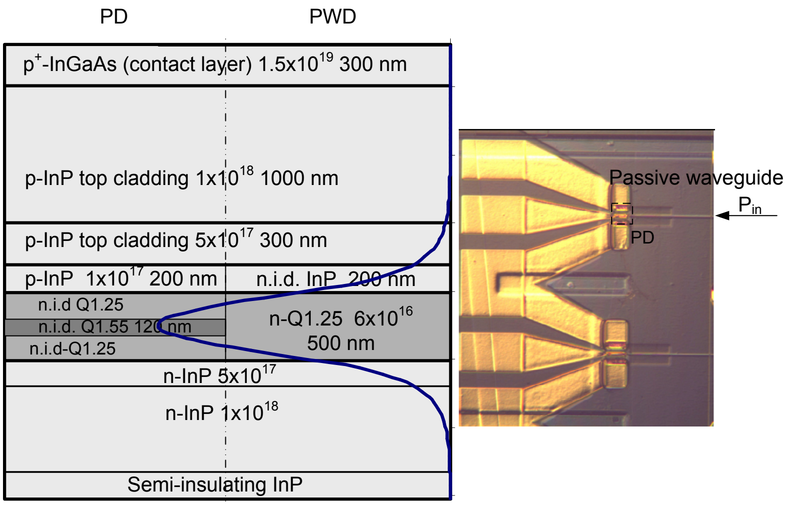

Figure 5.3: (left) Active-passive butt-joint layer stack with specifications based on a semi-insulating substrate.The unit for the doping level is cm^{-3}. (right) the top view of the fabricated PD.

Symbol	Values
v_e	6.0×10^6 cm/s, under high electric field [147]
v_h	4.0×10^6 cm/s, under high electric field [147]
d_{dep}	550 nm
C_p	12 fF, extracted from the experiment
ε_s	$13 \times 8.85 \times 10^{-12}$
μ_p	$75\,cm^2/s$ [148] in $1 \times 10^{18} cm^{-3}$ P-InP
μ_n	$1500\,cm^2/s$ [148] in $1 \times 10^{18} cm^{-3}$ N-InP
W_{gap}	$10\,\mu m$
d_{gn}	400 nm
W_{cn}	$50\,\mu m$
ρ_{cp}	$5 \times 10^{-6}\,\Omega \cdot cm^2$ for $1.5 \times 10^{19} cm^{-3}$ P-InGaAs contact [138, 147]
ρ_{cn}	$1.0 \times 10^{-3}\,\Omega \cdot cm^2$ for $1 \times 10^{18} cm^{-3}$ n-InP contact [138, 147]
R_L	$50\,\Omega$ load

Table 5.1: The parameters used for the calculation.

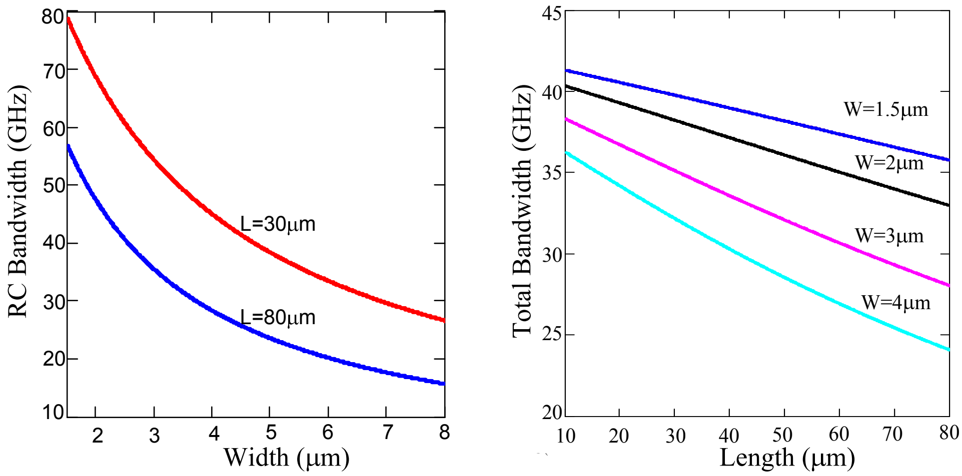

Figure 5.4: Simulated RC bandwidth (left) and the total bandwidth (right) based on the transit time and the RC time constant for PDs with different widths and lengths. The depletion layer thickness is calculated to be about 550 nm when the reverse bias voltage is higher than −4 V.

parameter	30 μm	80 μm
R_{cp}	11 Ω	4.2 Ω
R_{vp}	42 Ω	16 Ω
R_{vn}	1 Ω	0.3 Ω
$R_{ng}/2$	14 Ω	5.2 Ω
$R_{cn}/2$	34 Ω	12.5 Ω
R_{metal}	~1 Ω	~2 Ω

Table 5.2: Series resistance components and corresponding values based on the equations given above.

resistance (R_s) is about 103 Ω (40 Ω) for 30 μm (80 μm) long PD. The RC bandwidth is about 80 GHz (58 GHz). Therefore, the estimated total bandwidth is 40 GHz (36 GHz) for a 30 μm (80 μm) long PD, and limited by the transit time.

The transit time bandwidth can be improved by increasing the doping level in p-Q1.25 and n-Q1.25. If d_{dep} is smaller than 350 nm (f_{tr}>70 GHz), the RC bandwidth will become the limiting factor, especially due to the total series resistance of the small device. The calculated resistance components are listed in table 5.2. We can see that the p-layer sheet resistance and the n-contact resistance are dominant for the small devices. Some measures could lower the resistance, such as optimizing the n-contact resistivity or reducing the thickness of the p-InP layer. However, the latter will increase the transmission loss in the passive part due to the overlapping of the optical field with p-InGaAs.

5.4 Fabrication

As shown in Fig. 5.3, a semi-insulating substrate was used to reduce the RF loss and the parasitic capacitance to obtain a higher bandwidth. To further minimize the capacitance, these PDs are narrow (1.5 μm) and deeply etched through the film into the highly doped N-InP layer. All the waveguides were etched by reactive ion etching. Polyimide was spun for passivation and planarization. To form the metal contact, a Ti/Pt/Au layer stack was evaporated on the top p-InGaAs and the lateral ground contacts (n-InP) through lift-off. The gap distance between the p- and n-contact was designed 10 μm to prevent the short circuit due to the resolution limit of lift-off. To minimize the RF transmission loss, the contacts were electro-plated until the thickness of the gold was about 1.5 μm, which is four times larger than the skin depth (380 nm) at 40 GHz [149]. The photograph in Fig. 5.3 shows fabricated PDs with metal contacts, which were tapered from the PD to the GSG probe pads which have a 100 μm pitch. The central contact is 70 μm wide. The access waveguide is 3 μm wide and shallowly etched. The fiber-chip coupling facet is cleaved and has about 33% (26%) facet reflectivity (R_{facet}) for TE (TM) polarization.

5.5 Experimental result

5.5.1 Dark current

The dark current is the current through the diode in the absence of light. This current is due to the generation/recombination of carriers in the depletion region and any surface leakage, which occurs in the diode. It obviously limits the minimum power detected by the photodiode, since a photocurrent smaller than the shot noise of the dark current would be hard to measure. Thus, the dark current offers the possibility to judge the reliability of the device. The measured dark current of the deeply etched PD is low, as shown in Fig. 5.5. At -4 V, the dark current of the 30 μm and 80 μm long deeply etched photodetector is 18 nA and 38.3 nA. They are comparable with other reported photodetectors with a similar dimension. The dark current results mainly from the surface recombination, especially because these photodetectors are deeply etched. The longer one showed higher dark current due to a larger surface area.

5.5.2 Polarization dependence in responsivity

We use the setup in Fig. 5.6 to determine the external responsivity for different polarization states, a tunable laser was used as a light source, and the polarization was selected through a polarizer and coupled through a microscope-objective. The optical signal is coupled into the waveguide via the cleaved facet of the chip. The polarization controller is used to maximize the transmission power of the selected polarization. The source meter applies the

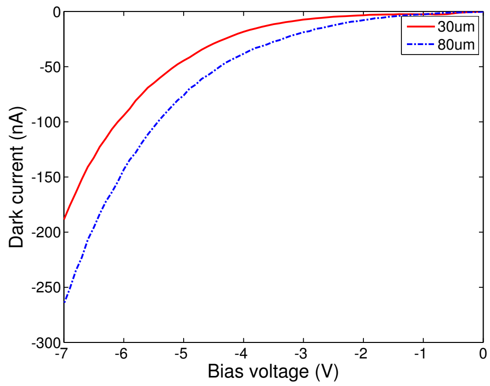

Figure 5.5: Measured dark current for 1.5 μm wide deeply etched 30 μm long (solid) and 80 μm long (dash) PDs.

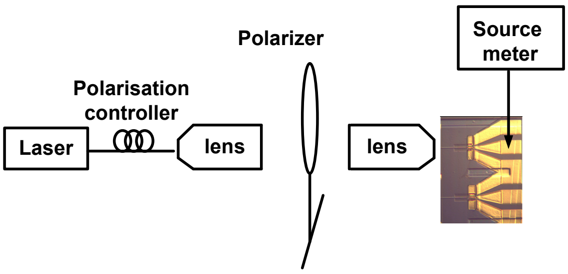

Figure 5.6: Measurement setup used for the characterization of the wavelength duplexer.

reverse voltage, and records the current. The measured photocurrents for TE and TM at $\lambda = 1.55\,\mu$m under -4 V are shown in figure 5.7 for two different lengths. The input optical power in Fig. 5.7 is the power from the laser (P_{laser}) multiplied by $1 - R_{\text{facet}}$ for TE and TM polarization. The 80 μm long PD has a higher responsivity than 30 μm long PD. The polarization dependence in responsivity (PDR) for 30 μm (80 μm) long PDs is small, less than 0.27 dB and (0.2 dB).

5.5.3 Bandwidth

On-wafer S-parameter measurements are performed in the range of 10 MHz to 67 GHz with a lightwave component analyzer (LCA) and a 50 GHz RF-probe, the measurement setup is shown in Fig. 5.8. The LCA has two output optical powers, 0 dBm and 5 dBm, and the total loss of the fiber path and three fiber connectors is about 1 dB. The PD was biased at -4.7 V through a 65 GHz bias tee, and the injected wavelength from the lightwave analyzer is 1.55 μm. The measured small signal frequency response (O/E) for both 0 dBm and 5 dBm

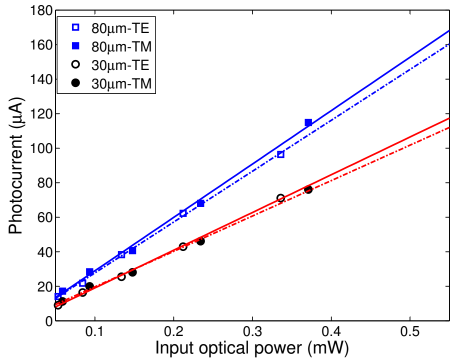

Figure 5.7: The measured photocurrent of 30 μm and 80 μm long PDs for both TE and TM polarization as a function of the input optical power ($P_{\text{laser}} \times R_{\text{facet}}$) at -4V. The straight lines are linear fits. The input optical power at the x-axis is the power level from the laser multiplied by $(1-R)$ for TE and TM polarizations without excluding the loss of the other bulk optical components in the measurement setup.

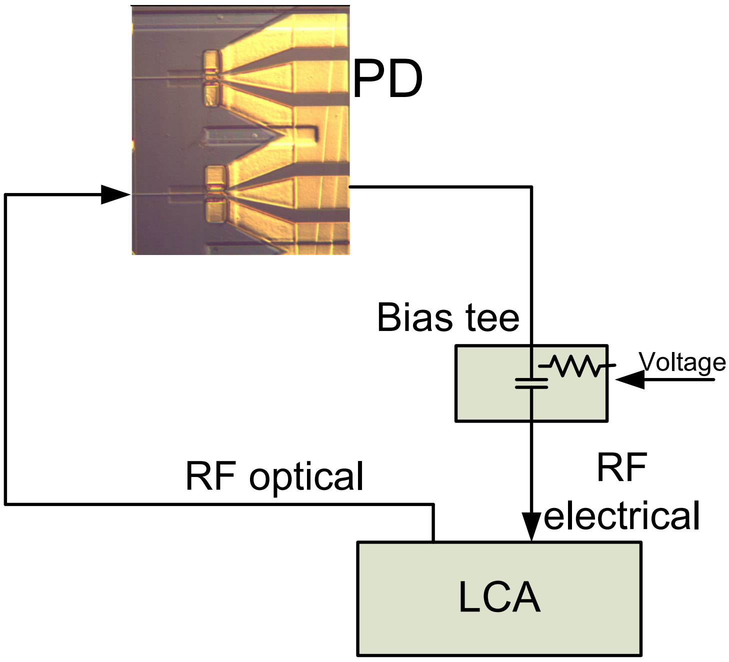

Figure 5.8: Setup for measuring the bandwidth of the photodetector.

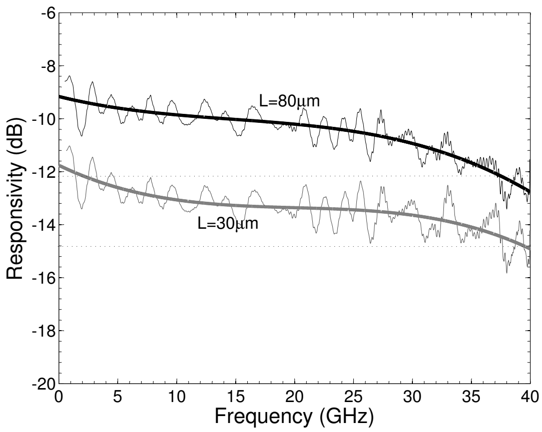

Figure 5.9: Frequency response of a 30 μm long PD (grey) and an 80 μm long PD (black) at 1.55 μm. The straight lines are cubic polynomial fitting.

input optical power is given in Fig. 5.9. The vertical axis is the actual responsivity relative to 1 A/W at different frequencies. Thus the measured RF responsivity of 30 μm (80 μm) long PD is about 0.25 A/W (0.35 A/W) at 10 MHz to 0.16 A/W (0.18 A/W) at 50 GHz. If we take 5 dB as fiber-chip coupling loss (1.5 dB uncoated facet, 3.5 dB mode mismatching), the internal quantum efficiency is about 64% (89%) at 10 MHz to 41% (46%) at 50 GHz. The measured 3 dB total frequency response is 40 GHz (37 GHz) for 30 μm (80 μm) long PD, which is in good agreement with the simulated total bandwidth in Fig. 5.4. The oscillation in the measurement is due to the reflection between the RF probes.

5.6 Photoreceiver

5.6.1 Introduction

As introduced in Chapter. 1, the PD is an indispensable component to detect the downstream data in the reflective transceiver for the user access network. In this section, we will present the design and measurement results of the photoreceiver chip of the transceiver module which consists of an InP-photodetector, and an amplifier chip[1] comprising a transimpedance amplifier (TIA) and a variable gain amplifier (VGA) based on SiGe. The two chips are wire bonded together. The photograph of the fabricated chips are shown in Fig. 5.10. The PD is the 30 μm long one presented in sect. 5.5. The electrical amplifier circuit is based on low cost SiGe. When the downstream data carried by the light is detected by the PD, the generated photocurrent will be pre-amplified and converted into a differential output voltage. The amplifier circuit also provides a DC bias voltage to the PD.

[1]The amplifier chip is designed by TNO Defence, Security and Safety.

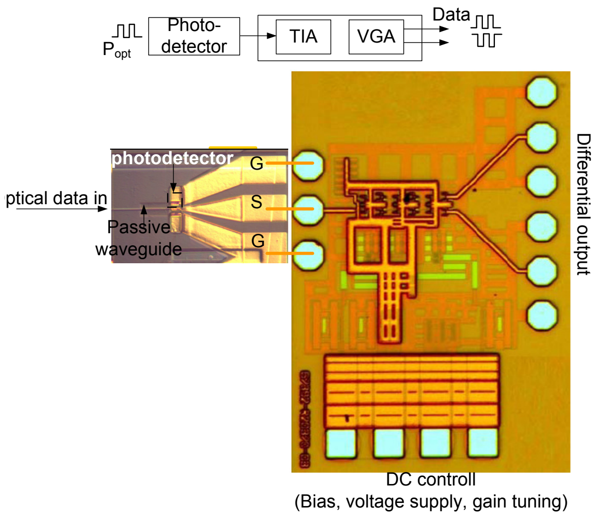

Figure 5.10: Block functionality diagram of the photoreceiver and the photograph of the fabricated photoreceiver consisting of an InP-photodetector and a SiGe amplifier connected with bonding wires.

The amplifier circuit is implemented in the low cost AMS 0.35 μm-SiGe BiCMOS process that includes high-speed SiGe Heterojunction Bipolar Transistors. Finally these two chips were bonded together through wires with 20 μm diameter.

5.6.2 Characterization

The bandwidth of the fabricated InP PD is about 40 GHz, and the external responsivity is 0.25 A/W, shown in Fig. 5.9. The measurement gain of the electrical amplifier is shown in Fig. 5.11, in which V1 and V2 are the tuning voltages. The purpose of the tuning voltage V1 is to vary the gain in the VGA depending on the input voltage swing. A second tuning voltage V2 is present to compensate for process variations. The VGA is designed to achieve a constant output voltage swing of 80~90 mV at the output. The bandwidth of this hybrid photoreceiver is mainly limited by the TIA, for which a transimpedance gain of approximately 1500 Ω and a bandwidth of 3 GHz was measured. The equivalent input noise current is 4.5 pA/$\sqrt{\text{Hz}}$.

To measure the performance of the hybrid photoreceiver, we injected light with λ =1545 nm from the tunable laser, modulated by a 10 GHz commercial Mach Zehnder modulator driven by the pulse pattern generator (PPG) up to 10 GHz. The input optical power was monitored by an in-line power meter. The modulated light was coupled into the photoreceiver chip through a lensed fiber. The light was absorbed by the PD which was reversely biased at −3 V. and the generated photocurrent was converted into voltage

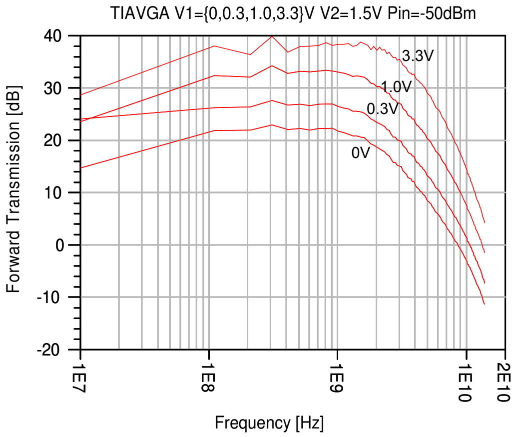

Figure 5.11: The measured gain and bandwidth of a SiGe based electrical amplifier at different gain control voltages.

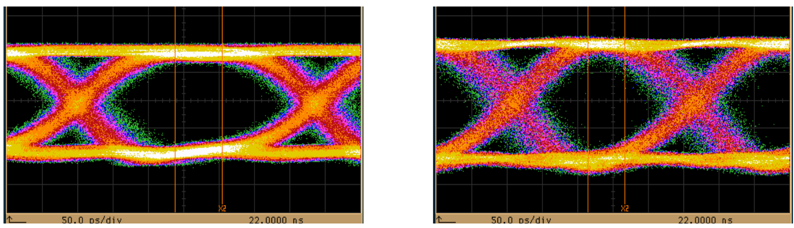

Figure 5.12: Eye diagrams for 3 Gbit/s (left) and 4 Git/s (right) with −12 dBm input optical power.

and amplified by the TIA and VGA. The output differential voltage from the photoreceiver was directly connected to a digital communication analyzer without additional electrical amplification to record the eye diagram. The tuning voltage V1 was set at 1.5 V, corresponding to about 30 dB gain in Fig. 5.11. The recorded eye diagrams for PRBS with $2^{31}-1$ word length at 3 Gbit/s and 4 Gbit/s are shown in Fig. 5.12 when the average input optical power is −12 dBm before the fiber chip coupling. The measured Q factors are better than 12.85 and 11.

5.7 Conclusion and discussion

By using a semi-insulating substrate and deep etching, a small-area waveguide PD based on an amplifier/laser layer stack achieved up to 40 GHz with 0.25 A/W external RF responsivity, and less than 0.27 dB polarization dependence. This result enables the monolithic integration of a light source and a high performance PD based on flexible butt-joint active-passive material without the need for a dedicated detector layer stack. It is suitable for 40 Gbit/s operation.

A photoreceiver for the user access network has been realized by hybrid integration of an InP PD and a SiGe amplifier through bonding wire. The eyes are clear open up to 4 Gbit/s with a Q factor higher than 11. The bandwidth of the photoreceiver is limited by the TIA. The further development of this receiver will include the phase detector and the clock recovery circuit.

The bandwidth of the PDs based on the current SOA layer stack is mainly limited by the transit time. It can be further improved by changing the doping profile in the film layer while the performance for the SOA is not influenced. When the depletion layer thickness is reduced to 350 nm, the RC bandwidth will become the limiting factor, mainly due to the high series resistance which results from the high n-InP contact resistivity and the thick p-top cladding layer for small area devices. In order to reduce the contact resistivity, we can either increase the doping level of the n-InP or change the metal alloy on n-InP. The p-layer sheet resistance can be reduced by decreasing the thickness of the top p-cladding layer, however, this will increase the transmission loss for passive components.

Chapter 6

Fabrication Technology

In the realization of a low cost transceiver for the user access network, fabrication technology plays a critical role in device performance and yield. This chapter will describe the technology in COBRA that has been used to fabricate the tunable duplexer, the reflective components, the SOA, the photodetector, the phase modulator and the integrated transceivers. We start with explaining the wafer preparation for active-passive integration in COBRA. Two important fabrication procedures, lithography and etching, which are carried out over the whole fabrication flow are described. The most commonly used lithographies and etchants in COBRA are listed. Afterwards, we describe the procedures of etching the waveguides with different profiles, passivation and planarization, and metallization. In the final part, the complete chip process steps are given for the realization of an integrated reflective transceiver on an N-InP substrate and an integrated transceiver on a semi-insulating substrate, which integrates a thermally tunable duplexer, a phase modulator, MMI loop mirrors, a SOA and a photodetector.

6.1 Introduction

In the previous chapters, we have introduced the constituent components of the transceiver, the tunable duplexer, the reflective SOA integrated with a MMI loop mirror, and a photodetector. In this chapter, we will describe the technology which is used to fabricate these components and the integrated transceivers presented in Chapter 7. It plays a critical role in their performance and yield.

In section 6.2, we will describe the wafer preparation for the active-passive integration. Two fabrication procedures which run through the whole processes will be introduced, namely lithography in section 6.3 and etching in section 6.4. Section 6.5 discusses the common fabrication procedures for the integrated devices in COBRA institute. In the last section, the complete fabrication processes for the devices in this thesis are illustrated.

6.2 Wafer epitaxy

A couple of methods are available to prepare material for active-passive integration, such as Quantum Well Intermixing (QWI) [150], Selective Area Growth (SAG) [151], multiple vertical waveguide structure technique using evanescent field coupling [152] and butt-joint coupling [153]. Among these methods, QWI is only applicable to the quantum well material, and it needs to selectively control the interdiffusion of the atoms between the quantum wells and their corresponding barriers, which is highly dependent on the induced dopants and the anneal temperature [154]. SAG using silica masking allows regions with different band gaps to be realized across a wafer in a single growth step, but such an approach does not allow complete control of the band gap in two dimensions [154]. The evanescent coupling method would need around several hundred micrometer coupling length, which makes the devices longer than those from the other methods. Butt-joint coupling method has been adopted in COBRA institute because of its flexibility in the material growth and device design, such as the layer thickness control, the doping concentration and the layer composition, although it encounters a problem in the reflection at the butt-joint, which needs to be suppressed as much as possible. By special design with angled entry and exit waveguide in the active region, the measured reflectivity at butt-joint can be lower than -50 dB, and the transmission loss at the butt-joint is lower than 0.19 dB [124].

All the wafers used for the devices in this thesis were grown by a low pressure Metal Organic Vapour Phase Epitaxy (MOVPE). The wafer for all passive devices is one-step growth in MOVPE, and doping was completed while growing.

To grow a wafer for an active-passive integration, typical three-step regrowth is employed to produce butt-joint coupling materials, as shown in Fig. 6.1. The procedures are as follows:

(A) The first growth deposits 1000 nm thick n-InP with gradual doping levels, a 500 nm thick film layer with a 120 nm thick Q1.55 sandwiched between two 190 nm thick Q1.25, and a 200 nm thick p-InP buffer cladding layer, see Fig. 6.1 (A).

(B) Afterwards, the material is taken out of the growth chamber and a 50 nm thick SiNx is deposited over the wafer with Plasma Enhanced Chemical Vapor Deposition (PECVD). The deposited SiNx works as a mask later to protect the active region. The active region is defined by a mask with pre-defined pattern through lithography (Fig. 6.1 (B)).

(C) The passive region without SiNx protection is etched away in the InP RIE until 50 nm below the active material (Q1.55) (Fig. 6.1 (C)).

(D) After cleaning, the wafer is put back to the MOVPE growth chamber to selectively grow the film layer for the passive region with n-Q1.25 ($N_d = 6 \times 10^{16}\text{cm}^{-3}$), and a 200 nm InP buffer cladding layer as well (Fig. 6.1 (D)).

(E) To continue with the third growth, the former deposited SiNx above the active region is removed, and a 1300 nm p-InP (300 nm with $3 \times 10^{17}\text{cm}^{-3}$ and 1000 nm with $1 \times$

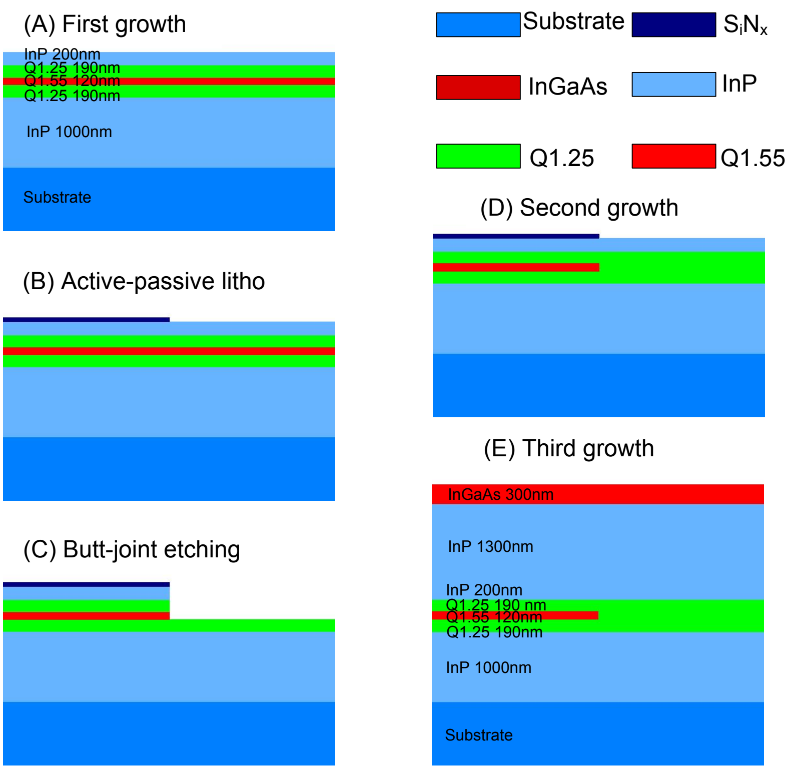

Figure 6.1: Schematic overview of the active passive wafer preparation using SiNx as a mask to define the active regions.

$10^{18}\mathrm{cm}^{-3}$) top cladding layer and a 300 nm P-InGaAs ($N_a = 1.5 \times 10^{19}\mathrm{cm}^{-3}$) contact layer were grown (Fig. 6.1 (E)). The thick p-InGaAs is needed to increase the tolerance for later polyimide etching back, see section 6.5.2.

The amount of the doping level in the active layer stack influences the series resistance of the SOA and the photodetector, and the optical absorption in the waveguide ridge. The series resistances of two photodetectors under reverse bias voltage have been calculated in Chapter 5. The series resistance of the SOAs are measured in Chapter 4 and Chapter 7. The doping level in the passive structure influences the propagation loss, switching efficiency and polarization dependence in switching voltage of the phase shifter, which have been investigated in Chapter 2.

Lithography	Mask	Photoresist	Exp. T(s)[1]	Developer	Dev. T(s)[2]
Active	N	HPR504(P)	~4	PLSI:H_2O = 1 : 1	~90
Waveguides	N	HPR504(P)	~4	PLSI:H_2O = 1 : 1	~90
Substrate etch[3]	P	AZ4533(P)	~55	AZ developer:H_2O = 1 : 1	~150
Deep etch	P	AZ4533(P)	~55	AZ developer:H_2O = 1 : 1	~150
Isolation	N	MaN440(N)	2 × 100	MaD332-s (100%)	~90
P-contact	N	AZ4533(P)	~55	AZ developer:H_2O = 1 : 1	~150
N-contact open[4]	N	MaN440(N)	2 × 100	MaD332-s (100%)	~90
Metallization	N	MaN440(N)	2 × 100	MaD332-s (100%)	~90
Plating	N	AZ4533(P)	~55	AZ developer:H_2O = 1 : 1	~150

[1]The exposure time depends on the waveguide structure. 2 × 100 means multi-exposure (100 seconds for twice with about 10 s cooling between)
[2]Developing time depends on the exposure time and structure. The given data below is approximate value used for the devices in this thesis.
[3]Devices on SI-substrate only (Chapter 4&5&7)
[4]Devices with lateral N-contact only(Chapter 4&5&7)

Table 6.1: Commonly used lithographies during the whole chip processing.

6.3 Lithography

Lithography is a technology to transfer the pre-defined pattern to the other material. In PIC, lithography is used to transfer the pre-defined patterns in the mask to the photoresist. In COBRA, the pre-defined waveguide pattern are written on the masks. Two kinds of masks are used: “negative field” and “positive field. “Negative field” means the mask plate is transparent while the pattern structures are chromium. “Positive field” means the mask plate is chromium while the pattern structures are transparent. Generally, “negative field” mask is used for high resolution structures, and “positive field” mask is used for a lower requirement for the resolution and it costs less.

Two types of photoresists are used: positive photoresist and negative photoresist. Positive photoresist becomes soluble in the developer when it is exposed to light while the unexposed photoresist stays. Negative resist becomes relatively insoluble to the photoresist developer when it is exposed to light, while the unexposed photoresist is dissolved by the photoresist developer.

The most commonly used lithographies for a circuit which integrates PWD, SOAs and high performance PDs in COBRA are listed in table. 6.1 according to the process sequence. The first column contains the names of the lithography and the names of the masks used in the lithography. The second column is the property of the mask plate, “negative (N)” or “positive (P)”. The third column is the property of the photoresist, “negative (N)” or “positive (P)” . The mask and the photoresist are correlated. The fourth column is the exposure time in the lithography machine. The fifth column is the corresponding developer for the photoresist in the second column. The sixth column is the developing time to obtain the pattern. All these lithographies are performed by means of vacuum contact exposure at a lithography machine MA6. Not all the listed lithographies have to be performed for each circuit, depending on the integrated components. Only the third generation transceiver (Chapter 7) required all the listed lithographies.

In the following sections, when a lithography is mentioned, it involves three procedures:

- spinning the photoresist on the sample;
- carrying out lithography with a mask in MA6, and expose the sample for a certain time under an ultraviolet (UV) lamp;
- developing the exposed sample in the corresponding developer for a certain time.

For example, the first row in table 6.1 means an “active lithography” which defines the regions for the active components with a mask named “active mask”. The procedure includes spinning a layer of positive photoresist HPR504, carrying out the “active lithography” in MA6 to transfer the active region in the “active mask” to the photoresist by exposing the sample for 4 seconds, and developing the sample in the developer (PLSI:H_2O=1:1) for 90 s.

Among these lithographies, “waveguide lithography” is the most critical one since a small width deviation will lead to a relatively large performance deterioration for the device. The width deviation can be introduced by an erroneous illumination, a wrong development time and a relative large distance between the chromium mask and the photoresist.

6.4 Etching

Etching is a procedure to remove a material. Two types of etching during the fabrication can be distinguished: wet chemically etching and dry etching. Wet chemically etching means that the material is removed by a chemical solution, while dry etching removes the material with a bombardment of ions (usually a plasma of reactive gases). Wet chemically etching is isotropic, while dry etching can be either isotropic or anisotropic. In our application, the common requirement for these two types of etching is that the etchants have to be selective between the mask material and the to-be-etched material (TBEM). The most commonly used wet and dry etchants are listed in table 6.2. The etch rate in the table is dependent on the concentration of the solution, the gas mixture ratio and the RF power of the dry etching machine. The etch rate given in the table is based on the gas ratio and the RF power at the second column.

6.5 Common fabrication procedures

6.5.1 Waveguide etching

To integrate the functional components, different waveguide ridge structures are needed in the photonic integrated circuits. From the etching depth point of view, there are two types of waveguides, shallowly etched (about 100 nm into the film) and deeply etched waveguides (etched through the film). The shallowly etched waveguide has a lower transmission loss,

TBEM	Etchant	W/D[1]	I/A[2]	Etch rate (nm/min)	Note[3]
InP	$HCl/H_3PO_4 = 1:4$	W	I	~400	
InP	$CH_4/O_2 = 20/80$ sccm RF power: 220W	D	A	~52	InP RIE
InGaAs	$H_2O_2/H_2SO_4/H_2O = 1/1/10$	W	I	~900	
InGaAs	$CH_4/O_2 = 20/80$ sccm RF power: 220W	D	A	~23	InP RIE
Q1.25	$H_2O_2/H_2SO_4/H_2O = 1/1/10$	W	I	~150	
Q1.25	$CH_4/O_2 = 20/80$ sccm RF power: 220W	D	A	~29	InP RIE
SiNx	$CHF_3/O_2 = 50/5$ sccm	D	A	~110	SiNx RIE
SiNx	10% (1%) HF	W	I	~114 (34)	
SiNx	BHF	W	I	~43	
Photoresist	O_2 plasma	D	I	-	stripper
Photoresist	acetone	W	I	dissolved	
Photoresist	$CHF_3/O_2 = 20/2$ sccm RF power:50 W	D	A	~100	SiNx RIE
Polyimide	$CHF_3/O_2 = 20/2$ sccm RF power:50 W	D	A	~100	SiNx RIE
Polyimide	$CF_4/O_2 = 15/35$ sccm RF power: 300W	D	I	~50	barrel etcher
Ti	HF or BHF	W	I	high	
Ti	Oxalic acid/KOH/H_2O_2 =4g/25ml/50ml	W	I	~30	
Au	$KI/I_2/H_2O$	W	I	~30	
Au	KCN	W	I	~30	

[1]Wet chemical etching / dry etching
[2]Isotropic / Anisotropic
[3]The corresponding machine names in the clean room.

Table 6.2: Commonly used etchants during the whole chip processing.

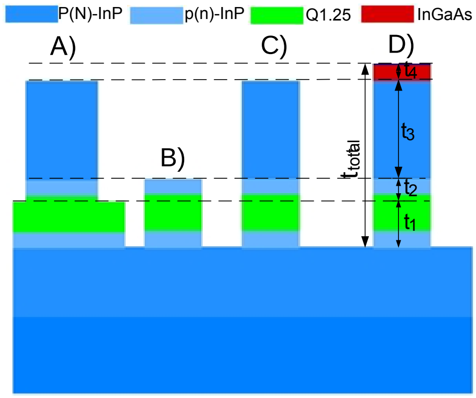

Figure 6.2: Four types of waveguide structures for the tunable wavelength duplexer. A) shallowly etched waveguides without the top InGaAs contact layer; B) deeply etched isolation waveguides without the p-InGaAs and p-InP layers; C) deeply etched waveguides without the top InGaAs contact layer; D) deeply etched waveguides with the top InGaAs contact layer.

but requires a larger bending radius, while the deeply etched waveguide has a higher transmission loss, but it can be bent with tens of micrometer of radius. From the function point of view, more types of waveguide structures are needed. If taking the tunable wavelength duplexer (Chapter 2) as an example, it needs four types of waveguides, shown in Fig. 6.2:

(A) shallowly etched waveguides without the top InGaAs contact layer: they are typically designed for the access or interconnect waveguides which require a low waveguide propagation loss.

(B) deeply etched isolation waveguides with the top p-doped layers removed: they are used to remove the electrical connection between two branches of the tunable MZI wavelength duplexer when they are tuned with the electro-optical effects.

(C) deeply etched waveguides without the top p-InGaAs contact layer: they are typical for the MMIs and curved waveguides. The performance of a deeply etched MMI is independent of the etching depth variation, and the bent radius of a deeply etched waveguide can be very small. The top InGaAs layer is removed to decrease the optical absorption caused by the highly p-doped InGaAs layer.

(D) deeply etched waveguides with the top InGaAs contact layer: they are phase shifters of the MZI wavelength duplexer. The top p-InGaAs layer servers as a contact layer.

To achieve above four different waveguide profiles, we need four etching steps and four optical lithographies interleaved between the etching steps. All these waveguides are etched with reactive ion etching (RIE) with a gas mixture of $CH_4/O_2 = 20/80\,\mathrm{sccm}$. Due to different etching rates of the materials in InP RIE (see table 6.2), it is more convenient to translate the difference in the waveguide profile into a difference in the etching time. They are written as:

$$t_{\text{total}} = t_1 + t_2 + t_3 + t_4 \tag{6.1}$$

$$t_{\text{SH}} = t_2 + t_3 + t_4 \tag{6.2}$$

$$t_1 = t_{\text{deep-sh}} = t_{400\,\text{nmQ1.25+200\,nmInP}} \tag{6.3}$$

$$t_2 = t_{100\,\text{nmQ1.25+200\,nmInP}} \tag{6.4}$$

$$t_3 = t_{\text{deep-deep}_{\text{iso}}} = t_{1300\,\text{nmInP}} \tag{6.5}$$

$$t_4 = t_{200\,\text{nmInGaAs}} \tag{6.6}$$

in which t_{total} is the total etching time for the deeply etched waveguides, t_{SH} is the total etching time for the shallowly etched waveguides, t_1 is the first etching time for the depth difference (400 nm Q1.25 and 200 nm InP) between the shallowly and deeply etched waveguides, t_2 is the second etching time equivalent to the etching time needed for 100 nm Q1.25 and 200 nm InP, t_3 is the third etching time for the layer difference (1300 nm p-InP) between the deeply etched waveguides and the deeply etched isolation waveguides, and t_4 is the fourth etching time to remove the top InGaAs contact layer.

All these four types of waveguides were etched by InP RIE. The detailed lithographies and four etching steps in practice are illustrated in Fig. 6.3, and the procedures are as follows:

(A) Clean the wafer surface with 10% H_3PO_4 for two minutes. Then a 50 nm or 80 nm SiNx is deposited over the whole surface with PECVD, see Fig. 6.3(A). The thickness of the SiNx is dependent on the deepest etching depth. The SiNx later works as a etching mask for the waveguides.

(B) Carry out the “waveguide lithography” (see table (6.1)) to transfer the waveguide pattern to the photoresist. Put the sample in the SiNx RIE which removes the SiNx uncovered by the photoresist. Then, remove the photoresist with O_2 plasma and aceton. Now, the waveguide pattern is transferred to the SiNx, see Fig. 6.3(B).

(C) Carry out the “deep etch lithography” to define the region to be deeply etched. Afterwards, evaporate 100 nm Titanium (Ti) over the whole surface. The Ti above the photoresist is removed by aceton through lift-off, and the rest Ti is going to protect the shallow region, see Fig. 6.3(C).

(D) Etch the whole sample for t_1 in InP RIE. The regions which are protected by Ti are not etched, see Fig. 6.3(D).

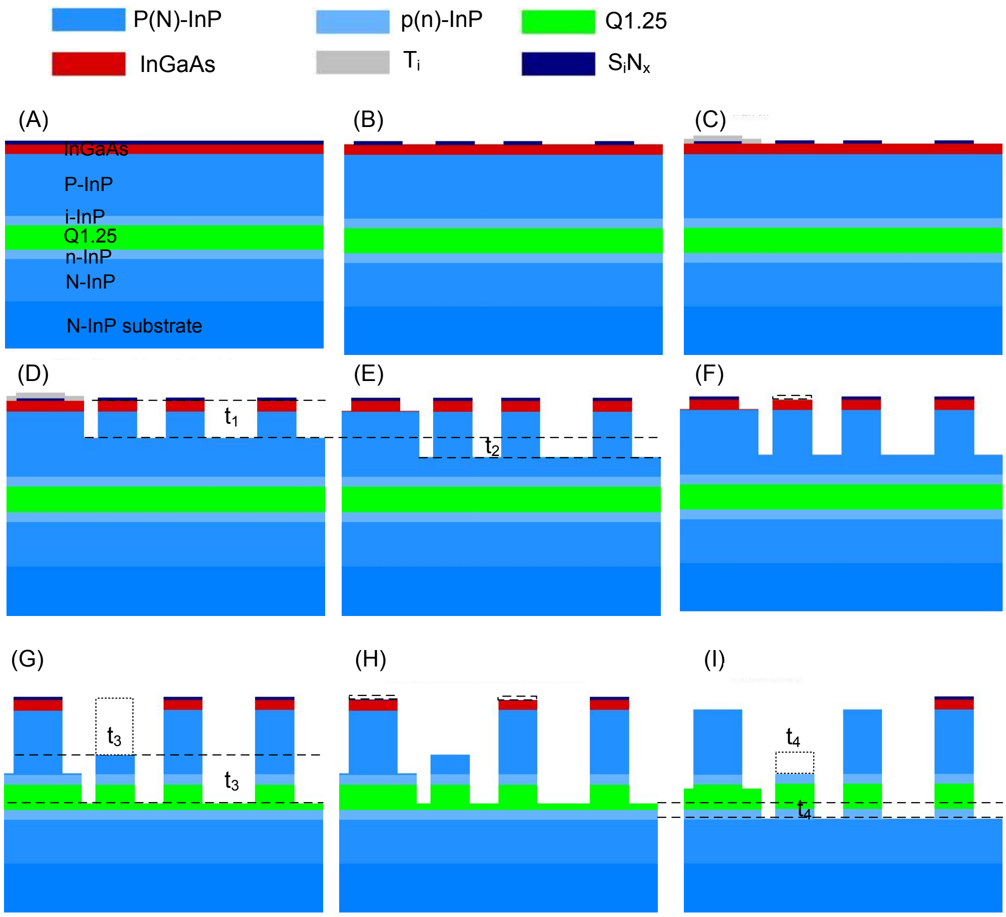

Figure 6.3: Illustration of process flow to achieve different waveguide structures.

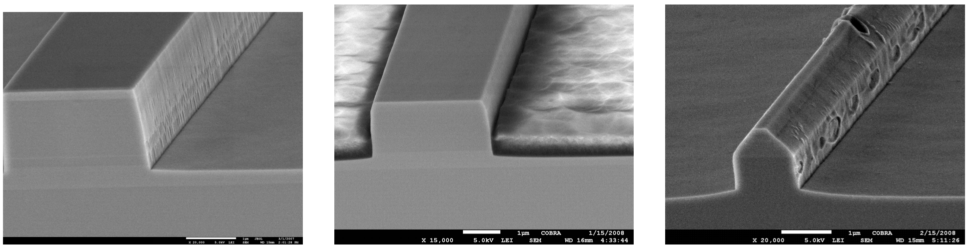

Figure 6.4: (left) Shallowly etched waveguide with SiNx above during RIE; (middle) Shallowly etched waveguide with rounded edge at the top after 8 minutes RIE etching without SiNx above; (left) Deeply etched isolation waveguide with rounded edge and less width after 34 minutes “maskless etching”.

(E) Remove Ti with a wet chemical etchant given in table (6.2). Then etch the whole sample for t_2 in InP RIE , see Fig. 6.3(E).

(F) Carry out the “Isolation lithography” to define the isolation region. Consequently, the isolation waveguides are exposed without photoresist protection. Remove the exposed SiNx on the isolation waveguide with 10% HF, see Fig. 6.3(F).

(G) Etch the whole sample for t_3 in InP RIE. The semiconductor material of the isolation waveguides without SiNx protection are etched away as well, see Fig. 6.3(G).

(H) Carry out the “P-contact lithography” to define the contact region. All the waveguides, except waveguide type (D) in Fig. 6.2, are exposed without photoresist protection. Then the whole sample is put into 10% HF for a second, and all the exposed SiNx is removed.

(I) Etch the whole sample for t_4 in InP RIE. The semiconductor material of the waveguides, except waveguide type (D) in Fig. 6.2, are etched away. After etching, remove the rest SiNx with 10% HF. So far, all the waveguide ridges are achieved.

The above calculation and fabrication procedures are valid for all the devices with different waveguide profiles. The total etching times (four times in this example) is dependent on the number of the waveguide types (four types in this example).

One thing which should be mentioned is the consequence of the “maskless etching” during the waveguide fabrication. “Maskless etching” means that the waveguide ridge was not protected by SiNx during etching process in InP RIE. For example the isolation waveguide (WG (B) in Fig. 6.2) was maskless etched for a total time of $t_3 + t_4$, as shown in Fig. 6.3, and the WG (A) and (C) were maskless etched for t_4. The consequence of maskless etching is shrinking and rounding of the waveguide, see Fig. 6.4. The left figure is a shallowly etched waveguide with SiNx above during InP RIE etching, and the right figure is a deeply etched isolation waveguide with 34 minutes maskless etching. The width of the isolation waveguide shrank about 150 nm, and the edge of the waveguide was rounded.

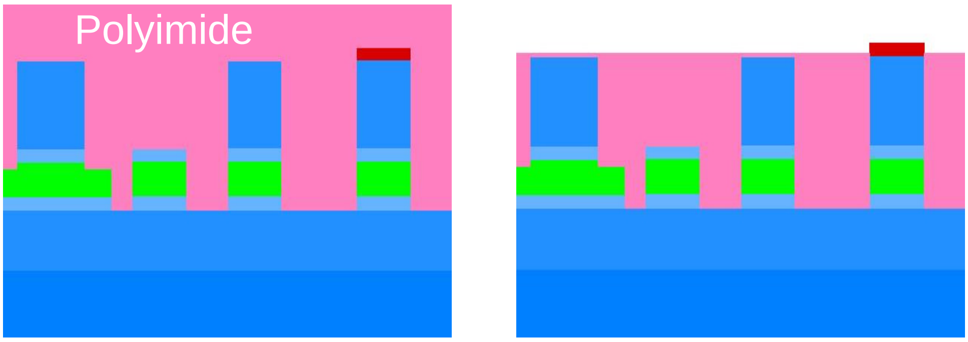

Figure 6.5: Illustration of the cross-section view after spinning the polyimide for passivation, planarization and etching back.

In order to avoid maskless etching in InP RIE, wet chemical etching could be a choice. But it is not always applicable due to a certain waveguide structure. For instance, because the isolation waveguide of the tunable duplexer is deeply etched, the chemical etchant which removes the top p-InP layer attacks the buffer n-InP below the film as well.

6.5.2 Passivation, planarization and etching back

To avoid a high leakage current and surface recombination, polyimide is used to passivate and planarize the devices, see Fig. 6.5(left). In the clean room practice, after spinning a layer of the polyimide, the polyimide is baked first on a hot plate whose temperature increases gradually from room temperature to 200°C. After each two layers, the polyimide is cured in a nitrogen oven at 300°C for one hour in order that the polyimide adheres to the sidewall well. The total number of the polyimide layer depends on the etching depth of the waveguide. Before the metallization, the polyimide is etched back in the barrel etcher to expose contact layer, see Fig. 6.5(right).

In case the lateral N-contacts are needed (for example the devices are fabricated on the semi-insulating substrate), additional process steps are required. After the p-InGaAs is exposed described above, the “N-contact open” lithography is carried out to define the region where the N-contacts locate. After the lithography, the N-InP contact regions are exposed, and the rest of the sample is covered by the photoresist. In order to obtain a gradual connection later from the N-InP contact to the metal probe pads, the photoresist is baked for 20 minutes at 120°C which creates a slope profile with an acute angle. This angled slope of the photoresist is transferred to the polyimide by a directionally etching in SiNx RIE. A photo which shows both exposed P- and N-contacts is given in Fig. 6.6(left). A polyimide slope which offers a smooth connection between the N-contact and the probe pads is shown in Fig. 6.6(right).

The passivation effect with polyimide has been checked with several 2 mm long deeply etched phase shifters with different widths. The SEM picture of a deeply etched waveguide

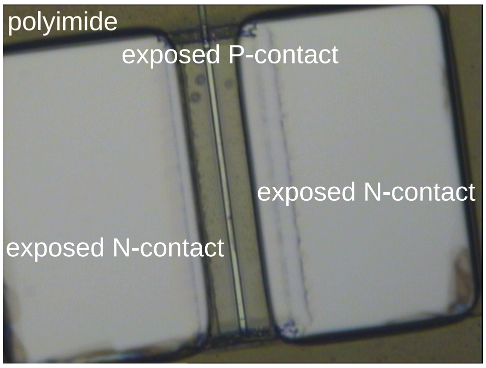

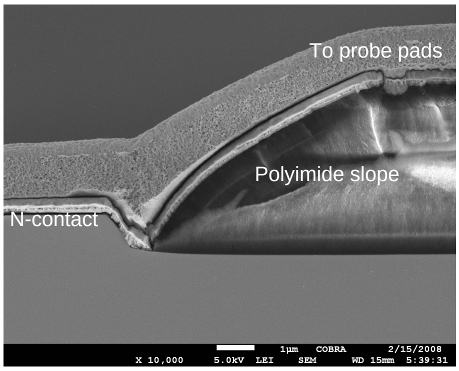

Figure 6.6: Exposed lateral N-contacts and P-contact of a photodetector on the semi-insulating substrate after etching back the polyimide in both barrel etcher and SiNx RIE before metallization (*left*) and the polyimide slop to connect the N-contact with the probe pads gradually (*right*).

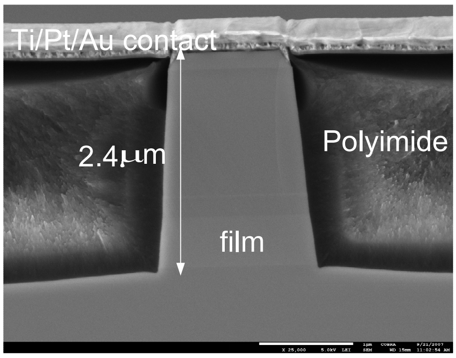

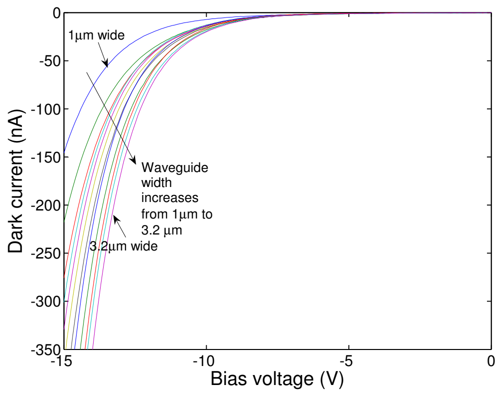

Figure 6.7: SEM picture of a fabricated deeply etched phase shifter passivated by the polyimide (*left*) and the measured dark current of 2 mm long deeply etched phase shifters with different widths (*right*).

phase shifter shows that the polyimide adheres to the side wall very well, and the measured dark currents are low, below −50 nA under −12 V bias voltage. The results are comparable with the phase shifters passivated by SiNx deposited at low temperature, but the devices passivated by the polyimide show a longer operation lifetime than those passivate by the SiNx in COBRA.

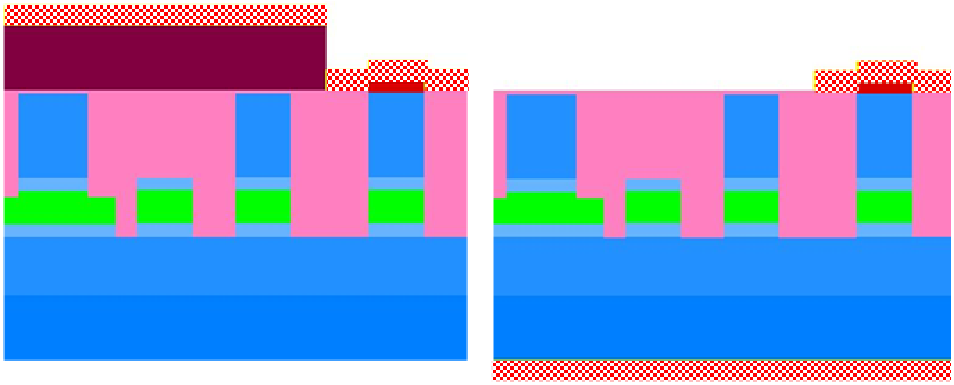

Figure 6.8: Illustration of the cross-Section view after evaporating 25/75/200 nm Ti/Pt/Au before lift-off (*left*) and Ti/Pt/Au at both top and bottom side of the sample after lift-off (*right*).

6.5.3 Metallization, annealing and electroplating

The main requirements for a ohmic contact are low contact resistance and high thermal stability, both of which are affected by the metallization, good adhesion and the interface between the metal and the semiconductor [155]. The Ti-Pt-Au metallization scheme is selected since both p- and n-contacts can be formed within one metallization step. The Pt and the Ti layers serve to improve the adhesion of the metal to the underlying semiconductor and act as a diffusion barrier for Au, and thus enhance the long-term reliability of the device [156] [157].

After metallization, the sample has to be annealed in a Rapid Thermal Processor in a Ar/H_2-ambient for 30 seconds at a temperature of 325°C to reduce the contact resistance. To further minimize the contact resistance and improve the uniformity of the electrode for the carrier injection, the fabrication proceeded with the electroplating. First we sputter a 100 nm thick gold seed layer over the sample surface; then the "plating lithography" is carried out to define the regions which need to be plated. Afterwards, the sample is placed inside a solution containing dissolved gold ions for some hours. The profile after plating is seen in Fig. 6.9(left). Then, the photoresist in Fig. 6.9(left) is removed by acetone and O_2−stripping at low power, and the Au seed layer is etched away by potassium cyanide (KCN), Fig. 6.9(right). An SEM picture of the evaporated and plated gold are seen in Fig. 6.10(left), and a SEM top view of a SOA with lateral N-contacts after the metallization is shown in Fig. 6.10(right).

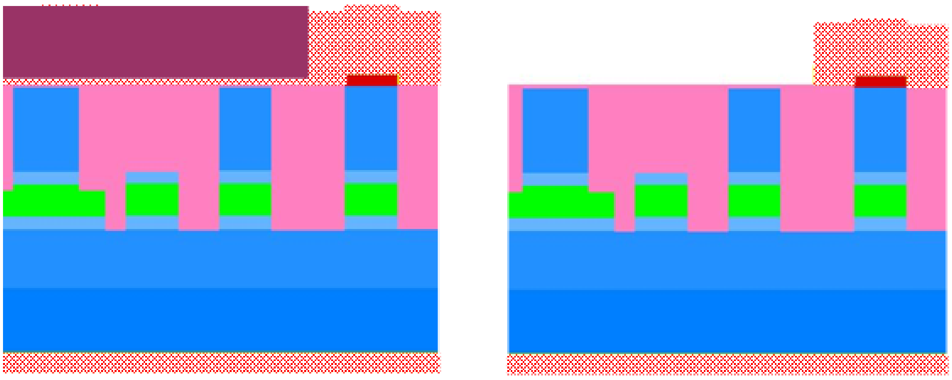

Figure 6.9: Illustration of the cross-Section view after sputtering 100 nm Au and plating (*left*) and the final view after removing the photoresist and etching away Au seed layer (*right*).

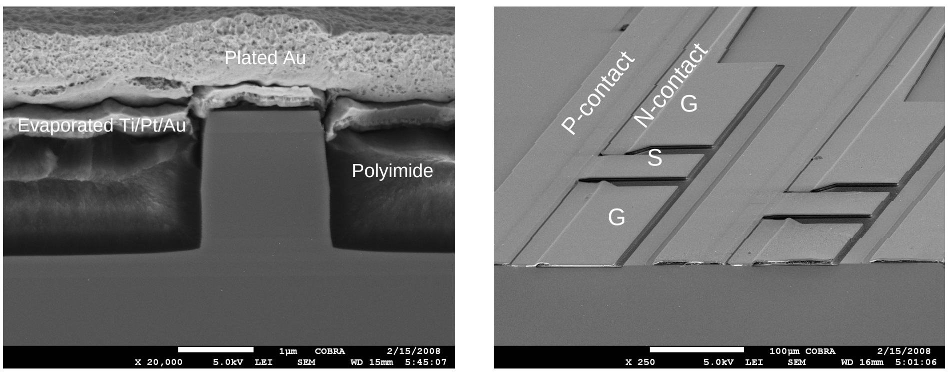

Figure 6.10: SEM pictures of the evaporated and the plated Au on a SOA (*left*) and the top view of the metal connection of a SOA (*right*).

6.6 Complete chip processing flow

In this section, the masks and the complete chip processing flows for the devices described in this thesis will be given. Since the fabrication process flow for the tunable duplexer were illustrated in Fig. 6.3, Fig. 6.5 and Fig. 6.8, the procedures will not be repeated. The process flow for an active-passive integrated devices on an N-InP substrate (Chapter 7) is given in Section 6.6.1. Section 6.6.2 will present the whole process flow for the active-passive integrated devices on the semi-insulating substrate (Chapter 4 and 5 and 7). These devices require lateral N-contacts. At the end, a full process flow for fabricating a RF submount which is used to assist performing RF measurements of the devices on the N-InP substrate is described.

6.6.1 Active-passive integrated devices on an N-InP substrate

An example device is the first generation transceiver (Chapter 7). In order to fabricate this transceiver, four masks are needed, namely a "waveguide mask", a "deep etch mask", a "p-contact mask", and a "metallization mask". This transceiver has three types of waveguide, a shallowly etched waveguide with top-InGaAs (SOA and PD), WG (A) and WG (C) shown in Fig (6.2). Therefore, three lithographies and three RIE etching steps are needed to fabricate these waveguides. The illustration of the whole process flow is shown in Fig. 6.11.

(A) Clean the wafer with 10% H_3PO_4 for two minutes to remove the oxidized layer. Deposit 50 nm SiNx on the top with PECVD.

(B) Carry out the "Waveguide lithography", etch SiNx in SiNx RIE and remove the photoresist with O_2 plasma and aceton.

(C) Carry out the "Deep etch lithography", and deposit 100 nm T_i before lift-off.

(D) Lift-off to remove the photoresist and Ti above.

(E) Etch the sample for t_1 in InP RIE, equal to the etching time needed for 400 nm Q1.25 and 100 nm InP.

(F) Remove Ti by chemical etchant, and etch the sample for t_2 in InP RIE. Time t_2 is corresponding to the time needed to etch away 1300 nm p-InP.

(G) Carry out the "P-contact lithography" to define the contact regions which need metal contact later with photoresist.

(H) Bake the photoresist for 20 minutes at a hot plate set at 120°C to avoid later BHF under-etching the SiNx. Afterwards, the sample was put into BHF solution, and the exposed S_iN_x are removed by BHF. Remove the photoresist with aceton and O_2 plasma.

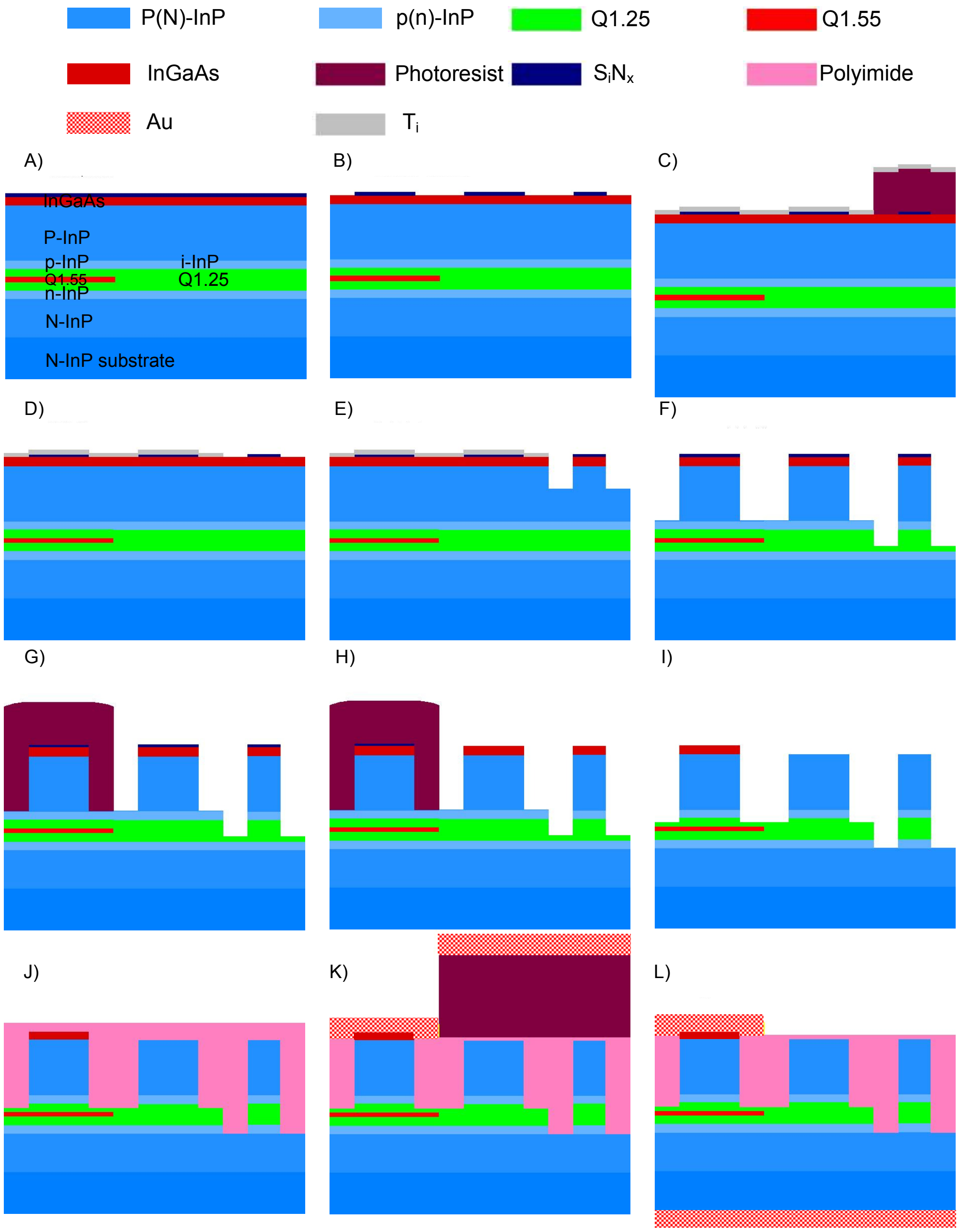

Figure 6.11: Complete fabrication process flow for the active-passive integrated devices on a N-InP substrate (Chapter 7).

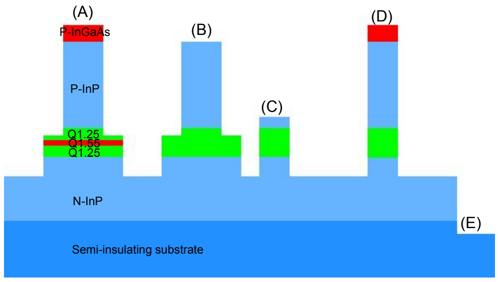

Figure 6.12: Five types of waveguides in the reflective transceiver which consists of a thermally tunable duplexer, a phase modulator, MMI loop mirrors, a SOA and a photodetector.

(I) Etch the sample for t_3 in InP RIE. The time t_3 is corresponding to the time needed to etch away 300 nm p-InGaAs layer. Remove the SiNx above the contact regions with BHF. So far, all the waveguide profiles have been obtained.

(J) Spin, bake and cure several layers of polyimide to passivate and planarize the sample.

(K) Etch back the polyimide in the barrel etcher until the p-InGaAs is exposed. Carry out the "metallization lithography" to define the region which needs metal contact later. The region which do not need metal was covered by the photoresist. Evaporate 300 nm Ti/Pt/Au on the sample.

(L) Lift-off in aceton to remove the photoresist and the metal above the photoresist. Evaporate Ti/Pt/Au at the back side of the sample to form N-contact.

6.6.2 Active-passive integrated devices on a semi-insulating substrate

The whole process flow described in this section is for the third generation transceiver (Chapter 7) which integrates a thermally tunable duplexer, a phase modulator, MMI loop mirrors, a SOA and a photodetector. The reflective SOA (Chapter 4) and the high performance photodetector (Chapter 5) which have fewer waveguide types are fabricated in the same wafer.

The full processing needs eight masks, a "waveguide mask", a "substrate etching mask", a "deep etching mask, an "isolation mask", a "p-contact mask", an "N-contact open mask", a "metallization mask" and a "plating mask". There are 5 types of waveguide profiles in total, as shown in Fig. 6.12, in which

(A) Waveguide (A) is a shallowly etched active waveguide with p-InGaAs on the top. It is for the SOA and the photodetector.

(B) Waveguide (B) is a shallowly etched waveguide without p-InGaAs on the top. It has low transmission loss and is for the access waveguides and the interconnect waveguides.

(C) Waveguide (C) is a deeply etched isolation waveguide. It is located at the two branches of a Michelson phase modulator to remove the electrical connection between. It is narrow and deeply etched to reduce the velocity mismatch between the microwave and the light.

(D) Waveguide (D) is a deeply etched waveguide with p-InGaAs on the top. It is for the phase shifters of the phase modulator and the thermally tunable duplexer.

(E) Waveguide (E) is a substrate etched waveguide. It is deeply etched into the substrate to increase the resistance between the SOA and the photodetector. It is later filled with polyimide to support the RF pads to reduce the microwave attenuation.

The illustration of the whole process flow is shown in Fig. 6.11.

(A) Clean the active-passive wafer with 10% H_3PO_4 for two minutes, and then deposit 80 nm SiNx on the top with PECVD. Carry out the "waveguide lithography" to transfer the waveguide pattern to SiNx.

(B) Carry out the "Substrate etch lithography" to define the region needed to be etched until the substrate and protect all the other waveguides with a thick photoresist. Etch the whole sample for t_1 in InP RIE, which is equivalent to the etching time for the depth difference between the waveguide type (E) and (D) in Fig. 6.12. Remove the photoresist with O_2 plasma and aceton.

(C) Carry out the "Deep etch lithography" to define the region to be deeply etched and protect the shallow waveguides with the photoresist. Etch the sample for t_2 in InP RIE, which is equivalent to the etching time for the depth difference between the waveguide type (D) and (B) in Fig. 6.12. Remove the photoresist with O_2 plasma and aceton.

(D) Etch all the waveguides for t_3 in InP RIE, which is equivalent to time needed for 100 nm Q1.25 and 200 nm InP above the film.

(E) Carry out the "Isolation lithography" to define the isolation waveguides and protect the other waveguides with the photoresist. Remove the exposed SiNx on the isolation waveguide with BHF. Etch the sample for t_4 in InP RIE, which is equivalent to the etching time needed for 1300 nm p-InP.

(F) Carry out the "P-contact lithography" to protect the waveguides which need metal contact later (waveguide (A) and (D) in Fig. 6.12) with the photoresist and expose the other waveguides. Remove the exposed SiNx with BHF, and etch the sample for t_5 in InP RIE, which is equivalent to the etching time needed for 300 nm p-InGaAs. Remove the photoresist which protects the waveguide (A) and (D), and remove the SiNx above with BHF.

(G) Spin several layers of polyimide to passivate and planarize the sample.

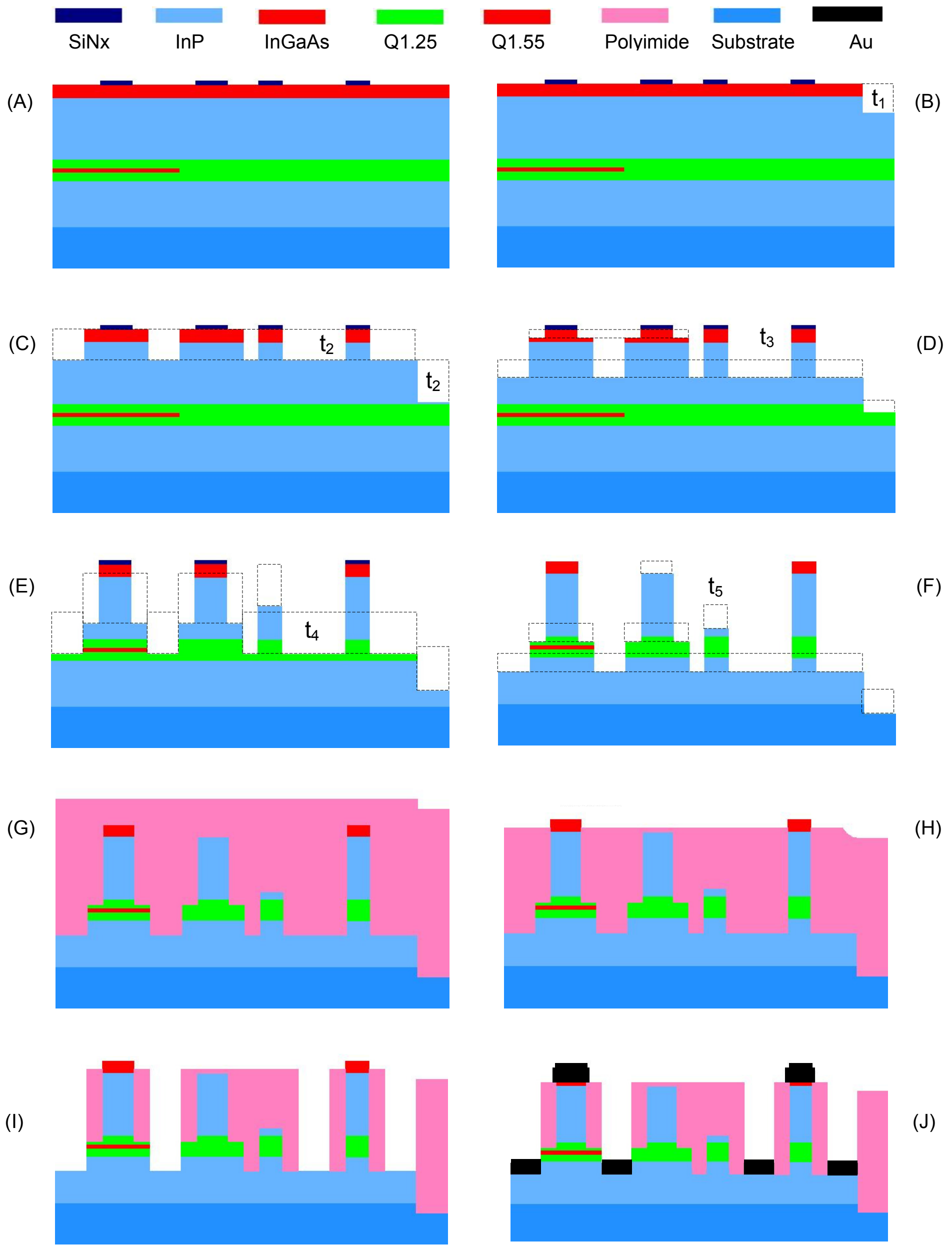

Figure 6.13: Complete fabrication process flow for the first monolithic integrated transceiver.

(H) Etch back the polyimide in the barrel etcher until the p-InGaAs exposes.

(I) Carry out the "N-contact open lithography" to expose the region which will have N-contacts later. Bake the photoresist which protects the rest of the sample to obtain a slope profile, and etch back in SiNx RIE until the N-InP exposes.

(J) Carry out the "Metallization lithography", and evaporate Ti/Pt/Au on the sample and lift-off.

(K) Sputter a 100 nm thick gold seed layer, and carry out the "Plating lithography" to define the region to be plated and protect the rest with the photoresist. Plating the whole chip for hours to increase the thickness of the metal. In the end, the seed layer was etched away by potassium cyanide (KCN).

6.6.3 RF submount

Design

To ease RF measurements for the devices on an N-substrate, a RF submount on an aluminum nitride (AlN) substrate is designed and fabricated. The mask layout for such a submount is shown in Fig. 6.14. It has bonding pads at one side and ground-signal-ground (GSG) pads at the other side. The bonding pads and the GSG pads were connected through a group of coplanar transmission lines. The signal line width is 22 μm and the gap is 11.5 μm. The bandwidth of the transmission lines is more than 30 GHz using the Momentum simulator, as shown in Fig. 6.15.

Fabrication

A metallization mask is needed to fabricate the RF submount, and the fabrication procedure is given as follows:

(A) Clean the surface of aluminum nitride (AlN) with BHF for two minutes and rinse it in the water.

(B) Clean the substrate with aceton and isopraponal

(C) Deposit a thin SiNx layer with PECVD

(D) Carry out the "metallization lithography" with negative photoresist MAN440

(E) Evaporate Ti/Au=50/200 nm

(F) Lift-off with acetone.

(G) Carry out the "plating lithography" with the metallization mask, but with a positive photoresist AZ4533. Sputter a gold seed layer, and electro-plating the device until the thickness of the metal reaches 1~1.5 μm.

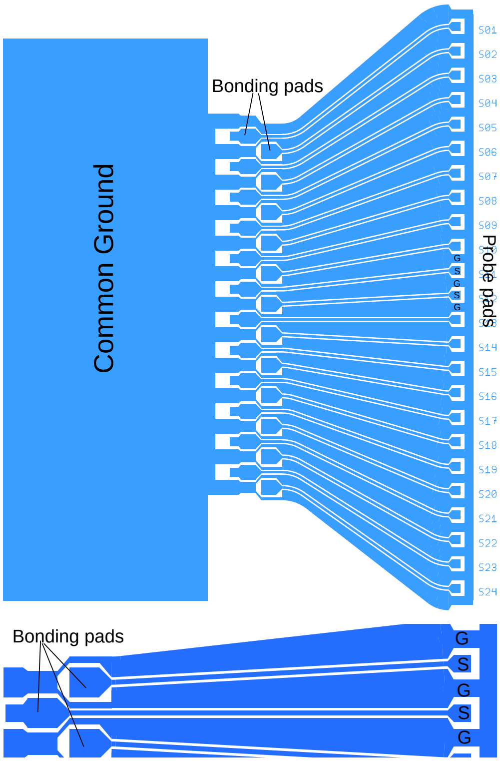

Figure 6.14: The full view (top) and zoomed transmission lines (bottom) of the RF submount.

Measurement

The 2-port S-parameters were measured to see the bandwidth of the transmission lines. The measurement was carried out with a network analyzer up to 20 GHz (due to the bandwidth limit of the network analyzer). The measured S parameters of this transmission line are shown in Fig. 6.16. which shows that this designed transmission lines have more than 20 GHz bandwidth since the S21 and S12 did not drop 3 dB yet at 20 GHz.

To use this submount, the device on an N-substrate is glued on the common ground of the submount (Fig. 6.14), and the p-metal contact of to-be-tested component is connected with the bonding pads of the transmission lines through wire bonding.

This submount has been successfully applied in the hybrid mode-locked laser, modulation measurement of a tunable wavelength duplexer (Chapter 7) and a reflective transceiver (Chapter 7).

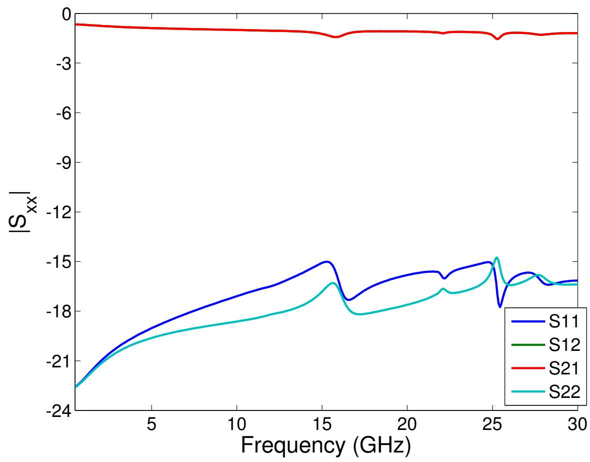

Figure 6.15: The simulated bandwidth of the transmission lines based on momentum simulator.

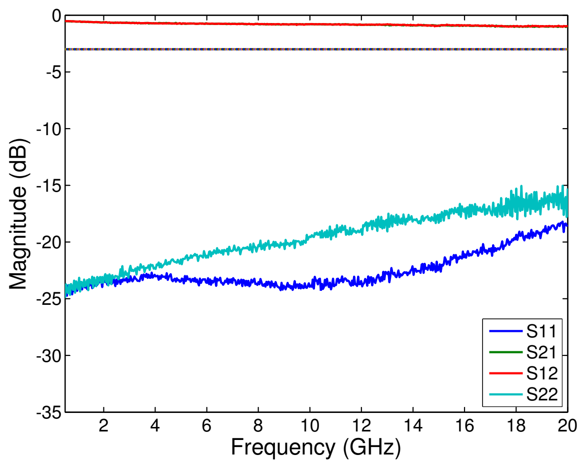

Figure 6.16: The measured S-parameters of the transmission line on the RF submount.

Chapter 7

Monolithic integrated colorless reflective transceiver

In this chapter, we present the design and the characterization results of three generations of reflective transceivers. The first generation transceiver consists of a wavelength duplexer, a RSOA and a photodetector. The measurement results show that the integrated RSOA achieves 1 Gbit/s operation and the integrated photodetector reaches 14 GHz bandwidth for the downstream data. The second generation transceiver is based on a semi-insulating InP substrate to facilitate flip-chip bonding and improve the bandwidth of the photodetector. In this device, the SOA achieves 1.25 GHz bandwidth, and the photodetector obtains 30 GHz bandwidth. In addition, the noises of the photodetector caused by biasing and modulating the SOA are investigated, and options for the noise reduction are discussed. The third generation transceiver is designed and fabricated, aiming for 10 Gbit/s operation. It integrates a thermally tunable wavelength duplexer, a SOA, a photodetector, two MMI-loop mirrors and a reflective Michelson phase modulator.

7.1 Introduction

Previously, we discussed all the constituent components of the transceiver: the wavelength duplexer (Chapter 2), the passive reflective components (Chapter 3), the reflective SOA (Chapter 4) and the photodetector (Chapter 5). In this chapter, we will discuss the monolithically integrated transceiver circuits.

In the next sections, the isolation level is a parameter to describe the performance of the wavelength duplexer, and the crosstalk (DC and RF) refers to the noise current of the photodetector due to simultaneously driving the RSOA with the electrical current.

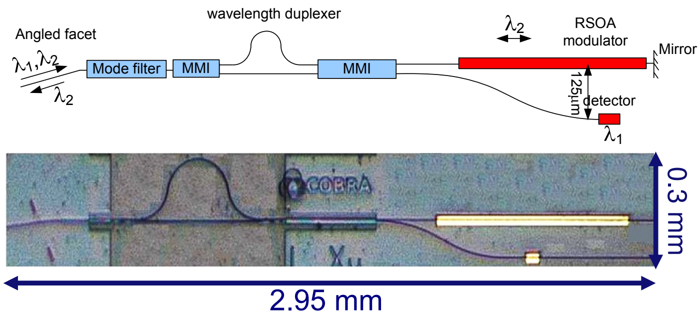

Figure 7.1: (*Top*) The layout of the integrated transceiver consisting of a wavelength duplexer, a reflective SOA modulator and a detector. (*Bottom*) Photograph of a fabricated transceiver.

7.2 The first generation integrated transceiver

A schematic view of the first generation integrated transceiver is shown in Fig. 7.1. It consists of a wavelength duplexer, a reflective SOA modulator, and a photodetector. In this chip, the wavelength duplexer is not designed to be tunable for the simplification, the RSOA modulator was employed as a upstream transmitter since it has proved a large wavelength range and 1.25 Gbit/s operation, as discussed in Chapter 4. The photodetector was located close to the RSOA modulator due to the predefined locations for the active material in the wafer. Given more freedom, the photodetector would be put as far as possible from the RSOA modulator because of large signal level difference between the upstream and the downstream signal.

The device works as follows. Two wavelengths (λ_1 and λ_2) from the local exchange enter the transceiver from the left side access waveguide. First, they are spatially separated by the wavelength duplexer. Then the downstream data, carried by λ_1, is guided to the photodetector where it is detected. The other wavelength λ_2 is a continuous wave (CW) signal which is routed by the wavelength duplexer to the RSOA where it is modulated, amplified and reflected back to the network.

7.2.1 Material and design parameters

The integrated transceiver is based on an active-passive butt-joint layer stack grown on an N-InP substrate, as shown in Fig. 7.2. The active part is used for realizing the RSOA modulator and the photodetector. In the passive part the wavelength duplexer and the routing waveguides are fabricated.

In this integrated transceiver, the MZI-wavelength duplexer has identical parameters in the MMIs and the length difference as the 200 GHz duplexer presented in Chapter 2. The fiber access waveguide is 3 μm wide and shallowly etched to reduce the transmission loss, and it is angled with 7° to minimize the facet reflectivity. The SOA is designed to be 2 μm

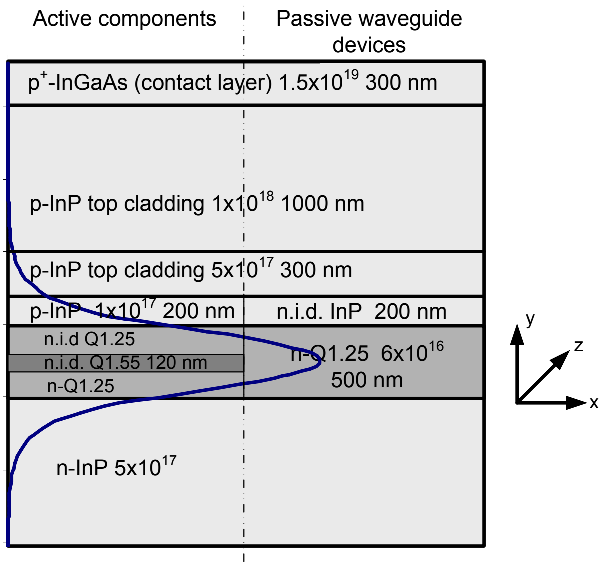

Figure 7.2: A cross section view of the active-passive layer stack with superimposed optical mode profile.

wide and 750 μm long for a sufficient gain to compensate the fiber-chip coupling loss. The absorption layer of the photodetector is Q1.55 (InGaAsP, $\lambda_{\mathrm{gap}} = 1.55\,\mu$m) as well, and the experiment shows that the absorption peak wavelength is around 1520 nm for a short photodetector. The length of the photodetector was predefined on the active-passive mask, and the maximum length of the photodetector is 60 μm. The quantum efficiency of such a photodetector is limited, however, a shorter photodetector can have a higher RF bandwidth. In order to suppress the first order mode, a 1×1 MMI mode filter [158] is inserted in the transceiver. The mode filter is shallowly etched, 6 μm wide and 98 μm long. The transmission of the fundamental mode and the first order mode has been simulated and shown in Fig. 7.3, from which we can see that the first order mode of both TE and TM polarization can be suppressed more than 10 dB when $L = 98\,\mu$m. To avoid lasing, the fiber access facet of the chip, where the light is coupled into and out of the device, is provided with an anti-reflection coating (AR) with 0.1% reflectivity. Another facet was HR coated with 90% reflectivity as a mirror to reflect the light back.

The material preparation and the fabrication processes of the integrated transceiver have been described in Chapter 6. A photo of the fabricated device can be seen in Fig. 7.1(bottom).

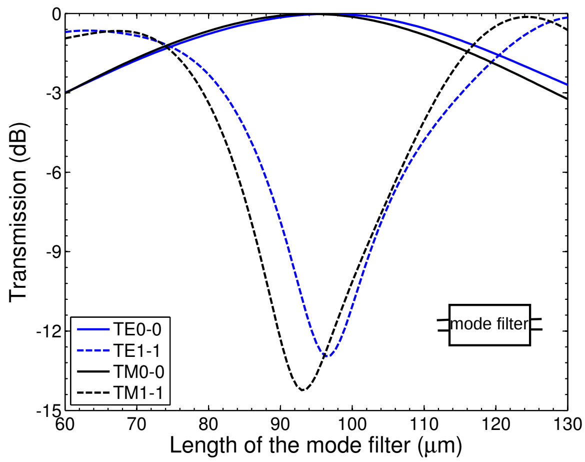

Figure 7.3: Transmission of the fundamental and the first order mode for both TE and TM polarization as a function of the length of the mode filter.

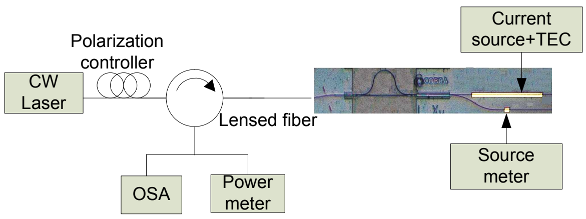

Figure 7.4: The static measurement setup for the integrated duplexer, the RSOA and the photodetector. The fiber access side is always the waveguide with the angled facet, and the other side of the chip was coated with 90% HR coating.

7.2.2 Characterization of the integrated transceiver

In this section, we will present the characterization results of the integrated transceiver, which include the channel spacing and the isolation level of the duplexer, the fiber-fiber gain and the modulation bandwidth of the RSOA, and the photoresponsivity and the bandwidth of the photodetector.

The measurement setup for the channel spacing and the isolation level of the duplexer, gain of the RSOA and the responsivity of the photodetector is shown in Fig. 7.4. A CW laser is used during the measurement of the gain of the integrated RSOA and the photo responsivity of the photodetector. The optical spectrum analyzer (OSA) and the power meter are used to record the ASE spectra and to measure the fiber-fiber gain of the integrated RSOA. The current source supplies the current to the RSOA, the temperature is controlled through a Peltier element, and the source meter applies the reverse bias voltage to the photodetector

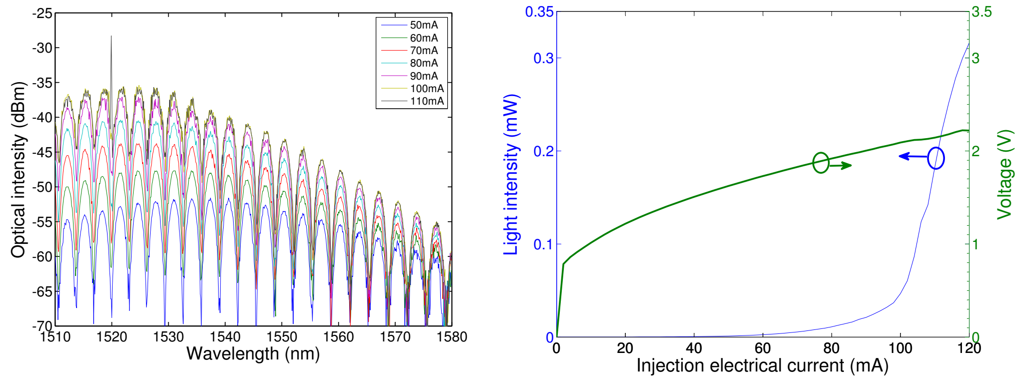

Figure 7.5: ASE spectra after the wavelength duplexer at different injection currents (*left*) and the output optical intensity and voltage as a function of the injection current (*right*).

and also records the photocurrent . The light is injected and collected through a lensed fiber near the angled facet at the left side as shown.

In the following sections, the optical input power is the optical power measured before the fiber-chip coupling. All measured results include the loss of the fiber-chip coupling (~4 dB) and the loss of the wavelength duplexer (~2 dB).

Wavelength duplexer of the transceiver

In order to measure the channel spacing and the isolation level of the duplexer, the ASE spectrum of the RSOA after passing the wavelength duplexer was recorded and shown in Fig. 7.5 (left). The modulation in the figure results from the wavelength selection of the duplexer. From the spectrum, we can see that the wavelength duplexer has about 15 dB isolation level between upstream and downstream data. At some wavelengths, the isolation level looks smaller due to the parabolic shape of the ASE spectrum of the SOA. The duplexer channel spacing is 203.2 GHz, within 2% deviation from the designed value.

Gain and modulation bandwidth of the RSOA

The gain of the RSOA is dependent on the the input optical power, the injection current and the wavelength. The maximum injection current on the SOA is limited by the lasing threshold current.

From the ASE spectrum and the output light intensity of the RSOA shown in Fig. 7.5 (right), we can see the RSOA lases at about 100 mA. With the parameters listed in table 4.1 in Chapter 4, the lasing threshold of the RSOA was predicted to be around 150 mA for a 750 μm long RSOA through rate-equation-based modeling, while the measured value is about 100 mA. The discrepancy between the simulation and the measurement is due to residual reflections. To investigate the source of the residual reflections, a high resolution

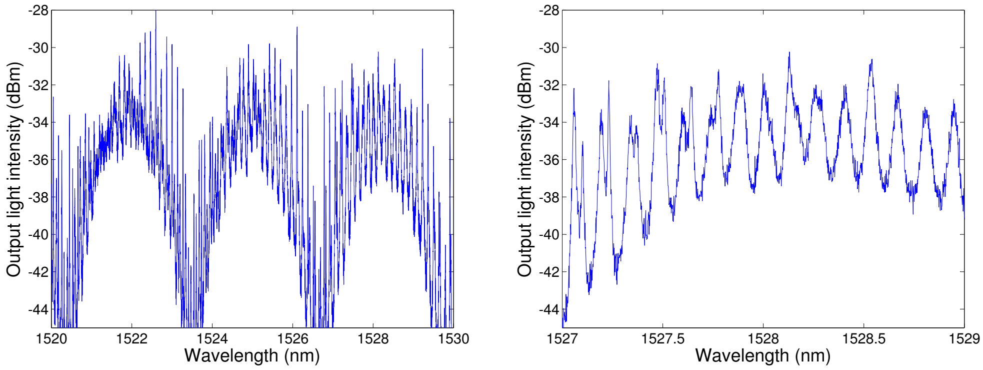

Figure 7.6: Subthreshold ASE spectrum (*left*), recorded with a high resolution OSA (0.8 pm). The large period (~3.2 nm) is due to the duplexer that acts as a wavelength filter. A zoom of the spectrum is shown in the right.

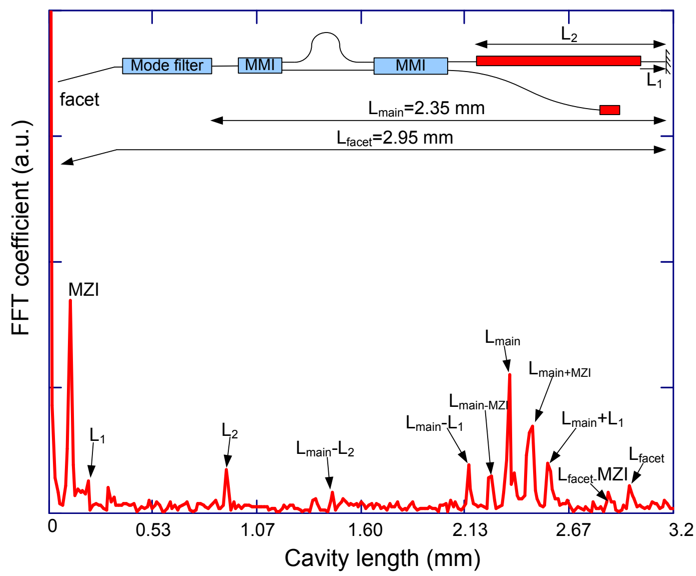

Figure 7.7: Reflection cavities inside the transceiver by analyzing the high resolution optical spectrum after a Fourier transformation.

subthreshold ASE spectrum was recorded, shown in Fig. 7.6, from which we can see that the main mode spacing is 0.134 nm, corresponding to a 2.35 mm long cavity. The reflection cavities have been resolved by means of a Fourier transformation [123], as shown in Fig. 7.7. The main reflection cavity (L_{main} =2.35 mm) matches the length from the right side

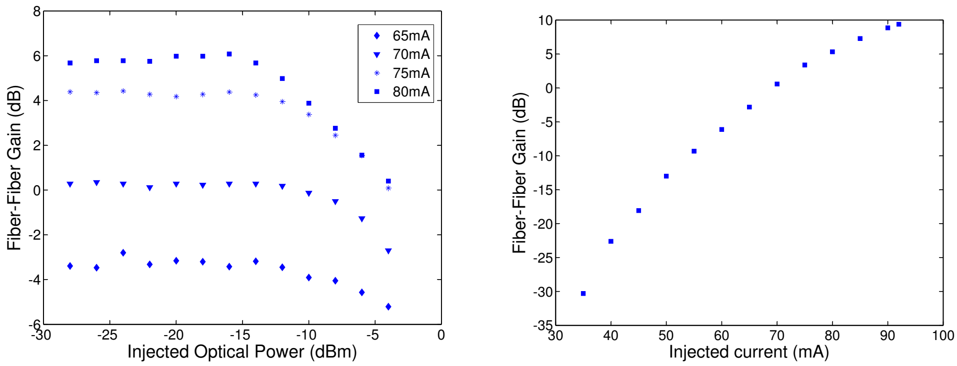

Figure 7.8: Fiber-fiber gain as a function of the input optical powers for $\lambda = 1523.6\,\text{nm}$ at different injection currents (*left*) and fiber-fiber gain as a function of the injection current when $P_{\text{in}} = -18\,\text{dBm}$ and $\lambda = 1523.6\,\text{nm}$ (*right*) . The temperature is set at 15°C and stabilized with a Peltier element.

of the mode filter to the HR coated facet, and the other cavities are located at two sides of the active-passive butt-joint (L_1 and L_2) and the AR facet in Fig. 7.7. The residual reflections at the butt-joint can be further suppressed by angling the waveguides entering the active material [124], and by using adiabatic curves to avoid possible reflections at waveguide junctions. The reflection from the mode filter can be reduced by providing the MMI with angle end facets [159].

In order to measure the gain as a function of the optical input power at a certain injection current, we couple a CW light into the transceiver at $\lambda = 1523.6\,\text{nm}$, corresponding to one of the peak transmission wavelengths of the wavelength duplexer. The light passes the wavelength duplexer and is guided to the RSOA. The amplified light travels back through the duplexer and the fiber circulator and is collected by the OSA which measures the output power. The same measurement was repeated for several input optical powers at different injection currents of the RSOA, and the measured fiber-fiber gain is shown in Fig. 7.8(left), from which we can see, the fiber-fiber gain is about 6 dB when the optical input power is below $-15\,\text{dBm}$ when $I_{\text{bias}} = 80\,\text{mA}$. The 3 dB-saturation input optical power is about $-7\,\text{dBm}$ when $I_{\text{bias}} = 80\,\text{mA}$. Therefore the distributed signal power in the user access network ($<-10\,\text{dBm}$) will not deeply saturate the RSOA.

To measure the amplification capability of the RSOA at different injection currents, we input -18 dBm optical power and obtained 10 dB fiber-fiber gain at 95 mA injection current, corresponding to about 23 dB on-chip gain, as shown in Fig. 7.8(right), from which we can see that the RSOA gain increases almost linearly with the injection current until 90 mA.

Since the device we designed has to be wavelength agnostic, it is necessary to investigate the dependence of the gain over the operation wavelength range. The measured fiber-fiber gains for different wavelengths at different injection currents are shown in Fig. 7.9, in which the modulation is again from the wavelength duplexer, and the envelope shows the wave-

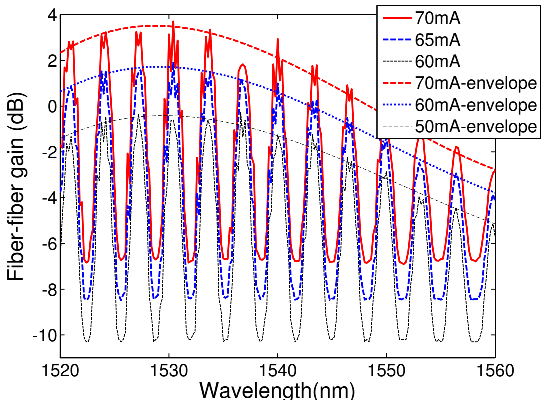

Figure 7.9: Fiber-fiber gain as a function of the wavelength at different injection currents when $P_{\text{in}} = -12\,\text{dBm}$. The gain spectrum is the envelope of the peak gain at different wavelengths.

length dependence of the gain, which is around 5 dB over a 40 nm operating wavelength range at 70 mA injection current. This wavelength dependent gain will cause different output optical powers at different wavelengths.

In Chapter 4, we have discussed the optimum bias conditions for the RSOA during the dynamic measurement, which are a high injection current and a high input optical power. The injection current should be sufficiently high to obtain a high gain and to shorten the effective carrier lifetime, but it should be in the linear region to obtain a high extinction ratio. The input optical power should be high to suppress the ASE noise and to shorten the effective carrier lifetime, but it should not deeply saturate the RSOA because modulating the RSOA in the saturation region results in a small extinction ratio. Based on the static measurement results on the gain-power and gain-current curves, the optimum bias current is between 80 mA and 85 mA which offers a sufficient fiber-fiber gain for the optical input power ($<-10\,\text{dBm}$) at the access network, and it is still in the linear region according to Fig. 7.8.

To test the dynamic performance of the integrated RSOA, we bonded the transceiver on a RF submount (see Chapter 6) through wire bonding, as shown in Fig. 7.10. The transceiver was measured with a setup as schematically shown in Fig. 7.11. The CW input light was supplied from a tunable laser HP81680. A pulse pattern generator (PPG) generates 1 GHz data with $2^{31}-1$ word length to modulate the RSOA. The series resistance of the RSOA is about $10\,\Omega$ at 80 mA, as shown in Fig. 7.5 (right). To reduce the RF reflection due to impedance mismatching between the RSOA and the PPG, a $35\,\Omega$ resistor was inserted between the bias tee and the PPG. The injected optical power before the lensed fiber was $-11\,\text{dBm}$. The temperature was set at 15°, and the bias current of the RSOA was 80 mA. After passing the polarization controller and the fiber circulator, the light was coupled into the device through a lensed fiber. The amplified and modulated light was reflected back through the fiber cir-

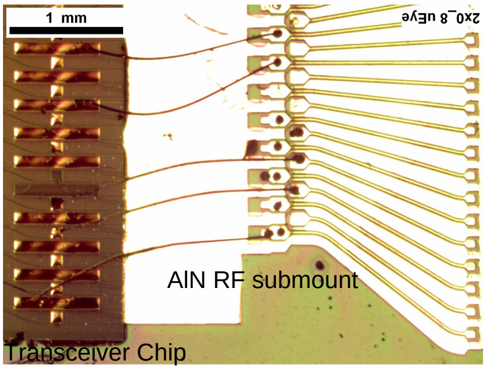

Figure 7.10: (*left*)Birdview of the bonded transceiver with the RF submount.

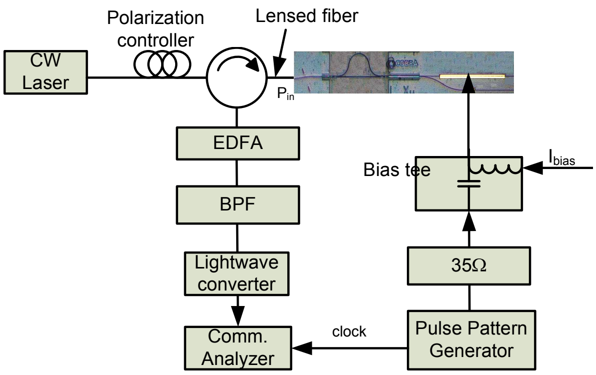

Figure 7.11: Eye diagram measurement setup of the transceiver for the RSOA.

culator and amplified by the EDFA. The bandpass filter (BPF) has a 2.5 nm bandwidth. The modulated light was firstly transformed into an electrical signal by the lightwave converter, and finally it was fed through an 800 MHz low pass filter to the digital communication analyzer. Fig. 7.12 shows a recorded eye-diagram for $\lambda = 1541.9$ nm, corresponding to one of the transmission peaks of the wavelength duplexer. The measured Q factor is up to 9, and the extinction ratio is 5.2 dB. From the Q factor, we can conclude that the transceiver can operate error free, which requires a Q factor of 6, at 1 Gbit/s with −11 dBm optical input power. The measurement has been repeated on different wavelengths from 1532.3 nm to 1541.9 nm, four channels in total, and the results are similar.

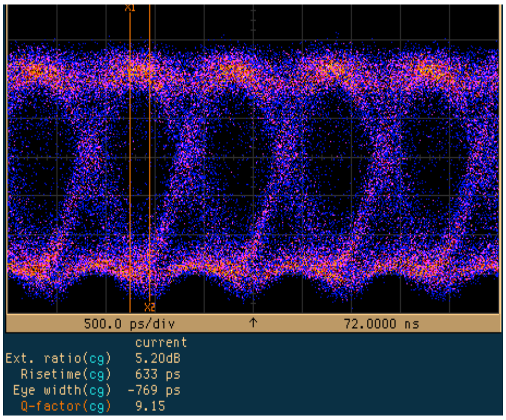

Figure 7.12: 1Gbit/s eye diagram at λ = 1541.9 nm with input optical power P_{in} = -11 dBm, 80 mA injection current and 0.78 V modulation amplitude.

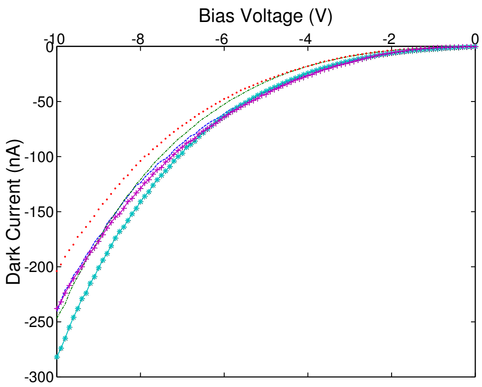

Figure 7.13: Measured dark currents of the photodetectors with different length varying from 30 μm to 60 μm in the transceiver chip.

Responsivity and bandwidth of the integrated photodetector

The measured dark currents of the photodetectors in the transceiver chip were less than 50 nA at -5 V reverse bias voltage, shown in Fig. 7.13, which is a typical value for a photodetector with similar size.

First we look at the relation between the photocurrent and the input optical power at different reverse bias voltages. A tunable laser supplied CW light at λ_{peak} = 1530.87 which was corresponding to one of the transmission peak wavelengths of the wavelength duplexer. The CW light was coupled into the chip from the angled facet, passed through the wave-

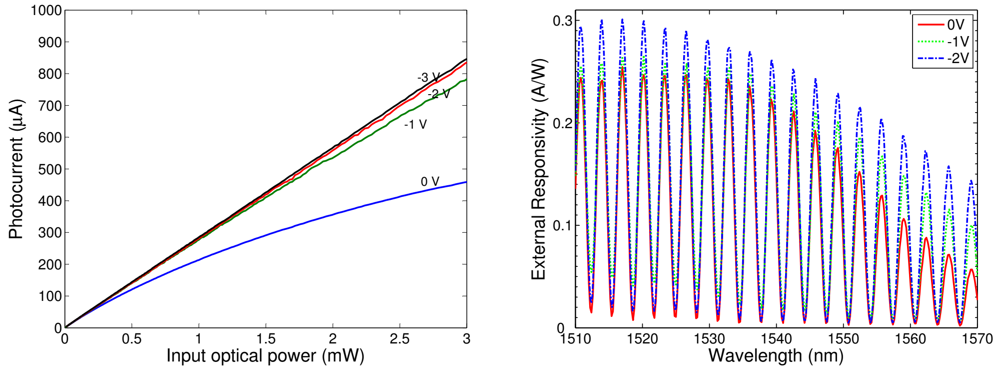

Figure 7.14: (*Left*) The photocurrent as a function of the input optical power input from the input angled side for 60 μm long photodetector at $\lambda_{\text{peak}} = 1530.87$. (*Right*) Responsivity of a 60 μm long detector as a function of the wavelength at different reverse bias voltages when $P_{\text{in}} = -4$ dBm.

length duplexer and later guided to the photodetector. The voltage was applied on the chip through a source meter, which recorded the photocurrent as well. The measurement results are shown in Fig. 7.14(left), from which we can see that the photocurrent increases linearly with the input optical power when the reverse voltage is higher than −2 V, which means that the absorption layer is completely depleted.

We also measured the responsivity as a function of the wavelength. The measurement results for a 60 μm long photodetector at different reverse bias voltages are shown in Fig. 7.14(right). The external responsivity is between 0.2 A/W to 0.3 A/W over a 50 nm wavelength range from 1510 nm to 1560 nm at a bias voltage of −2 V. The corresponding internal quantum efficiencies are 65% (0.2 A/W) to 95% (0.3 A/W) when the total loss including fiber-chip coupling loss (~4 dB due to the mode mismatch between the fiber and the angled facet) and the loss of the duplexer (~2 dB shown in Chapter 2) is 6 dB. The modulation in Fig. 7.14(right) results from the wavelength duplexer as well.

The bandwidth of the photodetector was characterized with a lightwave component analyzer (LCA) HP8703. Because the low frequency part of the HP8703 did not function, the on-wafer S-parameter measurement for the bonded photodetector was performed in the range of 2 GHz to 20 GHz through a 50 GHz RF-probe. The photodetector was biased at −6 V through a bias tee with 65 GHz bandwidth, and the injected wavelength is 1536 nm with −20 dBm optical input power before fiber-chip coupling (corresponding to about −26 dBm optical power at the photodetector). The measured small signal frequency response is given in Fig. 7.15, which shows a 3 dB bandwidth of 14 GHz for a 60 μm long wire bonded photodetector. The results include the influence of the bonding wire, the coplanar waveguide on the RF-substrate and the probe. The bandwidth of the photodetector is mainly limited by the long bonding wire in this case.

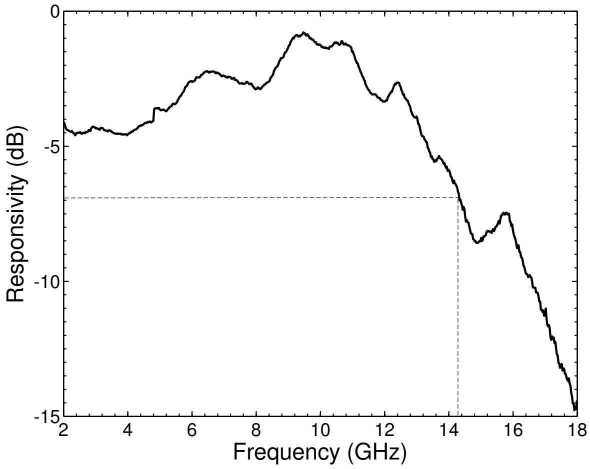

Figure 7.15: The measured frequency response of the wire bonded 60 μm long photodetector at $P_{\text{in}} = -20$ dBm and under -6 V bias voltage.

7.2.3 Conclusion and discussion

We have demonstrated a first colorless reflective monolithically integrated transceiver for the user access network. It consists of a wavelength duplexer, a RSOA modulator and a photodetector. The wavelength duplexer shows -15 dB isolation level between upstream and downstream. The integrated RSOA achieves 10 dB fiber-fiber gain at I_{bias} =95 mA at $\lambda = 1523.6$ nm, and the eyes are clearly open with a Q factor higher than 9 at 1 Gbit/s modulation rate when $P_{\text{in}} = -11$ dBm. The integrated photodetector shows an external responsivity of higher than 0.2 A/W (65% quantum efficiency) within a 50 nm wavelength range, and obtains a RF bandwidth of 14 GHz when $P_{\text{in}} = -20$ dBm, and the bandwidth is mainly limited by the long bonding wire.

Compared to the target specifications given in Table 1.3, the integrated transceiver presented in this section has achieved better results in the gain of the RSOA, and downstream bandwidth.

In order to further improve the bandwidth of the photodetector, a semi-insulating substrate can be used to reduce the parasitic capacitance and avoid the long bonding wire.

Moreover, since the distance between the RSOA and the photodetector in the first generation transceiver is only 125 μm, the measured DC crosstalk which is the additional current on the photodetector due to pumping the RSOA is more than 1 mA when the bias current on the RSOA is 90 mA, much higher than the detected signal photocurrent. The RF crosstalk was not able to be carried out on this bonded transceiver because of its backside ground contact. The detailed crosstalk on the photodetector due to driving the RSOA will be discussed in the next sections.

In the next section, a second generation integrated transceiver on semi-insulating sub-

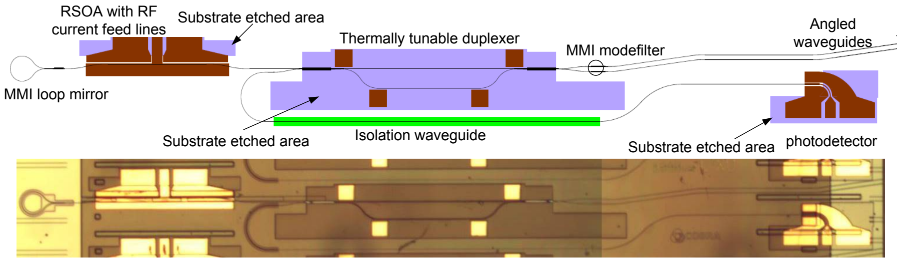

Figure 7.16: The mask layout of the second generation integrated transceiver based on semi-insulating substrate for higher bandwidth and less electrical and optical crosstalk (*top*) and a photo of the fabricated transceiver (*bottom*).

strate will be introduced, not only to facilitate the flip-chip bonding and improve the bandwidth of the photodetector, but also to reduce the electrical, optical and RF crosstalk between the RSOA and the photodetector. Based on the second generation transceivers, an analysis of the various noise contributions will be given.

7.3 Second generation transceiver on semi-insulating substrate

The transceiver is designed to be flip-chip bonded with the electrical amplifier and the electrical driver to avoid long bonding wires and to make the whole optical network unit (ONU) compact, therefore a new layout with ground-signal-ground (GSG) design is required. The mask layout of the second generation transceiver is shown in Fig. 7.16. Similar to the first generation transceiver, it consists of a wavelength duplexer, a RSOA integrated with a MMI loop mirror and a photodetector. The wavelength duplexer is thermally tunable to cover all the wavelength pairs in the headend station. The device is fabricated on an active-passive layer stack on a semi-insulating InP substrate, as shown in Fig. 5.3. The RSOA and the photodetector based on the same layer stack have achieved a bandwidth of 1.25 Gbit/s (Chapter 4) and 40 GHz (Chapter 5) respectively.

In the first generation integrated transceiver, the distance between the RSOA and the photodetector is only 125 μm, and since there is large difference in the signal levels between the RSOA (mA level) and the photodetector (μA level), the photodetector sees a large amount of additional noise introduced by biasing and modulating the RSOA, which prevents the photodetector operating simultaneously with the RSOA modulator. In the second generation transceiver, the photodetector and the SOA are separated with a distance of 4.5 mm to reduce the crosstalk level.

In order to minimize the electrical conductivity through the p-layer between the SOA and the photodetector, the conductive p-InP layer was removed from the interconnect waveguide between them by reactive ion etching, which is shown as “isolation waveguide” in Fig. 7.16. The total length of the “isolation waveguide” is 2.3 mm.

Furthermore, an area between the SOA and the photodetector was deeply etched into the semi-insulating substrate to reduce the area of the shared common N-InP connecting the SOA and the PD, and thus to increase the resistance between the SOA and the photodetector. This area is shown as the “substrate etched area” in Fig. 7.16. The substrate etched areas under the RSOA and the PD are meant to reduce the RF attenuation.

The design parameters for the constituent components are described in section 7.3.1. In section 7.3.2, the measured bandwidths of the RSOA and the photodetector are given. Detailed measurements and analysis on the additional crosstalk in the photodetector are presented in section 7.3.3 and then we discuss the results.

7.3.1 Design parameters

The wavelength duplexer has been designed with 500 GHz channel spacing and can be tuned thermally by injecting current through one of the electrodes on the MZI-arms. The metal electrode is 650 μm long and 400 nm thick so that the generated heat is enough to shift the phase of 2π at low injection current. The 3 dB MMI is deeply etched, 12 μm wide and 203 μm long.

The fiber access facet is 3.5 μm wide, and angled with 7° to reduce the facet reflectivity. A mode filter is inserted to filter the first-order modes. The SOA modulator is designed as a loop RSOA, which is described in detail in Chapter 4. The photodetector is shallowly etched for a lower dark current. It is 2 μm wide and 80 μm long for more than 90% internal quantum efficiency.

The fabrication procedures for this circuit has been described in Chapter 6. A photo of the fabricated chip is shown in Fig. 7.16 (bottom).

7.3.2 Modulation response of RSOA and photodetector

Due to the sidewall roughness caused by the five-step RIE etching (see Chapter 6) and p-dopant diffusion into the waveguide layer, the waveguide losses of this chip are high, but the wavelength duplexer, the RSOA modulator and the photodetector worked well. The ASE spectra measured at the angled waveguides at two different currents are shown in Fig. 7.17, which shows that the channel spacing between the upstream and the downstream is 500 GHz, matching the designed value. The isolation level of the wavelength duplexer is about 8 dB. The isolation level is poor, compared with the previous devices (~15 dB) introduced in Chapter 2. We believe that this is mainly due to the reduction of the MMI width during the mask fabrication (−200 nm) out of our expectation, and during the chip fabrication (~−80 nm).

The measured waveguide loss of this transceiver is high, up to 15 dB/cm for a 2 μm wide shallowly etched waveguide and 19 dB/cm for a 1.5 μm wide deeply etched waveguide, while a typical loss is around 4 dB/cm for a 2 μm wide shallowly etched waveguide and 7 dB/cm for a 1.5 μm deeply etched waveguide in the COBRA research institute. The excess loss the wavelength duplexer is up to 13 dB. These loss are very high, mainly result from the

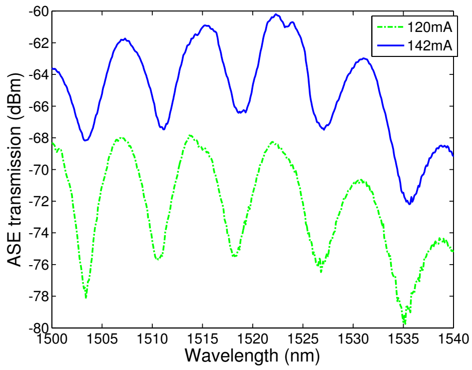

Figure 7.17: The measured ASE spectra of the second generation integrated transceiver at different injection currents.

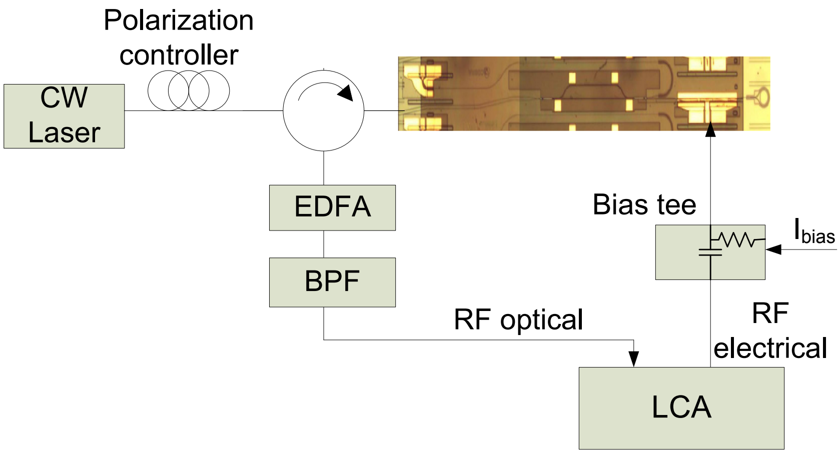

Figure 7.18: Measurement setup for the small signal response of the integrated transceiver.

following three aspects: 1) roughness at the interfaces between the semiconductor layers during the second and third growth; 2) reduced thickness of the buffer cladding layer from 200 nm to 130 nm which introduces higher free carrier absorption loss; 3) 5-step-etching procedure which caused extra surface and sidewall roughness due to the extra lithography and etching in RIE.

On-wafer S-parameter measurements of the RSOA are performed in the range of 10 MHz to 3 GHz with a lightwave component analyzer N4374B and a 50 GHz RF-probe, shown in Fig. 7.18(left). We couple 5 dBm optical power to compensate the high insertion loss of the wavelength duplexer. The fiber-chip coupling loss is estimated about 6 dB, thus the optical

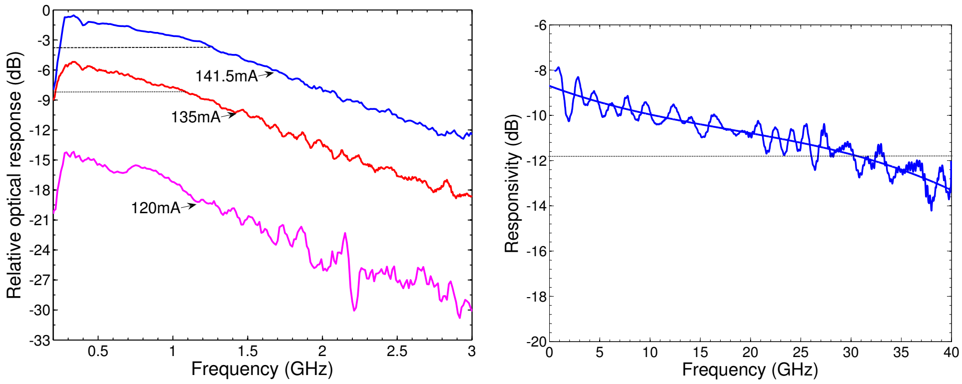

Figure 7.19: Small signal modulation results of the transceiver at different current (*left*) and the measured bandwidth and a cubic polynomial fitting curve of the 80 μm long shallowly etched photodetector (*right*) .

power at the SOA is estimated to be about −21 dBm. After the light is amplified and modulated, and reflected by the loop mirror and coupled back into the fiber, it is further amplified by an EDFA, and filtered by a bandpass filter. The measured small signal frequency response is shown in Fig. 7.19, from which we can see that the modulation bandwidth is about 1.25 GHz when $I_{\text{bias}} = 141.5$ mA. Due to high loss, the large signal modulation of the RSOA could not be carried out.

The "isolation waveguide" in Fig. 7.16 suffers even higher propagation loss because of maskless RIE etching (see Chapter 6) during fabrication. In order to characterize the bandwidth of the integrated photodetector, we cleaved the sample and measured the bandwidth of the photodetector individually with the measurement setup shown in Fig. 5.8. The shallowly etched 80 μm long photodetector achieved a bandwidth of 30 GHz at a reverse bias voltage of −6.7 V, as shown in Fig. 7.19(right). The external responsivity of the photodetector is 0.36 A/W (93% internal quantum efficiency) at 10 MHz and 0.26 A/W (65% internal quantum efficiency) at 30 GHz.

7.3.3 Noise of the photodetector due to biasing and modulating the SOA

The sensitivity of a photodetector is determined by its noise level. Besides the inherent dark current noise of the photodetector, several other factors increase the noise level of the photodetector when the RSOA is forwardly biased and modulated:

(A) optical signal detected by the photodetector due to reflection in the integrated circuit

(B) unguided optical signal propagating through the substrate detected by the photodetector

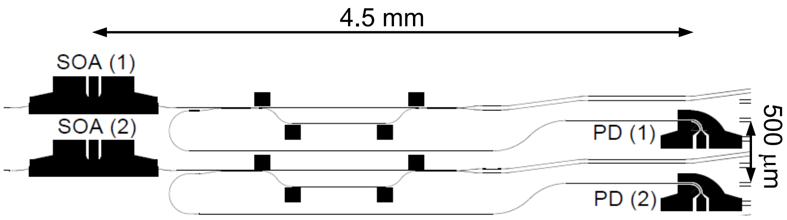

Figure 7.20: The devices used to investigate the noise levels due to biasing and modulating the RSOA.

(C) electrical connection due to non-perfect grounding of the N-InP layer which is shared by both the SOA and the PD.

In the next sections, we will experimentally investigate the contributions of the above crosstalk sources. The devices used to characterize the crosstalk levels are shown in Fig. 7.20, in which two integrated transceivers are involved, and numbered as (1) and (2). SOA (1) is biased with a forward injection current and has a cleaved facet at the left side for measuring the optical output power. The SOAs are 750 μm long, and the photodetectors (PDs) are 100 μm long. The distance between the SOA and the photodetector is 4.5 mm, and the spacing between the SOAs or PDs is 500 μm, as shown in Fig. 7.20.

In the next section, the detailed measurement procedures are explained.

Characterization of the noise sources

We start with the measurement of the resistance between the ground of the SOA (1) and the ground of PD (1), and between the p-contact of the SOA (1) and the p-contact of the PD (1), and they are 120 Ω and 2 MΩ respectively.

In order to distinguish crosstalk source (A) from the crosstalk source (C), we measure the current flowing through the PD (1) and the PD (2) where PD (1) is connected with SOA (1) through the waveguides. Both photodetectors are reversely biased at −3 V. The output ASE light intensity is collected at the left cleaved facet through a lensed fiber while scanning the electrical current on the SOA (1). The measured results are shown in Fig. 7.21. From the results, we can see that

- the current difference between PD (1) and PD (2) is negligible, which means that almost no guided light is detected by the PD (1), therefore crosstalk source (A) is negligible in this case because of the high waveguide propagation loss.
- the current of the PDs increases almost linearly with the injection current, while the light intensity of the SOA (1) shows a different trend, which proves that the current on the photodetectors results mostly from the electrical connection. Furthermore, since PD (2) shares only the N-InP layer with the SOA (1), we believe that the electrical connection is through the common N-InP layer (crosstalk source (C)). The influence of the unguided light is negligible when the SOA and the PD are far apart.

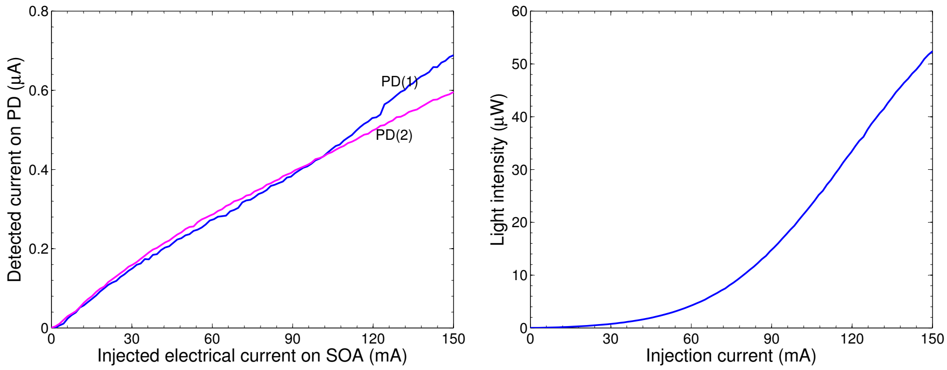

Figure 7.21: The measured current flowing through the photodetectors as a function of the injected current through the SOA (*left*). The collected output light intensity as a function of the injected current through the SOA (*right*).

Based on the above measured results, we can conclude that the non-perfect grounding on the N-InP (crosstalk source (C)) contributes most crosstalk.

When the loss of the transceiver is low, and the RSOA offers high signal gain, the noise due to the reflection of the guided modulated light should be taken into account. The optical crosstalk will be analyzed later in this section.

Until now, all the measurements are DC measurements. In reality, the RSOA is modulated with a RF signal, therefore in the next section the RF crosstalk between the SOA and the photodetector will be experimentally investigated.

RF noise

The RF noise comes from two parts, the modulated optical signal and the electrical RF driving signal. When the RSOA is modulated, both the signal and ASE will be modulated and amplified, which can be detected by the photodetector through the substrate and through the interconnect waveguide via residual reflections. Due to high waveguide loss, the optical crosstalk is not possible to be quantified through this measurement.

The electrical RF driving signal of the RSOA can have influence on the photodetector through the non-perfect N-InP ground shared by the SOA and the PD, as analyzed in the former section. Moreover, this RF driving signal can also transmit through other paths in the semiconductor material and through the air.

In order to quantify the crosstalk level due to the RF driving signal on the RSOA, we use a network analyzer and two RF probes to measure the electrical RF crosstalk (S_{21}), and the measurement setup is shown in Fig. 7.22. Probe 1 is fixed at SOA (1) which is forwardly biased with 120 mA electrical current, and probe 2 moves to three different locations. The reverse bias voltage on the PD (1), PD (2) or SOA (2) is added through a bias tee. The measured S_{21} parameter is shown in Fig. 7.23. The results show that the crosstalk level of PD (1)

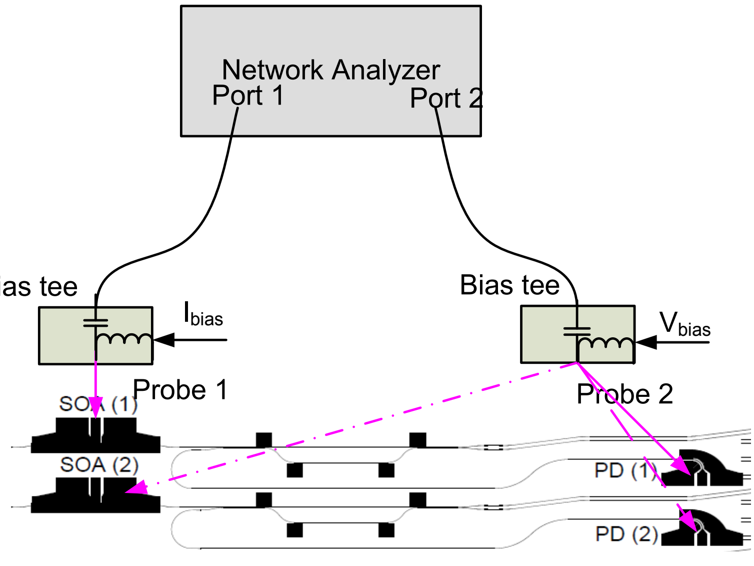

Figure 7.22: The measurement setup used to measure the RF crosstalk between the SOA and the PD.

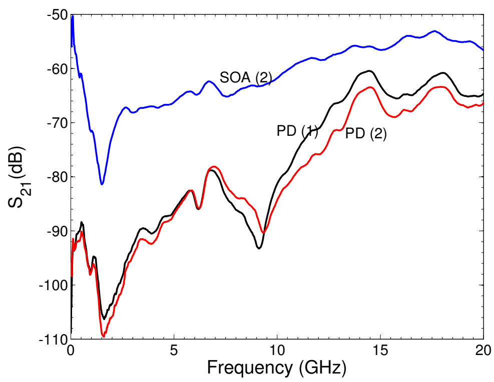

Figure 7.23: Total RF Crosstalk as a function of the frequency between the SOA and the photodetectors at different locations. SOA(2) in Fig. 7.20 works as a photodetector here under reverse bias voltage.

and PD (2) are almost identical. Since PD (2) shares only the N-InP with the SOA (1), the result proves that the RF crosstalk comes mostly through the common N-InP layer or through air. When the SOA and the PD are located closer to each other, the crosstalk level increases as expected.

Due to the limitation in the modulation bandwidth of the SOA, the measured RF crosstalk results mostly from the electrical crosstalk when the frequency is higher than 2 GHz. Below 2 GHz, both electrical and optical RF crosstalk contribute to the crosstalk on the PD. The measured S_{21} is around −90 dB and −70 dB at 3 GHz for PD (1 and 2) and SOA (2) used as a photodetector respectively.

In order to convert S_{21} to the crosstalk current flowing through the photodetector, the following equation is used to calculate the noise current on the photodetector due to RSOA electrical driving signal

$$\Delta I_{PD} = \Delta I_{SOA} \cdot 10^{S_{21}[\mathrm{dB}]/20} \tag{7.1}$$

in which ΔI_{SOA} is the modulation amplitude on the SOA , ΔI_{PD} is the measured modulation amplitude of the current on the photodetector due to the RF crosstalk, and S_{21} is the measured S-parameter.

Assuming that the modulation amplitude of the SOA is 40 mA (2 V peak-peak voltage over 50 Ω impedance), the current on the photodetector due to RF crosstalk $S_{21} = -90$ dB will be 1.26 μA for a distance of 4.5 mm.

To obtain an error free detection which means the quality factor Q should be at least 6. The quality factor Q is determined by the signal level S and the noise level N [160]

$$Q = \frac{\sqrt{S_1} - \sqrt{S_0}}{\sqrt{N_1} + \sqrt{N_0}} \tag{7.2}$$

in which S_1 and S_0 are the signal at 1 and 0 level respectively, and N_1 and N_0 are the noise power at 1 and 0 level respectively.

When the quantum efficiency of the photodetector is 100%, for an amplitude modulated signal of average power P_{ave}, a 50-percent duty cycle and an extinction ratio r, the photocurrent equivalents of the input powers for S_1 and S_0 are [160] :

$$\sqrt{S_1} = \frac{P_{ave} \cdot e \cdot 2 \cdot r}{h\nu \cdot (r+1)} \tag{7.3}$$

$$\sqrt{S_0} = \frac{P_{ave} \cdot e \cdot 2}{h\nu \cdot (r+1)} \tag{7.4}$$

Assuming that $\sqrt{N_0}$ is 0, and substituting $\sqrt{N_1} = 1.26\,\mu$A, $Q = 6$, equation (7.3) and (7.4) into equation (7.2), we find the $P_{ave} = 3.73\,\mu$W (−24.3 dBm) before the photodetector when the extinction ratio of the signal is higher than 10. The lower the extinction ratio of the signal is, the higher the signal power is required to achieve error free operation. If adding an additional loss of the tunable wavelength duplexer (2 dB) and the fiber chip coupling (4 dB), the optical power for error free operation with −90 dB RF crosstalk should be at least −18.3 dBm before the transceiver, which is a critical power requirement for the access network.

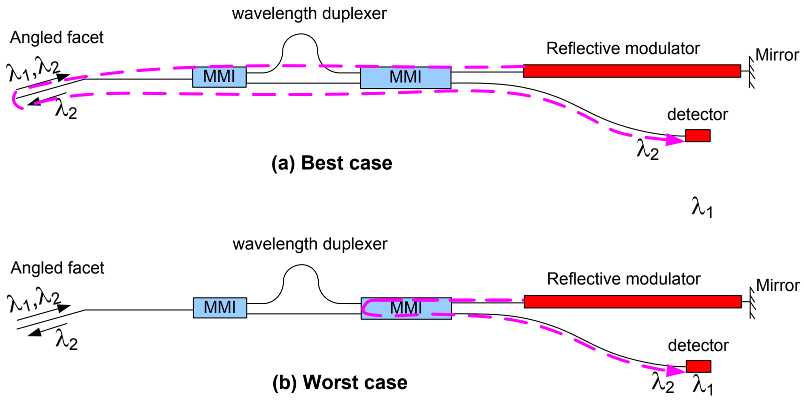

Figure 7.24: Two cases of optical reflection routes indicated with the dashed lines in the integrated transceiver.

When taking all the crosstalk contributions on the photodetector into account, the electrical RF crosstalk introduced by modulating the RSOA should be below −90 dB to relax the power requirement before the transceiver based on the above measurements and calculation.

Optical crosstalk due to reflections in the transceiver

The crosstalk due to the reflections in the transceiver can be significant in view of the large disparity between the upstream and downstream signal levels. In this section, we will analyze the optical crosstalk level due to the reflections. Two cases of optical reflection routes have been indicated in Fig. 7.24, and referred to as the best case and the worst case in the following analysis.

Assumption:

- A modulated upstream optical signal with a large optical power of 0 dBm at the facet is reflected back;
- −25 dBm downstream signal before the photodetector;
- 100% quantum efficiency (~1.24 A/W) of the photodetector.

Cases:

- Best case: there are no residual reflections inside the transceiver, except the facet reflection. The facet was angled with 7° and AR coated with a reflectivity of about 10^{-4}. The isolation level of the duplexer is at least 15 dB. Combining these two values, the return loss due to the facet reflectivity is about −55 dB.

Therefore, the reflected back upstream signal due to the facet is −55 dBm reaching the photodetector. Comparing with −25 dBm downstream signal (worst case), it is 30 dB below the signal level, sufficient for a good signal noise ratio.

By transferring −55 dB guided optical crosstalk due to the facet reflectivity into the current crosstalk on the photodetector, it is corresponding to −160 dB ($20 \times \log(10^{-5.5-3} \times 1.24)$), which is also much lower than the measured RF electrical crosstalk (−90 dB).

- Worst case: However, in practice, there are residual reflections in the transceiver. So the reflectivity can possibly go up to one order higher (10^{-3}). Furthermore, the worst case is that the reflected back upstream signal doesn't pass the whole wavelength duplexer, for example the reflection from a non-optimized MMI, as shown in Fig. 7.24. Taking all these worst factors into the consideration, the return loss is −33 dB (another 3 dB comes from the 3 dB MMI near to the photodetector and the SOA). Comparing with −25 dBm downstream signal, it starts to be comparable and problematic. Even though, −33 dB optical crosstalk is corresponding to −124 dB electrical crosstalk on the photodetector, which is still lower than the measured RF electrical crosstalk.

Based on reflection analysis shown in Fig. 7.7, the worst situation rarely happened if some measures were taken, for example the MMIs are designed with angled corners, the mode filter is integrated, and adiabatic waveguide bends are used to remove the waveguide offset.

On the other hand, the higher power the upstream signal has, the more critical the requirement on the residual reflections is, and the more problematic it becomes.

Conclusion on the crosstalk

The optical crosstalk is problematic when the residual reflection in the transceiver is high, especially when the upstream optical signal has high power. If the reflected upstream signal passes the wavelength duplexer, the residual reflectivity can be relaxed to 10^{-3} to achieve a sufficiently good signal noise ratio (>20 dB). Otherwise, the residual reflectivity has to be controlled below 10^{-4}. But comparing the optical crosstalk with the RF electrical crosstalk due to the common ground, the RF electrical crosstalk is more severe, and it is also very difficult to suppress it sufficiently.

Possible solutions to suppress the noise

Besides separating the SOA and the PD as far as possible, a solution can be considered to improve the performance of the transceiver:

- Improve the sensitivity of the photodetector by integrating an SOA before the photodetector. In [16, 160], it is shown that the sensitivity of the photodetector can be enhanced 7 dB, and it increases to 13 dB when an optical bandpass filter with 1.6 nm bandwidth is added between the SOA and the photodetector. In our application, the enhancement in the sensitivity of the photodetector can be achieved by integrating an SOA before the photodetector.

7.3.4 Conclusion

An integrated transceiver based on a semi-insulating substrate has been presented to improve the bandwidth of the photodetector and reduce the noise on the photodetector caused by the SOA. The results have shown that the bandwidth of the SOA is 1.25 GHz when biased with 140 mA current, and the shallowly etched photodetector obtains 30 GHz bandwidth at a reverse bias voltage of −6.7 V.

A series of measurements have been performed to investigate the crosstalks on the photodetector due to biasing and modulating the SOA. Both the DC and RF crosstalk are severe when the distance between the SOA and the PD is short . The noise is reduced from −70 dB to −90 dB by increasing the distance from 500 μm to 4.5 mm. A solution has been proposed to suppress the noise, by inserting an SOA preamplifier before the photodetector.

7.4 10Gbit/s integrated reflective transceiver

From the measurement results on the photodetector, 10 Gbit/s downstream data can be easily achieved with current design. However, the upstream bandwidth is limited to below 5 GHz due to the carrier life time of the RSOA modulator. In order to reach 10 Gbit/s colorless upstream operation, a new component is needed.

In this section, a novel transceiver which employs a reflective phase modulator to transmit the upstream data will be presented, aiming for 10 Gbit/s operation. In the following section 7.4.1, we will present the measurement results on a MZI phase modulator which is realized on the same layer stack as the integrated phase modulator in the transceiver. In section 7.4.2, we will describe the design of the first 10 Gbit/s transceiver which integrates a thermally tunable wavelength duplexer, a SOA, a reflective Michelson phase modulator and a photodetector.

7.4.1 MZI phase modulator on an N-InP substrate

Before designing an integrated transceiver with a phase modulator, we measured the bandwidth of a tunable wavelength duplexer, the same device presented in Chapter 2. It has the same layer stack as the passive part of the material for the active-passive integration, and it can operate as a phase modulator once we apply the RF voltage on one of the electrodes. The tunable duplexer is based on an N-InP substrate. In order to carry out the on-wafer RF measurement, we glued this duplexer on a RF submount (see Chapter 6) and bonded the p-metal of the duplexer to the bonding pads of the RF submount through gold bonding wires, as shown in Fig. 7.25. The bonding wires are about 2.3 mm long.

To see the system performance, we modulate this device with a $2^7 - 1$ pseudo random binary sequence (PRBS). The measurement setup is shown in Fig. 7.26. The CW laser is a tunable laser. The RF voltage was added on one side of the electrode through the RF submount, and the other side of the electrode was terminated with a 50 Ω load through the RF submount as well. The reverse bias voltage on the duplexer was set at −6.6 V. The optimum driving voltage should be equal to the switching voltage V_π to achieve maximum extinction

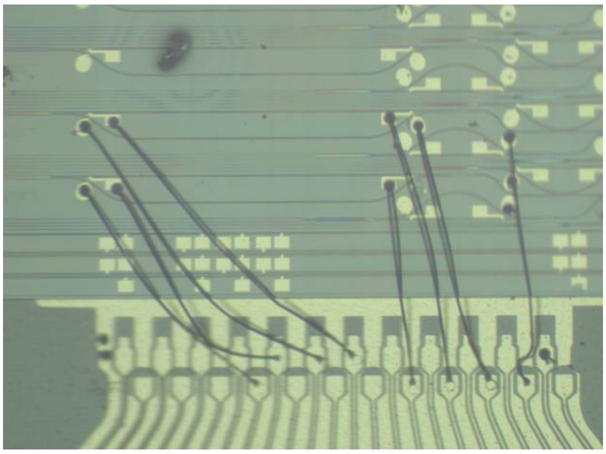

Figure 7.25: Tunable wavelength duplexer is bonded on a RF submount and operates as a phase modulator.

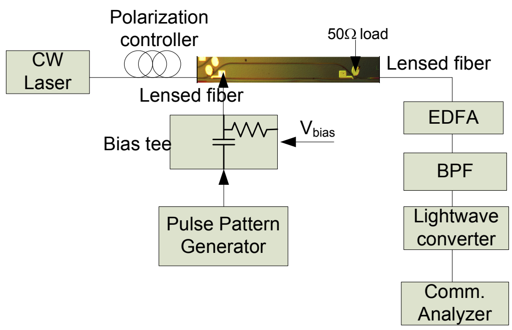

Figure 7.26: Measurement setup for modulating the tunable wavelength duplexer.

ratio when the bias voltage is at quarter phase point. For the MZI phase modulator tested here, the switching voltage is about 2.5 V near to −5 V bias voltage, and its extinction ratio under the static measurement (Chapter 2) is about 14 dB. However, the maximum peak-peak driving voltage of the pulse pattern generator is 2 V, therefore the extinction ratio did not reach its maximum value.

The obtained eye diagrams at different data rates are shown in Fig. 7.27. All the eyes are open. Below 8 Gbit/s, the quality factor (Q factor) is higher than 6 (required for error free operation), and the extinction ratio is about 6 dB. Besides, it is polarization insensitive (see Chapter 2).

The modulation bandwidth is mainly limited by the long bonding wires and the thin metal electrode (400 nm gold) on the duplexer. Thin gold layer has a higher RF attenua-

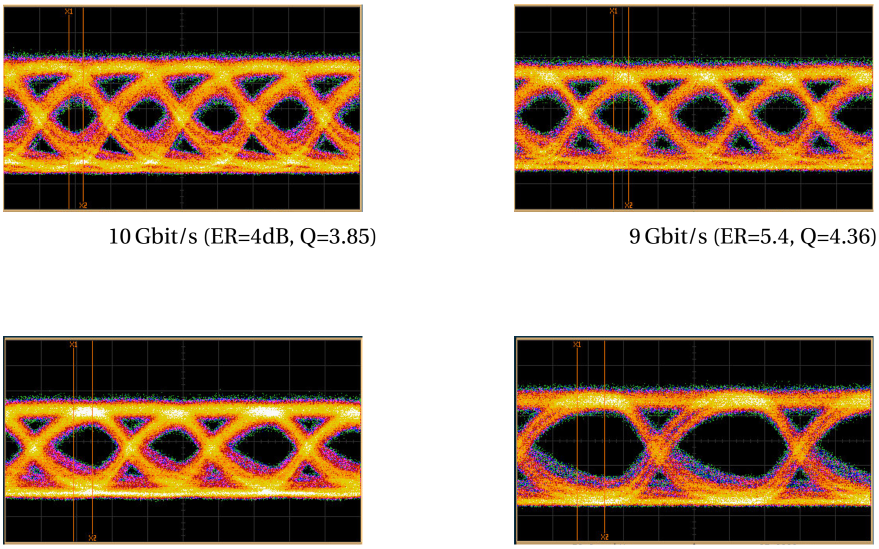

10 Gbit/s (ER=4dB, Q=3.85)

9 Gbit/s (ER=5.4, Q=4.36)

8 Gbit/s (ER=5.8,Q=6)

5 Gbit/s (ER=6.7, Q=7.45)

Figure 7.27: Eye diagrams at different data rates when the MZ-wavelength duplexer operated at $\lambda = 1545.75$ nm and was biased at -6.6 V.

tion which results in a smaller bandwidth and a smaller modulation extinction ratio. The frequency response can be improved by using a Coplanar Waveguide (CPW) design which reduces the RF attenuation, provides an impedance match and avoids the long bonding wires.

7.4.2 10Gbit/s transceiver integrated with a reflective Michelson PHM

The MZI-phase modulator on the same passive layer stack has achieved close to a modulation bandwidth of 10 Gbit/s with a long bonding wire, which motivated the design of a transceiver aiming for 10 Gbit/s operation by integrating a reflective phase modulator.

The mask layout and a photo of the fabricated device are shown in Fig. 7.28. It consists of a thermally tunable wavelength duplexer, a SOA, a photodetector and a reflective Michelson interferometer integrated with two MMI-loop mirrors.

The design of the wavelength duplexer, the SOA and the photodetector are the same as the one presented in section 7.3. The SOA and the PD are located close to each other due to the predefined location of the SOA and the PD on the active-passive material.

The reflective phase modulator is a Michelson interferometer, which is composed of a 2×2 3 dB MMI splitter, two branches with equal lengths and two identical MMI loop mirrors.

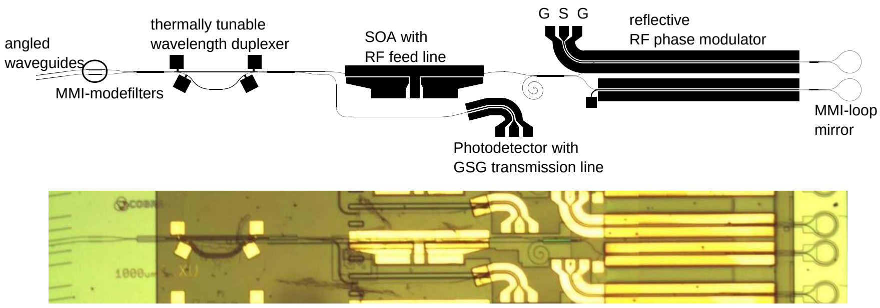

Figure 7.28: Mask layout of a transceiver integrated with a reflective MZI phase modulator.

When the phase on one of the two branches is changed, the output power of the reflected light will change due to the interference. Since the light travels forward and backward in both branches, the length of the phase shifter can be halved to achieve the same phase change at the same bias voltage. The phase shifting arms are deeply etched and 1.5 μm wide in order to reduce the microwave attenuation [149], and the length of the phase shifter is 1.4 mm. The Michelson phase modulator has a RF and a DC arm. The RF electrode has 50 Ω probe pads accommodated for high frequency probes. From the probe pads, a 1.5 μm thick CPW is tapered to a 50Ω line with a signal width of 6.8 μm, a gap of 5.6 μm and a ground line width of 50 μm. In principle, the reflected light (within the same modulation bit) can be modulated again by the reflected RF signal to increase the modulation efficiency.

For the fabrication procedure of this transceiver we refer to Chapter 6.

Although this device suffered very high loss due to the roughness at the interface between the material semiconductor layers, sidewall roughness and the p-dopant diffusion into the waveguide layer which caused high free carrier absorption, we believe that the present design is very promising for use in the user access network. Due to time constraints, a rerun of this device was not possible.

7.4.3 Conclusion and discussion

We have demonstrated an 8 Gbit/s phase modulator which has the same layer stack as the passive part of the active-passive integration material. We have designed and fabricated a transceiver which integrated a reflective Michelson interferometer aiming for 10 Gbit/s operation for the upstream data. However, due to excessive Zn-diffusion and sidewall roughness, the operation of the integrated transceiver could not be demonstrated.

7.5 Conclusion

Three generations of integrated transceivers have been designed and fabricated. The first generation transceiver achieves 1 Gbit/s for the upstream operation and 14 GHz bandwidth for the downstream. The small signal measurement has shown that the second generation transceiver on a SI-substrate achieves 1.25 GHz bandwidth for the upstream data and 30 GHz bandwidth for the downstream. However, due to high propagation loss, the operation of the second integrated transceiver could not be demonstrated.

In addition, the crosstalks on the photodetector caused by biasing and modulating the SOA were investigated, and an option for the crosstalk suppression was discussed.

A third generation transceiver has been designed and fabricated which integrates a thermally tunable wavelength duplexer, a SOA, a photodetector, two MMI-loop mirrors and a reflective Michelson phase modulator, aiming for 10 Gbit/s operation in the user access network.

Chapter 8

Conclusions and outlook

This chapter will first summarize the main results of the thesis, and then draw conclusions corresponding to the goals and achieved results. In the end the possible measures for further improvement and development are discussed.

8.1 Main results

In this thesis, we have studied different building blocks of photonic integrated circuits, namely the tunable wavelength duplexer, the MMI-loop mirror and the MMI reflector, the reflective SOA, the photodetector and the phase modulator. With these building blocks, we have realized several monolithic integrated colorless reflective transceivers for the user access network.

The reflective transceiver is composed of three basic components: a wavelength duplexer to separate the upstream and the downstream channels, a modulator to carry the upstream data, and a photodetector to detect the downstream signal. The main results are summarized below:

- A thorough analysis of the phase shifter has been carried out to investigate the influence of the layer thickness and the doping level on the waveguide transmission loss, switching efficiency and polarization dependence. Based on the simulation and the measurement results, we have obtained a polarization insensitive phase shifter layer stack with a high switching efficiency of $36°/(\mathrm{V}\cdot\mathrm{mm})$, and the transmission loss is 4 dB/cm for a 2 μm wide shallowly etched waveguide. This layer stack is used to realize a tunable wavelength duplexer which has achieved polarization insensitive transmission. Polarization insensitive tuning was achieved based on both electro-optical and thermal effects. In order to cover the whole wavelength operation range (2π phase shift), it needs about 6.2 V (2.1 mm long phase shifter) under EO effects, and 80 mW electrical power when employing thermal effect to tune the wavelength duplexer. The on-chip loss of the tunable duplexer is 5 dB, mainly due to the overlap between the optical field and InGaAs and metal contact layer. Furthermore, a switching time as low as 0.14 ns was measured on this tunable duplexer.

- To enhance the flexibility of photonic integrated circuits, we have investigated two components for on-chip reflection of light: the MMI loop mirror and the MMI reflector. Both components have very weak wavelength and polarization dependence. The MMI loop mirror has obtained a reflectivity of 65% ± 10%. The MMI reflector is a novel component, which has achieved up to 78% ± 10% reflectivity. The MMI loop mirror and the MMI reflector can be easily integrated together with other passive and active components, and provides a flexible way to achieve on-chip reflection of light in photonic integrated circuits.
- A reflective semiconductor optical amplifier (RSOA) is investigated as a colorless modulator to carry the upstream data. The realized RSOA consists of an SOA and an MMI loop mirror, and has achieved a modulation rate of 1.25 Gbit/s at 81 mA bias current with −14 dBm optical input power before the chip. By adjusting the input optical power and the injection current, the device can obtain a high Q factor and an extinction ratio up to 7.3 dB. This device has proved the possibility of colorless operation at 1 Gbit/s in the wavelength range from 1530 nm to 1560 nm.
- In monolithic integration of an SOA and a photodetector, the common active layer stack is optimized for the SOA operation. By reversely biasing the SOA layer stack, we have proved that a high performance PD (up to 40 GHz) can be made in an SOA layer stack. a fast photodetector with a bandwidth of up to 40 GHz. Furthermore, the series resistance of the photodetector has been analyzed and the options to reduce the resistance are given. In addition, the polarization dependence has been investigated for photodetectors in a SOA layer stack, and the results show that the polarization dependent responsivity is less than 0.27 dB, and it can operate within the whole operation wavelength range from 1530 nm to 1560 nm.
- When the SOA and the photodetector are integrated in a single device, besides the inherent and background noise, the photodetector experiences a large amount of crosstalk introduced by biasing and modulating the SOA. We experimentally investigated the additional crosstalks on the photodetector, and the results have shown that the large amount of crosstalk comes from the electrical connection through the common N-InP layer and the electrical RF crosstalk if modulating the SOA. The optical crosstalk between the SOA and the photodetector due to residual reflections has been analyzed. The optical crosstalk becomes critical when the upstream signal has high optical power after on-chip amplification and there exists residual reflections inside the chip. An SOA can be integrated as a pre-amplifier before the photodetector to improve the sensitivity of the photodetector.
- Three generations of reflective transceivers have been designed and fabricated. The first generation transceiver consists of a wavelength duplexer, a RSOA and a photodetector. The measurement results show that the integrated RSOA achieves 1 Gbit/s op-

eration and the integrated photodetector reaches 14 GHz bandwidth for the downstream data. The second generation transceiver is based on a semi-insulating InP substrate to facilitate flip-chip bonding and improve the bandwidth of the photodetector. In this device, the SOA achieves 1.25 GHz bandwidth, and the photodetector obtains 30 GHz bandwidth. The third generation transceiver is designed and fabricated, aiming for 10 Gbit/s operation. It integrates a thermally tunable wavelength duplexer, a SOA, a photodetector, two MMI-loop mirrors and a reflective Michelson phase modulator. However, the full functionality of the 10 Gbit/s transceiver was not achieved due to high waveguide loss. Possible solutions to these problems have been identified.

- A fabrication technology was adapted for the integration of the various components discussed above into a single circuit on a semi-insulating substrate.

8.2 Conclusions and outlook

The individual components of the transceiver can be demonstrated in the system by optimizing the geometry or fabrication technology. However, the realization of an integrated transceiver based on an SOA modulator and a sensitive photodetector on the available material system (active passive butt-joint) is difficult. The main problems are the electrical crosstalk and to a lesser extent, the optical crosstalk, besides the fabrication tolerance.

A new device layout has been proposed in the thesis by integrating a phase modulator to improve the bandwidth. The sensitivity of the photodetector can be further improved by integrating an extra SOA as a pre-amplifier.

References

[1] M. Kuznetsov, N. M. Froberg, S. R. Henion, H. G. Rao, J. Korn, K. A. Rauschenbach, E. H. Modiano, and vincent W.S. Chan, "A next generation optical regional access network," *IEEE Comm. Magazine*, vol. 38, pp. 66–72, Jan. 2000.

[2] *Global IP traffic forecast and methodology, 2006-2011.* Cisco 2007 white paper.

[3] *Minnesota Internet Traffic Studies.* http://www.dtc.umn.edu/mints/home.php.

[4] T. Koonen, "Fiber to the home/fiber to the premises: What, where, and when?," *Proceedings of the IEEE*, vol. 94, no. 5, pp. 911–934, 2006.

[5] D. Gutierrez, W. Shaw, F. An, Y. Hsueh, M. Rogge, G. Wong, L. G. Kazovsky, and K. S. Kim, "Next generation optical access networks," in *3rd International conference on Broadband communications, networks and systems, 2006*, pp. 1–10, Oct. 1–5 2006.

[6] K. S. Kim, "On the evolution of PON-based FTTH solutions," *Information Sciences*, vol. 149, Jan. 2003.

[7] N. Frigo, P. Iannone, and K. Reichmann, "A view of fiber to the home economics," *IEEE Comm. Magazine*, vol. 42, pp. S16–S23, Aug. 2004.

[8] H. Shinohara, "Broadband access in Japan: rapidly growing FTTH market," *IEEE Comm. Magazine*, vol. 43, pp. 72–78, Sept. 2005.

[9] PricewaterhouseCoopers, "Developing a generic approach for FTTH solutions using life cycle analysis methodology to determine the environmental benefits of FTTH deployments in the USA," in *Study report for FTTH Council*, pp. 1–30, October 2008.

[10] J. George, "Choosing the right FTTH technology to support current and future services," in *FTTH Council Quarterly Meeting*, pp. 1–34, Dec. 2008. Presentation slides.

[11] C. Park, *Broadband home network in Korea.* POFAC, Germany, 2006.

[12] *AON vs. PON - A comparison of two optical access network technologies and the different impact on operations.* KEYMILE 2008 white paper.

[13] A. Koonen and G. Khoe, "Flexible service delivery in access and local networks," in *Techn. Digest Optoelectr. and Comm. Conf. (OECC 2005)*, pp. 7A3–1, Seoul, Korea, July 2005.

[14] E. Klein, *Densely Integrated Microring-Resonator Based Components for Fiber-To-The-Home Applications.* PhD thesis, University of Twente, Twente, The Netherlands, 2007. ISBN 978-90-365-2495-7.

[15] J. Jin, D. Tian, J. Shi, and T. Li, “Fabrication and complete characterization of polarization insensitive 1310 nm InGaAsP-InP quantum well semiconductor optical amplifier,” *Semicond. Sci. Technol.*, vol. 19, pp. 120–126, 2004.

[16] M. Nikoufard, *Integrated Wavelength Division Multiplexing Receivers.* PhD thesis, TUE, Eindhoven, The Netherlands, 2008. ISBN 978-90-386-1814-2.

[17] P. Healey, P. Townsen, C. Ford, L. Johnston, P. Townley, I. Lealman, L. Rivers, S. Perrin, and R. Moore, “Spectral slicing WDM-PON using wavelength-seeded reflective SOAs,” *Electron. Lett.*, vol. 37, pp. 1181–1182, Sept. 2001.

[18] E. Wong, K. Lee, and T. Anderson, “Low-cost WDM passive optical network with directly-modulated self-seeding reflective SOA,” *Electron. Lett.*, vol. 42, Mar. 2006.

[19] H. D. Kim, S.-G. Kang, and C.-H. Lee, “A low-cost WDM source with an ASE injected Fabry-Perot semiconductor laser,” *IEEE Photon. Technol. Lett.*, vol. 12, pp. 1067–1069, Aug. 2000.

[20] D. J. Shin, Y. Keh, J. Kwon, E. Lee, J. Lee, M. Park, Y. Oh, S. Kim, I. Yun, H. Shin, D. Heo, J. Lee, H. SHin, H. Kim, S. Park, D. Jung, S. Hwang, Y. Oh, D. Jang, and C. Shim, “Low cost WDM-PON with colorless bidirectional transceivers,” *J. Lightwave Technol.*, vol. 24, pp. 158–164, Jan. 2006.

[21] H.-H. Lu, H.-L. Ma, Y.-W. Chuang, Y.-C. Chi, C.-W. Liao, and H.-C. Peng, “Employing injection-locked FabryšCPerot laser diodes to improve bidirectional WDMšCPON performances,” *Optics Commun.*, vol. 270, pp. 211–216, 2007.

[22] S.-J. Park, G.-Y. Kim, T. Park, E.-H. Choi, S.-H. Oh, Y. Baek, K.-R. Oh, Y.-J. Park, J.-U. Shin, and H.-K. Sung, “WDM-PON system based on the laser light injected reflective semiconductor optical amplifier,” in *Proc. 31th Eur. Conf. on Opt. Comm. (ECOC ’05)*, p. We3.3.6, Glasgow, Sept. 25–29 2005. Postdeadline Paper.

[23] J. Prat, C. Arellano, V. Polo, and C. Bock, “Optical network unit based on a bidirectional reflective semiconductor optical amplifier for fiber-to-the-home networks,” *IEEE Photon. Technol. Lett.*, vol. 17, pp. 250–252, Jan. 2005.

[24] A. Banerjee, Y. Park, F. Clarke, H. Song, S. Yang, G. Kramer, K. Kim, and B. Mukherjee, “Wavelength division multiplexed passive optical network (WDM-PON) technologies for broadband access: a review,” *J. Vac. Sci. Technol. B*, vol. 4, pp. 737–758, Nov. 2005.

[25] Z. Xu, Y. J. Wen, W.-D. Zhong, C.-J. Chae, X.-F. Cheng, Y. Wang, C. Lu, and J. Shankar, “High-speed WDM-PON using cw injection-locked Fabry-Perot laser diodes,” *Optics Express*, vol. 15, pp. 2953 – 2962, Mar. 2007.

[26] F. An, K. Kim, Y. Huseh, M. Rogge, W. Shaw, and L. Kazovsky, “Evolution, challenges and enabling technologies for future WDM-based optical access networks,” in *the 2nd Symposium on Photonics, Networking, and Computing*, Sept. 2003.

[27] W. Lee, M. Y. Park, S. H. Cho, J. Lee, C. Kim, G. Jeong, and B. W. Kim, “Bidirectional WDM-PON based on gain saturated reflective semiconductor optical amplifiers,” *IEEE Photon. Technol. Lett.*, vol. 17, pp. 2460–2462, Nov. 2005.

[28] Y. Inoue, T. Oguchi, Y. Hibino, S. Suzuki, M. Yanagisawa, K. Moriwake, and Y. Yamada, “Filter embedded wavelength division multiplexer for hybrid-integrated transceiver based on silica-based plc,” *Electron. Lett.*, vol. 32, pp. 847–848, Apr. 1996.

[29] H. Kimura, T. Yoshida, and K. Kumozaki, “Compact PLC-based optical transceiver module automatic tunable filter for multirate applications,” *Electron. Lett.*, vol. 39, pp. 1319–1321, Sept. 2003.

[30] M. Oguro, A. Goto, N. Kitamura, Y. Fukutomi, Y. Sakamoto, T. Masuta, and T. Tamura, "1.25 Gb/s bi-directional transceiver module using DFB-LD and PLC with spot-size conversion region," in *Proc. 52nd Electronic Components and Technology Conference 2002*, May 28–31 2002.

[31] T. Takeuchi, T. Sassaki, M. Hayashi, K. Hamamoto, K. Makita, K. Taguchi, and K. Komatsu, "A transceiver PIC for bidirectional optical communication fabricated by bandgap energy controlled selective MOVPE," *IEEE Photon. Technol. Lett.*, vol. 8, pp. 361–363, Mar. 1996.

[32] T. Koch, U. Koren, A. Gnauck, K. Reichmann, H. Kogelnik, G. Raybon, R. Gnall, M. Oron, M. Young, J. deMiguel, and B. Miller, "Simple in-line bidirectional 1.5μm/1.3 μm transceivers," in *IEEE Integrated Semiconductor Laser Conference, Davos*, pp. 166–167, Davos, Sept. 1990.

[33] R. Matz, J. Bauer, P. Clemens, G. Heise, H. Mahlein, W. Metzger, H. Michel, and G. Shulte-Roth, "Development of a photonic integrated transceiver chip for WDM transmission," *IEEE Photon. Technol. Lett.*, vol. 6, pp. 1327–1329, Nov. 1994.

[34] Y. Inoue, T. Oguchi, Y. Hibino, S. Suzuki, M. Yanagisawa, K. Moriwake, and Y. Yamada, "OEIC WDM transceiver modules for local access networks," *Electron. Lett.*, vol. 31, pp. 132–133, Jan. 1995.

[35] W. Metzger, J. Bauer, P. Clemens, G. Heise, M. Klein, H. Mahlein, R. Matz, H. Michel, and J. Rieger, "Photonic integrated transceiver for the access network," *Opt. and Quantum Electron.*, vol. 28, no. 1, pp. 51–56, 1996.

[36] H. Nakajima, A. Leroy, B. Pierre, P. Boulet, J. Charil, S. Grosmaire, A. Gloukhian, S. S. Y. Raffle, F. Mallecot, and F. Doukhan, "1.3μm/1.55μm in-line transceiver assembly with -27 dbm full duplexer sensitivity," *Electron. Lett.*, vol. 34, pp. 303–304, Feb. 1998.

[37] R. Kaiser, M. Hamacher, H. Heidrich, P. Albrecht, W. ebert, R. Gibis, H. Künzel, R. Löffler, S. Malchow, M. Möhrle, W. Rehbein, and H. Schroeter-Janßen, "Monolithically integrated transceivers on InP: The development of a generic integration concept and its technological challenges," in *Proc. IPRM98 conference*, pp. WA4–1 431–434, Tsukuba, Japan, May 11–15 1998.

[38] K.-S. Park, D.-K. Oh, H.-M. Kim, and K.-E. Pyun, "Compact photonic integrated circuit chip with low crosstalk for bidirectional transceivers," *Electron. Lett.*, vol. 34, pp. 79–80, Jan. 1998.

[39] M. Hamacher, R. Kaiser, H. Heidrich, P. ALbrecht, B. Borchert, K. Janiak, R. Loffler, S. Malchow, W. Rehbein, and H. Schroeter-Janssen, "Monolithic integration of lasers, photodiodes, waveguides and spot size converters on GaInAsP/InP for photonic IC applications," in *Techn. Digest Opt. Fiber Comm. (OFC '99), postdeadline papers*, pp. 21–24, San Diego, CA, USA, Feb. 1999.

[40] F. Mallecot, A. Leroy, A. Plais, C. Chaumont, M. Martineau, J. Jacquet, F. Doukhan, Y. Arnaudin, v. Tassin, J. Harari, D. Decoster, F. Laune, C. Tribouiller, and M. Josso, "Low cost PIC transceiver thermo optic modules fulfilling FSAN specifications," in *Techn. Digest Opt. Fiber Comm. (OFC '02)*, pp. 424–425, San Diego, California, USA, Mar. 17–22 2002.

[41] H. Terui, T. Kominato, K. Yoshino, F. Ichikawa, S. Hata, S. Sekine, M. Kobayashi, J. Yoshida, and K. Okada, "Optical module with a silica-based planar lightwave circuit for fiber optic subscriber system," *IEEE Photon. Technol. Lett.*, vol. 4, pp. 660–662, June 1992.

[42] T. Hashimoto, A. Kanda, R. Kasahara, I. Ogawa, Y. Shuto, M. Yanagisawa, A. Ohki, S. Mino, M. Ishii, Y. Suzuki, R. Nagase, and T. Kitagawa, "A bidirectional single fiber 1.25 Gbit/s optical transceiver module with SFP package using PLC," in *Electronic Components and Technology Conference (ECTC '03)*, vol. 53, pp. 279–283, May 2003.

[43] S. Moon, S. Han, J. Choi, S. Shin, M. Margalit, E. Avni, and G. Rogovsky, "Packaging for a FP-LD hybrid transceiver using filter integrated PLC platform with PD insertion trench," *Microwave and Optical Techn. Lett.*, vol. 48, pp. 489–491, Mar. 2006.

[44] P. Williams, P. Charles, I. Griffiths, N. Carr, J. Reid, N. Forbes, and E. Thom, "WDM transceiver OEICs for local access networks," *Electron. Lett.*, vol. 30, no. 8, pp. 1529–1530, 1994.

[45] N. Kitamura, "PLC based bi-directional optical module for access fiber network," in *Techn. Digest Opt. Fiber Comm. (OFC '07)*, pp. 195–197, Anaheim, California, USA, Mar. 25–29 2007.

[46] A. Z. et al., "Customer ONU: Cost and technology and standardization issues," in *Proc. Full Services Access Networks Conf., London, UK*, 1996.

[47] K.-Y. Kim, J. H. Song, J. Lee, S. Y. Kim, J. Cho, Y. S. Lee, D. Han, S. Jung, and Y. Oh, "Reduction of insertion loss of thin film filters embedded in PLC platforms," *IEEE Photon. Technol. Lett.*, vol. 17, pp. 1459–1461, July 2005.

[48] R. Nagarajan, C. Joyner, R. Schneider Jr., J. Bostak, T. Butrie, A. Dentai, V. Dominic, P. Evans, M. Kato, M. Kauffman, D. Lambert, S. Mathis, A. Mathur, R. Miles, M. Mitchell, M. Missey, S. Murthy, A. Nilsson, F. Peters, S. Pennypacker, J. Pleumeekers, R. Salvatore, R. Schlenker, R. Taylor, H.-S. Tsai, M. V. Leeuwen, J. Webjorn, M. Ziari, D. Perkins, J. Singh, S. Grubb, M. Reffle, D. Mehuys, F. Kish, and D. Welch, "Large-scale photonic integrated circuits," *IEEE J. Sel. Topics in Quantum Electron.*, vol. 11, pp. 50–65, Jan./Feb. 2005.

[49] R. Nagarajan, M. Kato, V. Dominic, S. Hurtt, A. Dentai, J. Pleumeekers, P. Evans, M. Missey, R. Muthiah, A. Chen, D. Lambert, P. Chavarkar, A. Mathur, J. Bäck, S. Murthy, R. Salvatore, H.-S. Tsai, D. Pavinski, C. Joyner, J. Rossi, R. Schneider, M. Ziari, M. Reffle, D. Mehuys, F. Kish, and D. Welch, "Multi-channel operation of a receiver photonic integrated circuit with an integrated semiconductor optical amplifier," in *Proc. 33rd Eur. Conf. on Opt. Comm. (ECOC '07)*, pp. 5.5.5 257–258, Berlin, Germany, Sep. 16–20 2007.

[50] R. Nagarajan, M. Kato, J. Pleumeekers, P. Evans, D. Lambert, A. Chen, V. Dominic, A. Mathur, P. Chavarkar, M. Missey, A. Dentai, S. Hurtt, J. Ba(e)ck, R. Muthiah, S. Murthy, R. Salvatore, S. Grubb, C. JOyner, J. Rossi, R. Schneider, M. Ziari, F. Kish, and D. Welch, "Single-chip 40-channel InP transmitter photonic integrated circuit capable of aggregate data rate of 1.6 Tbit/s," *Electron. Lett.*, vol. 42, June 2006.

[51] M. Kato, R. Nagarajan, J. Pleumeekers, P. Evans, A. Chen, A. Mathur, A. Dentai, S. Hurtt, D. Lambert, P. Chavarkar, M. Missey, J. Bäck, R. Muthiah, S. Murthy, R. Salvatore, C. Joyner, J. Rossi, R. Schneider, M. Ziari, F. Kish, and D. Welch, "40-channel transmitter and receiver photonic integrated circuits operating at per channel data rate 12.5 Gbit/s," *Electron. Lett.*, vol. 43, Apr. 2007.

[52] Y. Barbarin, X. Leijtens, E. Bente, J. Kooiman, and M. Smit, "Extremely small AWG demultiplexer fabricated on InP by using a double-etch process," in *Proc. IEEE/LEOS Symposium (Benelux Chapter)*, pp. 61–64, Enschede, The Netherlands, Nov. 2003.

[53] J. den Besten, M. Dessens, C. Herben, X. Leijtens, F. Groen, M. Leys, and M. Smit, "Low-loss, compact, and polarization independent PHASAR demultiplexer fabricated by using a double-etch process," *IEEE Photon. Technol. Lett.*, vol. 14, pp. 62–64, Jan. 2002.

[54] N. Yurt, K. Rausch, A. R. Kost, and N. Peyghambarian, "Design and fabrication of a broadband polarization and temperature insensitive arrayed waveguide grating on InP," *Optics Express*, vol. 13, pp. 5535 – 5541, July 2005.

[55] J. Mørk, M. L. Nielsen, and T. W. Berg, "The dynamics of semiconductor optical amplifiers. modeling and applications," *Optics & Photonics News*, vol. 14, pp. 42–48, July 2003.

[56] Z. Jia, J. Yu, G. Ellinas, and G.-K. Chang, "A novel full duplex wavelength reuse optical wireless architecture with directly modulated SOA as upstream colorless amplified modulator," in *Techn. Digest Opt. Fiber Comm. (OFC '07)*, pp. 1–3, Anaheim, California, USA, Mar. 25–29 2007.

[57] T. Ido, H. Sano, M. Suzuki, S. Tanaka, and H. Inoue, "High-speed MQW electroabsorption optical modulators integrated with low-loss waveguides," *IEEE Photon. Technol. Lett.*, vol. 7, pp. 170–172, Feb. 1995.

[58] K. Satzke, D. B. ans U. Cebulla, H. Haisch, D. Kaiser, E. Lach, K. Kühn, J. Weber, R. Weinmann, P. Wiedemann, and E. Zielinski, "Ultrahigh-bandwidth (42 GHz) polarisation-independent ridge waveguide electroabsorption modulator based on tensile strained InGaAsP MQW," *Electron. Lett.*, vol. 31, pp. 2030–2032, Nov. 1995.

[59] T. Ido, S. Tanaka, M. Suzuki, M. Koizumi, H. Sano, and H. Inoue, "Ultra-high-speed multiple-quantum-well electro-absorption optical modulators with integrated waveguides," *J. Lightwave Technol.*, vol. 14, pp. 2026–2034, Sept. 1996.

[60] J. Johnson, L.-P. Ketelsen, J. Grenko, S. Sputz, J. Vandenberg, M. Focht, D. Stampone, L. Peticolas, L. Smith, K. Glogovsky, G. Przybylek, S. Chu, J. Lentz, N. Tzafaras, L. Luther, T. Pernell, F. Walters, D. Romero, J. Freund, C. Reynolds, L. Gruezke, R. People, and M. Alam, "Monolithically integrated semiconductor optical amplifier and electroabsorption modulator with dual-waveguide spot-size converter input," *IEEE J. Sel. Topics in Quantum Electron.*, vol. 6, pp. 19–25, Jan./Feb. 2000.

[61] K. Asaka, Y. Suzaki, Y. Kawaguchi, S. Kondo, Y. Noguchi, H. Okamoto, R. Iga, and S. Oku, "Lossless electroabsorption modulator monolithically integrated with a semiconductor optical amplifier and a passive waveguide," *IEEE Photon. Technol. Lett.*, vol. 15, pp. 679–681, May 2003.

[62] K. Kawano, M. Kohtoku, M. Ueki, T. Ito, S. Kondoh, Y. Noguchi, and Y. Hasumi, "Polarisation-insensitive travelling-wave electrode electroabsorption (TW-EA) modulator with bandwidth over 50 GHz and driving voltage less than 2 V," *Electron. Lett.*, vol. 33, pp. 1580–1582, Aug. 1997.

[63] L. Mörl, D. Hoffmann, K. Matzen, C. Bornholdt, G. Mekonnen, and F. Reier, "Traveling wave electrodes for 50 GHz operation of opto-electronic devices based on InP," in *Proc. IPRM99 conference*, pp. 385–388, Davos, Switzerland, May 16–20 1999.

[64] K. Tsuzuki, H. Yasaka, T. Ishibashi, T. Ito, S. Oku, R. Iga, Y. Kondo, and Y. Tohmori, "10 Gbit/s, 100-km SMF transmission using an InP-based n-i-n Mach-Zehnder modulator with a driving voltage of 1.0 V_{pp}," in *Techn. Digest Opt. Fiber Comm. (OFC '01)*, p. PDP14, Los Angeles, California, USA, Feb. 22–27 2004.

[65] S. Akiyama, H. Itoh, T. Takeuchi, A. Kuramata, and T. Yamamoto, "Low-chirp 10-Gb/s InP-based Mach-Zehnder modulator driven by 1.2 V_{pp} single electrical signal," in *Proc. 30th Eur. Conf. on Opt. Comm. (ECOC '04)*, p. Mo4.4.6, Stockholm, Sweden, Sep. 5–9 2004.

[66] D. Caprioli, J. den Besten, E. Smalbrugge, T. de Vries, X. Leijtens, M. Smit, R. van Dijk, F. van Vliet, W. Pascher, and J. Binsma, "A 10 Gb/s travelling wave MZ-modulator for integration with a laser," in *Proc. 11th Eur. Conf. on Int. Opt. (ECIO '03)*, pp. 145–148, Prague, Czech Republic, April 2–4 2003.

[67] O. Kjebon, R. Schatz, S. Lourdudoss, S. Nilsson, B. Stålnacke, and L. Bäckbom, "30 GHz direct modulation bandwidth in detuned loaded InGaAsP DBR lasers at 1.55 μm wavelength," *Electron. Lett.*, vol. 33, pp. 488–489, Mar. 1997.

[68] P. Morton, T. Tanbun-Ek, R. Logan, N. Chand, K. Wecht, A. Sergent, and J. P.F. Sciortino, "Packaged 1.55 μm DFB laser with 25 GHz modulation bandwidth," *Electron. Lett.*, vol. 30, pp. 2044–2046, Nov. 1994.

[69] U. Koren, B. Miller, M. Young, T. Koch, R. Jopson, A. Gnauck, J. Evankow, and M. Chien, "High frequency modulation of strained layer multiple quantum well optical amplifiers," *Electron. Lett.*, vol. 27, pp. 62–64, Jan. 1991.

[70] K. Yamada, K. Nakamura, Y. Matsui, T. Kunii, and Y. Ogawa, "Negative chirp electroabsorption modulator using low wavelength detuning," *IEEE Photon. Technol. Lett.*, vol. 7, pp. 1157–1158, Oct. 1995.

[71] D. Zhou, Y. Lu, and J. Wang, "Electroabsorption modulators monolithically integrated with semiconductor optical amplifiers for zero insertion loss utilizing InGaAs/InGaAlAs MQW material," in *Techn. Digest Opt. Fiber Comm. (OFC '01)*, pp. WDD60–1, Anaheim, California, USA, Mar. 17–22 2001.

[72] I. Tafur Monroy, F. Öhman, K. Yvind, L. Jin Christiansen, J. Mørk, C. Peucheret, and P. Jeppesen, "Monolithically integrated reflective SOA-EA carrier re-modulator for broadband access nodes," *Optics Express*, vol. 14, pp. 8060–8064, Sept. 2006.

[73] S. Akiyama, H. Itoh, S. Sekiguchi, S. Hirose, T. Takeuchi, A. Kuramata, and T. Yamamoto, "InP based Mach-Zehnder modulation with capacitively loaded traveling wave electrodes," *J. Lightwave Technol.*, vol. 26, pp. 608–615, Mar. 2008.

[74] A. Umbach, R. Steingruber, A. Seeger, W. Ebert, D. Trommer, and G. Unterborsch, "Ultrafast, high power 1.55 μm side illuminated photodetector with integrated spot size converter," in *Techn. Digest Opt. Fiber Comm. (OFC '00)*, pp. 1–3, Baltimore, Maryland, USA, March 7-10 2000.

[75] A. Tauke-Pedretti, M. Dummer, J. S. Barton, M. N. Sysak, J. W. Raring, and L. A. Coldren, "High saturation power and high gain integrated photoreceivers," *IEEE Photon. Technol. Lett.*, vol. 17, pp. 2167–2169, Oct. 2005.

[76] B. Mason, S. Chandrasekhar, A. Ougazzaden, C. Lentz, J. Geary, L. Buhl, L. Peticolas, K. Glogovsky, J. Freund, L. Reynolds, G. Przybylek, F. Walters, A. Sirenko, J. Boardman, T. Kercher, M. Rader, J. Grenko, D. Monroe, and L. Ketelsen, "Photonic integrated reciever for 40 Gbit/s transmission," *Electron. Lett.*, vol. 38, pp. 1196–1197, Sept. 2002.

[77] M. Smit, S. Oei, F. Karouta, R. Nötzel, J. Wolter, E. Bente, X. Leijtens, J. van der Tol, M. Hill, H. Dorren, D. Khoe, and H. Binsma, "Photonic integrated circuits: where are the limits?," in *Technical Digest Integr. Photon. Res. and Apps. (IPRA '05)*, p. IWB1, San Diego, USA, Apr. 11–Apr. 15 2005.

[78] J. den Besten, D. Caprioli, R. van Dijk, F. van Vliet, W. Pascher, J. Binsma, B. Smalbrugge, T. de Vries, X. Leijtens, and M. Smit, "A velocity-matched traveling-wave Mach-Zehnder modulator on InP," in *Proc. IEEE/LEOS Symposium (Benelux Chapter)*, pp. 65–68, Enschede, The Netherlands, Nov. 2003.

[79] C. Vreeburg, *InP-based Photonic Integrated Circuits for Wavelength Routing and Switching.* PhD thesis, Delft University of Technology, Delft, The Netherlands, 1997. ISBN 90-9011143-3.

[80] C. Herben, C. Vreeburg, D. Maat, X. Leijtens, M. Smit, F. Groen, J. van der Tol, and P. Demeester, "A compact integrated single-PHASAR optical crossconnect on InP," in *Proc. IEEE/LEOS Symposium (Benelux Chapter)*, pp. 42–45, Eindoven, The Netherlands, Nov. 1997.

[81] D. Maat, *InP-based integrated MZI switches for optical communications.* PhD thesis, Delft University of Technology, Delft, The Netherlands, 2001. ISBN 90-9014700-4.

[82] C. Vreeburg, T. Uitterdijk, Y. Oei, M. Smit, F. Groen, J. van der Tol, P. Demeester, and H. Frankena, “Compact integrated InP-based reconfigurable add-drop multiplexer,” in *Proc. IEEE/LEOS Symposium (Benelux Chapter)*, pp. 100–103, Enschede, The Netherlands, Nov. 1996.

[83] L. Babaud, F. Groen, X. Leijtens, M. Bertogna, J. den Besten, Y. Barbarin, Y. Oei, F. Karouta, J. Binsma, and M. Smit, “First integrated continuously tunable AWG-based laser using electro-optical phase shifters,” in *Proc. 12th Eur. Conf. on Int. Opt. (ECIO ’05)*, pp. 156–159, Grenoble, France, April 6–8 2005.

[84] M. Renaud, M. Bachman, and M. Erman, “Semiconductor optical space switches,” *J. of Sel. Topics in Quantum Electron.*, vol. 2, pp. 277–288, June 1996.

[85] L. Xu, X. Leijtens, M. Sander-Jochem, T. de Vries, Y. Oei, P. van Veldhoven, R. Nötzel, and M. Smit, “InP based polarisation insensitive tunable duplexer and integrated reflective transceiver,” in *Proc. 13th Eur. Conf. on Int. Opt. (ECIO ’07)*, p. WA2, Copenhagen, Denmark, April 25–27 2007.

[86] S. Abdalla, S. Ng, P. Barrios, D. Celo, A. Delage, S. El-Mougy, I. Golub, J. He, S. Janz, R. McKinnon, P. Poole, S. Raymond, T. Smy, and B. Syrett, “Carrier injection based digital optical switch with reconfigurable output waveguide arms,” *IEEE Photon. Technol. Lett.*, vol. 16, pp. 1038–1040, Apr. 2004.

[87] J. Vinchant, A. Goutelle, B. Martin, F. Gaborit, P. Pagnod-Roisiaux, J. L. Peyre, J. Le Bris, and M. Renaud, “New compact polarization insensitive 4×4 switch matrix on inp with digital optical switches and integrated mirrors,” in *Proc. 24th Eur. Conf. on Opt. Comm. (ECOC ’93)*, pp. PD13–16, Montreus, Switzerland, Sep. 12–16 1993.

[88] S. Agashe, K. Shiu, and S. Forrest, “Compact polarization insensitive InGaAsP-InP 2×2 optical switch,” *IEEE Photon. Technol. Lett.*, vol. 17, pp. 52–54, Jan. 2005.

[89] J. Nees, S. Williamson, and G. Mourou, “100 GHz travelling-wave electro-optic phase modulator,” *Appl. Phys. Lett.*, vol. 54, no. 20, pp. 1962–1964, 1989.

[90] H. Zappe, *Introduction to Semiconductor Integrated Optics.* Boston: Artech House Publishers, 1995. ISBN 0-089006-789-9.

[91] J. Vinchant, J. Cavaillès, M. Erman, P. Jarry, and M. Renaud, “InP/InGaAsP guided-wave phase modulators based on carrier-induced effects: theory and experiment,” *J. Lightwave Technol.*, vol. 10, no. 1, pp. 63–69, 1992.

[92] B. R. Bennett, R. A. Soref, and J. A. D. Alamo, “Carrier-induced change in refractive index of InP, GaAs, and InGaAsP,” *IEEE J. Quantum Electron.*, vol. 26, pp. 113–122, Jan. 1990.

[93] S. Adachi, *Properties of group-IV, III-V and II-VI semiconductors.* Chichester, England: John Wiley and Sons, 2005. ISBN 0-470-09032-4.

[94] R. Hunsperger, *Integrated Optics: Theory and Technology.* Springer Verlag, 1984.

[95] T. Uitterdijk, *Integrated Electro-Optical Switches On InP.* PhD thesis, Delft University of Technology, Delft, The Netherlands, 1997. ISBN 90-9010549-2.

[96] H. Bach, J. Krauser, H. Nolting, R. Logan, and F. Reinhart, “Electro-optical light modulation in InGaAsP/InP double heterostructures diodes,” *Appl. Phys. Lett.*, vol. 42, no. 8, pp. 692–694, 1983.

[97] W. Franz, “Einfluss eines elektrischen Feldes auf eine optische Absorptionskante,” *Zeitschrift fuer Naturforschung*, vol. 13a, pp. 484–489, 1958.

[98] L. Keldysh, "The effect of a strong electric field on the optical properties of insulating crystals," *Soviet Physics JETP*, vol. 34, pp. 788–790, 1958.

[99] M. van Stralen, K. Haak, and H. Blok, "On the classification of discrete modes in lossy planar waveguides: the modal analysis revisited," *Opt. and Quantum Electron.*, vol. 29, pp. 243–262, 1997.

[100] C. Blaauw, F. Shepherd, and D. Eger, "Secondary ion mass spectrometry and electrical characterization of Zn diffusion in n-type InP," *J. Appl. Phys.*, vol. 66, pp. 605–610, July 1989.

[101] V. Swaminathan, C. Reynolds Jr, and M. Geva, "Effect of Zn on the electro-optical characteristics of metalorganic chemical vapor deposition grown 1.3 μm InGaAsP/InP lasers," *Electron. Lett.*, vol. 32, pp. 661–662, Mar. 1996.

[102] M. Camargo Silva, J. Zucker, L. Carrion, C. Joyner, and A. Dentai, "Growth optimization for p-n junction placement in the integration of heterojunction bipolar transistors and quantum well modulators on InP," *IEEE J. Sel. Topics in Quantum Electron.*, vol. 6, pp. 26–30, Jan./Feb. 2000.

[103] G. Van Gurp, P. Boudewijn, M. Kempeners, and D. Tjaden, "Zinc diffusion in n-type indium phosphide," *J. Appl. Phys.*, vol. 61, no. 5, pp. 1846–1855, 1987.

[104] I. Yun and K. Hyun, "Zinc diffusion process investigation of InP-based test structures for high-speed avalanche photodiode fabrication," *Microelectronics Journal*, vol. 31, 2000.

[105] D. May-Arrioja, P. Likam Wa, I. Shubin, and P. Yu, "Integrated InGaAsP MQW Mach-Zehnder modulator," *Microelectronics Journal*, vol. 39, pp. 660–663, 2008.

[106] M. Bachmann, M. Smit, P. Besse, E. Gini, H. Melchior, and L. Soldano, "Polarization-insensitive low-voltage optical waveguide switch using InGaAsP/InP four-port Mach-Zehnder interferometer," in *Techn. Digest Opt. Fiber Comm. (OFC '93), Vol. 4*, pp. 32–33, San Jose, California, USA, Feb. 21–26 1993.

[107] R. Krähenbühl, R. Kyburz, W. Vogt, M. Bachmann, T. Brenner, E. Gini, and H. Melchior, "Low-loss polarization insensitive InP/InGaAsP optical space switches for fiber optical communications," *IEEE Photon. Technol. Lett.*, vol. 8, pp. 632–634, May 1996.

[108] D. Maat, Y. Zhu, F. Groen, H. van Brug, H. Frankena, and X. Leijtens, "Polarization-independent dilated InP-based space switch with low crosstalk," *IEEE Photon. Technol. Lett.*, vol. 12, pp. 284–286, Mar. 2000.

[109] J. Zucker, K. Jones, T. Chiu, B. Tell, and K. Brown-Goebeler, "Strained quantum wells for polarization-independent electrooptic waveguide switches," *J. Lightwave Technol.*, vol. 10, pp. 1926–1930, Dec. 1992.

[110] A. Sneh, J. Zucker, B. Miller, and L. Stulz, "Polarization insensitive InP based MQW digital optical switch," *IEEE Photon. Technol. Lett.*, vol. 9, pp. 1589–1591, Dec. 1997.

[111] X. Leijtens, P. Le Lourec, and M. Smit, "S-matrix oriented CAD-tool for simulating complex integrated optical circuits," *J. of Sel. Topics in Quantum Electron.*, vol. 2, pp. 257–262, June 1996.

[112] "Polarization independent low crosstalk polymeric AWG-based tunable filter operating around 1.55μm," *IEEE Photon. Technol. Lett.*, vol. 11, pp. 1141–1143, Sept. 1999.

[113] M. Smit and C. van Dam, "PHASAR-based WDM-devices: principles, design and applications," *J. of Sel. Topics in Quantum Electron.*, vol. 2, pp. 236–250, June 1996.

[114] S. R. Selmic, G. A. Evans, T. M. Chou, J. B. Kirk, J. N. Walpole, J. P. Donnelly, C. T. Harris, and L. J. Missaggia, "Single frequency 1550 nm AlGaInAs-InP tapered high power laser with a distributed Bragg reflector," *IEEE Photon. Technol. Lett.*, vol. 14, pp. 890–892, July 2002.

[115] B. Docter, T. Segawa, T. Kakitsuka, S. Matsuo, T. Ishii, Y. Kawaguchi, Y. Kondo, H. Suzuki, F. Karouta, and M. Smit, "Short-cavity DBR laser using vertical groove gratings for large-scale photonic integrated circuits," *IEEE Photon. Technol. Lett.*, vol. 19, pp. 1469–1471, Oct. 2007.

[116] K. Kasunic, "Design equations for the reflectivity of deep-etch distributed Bragg reflector gratings," *J. Lightwave Technol.*, vol. 18, pp. 425–429, Mar. 2000.

[117] N. Ulbrich, G. Scarpa, A. Sigl, J. RoBkopf, G. Bohm, G. Abstreiter, and M.-C. Amann, "High-temperature (T≥470K) pulsed operation of 5.5 μm quantum cascade lasers with high-reflection coating," *Electron. Lett.*, vol. 37, no. 22, pp. 1341–1342, 2001.

[118] L. Soldano and E. Pennings, "Optical multi-mode interference devices based on self-imaging: Principles and applications," *J. Lightwave Technol.*, vol. 13, pp. 615–627, Apr. 1995.

[119] T. Koch and U. Koren, "Semiconductor photonic integrated circuits," *IEEE J. Quantum Electron.*, vol. 27, pp. 641–653, Mar. 1991.

[120] R. Hanfoug, M. Smit, L. Augustin, Y. Barbarin, J. van der Tol, E. Bente, F. Karouta, D. Rogers, Y. Oei, and X. Leijtens, "A multimode interference coupler with low reflections," in *Proc. IEEE/LEOS Symposium (Benelux Chapter)*, pp. 97–100, Mons, Belgium, Dec. 2005.

[121] P. Besse, J. S. Gu, and H. Melchior, "Reflectivity minimization of semiconductor laser amplifiers with coated and angled facets considering two dimensional beam profiles," *IEEE J. Quantum Electron.*, vol. 27, no. 6, pp. 1830–1836, 1991.

[122] J. Thomson, H. Summers, P. Hulyer, P. Smowton, and P. Blood, "Determination of single-pass optical gain and internal loss using a multisection device," *Appl. Phys. Lett.*, vol. 75, no. 17, pp. 2527–2529, 1999.

[123] D. Ackerman, L. Zhang, L.-P. Ketelsen, and J. Johnson, "Characterizing residual reflections within semiconductor lasers, integrated sources, and coupling optics," *IEEE J. Quantum Electron.*, vol. 34, pp. 1224–1230, July 1998.

[124] Y. Barbarin, E. Bente, C. Marquet, E. Leclère, T. de Vries, P. van Veldhoven, Y. Oei, R. Nötzel, M. Smit, and J. Binsma, "Butt-joint reflectivity and loss in InGaAsP/InP waveguides," in *Proc. 12th Eur. Conf. on Int. Opt. (ECIO '05)*, pp. 406–409, Grenoble, France, April 6–8 2005.

[125] J. Tang and K. Shore, "Amplification of strong picosecond optical pulses in semiconductor optical amplifiers," *IEE Proc.-Optoelectron.*, vol. 146, pp. 45–50, Feb. 1999.

[126] Y. Barbarin, *1.55 μm integrated modelocked semiconductor lasers.* PhD thesis, Technische Universiteit Eindhoven, Eindhoven, The Netherlands, 2007. ISBN 978-90-386-2013-8.

[127] Y. Barbarin, E. Bente, L. Mussard, G. Servanton, Y. Oei, R. Nötzel, and M. Smit, "Gain measurements of Fabry-Perot InP/InGaAsP lasers using an ultra high resolution spectrometer," *Appl. Opt.*, vol. 45, no. 35, pp. 9007–9012, 2006.

[128] R. Olshansky, C. Su, J. Manning, and W. Powazinik, "Measurement of radiative and nonradiative recombination rates in InGaAsP and AlGaAs light sources," *IEEE J. Quantum Electron.*, vol. 20, pp. 838–854, Nov. 1984.

[129] K. Petermann, *Laser diode modulation and noise.* the Netherlands: Kluwer Academic Publishers, 1988.

[130] G. Grosskopf, R. Ludwig, R. Schnabel, and H. G. Weber, "Characteristics of semiconductor laser optical amplifier as phase modulator," *Electron. Lett.*, vol. 25, no. 17, pp. 1188–1189, 1989.

[131] N. Storkfelt, B. Mikkelsen, D. Olesen, M. Yamaguchi, and K. Stubkjaer, "Measurement of carrier lifetime and linewidth enhancement factor for 1.5 μm ridge waveguide laser amplifier," *IEEE Photon. Technol. Lett.*, vol. 3, no. 7, pp. 632–634, 1991.

[132] C. Joergensen, T. Durhuus, C. Braagaard, B. Mikkelsen, and K. Stubkjaer, "4 Gb/s optical wavelength conversion using semiconductor optical amplifier," *IEEE Photon. Technol. Lett.*, vol. 5, no. 6, pp. 657–659, 1993.

[133] T. Durhuus, B. Mikkelsen, C. Jorgensen, S. Danielsen, and K. Stubkjaer, "All-optical wavelength conversion by semiconductor optical amplifiers," *J. Lightwave Technol.*, vol. 14, pp. 942–945, 1996.

[134] M. L. Nielsen and J. Mørk, "Bandwidth enhancement of SOA-based switches using optical filtering: theory and experimental verification," *Optics Express*, vol. 14, pp. 1260 – 1265, Feb. 2006.

[135] J. Mørk, A. Mecozzi, and G. Eisenstein, "The modulation response of a semiconductor laser amplifier," *IEEE J. Sel. Topics in Quantum Electron.*, vol. 5, pp. 851–860, June 1999.

[136] H. Ghafouri-Shiraz, *Fundamentals of laser diode amplifiers.* England: John Wiley & Sons, 1995. ISBN 0-471-95872-7.

[137] Y. Yamamoto, S. Saito, and T. Mukai, "AM and FM quantum noise in semiconductor lasers–part ii: comparison of theoretical and experimental results for AlGaAs lasers," *IEEE J. Quantum Electron.*, vol. 19, no. 1, pp. 47–58, 1983.

[138] M. Heck, *Ultrafast Integrated Semiconductor Laser Technology at 1.55 μm.* PhD thesis, Eindhoven University of Technology, Eindhoven, The Netherlands, 2008. ISBN 978-90-386-1694-0.

[139] T. Yamatoya and F. Koyama, "Noise suppression of spectrum-sliced light using semiconductor optical amplifier," *Electronics and Communications in Japan, Part2*, vol. 86, no. 2, pp. 417–423, 2003.

[140] L. Augustin, *Polarization Handling in Photonic Integrated Circtuits.* PhD thesis, Technische Universiteit Eindhoven, Eindhoven, The Netherlands, 2008. ISBN 978-90-386-1854-8.

[141] J. den Besten, R. Broeke, M. van Geemert, J. Binsma, F. Heinrichsdorff, T. van Dongen, E. Bente, X. Leijtens, and M. Smit, "An integrated 4 × 4-channel multi-wavelength laser on InP," *IEEE Photon. Technol. Lett.*, vol. 15, pp. 368–370, Mar. 2003.

[142] Y. Barbarin, E. Bente, M. Heck, J. den Besten, G. Guidi, Y. Oei, J. Binsma, and M. Smit, "Realization and modeling of a 27-GHz integrated passively mode-locked ring laser," *IEEE Photon. Technol. Lett.*, vol. 17, pp. 2277–2279, Nov. 2005.

[143] J. Schlafer, C. Su, W. Powazinik, and R. Lauer, "20 GHz bandwidth InGaAs photodetector for long wavelength microwave optical links," *Electron. Lett.*, vol. 21, no. 7, pp. 496–497, 1985.

[144] K. Kato, "Ultrawide-band/high-frequency photodetectors," *IEEE Transactions on Microwave Theory and Techniques*, vol. 47, pp. 1265–1281, July 1999.

[145] H. Jiang and P. Yu, "Equivalent circuit analysis of harmonic distortions in photodiode," *IEEE Photon. Technol. Lett.*, vol. 10, pp. 1608–1610, Nov. 1998.

[146] S. Dimitrijev, *Understanding semiconductor devices.* OXFORD university press, 2000.

[147] K. Steenbergen, *High Capacity Integrated Optical Receivers.* PhD thesis, Delft University of Technology, Delft, The Netherlands, 1997. ISBN 90-9010676-6.

[148] H. Neitzert, R. Fang, M. Kunst, and N. Layadi, "CH_4/H_2 reactive ion etching induced damage of InP," *Journal of Vaccuum Science Technology*, vol. 18, no. 6, pp. 2803–2807, 2000.

[149] J. den Besten, *Integration of Multiwavelength Lasers with Fast Electro-Optical Modulators.* PhD thesis, Technische Universiteit Eindhoven, Eindhoven, The Netherlands, 2004. ISBN 90-386-1643-0.

[150] E. Skogen, J. Barton, S. Denbaars, and L. Coldren, "A quantum-well-intermixing process for wavelength-agile photonic integrated circuits," *IEEE J. Sel. Topics in Quantum Electron.*, vol. 8, pp. 863–869, Jul./Aug. 2002.

[151] N. Futakuchi, X. Song, D. Miyashita, M. Kato, and Y. Nakano, "Fabrication of InGaAsP/InP Mach-Zehnder interferometer optical amplifier switches by metalorganic vapor phase selective area epitaxy," in *Proc. IPRM01 conference*, pp. 583–586, Nara, Japan, May 14–18 2001.

[152] L. Xu, M. Gokhale, P. Studenkov, J. Dries, C.-P. Chao, D. Garbuzov, and S. Forrest, "Monolithic integration of an InGaAsP-InP MQW Laser/Waveguide using a Twin-Guide structure with a mode selection layer," *IEEE Photon. Technol. Lett.*, vol. 9, pp. 569–571, May 1997.

[153] J. Binsma, M. van Geemert, F. Heinrichsdorff, T. van Dongen, R. Broeke, and M. Smit, "MOVPE waveguide regrowth in InGaAsP/InP with extremely low butt joint loss," in *Proc. IEEE/LEOS Symposium (Benelux Chapter)*, pp. 245–248, Brussels, Belgium, Dec. 2001.

[154] J. Marsh, O. Kowalski, S. McDougall, B. Qiu, A. McKee, C. Hamilton, R. D. L. Rue, and A. C. Bryce, "Quantum well intermixing in material systems for 1.5 μm (invited)," *J. Vac. Sci. Technol. B*, vol. 16, pp. 810–816, Apr. 1998.

[155] D. G. Ivey and P. Jian, "Microstructural analysis of Au/Pt/Ti contacts to p-type InGaAs," *Journal of Materials Science: Materials in Electronics*, vol. 6, pp. 219–227, 1995.

[156] S. N. G. Chu, A. Katz, T. Boone, P. M. Thomas, V. G. Riggs, W. C. Dautremont-Smith, and W. D. Johnston, Jr., "Interfacial microstructure and electrical properties of the Pt/Ti ohmic contact in p-$In_{0.53}Ga_{0.47}As$ formed by rapid thermal processing," *J. Appl. Phys.*, vol. 67, pp. 3754–3760, July 1990.

[157] A. Katz, B. Weir, and W. Dautremont-Smith, "Au/Pt/Ti contact to p-$In_{0.53}Ga_{0.47}As$ and n-InP layers formed by a single metallization common step and rapid thermal processing," *J. Appl. Phys.*, vol. 68, pp. 1123–1128, May 1990.

[158] R. Broeke, *A Wavelength Converter Integrated with a Discretely Tunable Laser for Wavelength Division Multiplexing Networks.* PhD thesis, Delft University of Technology, Delft, The Netherlands, 2003.

[159] R. Hanfoug, L. Augustin, Y. Barbarin, J. van der Tol, E. Bente, F. Karouta, D. Rogers, S. Cole, Y. Oei, X. Leijtens, and M. Smit, "Reduced reflections from multimode interference couplers," *Electron. Lett.*, vol. 42, pp. 465–466, Apr. 2006.

[160] N. Olsson, "Lightwave systems with optical amplifiers," *J. Lightwave Technol.*, vol. 7, pp. 1071–1082, July 1989.

Nomenclature

AON	Active Optical Network
AR	Anti-Reflection
ASE	Amplified Spontaneous Emission
AWG	Array Waveguide Grating
BBP	BroadBand Photonics
BM	Burst Mode
BPF	Band Pass Filter
COBRA	COmmunication technologies; Basic Research and Applications
CW	Continuous Wave
CWDM	Coarse Wavelength Division Multiplexing
DBR	Distributed Bragg Reflector
DFB	Distributed FeedBack
EA	Electro-Absorption
EDFA	Erbium Doped Fiber Amplifier
EO	Electro-Optical
FP	Fabry Perot
FSR	Free Spectral Range
FTTH	Fiber-to-the-home
GSG	Ground-Signal-Ground
ICP	Inductively Coupled Plasma

ISDN	Integrated Services Digital Network
LCA	Lightwave Component Analyzer
MI	Michelson Interferometer
MMI	Multi-Mode Interference
MOVPE	Metal Organic Vapour Phase Epitaxy
MZI	Mach-Zehnder Interferometer
PDL	Polarization Dependent Loss
PDV	Polarization Dependence in switching-Voltage
PECVD	Plasma Enhanced Chemical Vapor Deposition
PHM	Phase Modulator
PIC	Photonic Integrated Circuit
PLC	Planar Lightwave Circuit
PON	Passive Optical Network
PRBS	Pseudo-Random-Binary-Sequence
PWD	Passive Waveguide Devices
QWI	Quantum Well Intermixing
RF	Radio Frequency
RIE	Reactive Ion Etching
RSOA	Reflective Semiconductor Optical Amplifier
Rx	Receiver
SAG	Selective Area Growth
TBEM	To-Be-Etched-Material
TFF	Thin Film Filter
WASMF	WAveguide Scattering Matrix Formalism
WD	Wavelength Duplexer
WGPD	WaveGuide PhotoDetector
WGPHS	WaveGuide PHase Shifter

Summary

Monolithic Integrated Reflective Transceiver in Indium Phosphide

The work presented in this thesis is about an InP based monolithic integrated reflective transceiver meant for use in future fiber access networks at the user site. The motivation for this research results from the users' demands for ever-increasing bandwidth at low cost of operation, administration and maintenance. We investigated solutions to these challenges with a network concept using a dynamically reconfigurable optical network topology with a wavelength router and a colorless optical network unit. This work focuses on developing the optical part of the optical network unit, a reflective transceiver.

This reflective transceiver consists of three basic components: a tunable wavelength duplexer, a photodetector and a reflective modulator. The tunable wavelength duplexer separates two wavelengths, one for the downstream and one for the upstream signals, and guides them to the photodetector and the reflective modulator. The photodetector detects the downstream data. The reflective modulator modulates the light carrier with the upstream data and reflects it back to the network.

The integrated transceiver was realized by monolithically integrating these components on a common active-passive butt-joint layer stack based on InP technology. This approach not only offers high bandwidth for both downstream data and upstream data, but also lowers the cost of the device and the network operation because of the colorless operation at the user site.

The main results obtained within this work are summarized as follows: an efficient and polarization insensitive tunable wavelength duplexer was realized; a new method to fabricate a reflective SOA has been proposed and demonstrated; a high performance waveguide photodetector based on SOA layer stack was successfully fabricated; a low cost photoreceiver which includes an InP photodetector and a SiGe amplifier was demonstrated; a working monolithic integrated reflective transceiver based on InP was successfully realized and demonstrated; two monolithic integrated transceivers aiming for higher bandwidth have been designed and fabricated. In addition, a novel MMI reflector has been proposed and realized with high reflectivity.

This work was funded by Dutch Ministry of Economic Affairs through the Freeband Project Broadband Photonics Access, the Smartmix project Memphis and the NRC Photonics.

Acknowledgments

Writing this part is like writing my memoirs of the last four years. I am glad that I can borrow such an opportunity to show my gratitude to all of you.

First I would like to thank Prof. Meint Smit, who gave me a chance to get into the field of photonic integrated circuits in InP, and to fulfill my dream of becoming a researcher.

My special thanks are given to my daily supervisor and copromotor, Dr. Xaveer Leijtens. If Meint brought me in the field of PIC, you were the one who guided me through. No matter when and where, you were always there. When I obtained good results, you were the first one to share my cheer, and when things went wrong, you were the first one to help me analyze the problems. Without you, I would not be able to finish my research on time, publish the papers and get awarded in the conferences. It was also you who let me feel that "Boss" could be a "friend".

I am thankful to all my doctorate committee members for participating in my defense and their interest in my work. I appreciate all your expert comments on my draft thesis which contributed greatly to the value of my thesis.

Erwin Bente, thank you for your making all the measurement setup "intelligent" which saved us a lot of time in the optic laboratory (OLA). I am grateful for your help in the numerical model to analyze the reflective SOA. Jos van der Tol, your quick thinking have impressed me, and your comments on my slides and posters contributed a lot to all the presentations I gave in the conferences. Siang Oei and Fouad Karouta, you two made the technology possible for the integration. Siang, you were always there to help solve technology problems. Fouad, though I have beaten you twice in table tennis, I have to admit that you won more often. Hans Moerman, thank you for all your help in solving my computer problems and the adjustment of my working place.

All the chips I made during the last four years would not have worked without you, my clean room technician colleagues. Ben van Roy, thank you for your guiding me around the clean room at my first working day at OED, and showing me one of the most important things: the fastest exit route when emergent situations would happen. Luckily, those routes were never needed. Barry Smalbrugge, you are a golden heart man, always willing to help. You have been dealing with the most "dangerous" things (DEGUSSA!!) for us in the clean room, and you have cleaved most of samples for all the Ph.D students because we know Barry does it best. Moreover, I have been always wondering how you could write so many songs for everybody. Tjibbe de Vries, you are the "Batman" in the clean room. No matter which problem popped out, your name was given as the first answer. Erik Jan Geluk, you are the best SEM “camera” and “treasure” man for FC2000. No matter how difficult SEM or SEI picture is, you can make the best image out, and you are in charge of gold, platinum and titanium. Besides, you help me get experienced with the SEM and the FC2000 machine. Kitty Sander, although we have only worked together during the first two years, thank you for your help in the clean room. Huub and Jeroen, you joined the OED group when I was about to finish my Ph.D. It is nice to get to know you and I hope that we can cooperate in the future.

No material, no chips. Therefore I would like to thank Richard Nötzel and René van Veldhoven from the Physics Department for the material growth.

A lot of measurements have been carried out under the support from TUE/ECO group. Patryk, I am very glad to cooperate with you during the last four years. Oded, Nicola, Kevin, Piet and Hyundo, thank you all for the support and nice discussions.

Outside TUE, I would like to thank all the BBP project partners for very close cooperation, and helpful discussion in the last four years.

Among all the peers in the OED group, first I would like to thank Jan Hendrik who helped me start with the mask design and Fabry-Perot measurement. Pietro, we had a lot in common: we shared the same promotor and the same supervisor, we finished our Ph.D almost at the same time, and the most important is that we had almost all the lunch in Kennisspoort together where we exchanged our different views on the “mooie dingen”. I wish you success in the USA. Martijn, thank you for your nice and inspirational discussions during the last four years, and don’t worry about your teasing me, which you mentioned in your thesis, since I have never taken it seriously. Yohan, firstly thank you for your help in the OLA when I just started my Ph.D, and I really enjoyed the sport nights we played badminton together. Mahmoud, thank you for your help during my first two years when you were in our group. Martin, I really admire your diligence and dedication to your cutting-edge research.

Mirvais, Stefano, Youcai and Bauke, you have been my officemates during the last four years, and I enjoyed all the discussions with you on work and life. Bauke and Milan, I wish you great success with your Ph.D research. Boudwijn, cooperating with you is a pleasure and good luck with your thesis writing and the coming defense. Frederic, Els, Uzma, Rabah, Luc, Jose, and Genia, thank you for your willingness to help me during the last four years. Jing, Saeed and Rui, I wish you three enjoying the atmosphere at OED group and success in the coming years.

For a non-EU foreigner, there are always a lot of government formalities to go through. Therefore I would like to express my gratitude to Yvonne, Femke, Susan, José, and Els for their help in handling those administration work. Els, you were like a mother taking care of me when we lived together. Besides, you helped me a lot in Dutch.

Dilna, my sister in the Netherlands, we had so many chats at home, cooked so many different delicious foods and danced Salsa together. I also would like express my thanks to the members of the Chinese Girls’ Dancing Group at TUE, Jing Li, Shudong Chen and Xiaohan Wang, with whom I shared a lot of joy in dancing, chatting and public dancing performances.

Family is the backbone in my life. I am a specially lucky one since I have really big families in both China and the Netherlands. Baba and Mama, I never said thanks or love to you face-to-face due to typical Chinese reserved manners, and these words are also far from enough to express my true love to you. Thank you for always being there and your full support through all my life. Unlike most Chinese families, I have three dearest elder sisters, who are always tolerant, supportive and “spoiling” me in doing all the housework and taking care of me at all the aspects when I am in China. My lovely nephew (Tairan) and niece (Weishi) are the delight of my family, and only before them I could pretend to show my Chinese “majesty” as being an aunt. My family in the Netherlands: Oma, ik wens dat we nog lang samen kunnen puzzelen. Daddy and Mum, you are my parents-in-law, but have been like my own parents to support and love me in my daily life since I came to Europe. Judith and Rene, thank you for your all-along support, and Julia, “je bent altijd mijn kleine grote vriendin”.

Brian, my dearest husband, is the one who shares my life. Thank you for your love, constant support, patience and tolerance.

Curriculum Vitæ

Ling Xu was born in Shucheng, China in November 1978. In September 1994, she entered Shanghai Tiedao University (now Tongji University since the year of 2000) to pursue her Bachelor degree in Automatic Control. After graduation in June 1998, she joined Nanjing Audio Equipment Co.,Ltd as an International Marketing Engineer, and later Elgin Chemical Corporation as a General Manager Assistant until September 2001.

In March 2004 she received her Master degree in Communication and Information System from Shanghai University, China. Her Master thesis is entitled "Polarization maintaining optic fibres and their applications in the optic fibre electrical current sensor". After her study, she started working for Siemens AG (Shanghai Office) as a Sales Representative for low voltage products.

Since March 2005, she has been working towards the Ph.D degree within the field of photonic integrated circuits in the Opto-Electronic Devices group at Eindhoven University of Technology.

Since April 2009, she continues her research in integrated optics for sensor application at Holst Centre, the Netherlands.

List of publications

- L.Xu, X.J.M. Leijtens, B. Docter, T. de Vries, E. Smalbrugge, F. Karouta and M.K. Smit, “MMI-Reflector: A Novel On-chip Reflector for Photonic Integrated Circuits,” in Proc. 35th Eur. Conf. on Opt. Comm. (ECOC ’09), Vienna, Austria, Sept. 20-24, 2009
- L. Xu, M. Nikoufard, X. Leijtens, T. de Vries, E. Smalbrugge, R. Nötzel, Y. Oei, andM. Smit, “High performance InP based photodetector in an amplifier layer stack on semi-insulating substrate,” IEEE Photon. Technol. Lett., Vol.20, issue 23, pp1941-1943, 2008
- L. Xu, X. Leijtens, P. Urban, E. Smalbrugge, T. de Vries, Y. Oei, R. Nötzel, H. de Waardt, and M. Smit, “Novel reflective SOA with MMI-loop mirror based on semiinsulating InP” in Proc. IEEE/LEOS Symposium (Benelux Chapter), Enschede, The Netherlands, Nov. 27-28, 2008
- L. Xu, M. van Heijningen, G. van der Bent, P. Urban, X. Leijtens, E. Smalbrugge, T. de Vries, R. Notzel, Y. Oei, H. de Waardt, and M. Smit, “4 Gbit/s hybrid InP-SiGe photoreceiver for the access network,” in Proc. IEEE/LEOS Symposium (Benelux Chapter),), Enschede, The Netherlands, Nov. 27-28, 2008
- L. Xu, X. Leijtens, P. Urban, E. Smalbrugge, T. de Vries, Y. Oei, R. Nötzel, H. de Waardt, and M. Smit, “InP based monolithic integrated colorless reflective transceiver,” in Proc. 14th Eur. Conf. on Int. Opt. (ECIO ’08), Post-deadline papers, X. Leijtens, Ed. Eindhoven, the Netherlands, June 11–13 2008, pp. FrPD4, 13–16, ISBN 978-90-386-1318-5
- L. Xu, M. van Heijningen, G. van der Bent, P. Urban, X. Leijtens, E. Smalbrugge, T. de Vries, R. Notzel, Y. Oei, H. de Waardt, and M. Smit, “Hybrid InP-SiGe photoreceiver for the access network,” in Proc. IEEE/LEOS Annual Meeting, Newport Beach, CA, USA, Nov.9-13, 2008
- M. Nikoufard, L. Xu, X. Leijtens, T. de Vries, E. Smalbrugge, R. Nötzel, Y. Oei, and M. Smit, “High bandwidth waveguide photodetector based on an amplifier layer stack on an active-passive semi-insulating InP at 1.55 μm,” in Proc. 14th Eur. Conf. on Int. Opt. (ECIO) 2008, X. Leijtens, Ed. Eindhoven, The Netherlands, June 11–13 2008, pp. 143– 146, ISBN 978-90-386-1317-8

- L.Xu, X. Leijtens, M. Sander-Jochem, T. deVries, Y. Oei, P. vanVeldhoven, R. Nötzel, and M. Smit, "1.55 μm extremely efficient and polarization insensitive tunable mach-zehnder wavelength duplexer based on an InGaAsP/InP ridge waveguide structure," in Proc. SPIE Asia Pacific Optical Communications (APOC). Wuhan, China, November 1–5 2007

- L. Xu, X. Leijtens, M. Sander-Jochem, T. de Vries, Y. Oei, P. van Veldhoven, R. Nötzel, and M. Smit, "InP based polarisation insensitive tunable duplexer and integrated reflective transceiver," in Proc. 13th Eur. Conf. on Int. Opt. (ECIO '07). Copenhagen, Denmark, April 25–27 2007, p.WA2.

- L. Xu, X. Leijtens, T. de Vries, Y. Oei, P. van Veldhoven, R. Nötzel, and M. Smit, "Eficient deeply etched InP/InGaAsP phase shifters with low dark current," in Proc. IEEE/LEOS Symposium (Benelux Chapter). Brussels, Belgium, Dec. 2007, pp. 115–118

- P. Urban, E. Klein, L. Xu, E. Pluk, A. Koonen, G. Khoe, and H. deWaardt, "1.25-10 Gbit/s reconfigurable access network architecture," in International Conference on Transparent Optical Networks (ICTON '07). Rome, Italy, July 1–5 2007, pp. 293–296.

- L. Xu, X. Leijtens, J. den Besten, M. Sander-Jochem, T. de Vries, Y. Oei, P. van Veldhoven, R. Nötzel, and M. Smit, "An integrated transceiver based on a reflective semiconductor optical amplifier for the access network," in Proc. IEEE/LEOS Symposium (Benelux Chapter). Eindhoven, The Netherlands, Nov. 2006, pp. 77–80

- L. Xu, X. Leijtens, M. Sander-Jochem, Y. Oei, and M. Smit, "Modeling and design of a high-speed reflective transceiver for the access network," in Proc. IEEE/LEOS Symposium (Benelux Chapter). Mons, Belgium, Dec. 2005, pp. 137–140